

Sheffield Hallam University

The production of low-cost solar grade silicon from rice husk.

ORHOLOR, Ayomanor Benedict.

Available from the Sheffield Hallam University Research Archive (SHURA) at:

<http://shura.shu.ac.uk/23502/>

A Sheffield Hallam University thesis

This thesis is protected by copyright which belongs to the author.

The content must not be changed in any way or sold commercially in any format or medium without the formal permission of the author.

When referring to this work, full bibliographic details including the author, title, awarding institution and date of the thesis must be given.

Please visit <http://shura.shu.ac.uk/23502/> and <http://shura.shu.ac.uk/information.html> for further details about copyright and re-use permissions.

SHEFFIELD HALLAM UNIVERSITY
ADSETTS LEARNING CENTRE
CITY CAMPUS, SHEFFIELD
S1 1WB

102 114 787 7



ProQuest Number: 10760399

All rights reserved

INFORMATION TO ALL USERS

The quality of this reproduction is dependent upon the quality of the copy submitted.

In the unlikely event that the author did not send a complete manuscript and there are missing pages, these will be noted. Also, if material had to be removed, a note will indicate the deletion.



ProQuest 10760399

Published by ProQuest LLC (2018). Copyright of the Dissertation is held by the Author.

All rights reserved.

This work is protected against unauthorized copying under Title 17, United States Code
Microform Edition © ProQuest LLC.

ProQuest LLC.
789 East Eisenhower Parkway
P.O. Box 1346
Ann Arbor, MI 48106 – 1346

**The Production of Low-Cost Solar Grade Silicon from
Rice Husk**

Ayomanor Benedict Orholor

**A thesis submitted in partial fulfilment of the requirements of
Sheffield Hallam University for the degree of
Doctor of Philosophy**

January 2017

Declaration

I hereby declare that the work described in this thesis is my own work, done by me and has not been submitted for any other degree anywhere.

Ayomanor Benedict Orholor

Acknowledgement

To God be the glory. I wish to express my profound gratitude and thanks to all who were instrumental to my completion of the research that resulted to this thesis. I sincerely thank the former Rector Dr. P. Salami of the Federal Polytechnic Nasarawa, Nigeria, for nominating me for this programme. I also thank the present Rector Prof. S. S. Abdulkadir of Federal Polytechnic Nasarawa, for upholding my nomination. I thank the Registrar Hajia F. J. Sabo and other staffs of the Polytechnic for their role in my nomination for this programme. In a special way, I thank the Tertiary Education Trust Fund (TETFUND) Nigeria, for actually funding this programme and a sincere appreciation to Mr. S. Iyen and Dr. Hilda Oyekwere of Federal Ministry of Education, Abuja, Nigeria for their effort toward my nomination.

My profound gratitude and thanks go to my director of studies and principal supervisor, Dr Karen Vernon Parry for giving me the opportunity to work on this project and under their joint supervision throughout my study. I remain indebted to her for training and mentoring me in this field. I also thank my 2nd supervisor, Dr. Hassan Aseel for his assistance and support. I appreciate the encouragement from my former and present colleagues in MERI, Dr. Obi Kingsley, Dr. A. Alkali, Dr M. Abdel, Dr. T. Pham Mrs C. Ozoegwu, Dr. O. I. Olusola, Dr. M. L. Madugu, Shakeel Ahmed, Mohammed Abubakar, Maruf Raheem, Badmos Tajudeen and A. Ogunsanwo. Special thanks to Prof. D. J. Cleaver and Dr. K. Doherty for their useful advice and to H. Corrie, T. Rachel and H. Gail for the support and assistance.

I wish to acknowledge the following individuals for providing me with training and technical guidance on the analytical techniques presented in this work; Z. Deeba, V. Patel, R. Burton, S. Creasy, Dr. A. Bell, A. Paul, K. Burak, L. Daniel and Dr. F. Cleg all of MERI, Sheffield Hallam University are thanked for assisting with SEM, XRF, EDS, RAMAN SIMS and XRD measurements. I will also use this opportunity to thank Dr. J. Hywel and Dr. R. Aucklah for their assistance with controlled atmosphere furnace as Xera Carb, Sheffield, UK.

My family is not left out. My love and special thanks to my lovely wife, Grace Elohor Ayomanor for helping me morally and financially during the research period and for her endurance of the late night hours I had to spend in the laboratory or Library away.

from her and our unborn baby Reign Oghenevwede Ayomanor. I appreciate the encouragement I received from all my brothers: Matthew Omagbemi, Rev. Vincent Omagbemi, Kenneth Ayomanor, Happy Wilkie, Kingsley Okpogoro and Felix Ayomanor; My sisters: Stella Odunwa, Blessing Ademi, Gloria Ayomanor, Vera Ayomanor, Patricia Ayomanor and Precious Ayomanor and to my relatives and friends: Bros Godwin Uweru, Elijah Ogunsanya, Freeborn Smart, Father Jeff Omosoga, Matthew Bayford, Samson Efemini, Raymond Achi, Sunny Idigu and Daniel Kogoro In a special way I say thank you and I really appreciate those who must have in one way or the other contributed financially to my research.

Dedication

This work is dedicated to Almighty God for his grace and mercy throughout the research period and to Late Barrister A. E. Ayomanor/ Late Madam Victoria Chokor.

Ayomanor Benedict Orholor

List of Conferences/Publications

- B. O. Ayomanor, O. S. Elsherif, K. D. Vernon-Parry, A. D. Onojah and M. Murray, Characterization of Crystalline Metallurgical-Grade Silicon prepared from Rice Husk Ash, UK Semiconductors & UK Nitrides Consortium Summer Meeting, 4-5 July 2012, Sheffield, United Kingdom. (Poster presentation B-P-3).
- B. O. Ayomanor, K. D. Vernon-Parry, Purification of metallurgical-grade silicon prepared from rice husk ash using aluminium as impurity getter, Gettering and Defect Engineering in Semiconductor Technology XV, 22-27 September 2013, Oxford, United Kingdom. (Attended)
- B. O. Ayomanor, K. D. Vernon-Parry, Potential Synthesis of Solar-Grade Silicon from Rice Husk Ash, Gettering and Defect Engineering in Semiconductor Technology XV, 20-25 September 2015, Bad Staffelstein, Germany. (poster presentation)
- B. O. Ayomanor, K. D. Vernon-parry, Purification of Rice Husk Ash up to Solar-Grade Silicon Using the Hydrometallurgical Method, 7th International Hydrometallurgy Conference, 22-25 June 2014, Victoria, British Columbia, Canada. (Poster presentation)
- 54TH Annual Conference of Metallurgists, hosting America's Conference on Aluminum Alloys, 23-26 August 2015, Toronto, ON, Canada. (Attended)
- Ayomanor, B. O., & Vernon-Parry, K. (2016). Potential Synthesis of Solar-Grade Silicon from Rice Husk Ash. Solid State Phenomena, 242.
- MERI Symposium Day - Sheffield Hallam University, 21 June, 2012. (Poster presentation)
- MERI Symposium Day - Sheffield Hallam University, 23 May, 2013. (Oral presentation)

Abstract

Rice husk, an agricultural waste product obtained in large quantities in many countries including Nigeria, is very rich in siliceous materials. It has been known for several decades that, with careful processing, rice husk can be a source of metallurgical grade silicon. In Nigeria this would have the benefit of transforming large volumes (> 600,000 tonnes per annum) of agricultural waste into a partial solution to that country's issue with energy distribution.

In this work, silica of between 95.24% and 98.03% purity has been prepared from RHA (ashed at 700°C, 800°C, 900°C and 1000°C for either 5hrs or 12 hours). Additionally, the silica value was boosted by use of hydrometallurgical purification process. The improved purification processes yielded 99.18% and 99.51% of silica. Removal of many metallic trace impurities was significant: MgO (98.33%), Al₂O₃ (96.77%), Mn₃O₄ (80%), SO₃ (55%), CaO (97.92%), B (73.91%) and P₂O₅ (88.34%) are removed by leaching. Impurities such as Na₂O, Fe₂O₃ and K₂O are almost completely leached out beyond detection of the XRF after the final processing step.

Metallothermic reduction of the purified RHA with magnesium was investigated and post hydrometallurgical purification to further eliminate all soluble impurity. XRF and EDS showed P was reduced below their detection limit. The XRD showed that RHA transformation from amorphous to crystalline material depends on temperature and time. TEM investigation shows that derived silicon consist of agglomerate polycrystalline materials. TG analysed the the devolatilization, combustion and mass gain in RHA. The effectiveness of each stage of hydrometallurgical process in removing impurity elements was presented. While the hydrometallurgical purification of RHA is effective in removing impurities such as Ti and Fe to levels below the limits of detection of X-ray fluorescence (XRF), B levels was reduced to 22 ppm. Solvent refining process was done using Sn as a selected gettering metal for B in silicon.

List of Tables	xv
Chapter 1: Introduction.....	1
1.1 General background of study	1
1.2 Rice (<i>Oriza Sativa</i>)	2
1.2.1 Rice husk (RH)	3
1.2.2 Rice Husk Ash (RHA)	3
1.3 Silicon.....	4
1.4 Aim.....	5
1.5 Objectives.....	5
1.6 Justification/Significance	5
1.7 Summary	6
2 LITERATURE REVIEW	9
2.1 Silicon from quartz, silicon solar cells and silicon solar cell technology	9
2.2 Solar Cell.....	10
2.3 Global energy supply and consumption	11
2.4 Non-renewable and renewable energy sources	14
2.5 Biomass	15
2.5.1 Solar Energy.....	17
2.6 Solar radiation and air mass coefficients.....	17
2.7 Solar energy conversion and technologies	20
2.7.1 Photo-thermal solar energy conversion	20
2.7.2 Thermo-photovoltaic solar energy conversion	21
2.7.3 Photo-chemical solar energy conversion	24
2.7.4 Photovoltaic solar energy conversion	24
2.8 Production of solar grade silicon.....	28
2.8.1 Siemens/Trichlorosilane (TCS).....	28
2.8.2 Silane/ Fluidized bed reactor (FBR)	30
2.9 Upgrading metallurgical grade silicon (UMG-Si): Emerging technology?	31
2.10 Production of MG-Si silicon from rice husk ash.....	32
2.10.1 Silica Preparation from Rice Husk Ash.....	32
2.10.2 Thermal Decomposition of Rice Husk	32
2.10.3 Rice Husk Ash Utilization.....	34
2.10.4 Ash Analysis	36
2.11 Effect of Various Impurities in Silicons	37

2.11.1 Atoms from Group IIIA (B, Al, Ga...) or VA (P, As, Sb...)	38
2.11.2 Transition metals and non-metals.....	38
2.12 Factors Influencing RH Ash Properties.....	40
2.12.1 Temperature	40
2.12.2 Geographical Region	40
2.13 Health Issues.....	41
2.14 Phase transformation diagram of RHA	41
2.15 Purification processes in silicons.....	42
2.16 Electrical Characteristics	48
2.16.1 Semiconductors and p-n junctions.....	48
2.17 Depletion region	52
2.18 Solar cell operation.....	56
2.18.1 Creation of an active layer.....	59
2.19 Summary.....	60
3 EXPERIMENTAL TECHNIQUES	80
3.1 Introduction	80
3.1.1 Classification of analytical techniques used in characterisation	80
3.2 Compositional characterisation.....	80
3.2.1 X-Ray Fluorescence (XRF)	81
3.2.2 Energy dispersive X-ray (EDX)	82
3.3 Structural characterisation.....	84
3.3.1 Powder X-ray diffractometer (XRD):.....	84
3.3.2 Thermogravimetric Analysis (TGA).....	87
3.4 Morphological characterisation.....	90
3.4.1 Scanning electron microscopy (SEM).....	90
3.4.2 Transmission Electron Microscopy	91
3.5 Optical Characterisation.....	93
3.5.1 Raman Spectroscopy	93
3.5.2 Fourier Transform Infrared Spectrometer (FTIR).....	95
3.6 Device characterisation Techniques.....	97
3.7 Electrical characterisation	98
3.7.1 Conductivity measurement - Direct current (DC).....	98
3.7.2 Hall Effect measurement.....	99
3.8 Current-Voltage (I - V) characterisation	101

3.8.1	I-V Characteristics under dark condition.....	102
3.8.2	I-V characterisation under illumination.....	107
3.9	Capacitance-Voltage (C-V) characterisation	109
3.10	Spectral response (SR) characterisation	111
3.11	Summary.....	113
4	MATERIALS AND METHOD.....	119
4.1	Source of Materials	119
4.1.1	Rice Husk (RH)	119
4.2	Methodology/ Procedure.....	119
4.3	Ash Analysis	121
4.4	Rice Husk Ash Quantitative and Qualitative Evaluation	121
4.5	Purification of Rice Husk Ash Silica	121
4.5.1	Treatment with an oxidant.....	121
4.5.2	Alkali leaching.....	122
4.5.3	Digestion of RH ash in dilute hydrochloric acid.....	122
4.5.4	Neutralization of HCl acid digested samples	122
4.5.5	Dry thermal treatment.....	123
4.6	Production of Metallurgical-Grade Silicon	123
4.7	Post purification of metallurgical-grade silicon by alloying process	125
4.8	Summary	126
5	RESULTS AND DISCUSSIONS	128
5.1	Processing and pyroprocessing of rice husk	128
5.1.1	Rice husk ash content	128
5.1.2	Rice husk ash silica	129
5.2	Characterization of RHA.....	130
5.2.1	X-ray fluorescence spectrometry (XRF)	130
5.2.2	X-ray diffraction (XRD) of RHA	132
5.2.3	Thermal analysis on RHA	137
5.2.4	Scanning electron microscopy (SEM).....	138
5.2.5	Attenuated total reflection Fourier transform infrared (ATR-FTIR) spectroscopy	139
5.3	Impurities evaluation using XRF and ICP	140
5.4	Purification process	144
5.4.1	pH Neutralization.....	146

5.4.2	Effect of individual processing steps	146
5.4.3	Effect of leaching on RHA	149
	Effect of each leaching processing steps on RHA purification	151
5.4.4	Effect of heat on mass of ash silica.....	152
5.5	Summary	154
6	METALLURGICAL GRADE SILICON (MG-Si) DERIVED FROM RHA	155
6.1	Processing and Pyroprocessing of MG-Si from RHA	155
6.2	Hydrometallurgy process of MG-Si.....	155
6.3	MG-Si derived from RHA Results and Discussions	155
6.3.1	Qualitative analysis of derived MG-Si from RHA and Commercial grade Si using X-ray diffraction (XRD)	158
6.3.2	Qualitative analysis of derived MG-Si for B1000 using transmission electron microscopy (TEM)	159
6.3.3	Morphology of MG-Si from RHA.....	160
6.3.4	X-ray Mapping using Energy Dispersive X-ray Spectrometer (EDS) of MG-Si	161
6.3.5	Thermal effect on MG-Si	166
6.3.6	Particle size effect on MG-Si.....	166
6.4	Refined silicon composition.....	167
6.5	Summary	170
7	Conclusion.....	172
7.1	Challenges encountered and Future work	173
7.1.1	Introduction.....	173
7.2	Challenges encountered in the course of this research.....	173
7.2.1	Drying of RH material	173
7.2.2	Ashing of RH material.....	173
7.2.3	Boron analysis	174
7.3	Future work	174

List of Figures

Figure 2.1: Distribution of world energy sources	12
Figure 2.2: BP Statistical review of world energy 2015 (BP Energy Review, 2015)	13
Figure 2.3: Schematic diagram of energy generation from rice husk combustion	16
Figure 2.4: The solar spectrum showing the spectral irradiance vs. photon wavelength in the UV, VIS and IR regions for a 5250°C blackbody, which approximates the sun spectrum of the sun as well as a spectrum at the earth's surface that survives the absorption of molecules such as H ₂ O and CO ₂ in the earth atmosphere (Katai, 2011).....	17
Figure 2.5: Schematic of the sun's position for the determination of air mass (AM).....	18
Figure 2.6: Schematic of the basic principle of operation of a photo-thermal converter.....	21
Figure 2.7: Schematic of the operating principal of a TPV. The heat source can be a solar concentrator consisting of a system of lenses with antireflection coatings.....	22
Figure 2.8: Schematic layer widths of p-i-n junction structure for amorphous silicon	25
Figure 2.9: Schematic of the structural layer of basic silicon cell.....	26
Figure 2.10: Energy diagram of a n-p junction in silicon	26
Figure 2.11: Siemens (Trichlorosilane) the dominant polysilicon technology (left) and silane (Fluidized bed reactor) the challenging technology (right).....	29
2.12: Schematic representation of a furnace for production of metallurgical grade silicon (Schei et al, 1998)	32
Figure 2.13: Schematic diagram of the effect of metal atom impurities on p-type solar cell efficiency (Ceccaroli and Lohne, 2003)	39
Figure 2.14: Transformation of silica from amorphous state to crystalline state (Hefferan and O'Brien, 2010)	42
Figure 2.15: Diagram of post purification process	47
Figure 2.16: Schematic of a silicon crystal lattice doped with impurities to produce n-type and p-type semiconductor material	49
Figure 2.17 Minority carrier concentration in a p-n junction with (dashed line) and without (solid line) light injection	51
Figure 2.18: A simplified energy band diagram for the formation of p-n junction (a) before junction formation and (b) after junction formation	52
Figure 2.19: Schematic of the space-charge distribution of an abrupt p-n junction in thermal equilibrium.....	53
Figure 2.20: Efficiency loss processes in a p-n junction solar cell: (1) thermalisation loss; (2) junction loss; (3) contact loss and (4) recombination loss.....	57
Figure 2.21: A schematic of a p-n junction solar cell along with the front and back ohmic contacts. On the left an incoming photon generates an electron-hole pair; the hole diffuses across the junction and contributes to the current. On the right, is hole from the generated electron-hole pair trapped by an impurity and does not contribute to the current.....	59
Figure 3.1: Illustration of the basic principle of x-ray fluorescence.....	82
Figure 3.2: illustration of the basic principle of energy dispersive X-ray	83
Figure 3.3: The scattering of x-ray from a set of planes	85
Figure 3.4: Systematic X-Ray Powder Diffractometer.....	86
Figure 3.5: XRD peak showing FWHM	87

Figure 3.6: Schematic drawing of a Thermogravimetric Analyzer	89
Figure 3.7: Schematic operation of SEM	91
Figure 3.8: Schematic operation of TEM	92
Figure 3.9: Schematic illustration of Raman energy levels.....	95
Figure 3.10: Schematic diagram of Michelson interferometer	96
Figure 3.11: Schematic of an ATR-FTIR system	97
Figure 3.12: Schematic of circuit arrangement to illustrate I-V measurement of a semiconductor with resistance, R	98
Figure 3.13: Schematic illustration of a typical I-V characteristic of a semiconductor for the determination of resistance	99
Figure 3.14: Illustration of Hall Effect in a semiconductor carrying a current I in a magnetic field B perpendicular to the direction of current flow. A Hall voltage V_H is developed perpendicular to I and B	100
Figure 3.15: Schematic illustration of equivalent circuit of a diode showing shunt resistance (R_{sh}), series resistance (R_s) and depletion capacitance (C_D).....	102
Figure 3.16: Typical log-linear I-V characteristics of a diode showing both forward current (I_F) and reverse current (I_R). Here both forward and reverse characteristics are plotted to be in the same quadrant for convenience, by changing the sign of the reverse bias voltage to positive from negative.	103
Figure 3.17: Typical linear-linear I-V characteristics of a diode under dark condition	105
Figure 3.18: Ideal equivalent circuit of a solar cell under illumination	107
Figure 3.19: I-V characteristics of a solar cell under dark and illumination conditions	108
Figure 3.20: Equivalent circuit of a practical solar cell showing the presence of R_s and R_{sh}	109
Figure 3.21: Schematic illustration of C_D vs V characteristics of a diode under forward and reverse bias conditions	110
Figure 3.22: Schottky-mott plot of an ideal diode.	110
Figure 4.1: Schematics of rice husk.....	119
Figure 4.2: Schematic of rice husk ash	120
Figure 4.3: Schematic of RHA leaching with deionized water	122
Figure 4.4: Schematic of RHA digested in HCl (colour changes to yellow colour).....	122
Figure 4.5: Schematic of derived MG-Si from rice husk ash	123
Figure 4.6: Diagram of the processes from RH to thermal decomposition of RH to metallurgical-grade silicon.....	124
Figure 4.7: Quality ranges of different silicon products: Basic stage of refining, metallurgical-grade; HP1, high purity; HP2, high purity, advance stage of refining; Terrestrial solar grade; CZ, Czochralski and Polycrystals hyperpure, final stage of refining (Sirtl et al, 1979)	125
Figure 4.8: Schematic of solidified Si-Sn alloy.....	126
Figure 4.9: Sketch of grind Si-Sn alloyed powder separation process (a, b and c).....	126
Figure 5.1: Offset XRD diffractograms of RHA. (Symbols Q, A and C means peak positions of Quartz, Anorthite and Cristobalite respectively).	133
Figure 5.2: Offset XRD diffractograms of RHA twelve months after ashing (Symbols Q and C means peak positions of Quartz and Cristobalite respectively)	134

Figure 5.3: Offset XRD diffractograms of leached figure 5.1. (symbol Q and C means peak positions of Quartz and Cristobalite respectively)	135
Figure 5.4: Offset XRD diffractograms of RHA derived from batch B sample. (Symbols Q and C means peak positions of Quartz and Cristobalite respectively).....	136
Figure 5.5: Offset XRD Diffractogram of RHA. (Symbols Q and C means peak positions of Quartz, Amorphous and Cristobalite respectively).	137
Figure 5.6: Thermogravimetric analysis offset curves of raw rice husk (RRH) and ground rice husk (GRH).	138
Figure 5.7: Typical micrograph of 900°C for 5hrs (a) RHA undamaged finger-like structure, (b) porous, honeycomb-like structure, (c) well-organized outer corrugated structure, (d) the structure with many residual pores of large internal surface area.....	139
Figure 5.8: ATR spectrogram of RH and RHA. (a) original spectra, (b) off-set spectra....	140
Figure 5.9: pH neutralization of batch C acid leached RHA.....	146
Figure 5.10: Offset XRD diffractograms of C700 during different steps of purification process. (symbol Q means peak position of quartz). ICSD reference code 01-083-2465 used.....	147
Figure 5.11: Offset XRD diffractograms of C800 during different steps of purification process. (Symbols Q mean peak positions of Quartz). ICSD reference code 01-033-1161 used.....	147
Figure 5.12: Offset XRD diffractograms of C900 during different steps of purification process. (Symbols Q and C means peak positions of Quartz and Cristobalite respectively). ICSD reference code 01-085-0335 used	148
Figure 5.13: Offset XRD diffractograms of C1000 during different steps of purification process. (Symbols Q and C means peak positions of Quartz and Cristobalite respectively). ICSD reference code 01-085-0335 and 01-082-0512 used.....	148
Figure 5.14: graphs of impurity content for each purification steps. (Symbols a, b, c, d and e represents graph of purification steps for SO ₃ -Fe ₂ O ₃ , CaO-TiO ₂ , MgO-P ₂ O ₅ , Na ₂ O-Al ₂ O ₅ and Mn ₃ O ₄ -K ₂ O for batches B and C RHA respectively)	149
Figure 5.15: Graphs of boron impurity content at each leaching step normalised to initial boron concentration	150
Figure 5.16: Effect of each processing step on the removal of impurities in batch B RHA as determined by X-ray Fluorescence analysis	151
Figure 5.17: Effect of each processing step on the removal of impurities in batch C RHA as determined by X-ray Fluorescence analysis	151
Figure 5.18: present residual unburnt carbon. a) C700 RHA. b) C700 leached RHA. c) C700 HNO ₃ leached RHA and d) C700 HCl leached RHA.....	152
Figure 5.19: Present residual mass versus temperature after leaching. a) C700 is mass loss, devolatilization and slow combustion of RHA. b) C800 is mass loss, devolatilization and slow combustion of RHA. c) C900 is devolatilization and mass gain of RHA and d) C1000 is mass gain RHA.....	153
Figure 5.20: Present mass loss (removal of moisture), release of organic volatile matters (devolatilization), oxidation of fixed carbon (slow combustion) and mass gain.....	154

Figure 6.1: Offset X-Ray diffractograms for batch A RHA reduced with magnesium and a commercial grade Si (symbols Si, Mg ₂ Si, MgO and S: Peak positions of silicon, silicide, Magnesium oxide and spinel respectively).....	158
Figure 6.2: Offset X-Ray diffractograms for batch C RHA reduced with magnesium and a commercial grade MG-Si (symbols Si, Mg ₂ Si, MgO and S: Peak positions of silicon, silicide, Magnesium oxide and spinel respectively).	158
Figure 6.3: (a) Bright-field TEM micrograph of a particle of RHA-derived silicon. (b) Ring diffraction pattern obtained from selected area of particles of RHA-derived silicon.....	159
Figure 6.4: Micrographs of the outer and inner surfaces of MG-Si from RHA. (a) Finger-like shape MG-Si with asperities and cracks. (b) Corrugated outer epidemic of MG-Si with asperities. (c) A thick skin-like outer surface of MG-Si with deposit of leached off debris. (d) & (e) Aggregated, multiphase MG-Si particle.....	160
Figure 6.5: X-ray mapping of B700 MG-Si. (a) EDS micrograph of Si sample derived from RHA. (b) Mg mapping of Si sample. (c) Si mapping of Si sample. (d) Al mapping of Si sample. (e) O mapping of Si sample	161
Figure 6.6: X-ray mapping of an impurity phase in batch C700 derived MG-Si (a, b, c and d) and EDS analysis e.....	162
Figure 6.7: X-ray mapping of an impurity phase in batch C800 derived MG-Si (a, b, c and d) and EDS analysis e.....	163
Figure 6.8: X-ray mapping of an impurity phase in batch C900 derived MG-Si (a, b, c and d) and EDS analysis e.....	164
Figure 6.9: X-ray mapping of an impurity phase in batch C1000 derived MG-Si (a, b, c and d) and EDS analysis e.....	165
Figure 6.10: Present derived MG-Si residual mass versus temperature. (left) mass loss and devolatilization of MG-Si. (right) Slow combustion and mass gain	166
Figure 6.11: Raman spectra of polycrystalline silicon derived from RHA batch C at different temperature. Using laser power of 5mW and wavelength of 532nm	166
Figure 6.12: The EDS analysis of impurities in Si-Sn refined alloy powder.....	167
Figure 6.13: The microstructure of impurity phases in refined Si-Sn alloyed powder	168
Figure 6.14: The microstructure of impurity phases in centrifuged refine Si-Sn alloyed powder	169
Figure 6.15: The EDS analysis of impurities in Si refined from Si-Sn alloy powder.	170

List of Tables

Table 2.1: Comparisons of LOI in RHA (Cook et al, 1989) with those of some other locations	37
Table 2.2: Typical chemical analyses of silicon products for the semiconductor	40
Table 2.3: Purification of silicon by leaching (Dietl, 1987)	43
Table 2.4: Segregation coefficient of some impurities in metallurgical grade silicon at melting point of silicon (Davis et al, 1980; Trumbore, 1960)	45
Table 4.1: Rice husk ash produced batch A.....	120
Table 4.2: Rice husk ash produced batch B	120
Table 4.3: Rice husk ash produced batch C	121
Table 5.1: Silica content in rice husk ash heated for 5 hours at different temperature for batch A	128
Table 5.2: Silica content in rice husk ash heated for 5 hours at different temperature for batch B	128
Table 5.3: Silica content in rice husk ash heated for 12 hours at different temperature for batch C	129
Table 5.4: Batch A chemical analysis of RHA using X-ray fluorescence spectrometry (XRF).....	130
Table 5.5: Batch B chemical analysis of RHA using x-ray fluorescence spectrometry (XRF) and inductively coupled plasma (ICP).....	131
Table 5.6: Batch C chemical analysis of RHA using x-ray fluorescence spectrometry (XRF) and inductively coupled plasma (ICP).....	132
Table 5.7: Impurities in batch A	141
Table 5.8: Impurities in batch B	142
Table 5.9: Impurities in batch C	143
Table 5.10: Impurities after leaching batch B	144
Table 5.11: Impurities after leaching batch C	145
Table 6.1: Quantitative analysis of highest purity batch A700 derived MG-Si using X-ray fluorescence (XRF).	156
Table 6.2: Quantitative analysis of highest purity batch B700 derived MG-Si using X-ray fluorescence (XRF) and Inductive couple plasma optical emission spectrometry (ICP-OES) technique	156
Table 6.3: Batch C Quantitative analysis of all obtained elements in MG-Si derived from C700, C800, C900 and C1000 using X-ray fluorescence (XRF) and Inductive couple plasma optical emission spectrometry (ICP-OES) techniques for B only	157

List of abbreviations and symbols used

Abbreviation	Meaning
Batch A	Purely rice husk from rice mill
Batch B	Rice husk mix with tiny rice grain
Batch C	Rice husk containing dirt from rice husk dumping site
A700	Batch A rice husk ashed at 700°C for 5hrs
A800	Batch A rice husk ashed at 800°C for 5hrs
A900	Batch A rice husk ashed at 900°C for 5hrs
B700	Batch B rice husk ashed at 700°C for 5hrs
B 800	Batch B rice husk ashed at 800°C for 5hrs
B 900	Batch B rice husk ashed at 900°C for 5hrs
B1000	Batch B rice husk ashed at 1000°C for 5hrs
C700	Batch C rice husk ashed at 700°C for 12hrs
C 800	Batch C rice husk ashed at 800°C for 12hrs
C 900	Batch C rice husk ashed at 900°C for 12hrs
C1000	Batch C rice husk ashed at 1000°C for 12hrs
η_{TPV}	conversion efficiency of the thermo-photovoltaic
R_{ph}	responsivity of the semiconductor to incoming photons
ϕ_B	barrier height
ϕ_{BO}	barrier height at zero bias
$A(\lambda)$	absorbance of the cell
A_c	collector area
A_{cell}	area of the solar cell
AM	air mass
AM0	this means zero atmosphere
AM1	air mass for spectrum that has travelled through the atmosphere when the sun is directly at its zenith
AM1.5	A solar spectrum that has passed through 1.5 atmosphere thickness
AM2	the spectrum when the sun is at an angle Z = 60° relative to the zenith
AM3	situation when Z = 70°
AR	antireflection
a-Si	amorphous silicon
ATR-FTIR	attenuated total reflection Fourier transform infrared
B	magnetic field
CB	conduction band
C_D	depletion layer capacitance per unit area
CO_2	carbon dioxide
CV	capacitance -voltage
CVD	chemical vapour deposition
Cz	Czochralski (process)
DC	Direct current

D_p, D_n	diffusion coefficient of holes or electrons
e	electron
ϵ	dielectric permittivity of the material
EDX	energy dispersive x-ray (analysis)
E_g	bandgap energy of semiconductors
EGS	Electronic grade silicon
E_m	maximum build-in electric field
$E_n(\lambda, T)$	emissive power of a black-body at wavelength, λ and temperature, T
ϵ_0	dielectric permittivity of free space
ϵ_s	relative dielectric permittivity, also called the dielectric constant of the semiconductor material
eV	electron volt
FBR	fluidized bed reactor
FTIR	Fourier transform infrared spectrometer
Fz	float zone
G	solar irradiance
G_r	generation rate
H_2O	water
$\hbar\omega$	photon energy
I	solar intensity or solar irradiance, also current
ICP-OES	inductively coupled plasma optical emission spectrometry
I_o	maximum solar irradiance
IPCC	inter-governmental panel on climate change
IR	infrared radiation
I_s	reverse saturation current
IV	current-voltage
J_L	photocurrent density
J_{mp}	current density at maximum power point
J_{ph}	total photo-generated current density
$J_{ph}(x)$	photon flux
k	Boltzmann constant
L	optical path length
L_o	vertical path length
LOI	loss on ignition
L_p, L_n	hole or electron diffusion length
MG-Si	metallurgical-grade silicon
p	hole
P_{abs}	energy absorbed by the solar cell per unit time
P_{inc}	energy per unit time emitted by the radiator
P_n	minority carrier concentration
P_{n0}	minority carrier concentration at thermal equilibrium
P_{op}	optical power per unit area

PV	photovoltaic
q	electron charge
Qu	useful energy gain of the solar collector
RH	Rice husk
RHA	Rice husk ash
R_r	recombination rate
Si	silicon
S _o G-Si	solar grade silicon
S _{R,C}	geometric factor of the radiator cell
STC	silicon tetrachloride
TCS	trichlorosilane
TEM	transmission electron microscopy
TGA	thermo-gravimetric analysis
TPV	thermo-photovoltaic
U	net recombination rate
UMG-Si	upgrading metallurgical grade silicon
UV	ultraviolet radiation
V	external bias voltage
VB	valence band
V _{bi}	built-in potential
V _g	Eg/e is the bandgap voltage
VIS	visible radiation
V _{mp}	voltage at maximum power point
V _{oc}	open circuit voltage
w _p , w _n	distances by which the depletion region extends into the p-type and n-type semiconductor
XRD	X-ray diffraction
XRF	X-ray fluorescence
Z	angle between zenith and the sun position
α	absorption coefficient
$\epsilon(\lambda, T)$	spectral emittance at wavelength, λ and temperature, T
η	efficiency
η_{cell}	efficiency of the solar cell
$\tau(\lambda)$	transmittance of the filter between the emitter and the solar cell
τ_p, τ_n	minority carrier lifetime hole or electron
χ_p, χ_n	electrons affinity in p- and n-type materials
ϕ_p, ϕ_n	difference in work functions of p or n type materials
β	change in effective barrier height with bias voltage
R	resistance
ρ	resistance per unit length per unit cross-sectional area
L	thickness of the semiconductor
A	cross-sectional area of the semiconductor
σ	conductivity

V_H	Hall voltage
R_H	Hall coefficient
r_H	Hall factor
τ	mean free time between collision
J_x	magnitude of x-component of the applied current density
B_z	z-component of the applied magnetic field
t	thickness of the sample
μ_H	Hall mobility
μ	drift mobility
R_s	series resistance
R_{sh}	shunt resistance
R.F	rectification factor
n	diode ideality factor
I_F, I_R	forward current, reverse current
V_{BD}	breakdown voltage
V_T	threshold (or cut-in) voltage
P_m	maximum output power
I_m, V_m	current and voltage at the maximum output power
FF	fill factor
I_{sc}	short circuit current
P_{in}	input power
S	spectral responsivity
EQE	external quantum efficiency
IQE	internal quantum efficiency
HP1	high purity 1
HP2	high purity 2
TSG	terrestrial solar grade
Si_{com}	commercial grade silicon
MG-Si _{A700}	metallurgical grade Si derived from A700
MG-Si _{B700}	metallurgical grade Si derived from B700
MG-Si _{C700}	metallurgical grade Si derived from C700
MG-Si _{C800}	metallurgical grade Si derived from C700
MG-Si _{C900}	metallurgical grade Si derived from C700
MG-Si _{C1000}	metallurgical grade Si derived from C700

Chapter 1: Introduction

The increasing energy-related climate change coupled with spiralling cost and unsustainable nature of fossil fuels has in recent years increased interests in the need for innovative renewable energy alternatives worldwide, the development of this technology to meet terrestrial energy demands has been limited, even though solar photovoltaic power generation in industry like the space industry is a proven technology.

The high cost associated with manufacturing materials used in the fabrication of solar cells poses as one of the issues that have limited the widespread use of solar photovoltaic power as it leads to high cost in electrical energy produced compared to those of more traditional sources. Silicon in form of monocrystalline or polycrystalline is currently the dominant semiconductor material used in the fabrication of most commercially available solar cells, commanding over 90% of all PV technology market share (Swanson, 2006).

The carbothermic and siemens process are required for metallurgical grade and electronic grade silicon respectively on commercial scale. Metallurgical grade silicon is typically 98-99.5% and usually containing high content of electro-active impurities such as B(5-70 ppm), P(5-100 ppm), Al(3000-5000 ppm) and transition metal known to reduce the conversion efficiencies of p-n junction in silicon solar cells and panels. On the other hand, electronic grade silicon which contains total impurities less than one part per billion (< 1ppb) is too expensive for solar cells production on large scale (Ceccaroli and Lohne, 2003). Generally, it is recognised that B and P levels have to be reduced to less than 1ppm each for the silicon feedstock to have purity in the range of 5-7N for efficient solar cells fabrication.

1.1 General background of study

Currently, solar cells are manufactured using electronic-grade silicon (EG) which makes them very expensive. The cost of manufacturing Si-based solar cells could be considerably reduced if a new and inexpensive source material is used. The search for economical methods to produce silicon needed for solar cell applications has been ongoing for more than three decades (Barati et al, 2012). The sources of raw materials for these methods has been largely limited to silica in form of quartz and volatile compounds; thereby, limiting examination to silica source from rice husk. The processing methods that have received most research

attention have been the upgrading of metallurgical grade silicon by modification of conventional production methods and by pyrolytic decomposition of halosilanes i.e. the so-called Siemens Process. These two methods are commonly referred to as the metallurgical and chemical routes to solar grade silicon (SoG-Si) synthesis. Although, the chemical route has been used successfully to meet and exceed the typical purity requirements for SoG-Si, the potential for lowering costs and increasing the volume of production has been very limited. The unit processing steps involved in the chemical route approach can be complex, energy intensive and of long duration, as is discussed by Braga et al (2008). A metallurgical route combined with directional solidification has been successful in removing metallic impurities with low segregation coefficients from silicon. However, this route has been ineffective economically in removing impurities with high solubility e.g. B, P, Al which are dopant elements. The latter are known to be very deleterious to the performance of solar cells, as is discussed in Istratov et al (2006). Thus, the logical and consequently typical approach has been to use very high purity silica and reductant raw materials that are almost free of impurities and more economically viable. It is against this background, that the potential of silica obtained from rice husk, an agricultural waste product, is explored in this work for the production of solar grade silicon, as an alternative approach to synthesis of low cost solar grade silicon. Rice husk silica has only been explored by relatively few research groups as a source of solar cell material. However, the narrow and isolated experimental conditions from previous works as well as lack of an optimized process have limited the engineering application of such results. Thus, the lack of a commercially viable route for synthesis of bulk high purity silicon using silica from rice husk that is considered to be biomass waste material provides me a good motivation to explore and conduct further research into the feasibility of this approach.

1.2 Rice (*Oriza Sativa*)

Rice covers 1% of the earth's surface and is a primary source of food for billions of people globally. Approximately, 741.3 million tonnes of rice paddy were produced between the year 2012 and 2014 (STAT FAO, 2015) of which Nigeria produced 4.8 million tonnes of the rice paddy. On average, 20% of the rice paddy is husk (Beagle, 1978). In the majority of rice producing countries, the husk produced from the processing of rice is either burnt or dumped as waste.

1.2.1 Rice husk (RH)

Rice husk is a by- product from milling rice that is used as energy source in many industries such as biomass power plant. Burning rice husk generates rice husk ash (RHA) which is rich in silica and can be an economically valuable raw material for production of silica. The chemical contents of RH are found to vary from sample to sample assumed to be due to different geographical conditions, type of paddy, climatic variation, soil chemistry and fertilizers used in the paddy growth (Genieva et al, 2008). RH, if properly burnt yields about 20% (average) ashes which exceeds 90wt% SiO₂ (Zhang et al, 2010). RH silica is originally amorphous and is therefore expected to convert to crystalline form during high temperature processing. Agro-industrial wastes are abundant in Nigeria among which RH occupies very important position. RH is insoluble in water because of its high silica and lignin content, tough, woody and abrasive in nature with low nutritive properties and resistance to weathering (Genieva et al, 2008). Secondly, its silica content is highest among all of them. In 2002 Nigeria produced about 3,367,000 tonnes of rice per annual from which 673,400 tonnes of RH are separated as by-product (Frolking et al, 2002). In 2014, Nigeria produced 4.8 million tonnes of rice paddy, a 42.6% increment in RH in 12 years. Such huge amounts are not utilized properly, as common practice is to burn the rice husk which is wasteful exercise. Heap burning of RH causes pollution hazards for surrounding population and has disposal problems as rice husk is merely carried to an open location where it is burnt in the open air.

1.2.2 Rice Husk Ash (RHA)

The chemical composition of rice husk ash depends upon a number of factors, e.g the type of soil for growing rice plants, the fertilizing practices, environment, temperature and duration of burning. These factors influence both the percentage of silica and its mineralogical nature. The heap burning method produces poor quality RHA. It consists of large amount of unburnt carbon which lowers the silica content. Secondly, the original amorphous nature (Patel et al, 1987) of the silica is destroyed and the resulting ash is largely of crystalline character; consequently, it becomes comparatively less chemically reactive (Mehta, 1977). RHA if obtained from the rice husk by particular burning temperature and time will yield high purity rice husk silica material suitable for silicon production.

1.3 Silicon

Silicon makes up 25.7% of the Earth's crust by weight and is the second most abundant element, being exceeded only by oxygen. Silicon is not found free in nature, but occurs chiefly as oxide and silicates. Sand, quartz, rock crystal and jasper are some of the forms in which the oxide appears. Granite, asbestos, mica etc. are but a few of the numerous silicate minerals. Silicon is prepared commercially by heating silica and carbon in a furnace to about 2000°C.

Silicon is a group IV element which adopts the tetrahedral crystal structure in which the four outer valence electrons of silicon atoms involved in covalent bonding. The valence electron orbitals involving in covalent bonding form the energy band known as valence band (VB); and the almost empty band above is called the conduction band (CB). Silicon has an indirect bandgap, that is, bandgap that the energy minimum in the conduction band and the energy maximum in the valence band are separated by 1.1 eV at room temperature, these points occur at different value of the crystal momentum. Thus, a phonon and a photon with relatively small energy are required for an electron to be promoted from the valence band into the conduction band CB. Silicon is a chemical element which has the symbol Si and atomic number 14. It is a tetravalent metalloid which is less reactive than its chemical analogue carbon and is the eighth most common element in the universe by mass. Its outer electron orbits are half filled. Silicon has numerous known isotopes, with mass number ranging from 22 to 44. ^{28}Si is the most abundant isotope, at 92.23%, ^{29}Si 4.67%, and ^{30}Si 3.1% are stable. ^{32}Si is a radioactive isotope produced by cosmic ray; its half-life has been determined to be approximately 170 years. Crystalline silicon with its natural advantages of being an abundant element makes it remains material of choice for large-scale commercial production of photovoltaic modules. Silicon in microelectronic industry has become by far most studied material of all the semiconductor materials; and it has been used in photovoltaics due to its dominance (Cuevas et al, 1999). Most of the technological processes and much of the accumulated knowledge have been directly transferred to photovoltaic (PV) applications with great benefit. However, there is no guaranteed that crystalline silicon would maintain its dominant position in photovoltaics in the medium to long term, at least not in the form of wafers sawn from bulk ingots. Lately, the sources of silica

and silicon in biomass resources such as rice husk are being researched intensively for several industrial applications (Shinohara and Yasushi, 2004). Nevertheless, the question remains as to whether rice husk ash (RHA) can be purified by a cost-effective, low technology route to produce solar-grade silicon suitable for use in photovoltaic devices, even though it has been known for several decades that, with careful processing, rice husk can be a source of metallurgical grade silicon (Ikram and Akhter, 1988). The work presented in this thesis is rooted to technology that is devoted to exploring ways of manufacturing and improving the performance of silicon solar cell from rice using widely available techniques.

1.4 Aim

The aim of this research work is to use rice husk, an agricultural waste product, very rich in siliceous materials and very easily obtainable in large quantities in many countries, e.g. Nigeria, as an alternative source for low-cost Si-based solar cells. This work will also explore a technique that will remove or reduce the high segregation impurities; as well as focus on the use of rice husk metallurgical-grade silicon, a material that has become increasingly important in the commercial sphere for polycrystalline silicon and cheaper to produce than single-crystal Czochralski-grown (Cz) silicon.

1.5 Objectives

The objective of this research is to identify and optimize conditions for roasting rice husk considered to be a biomass waste by-product, into clean silica of over 99.3% required for the production of solar grade silicon. To investigate the possibility of producing low-cost solar grade silicon from the derived high purity rice husk silica via hydrometallurgy leaching processes and consider best optimisation techniques suitable for the silicon production.

1.6 Justification/Significance

Production of solar-grade silicon from rice husk ash (RHA) will add an economical value to the raw material. If rice husk (RH) is properly burnt, 80% - 95% silica will be obtained. The utilization of RHA will go a long way in the reduction of agro-industrial wastage of rice husk as well as solving the disposal problems of RH. RHA produced under controlled condition gives the required mineralogical nature i.e. amorphous or crystalline silica with carbonaceous material burnt out. Currently, 94% of solar cells produced from silicon shows that

38% is single-crystalline, 49% is poly-crystalline, 4% is amorphous and 3% is silicon ribbons (Miles et al, 2007). This research is to seek ways to further enrich the 80% - 95% silica obtained from RHA by processing it further via solid-liquid extraction (acid leaching) and liquid-liquid extraction (metal lixiviation) by the following procedures: Treatment with an oxidant, alkali leaching, digestion with HCl, dry thermal treatment with magnesium and low temperature purification process of metallurgical silicon using Sn as a metallic medium to produce silicon with poly-crystalline properties.

1.7 Summary

This chapter begins with the introduction of problem involves or encountered during production of solar grade silicon for solar cells fabrication. A general background of study, it further discussed rice and its viability to silicon production when the husk from the rice is burnt at a particular temperature and time. The aims and objectives of the work along with its justification/significant to the work were presented in this thesis.

References

- Barati, M., Larbi, K. K., Roy, R., Lakshmanan, V. I., & Sridhar, R. (2012). *U.S. Patent No. 8,337,795*. Washington, DC: U.S. Patent and Trademark Office.
- Beagle, E.C. (1978). Rice Husk conversion to energy. Rome, Italy. FAO Agricultural Services Bulletin 37.
- Braga, A. F. B., Moreira, S. P., Zampieri, P. R., Bacchin, J. M. G., & Mei, P. R. (2008). New processes for the production of solar-grade polycrystalline silicon: A review. *Solar energy materials and solar cells*, 92(4), 418-424.
- Ceccaroli, B., & Lohne, O. (2003). Solar grade silicon feedstock. *Handbook of photovoltaic science and engineering*, 169-217.
- Cuevas, A., Stocks, M., McDonald, D., Kerr, M. and Samundsett, C., 1999. Recombination and trapping in multicrystalline silicon. *Electron Devices, IEEE Transactions on*, 46(10), pp.2026-2034.
- Frolking, S., Qiu, J., Boles, S., Xiao, X., Liu, J., Zhuang, Y., and Qin, X. (2002). Combining remote sensing and ground census data to develop new maps of the distribution of rice agriculture in China. *Global Biogeochemical Cycles*, 16(4).
- Genieva, S. D., Turmanova, S. C., Dimitrova, A. S., & Vlaev, L. T. (2008). Characterization of rice husks and the products of its thermal degradation in air or nitrogen atmosphere. *Journal of Thermal Analysis and Calorimetry*, 93(2), 387-396.
- Ikram, N., & Akhter, M. (1988). X-ray diffraction analysis of silicon prepared from rice husk ash. *Journal of materials science*, 23(7), 2379-2381.
- Istratov, A. A, et al. (2006). Control of metal impurities in “dirty” multicrystalline silicon for solar cells. *Materials science and engineering: B*, 134 (2), 282-286.
- Mehta, P. K. (1977). Properties of blended cements made from rice husk ash. In: *ACI Journal Proceedings, ACI*.
- Miles, R. W., Zoppi, G. and Forbes, I. (2007). Inorganic photovoltaic cells. *Materials today*, 10(11), 20-27.

Patel M., Karera, A. and Prasanna, P. (1987). Effect of thermal and chemical treatments on carbon and silica contents in rice husk. *Journal of materials science*, 22 (7), 2457-2464.

Shinohara, Y., & Kohyama, N. (2004). Quantitative analysis of tridymite and cristobalite crystallized in rice husk ash by heating. *Industrial Health*, 42(2), 277-285.

STAT, FAO (2015). FAO(Food and agriculture Organisation); Rice market monitor,

http://www.fao.org/fileadmin/templates/est/COMM_MARKETS_MONITORING/Rice/Images/RMM/RMM_AP15.pdf

Swanson, R. M. (2006). A vision for crystalline silicon photovoltaics. *Progress in photovoltaics: Research and Applications*, 14(5), 443-453.

Zhang, L, XU, C. C., and Champagne, P. (2010). Overview of recent advances in thermo-chemical conversion of biomass. *Energy conversion and management*, 51 (5), 969-982.

2 LITERATURE REVIEW

2.1 Silicon from quartz, silicon solar cells and silicon solar cell technology

Silicon mainly occurs as silicon dioxide (SiO_2) in quartz and sand. It is extracted mainly by quartzite reduction with carbon in an arc furnace (Dietl et al, 1981). Gay-Lussac and Thenard (1811) were thought to have prepared impure amorphous silicon, through the heating of potassium metal with silicon tetrafluoride, but they did not purify and characterize the product, nor identify it as a new element. Berzelius prepared amorphous silicon using approximately the same methods as Gay-Lussac (potassium metal and potassium fluorosilicate), purifying the product to a brown powder by repeatedly washing it. Crystalline silicon in its common form was not prepared until 31 years later, by Deville (Voronkov, 2007). The photovoltaic effect was first experimentally demonstrated by a French physicist A.E. Becquerel in 1839. He was credited as being the first to demonstrate the effect by illuminating platinum electrodes coated with silver chloride inserted into acidic solution (Becquerel, 1839). About forty years later, William Adams and Richard Day in 1876 found that a photocurrent could be produced in a sample of selenium when contacted by two heated platinum contacts following the investigation of photoconductive effect in selenium and the anomalies they noted when Pt contacts were pushed into the Se bar. They demonstrated that it was possible to start a current in Selenium merely by the action of light (Adam and Day, 1877). However, it was not until 1883 that the first solid state photovoltaic cell was built by Charles Fritts who coated the semiconductor selenium with an extremely thin layer of gold to form the junctions (Frits, 1883). The device was only 1% efficient. In 1888, Russian physicist Aleksandr Stoletov built the first photoelectric cell based on the outer photoelectric effect discovered by Heinrich Hertz earlier in 1887 (Gevorkian, 2007). The most efficient photovoltaic devices used before 1940s, were Se, Cu_2O or Ti_2S due to their absorbing layer with a rectifying metal contact (Green, 1990). The first semiconductor p-n junction solar cells were described in 1941 by Russel Ohl of Bell laboratories (Ohl, 1941). A comprehensive review article by M.A. Green (1993) on the evolution, high efficiency design and efficiency enhancement, outlined the time line of record efficiencies of silicon solar cells from 1941 to 1990, showing growth in efficiency from <1% in 1941 to >23% in 1990. In 1998 the monocrystalline silicon solar cell reached a confirmed efficiency of 24.4%

(Zhao et al, 1998). This value was later revised upwards to 25.0% and represented for a 4 cm² solar cell area by M. A. Green (Green, 2009). This is the record efficiency to date for silicon. Multicrystalline silicon solar cells also reached confirmed record efficiencies of 20.3% in 2004 for a 1 cm² area device (Schultz et al, 2004), while Moslehi et al produced thin film silicon solar cell with record efficiency of 20.1% for 242.6 cm² solar cells as contained in the periodic report of solar cell efficiencies by M. A. Green et al (Green et al, 2015).

Silicon solar cells are fabricated using solar-grade silicon which has purity in the order of 99.9999% (6N) or higher e.g Silane process. Silicon used in microelectronics is called device-grade or high-purity silicon reaching 99.9999999% (9N) purities, that is, it contains impurity levels less than one part per billion e.g Siemens process (Ranjan et al, 2011). However, the production of these grades of silicon is capital intensive, requiring huge amount of electrical and thermal energy as well as advanced chemical processing steps. Most photovoltaic solar cells produced to date have been based on silicon p-n junctions but now relying on junctions more controllably formed by diffusing one polarity dopant into a wafer substrate of opposite polarity (Green, 2002). The solar cell industry is a player in the renewable energy segment. Electricity generation from solar cells is deemed to be one of the key technologies of the 21st century (Braga, 2008). Solar cell power generation has recently been increasing rapidly due to the fact that it provides clean and renewable energy. However, serious shortage and increased costs of solar-grade silicon (S_oG-Si) arose around 2006 – 2008 due to unsustainably rapid expansion in solar cell production (Yasuda and Kouji, 2010). The global solar cell market is still being affected by the constrained activity. Among new technologies for production of S_oG-Si under research, the metallurgical process is one of the most promising methods (Woditsch and Koch, 2002). Solar cell electricity presents an elegant means for electricity generation as there are no moving parts, no noise and zero emissions (Xakalashe and Buhle, 2012).

2.2 Solar Cell

Basically, solar cell (also called photovoltaic cell) is an electrical device that converts the energy of light directly via photovoltaic effect into electricity needed for energy supply and consumption. It is a form of photoelectric cell (in that its

electrical characteristics – e.g. current, voltage, or resistance – vary when light is incident upon it) which when exposed to light, can generate and support electric current without being attached to any external voltage source. Photovoltaic is the field of technology and research related to the application of photovoltaic cells in producing electricity from light; though it is often specifically referred to the generation of electricity from sunlight. Cells can be described as photovoltaic even when the light source is not necessarily sunlight (lamplight, artificial light etc.). In such cases the cell is sometimes used as a photodetector (for example infrared detectors), detecting light or other electromagnetic radiation near the visible range, or measuring light intensity. The operation of a photovoltaic (PV) cell requires 3 basic attributes:

1. The absorption of light and generating of electron-hole pairs.
2. The separation of charge carriers of opposite types.
3. The separate extraction of those carriers to external circuit

A typical silicon solar cell is an n-p junction made in a wafer of p type silicon approximately 100cm^2 in area and a few hundred microns ($300\text{-}500\text{ }\mu\text{m}$) thick in order to absorb as much light as possible. Thus, to improve its diffusion lengths, a light doped ($\sim 10^{16}\text{ cm}^{-3}$) is introduced. Heavily doped ($\sim 10^{19}\text{ cm}^{-3}$) is introduced to reduce sheet series resistance for n type emitter. A reasonable thin layer should be used to allow as much light as possible to pass through to the base, but thick enough to keep series resistance reasonably low. The principles and operations of silicon solar cell will fully be discussed in this chapter with efficiency while I briefly go onto introduce other forms of energy production, supply and consumption within the globe.

2.3 Global energy supply and consumption

The world's energy consumption has risen dramatically due to variety of reasons that includes the increase in the world population and industrialization since latter half of 20th century; therefore necessitating serious research, development and monitoring of various global energy supplies and consumption in recent years needed for sustainable energy supply. The energy crisis of the 1970s taught the world serious lessons on the need for sustainable global energy supplies (Horowitz, 2005 and The 1970's Energy Crisis). The BP's annual 'Statistical Review of World Energy 2015' for the year 2014, indicates that oil still remains

the dominant fuel for energy generation with 33% of the global total energy consumption as at 2014, although this value stands as the lowest share on record for oil for 15 years running (BP Energy Review, 2015). Oil is followed in sequence by coal, natural gas, hydroelectricity, nuclear energy and finally renewable energy (BP Energy Review, 2015), as shown in figure 2.1 and 2.2.

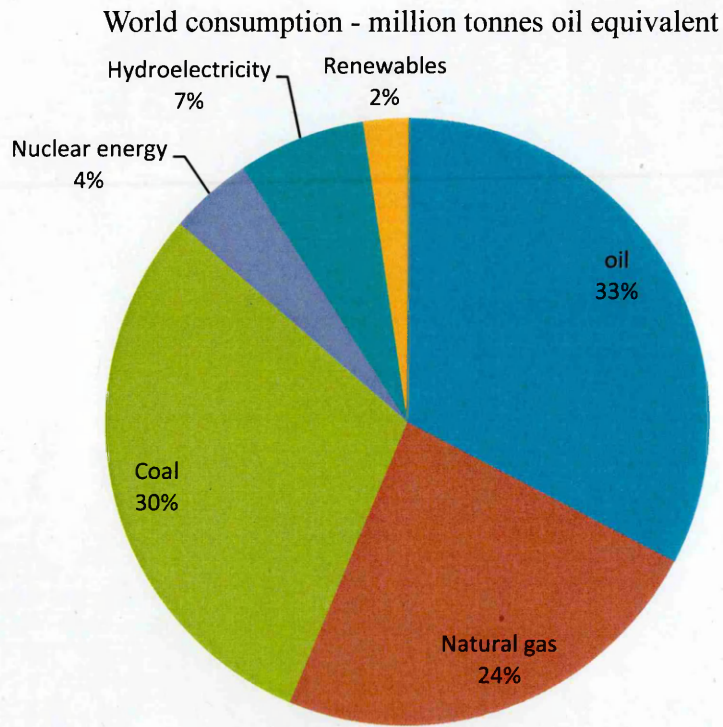


Figure 2.1: Distribution of world energy sources

World primary energy consumption grew by a below-average 0.9% in 2014, the slowest rate of growth since 1998 other than the decline in the aftermath of the financial crisis. Growth was below average in all regions except North America and Africa. All fuels except nuclear grew at below-average rates. Oil remains the world's dominant fuel. Hydroelectric and other renewables in power generation both reached record shares of global primary energy consumption (6.8% and 2.5%, respectively).

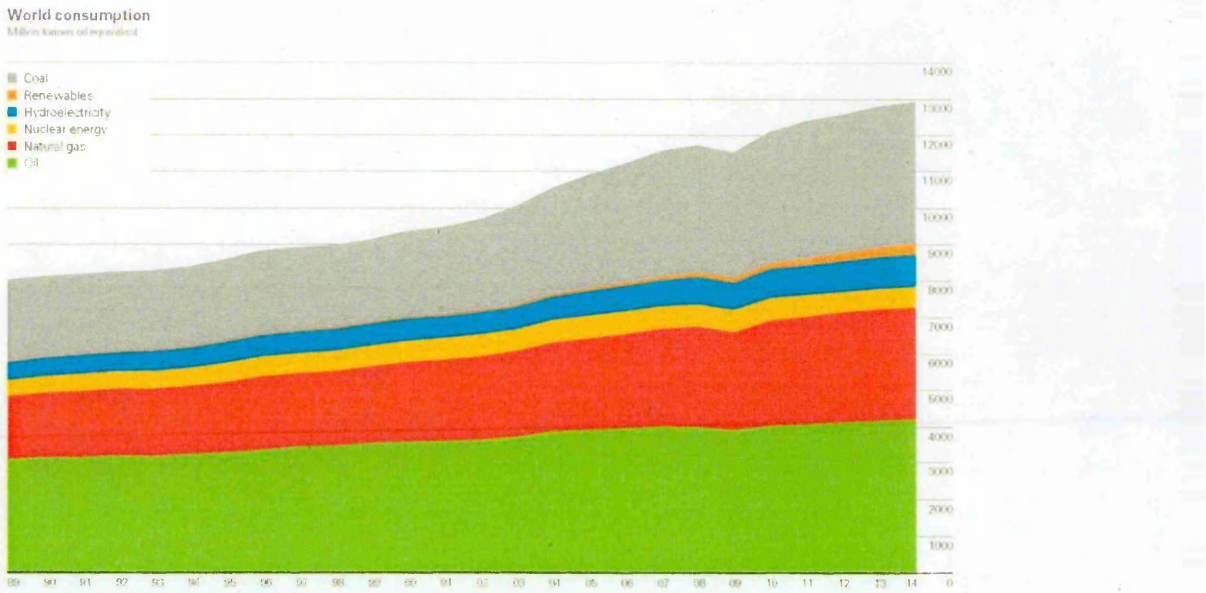


Figure 2.2: BP Statistical review of world energy 2015 (BP Energy Review, 2015)

Be it as it may, these major global energy sources are not without serious environmental concerns ranging from CO₂ emission to oil spillage on land and water as well as nuclear waste contamination, all of which eventually contribute to the big issues of environmental degradation and global warming making headlines today. The climate change report released in September 2013 by the Inter-governmental Panel on Climate Change (IPCC) blames this on the activities of humans which have eventually resulted to increase in the greenhouse gas content of the atmosphere (Koch et al, 2013). These human activities eventually boil down to heavy dependence on energy source which produce these greenhouse gases in both our industrial and domestic activities without adequate consideration of the accompanying adverse environmental effects such as global warming and pollution.

Nevertheless, BP's 2015 annual Statistical Review of world energy indicates that renewable energy sources (which more or less produce less adverse environmental effects) grew by about 12% in power generation, accounting for a record 3% of global energy consumption up from 0.9% a decade ago (BP Energy Review, 2015). This is encouraging news for the pursuit of renewable energy sources. Renewable energy is so important because it is apparently infinite, clean and at least depends on how it is generated. Some technology is not very "clean". For

example the estimated life span of the sun is another 7 billion years, while generating energy at the rate of about 4×10^{27} W (Cain, 2012). The primary renewable energy sources include the sun, wind, biomass, tide, wave and the earth's heat (Foster et al, 2010). With renewable energy taking last position in the rank of global energy sources according to the BP's Statistical Review of world energy and the detrimental climate change issues, there is a serious campaign for massive research and development activities in search of alternative, renewable and clean energy supplies for an encouraging environment and survival of man and other living things on earth. The major conventional energy sources in the world today include oil, natural gas, hydroelectricity, coal and nuclear. Among these, oil, coal and natural gas are collectively called fossil fuels. They are derived from deposits of dead organic matter that have built up over millions of years. The major characteristic of this energy source is the production of large amounts of carbon dioxide when burnt and other greenhouse gas emissions which play very prominent role in global warming (Shakun, 2012 and Sundquist, 1993). For this reason, there have been efforts over the years to find alternative energy sources which produce minimal carbon dioxide and other greenhouse emission. Hydroelectricity and nuclear energy belong to this class of energy sources, although nuclear energy production has its own problems of nuclear contamination. It is therefore clear that the word "alternative" in energy terms does not necessarily imply "safe" or "sustainable". For example nuclear energy is not as safe as hydroelectricity given its inherent nuclear radiation issue, such as in the case of the Fukushima nuclear power station radioactive contamination in Japan, triggered by the 2011 earthquake and tsunami. This in fact creates confusion sometimes when classifying energy sources in terms of their level of safety. For this reason, the classification of energy sources in this thesis will be based on renewable and non-renewable sources.

2.4 Non-renewable and renewable energy sources

Energy sources that cannot be replenished once they are used are said to be non-renewable (Dincer, 2000). This replenishment is actually done naturally. Based on this, most of the major conventional energy sources are non-renewable and therefore stand a chance of running out in future. All energy sources derived from fossil fuel belong to this class including oil, coal and natural gas (Dincer, 2000).

As mentioned earlier these energy sources take thousands and millions of years to form and therefore they are not easily replenished.

On the other hand, energy sources that are easily replenished in nature once they are used are called renewable energy sources (Dincer, 2000). These renewable energy sources include solar and biomass. These sources are practically infinite and can be used again and again without fear of exhaustion. The sun for instance has been estimated to continue to produce solar radiation for another 7 billion years (Cain, 2012). Also biomass, which is mostly derived from plants, continues to be available as long as there are plants. Biomass can be converted into biofuel using different methods. In fact, in some developing countries like Nigeria today, biomass remains the major source of fuel for domestic use. A typical example of this kind of fuel is firewood. Because the project described in this thesis is based on the conversion of the sun's energy into electricity, and the sun being a renewable energy source, a brief description of the above mentioned renewable energy sources will be presented in the following sub-sections.

2.5 Biomass

Biomass mostly refers to all plant-based organic materials obtained from living or recently living plants (Hoogwijk et al, 2003; McKendry, 2002). Through the process of photosynthesis, these plants convert the solar energy of the sun to chemical energy stored in the plant. Biomass energy is therefore energy derived from biomass. The conversion of biomass into energy can be done in different ways giving rise to the different biomass energy technology applications. These involve converting biomass into solid, liquid or gaseous fuels called biofuels, principally used for transportation (Wahlund et al, 2004; Alonso et al, 2010). This can be done through thermal, chemical or biochemical means. Examples of such biofuels include bio-ethanol, methanol, ethylene (or ethylene glycol) and propylene (or propylene glycol) (Wahlund et al, 2004, Sun and Liu, 2011). Another method of bioenergy production is by direct combustion or burning of biomass such as wood to produce heat energy for direct application such as cooking and space heating and for indirect generation of electricity by heating water to produce steam for operating turbines (Wahlund et al, 2004; Heinimo and Junginger, 2007).

In a broader sense, biomass includes both plant and animal materials that can be converted into industrial chemicals for the production of bioenergy. In recent times, biomass has been extended to sources such as waste from industrial and agricultural activities. These are called lignocellulosic biomass e.g rice husk (RH). Biomass has always been a major energy source for humans from ancient times and has been projected to contribute up to 15% of the global primary energy supply by 2050 (Fischer and Schrattenholzer, 2001). Rice husk an agricultural waste from rice milling has an energy content of 12.1 to 15.2 MJ kg⁻¹ (Kapur et al, 1996) with energy potential of about 1.7 to 2.1 EJ year⁻¹. A schematic diagram of energy generation from rice husk ash and steam used in places like USA and India is shown in Fig. 2.3

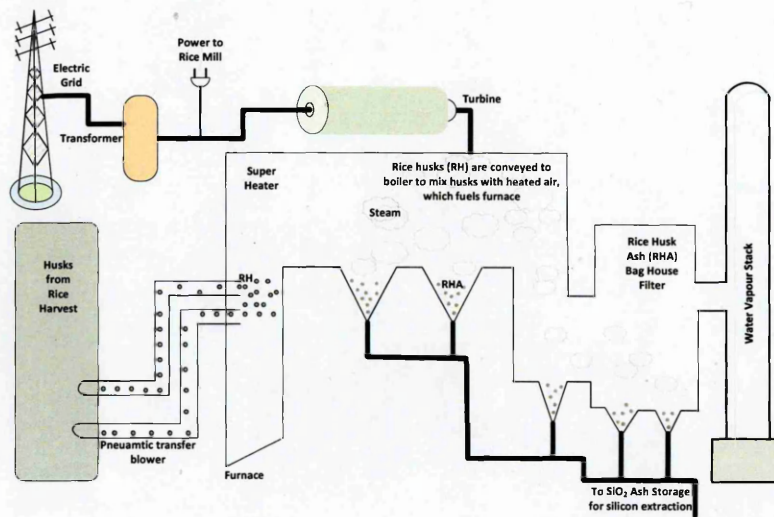


Figure 2.3: Schematic diagram of energy generation from rice husk combustion

For calculation of energy released from combustion, cellulose ($C_6H_{10}O_5$) is considered to be the combustion material; noting that rice husk atomic ratio of C/H is 0.59, very close to the stoichiometry ratio of 0.6 in cellulose (Larbi et al, 2012). The process diagram for production of rice husk ash and steam is shown in Fig. 2.3. Husks from rice harvest are transferred to the furnace by a blower where the rice husks are conveyed to the boiler to mix husks with heated air; while rice husk ash produce drop through filters to RHA bag house for silicon extraction or other RHA useful purposes, the steam goes into the turbine to rotate it for power generation that is utilised for electricity supply to the rice mill and the remaining power transferred to national grid through a transformer.

2.5.1 Solar Energy

Solar energy is simply energy based on the sun's electromagnetic radiation. Figure 2.4 shows the solar spectrum comprising electromagnetic radiation of various wavelengths or frequencies (Katai, 2011). This spectrum covers the ultraviolet (UV) radiation (100 - 400) nm, the visible (VIS) radiation (400 - 700) nm and the infrared (IR) radiation (700 nm and above). This covers most of the important spectrum for terrestrial solar energy application especially through solar thermal and photovoltaic technologies. Further discussion on solar energy conversion through various technologies is presented in the following sections.

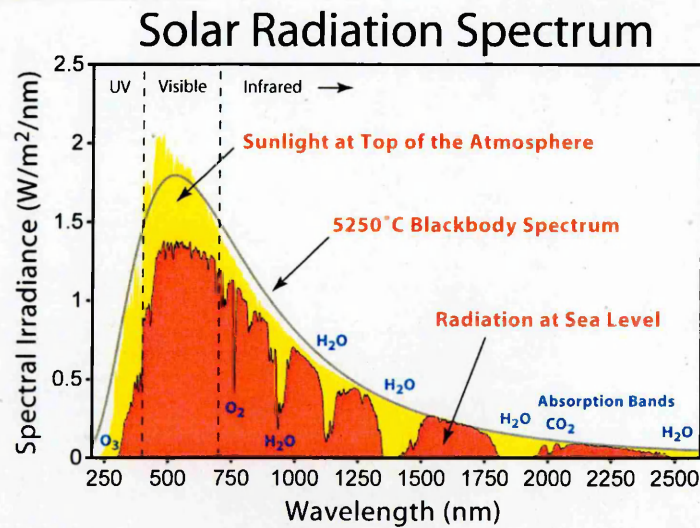


Figure 2.4: The solar spectrum showing the spectral irradiance vs. photon wavelength in the UV, VIS and IR regions for a 5250°C blackbody, which approximates the sun spectrum of the sun as well as a spectrum at the earth's surface that survives the absorption of molecules such as H₂O and CO₂ in the earth atmosphere (Katai, 2011)

2.6 Solar radiation and air mass coefficients

The sun can be approximated to a black body radiator operating at an effective temperature of 5777 K (Nelson, 2004). As the solar spectrum passes through the atmosphere, it gets attenuated due to absorption and scattering by the molecules and particles present in the atmosphere; As a result, some of the components of the spectrum are stripped off before the sunlight reaches sea level at the Earth's surface (Riordan, 1986). For example a large portion of the short-wavelength ultraviolet component of the solar spectrum is absorbed by the ozone layer in the upper part of the atmosphere. Also water vapour, molecular nitrogen, carbon dioxide as well as oxygen, contribute to this absorption and scattering of different wavelengths of the solar spectrum before it reaches the surface of the Earth. As a

result, the solar intensity varies with altitude as well as with the sun's zenith angle as the solar spectrum travels through the atmosphere.

The solar spectrum is usually characterised after traveling through the atmosphere using the "air mass coefficient" or simply the "air mass" (AM). This AM is mostly used to characterize the performance of solar cells under standardized conditions; as this is simply defined as the ratio of the optical path length (L) of the solar spectrum through the atmosphere to the vertical path length (L_o) normal to the Earth's surface at sea level (atmosphere thickness) when the sun is at the zenith as shown in figure 2.5

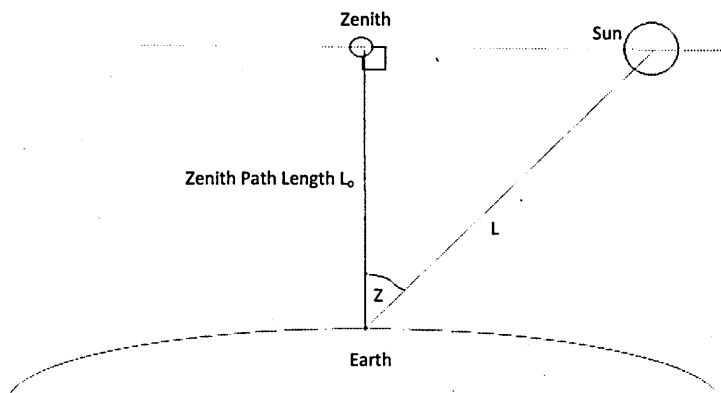


Figure 2.5: Schematic of the sun's position for the determination of air mass (AM).

Then

$$AM = \frac{L}{L_o} \approx \frac{1}{\cos Z} \quad (1)$$

where Z is the angle between the zenith and the position of the sun at the time in question (Nelson, 2004)

The variation of Z with time of the day and seasons of the year causes the air mass variation to be dependence on the sun's elevation and the position of the observer on the Earth's surface. Equation (1) is a very simple approximation and does not take into account the curved nature of the Earth's surface. Improvements to this model (1) have been proposed by different people (Nelson, 2004; Matson et al, 1984; Kasten, 1993 and Bird, 1982) although it is accurate for values of Z up to $\sim 70^\circ$. Different AM values correspond to different levels of attenuation undergone by the solar radiation when the sun is at different angles relative to the zenith.

AM0: This means zero-atmosphere and represents the spectrum outside the atmosphere where there is essentially no attenuation to the radiation from the sun. AM0 is used as the standard for the characterisation of solar cells used in space application such as those used for powering communication satellites in space (Riordan, 1986; Nelson, 2004 and Matson et al, 1984).

AM1: This is the air mass for the spectrum that has travelled through the atmosphere when the sun is directly at its zenith above the point on the Earth under consideration. AM1 is regarded as one atmosphere thickness, and under this condition, $Z = 0^\circ$, giving the value of unity to Equation (1.1). AM1 can be used for characterising solar cells meant for use in equatorial and tropical regions of the Earth (Riordan, 1986; Nelson, 2004; Matson et al, 1984; Bird, 1982 and Bird et al, 1985).

AM1.5: This is the solar spectrum that has passed through 1.5 atmosphere thickness. It represents the air mass when the sun is at an angle of $Z= 48.2^\circ$ to the Earth's surface. In fact, AM1.5 is used as the average air mass of the solar spectrum at mid-latitudes. This is because the air mass of the spectrum in the region actually fluctuates roughly about this value within the day. This is the air mass generally adopted by the global solar energy industry as a standard for the characterisation of solar cells and solar panels for all terrestrial applications (Riordan, 1986; Nelson, 2004; Matson et al, 1984; Bird, 1982 and ASTMG-173-03, 2014).

AM2 and AM3: The AM2 corresponds to the spectrum when the sun is at an angle $Z = 60^\circ$ relative to the zenith and AM3 corresponds to the situation with $Z = 70^\circ$. These two cover the range for characterising the average performance of solar cells in regions of high latitudes such as northern Europe as well as in temperate zones where winter, for instance, affects the spectra irradiance (Riordan, 1986; Nelson, 2004; Matson et al, 1984; Bird, 1982 and Bird et al, 1985).

Solar intensity or solar irradiance (I) is the power per unit area of solar radiation. The value of I varies as the solar radiation reaches the Earth's surface as a result of the aforementioned attenuation that takes place in the atmosphere (Riordan, 1986). When the radiation is released from the sun before any attenuation, the

maximum solar irradiance I_o is obtained. This value is also called the total solar irradiance. It is also called the total solar constant with an average value of about 1367 Wm^{-2} (Gueymard, 2004 and Mendoza, 2005). The solar intensity is related to the air mass according to Equation (2) (Kitai, 2011).

$$I = 1.1 \times I_o \times 0.7^{(AM)^{(0.678)}} \quad (2)$$

Therefore, for AM1.5 condition, the average value of irradiance is about 1000 Wm^{-2} . This is the value used in different research laboratories for the purpose of comparing performance of solar cells.

2.7 Solar energy conversion and technologies

The conversion of solar radiation or solar energy into other useful energy forms and sources takes different routes. In all cases, the primary components are photons which come from solar radiation. These conversion routes and the corresponding technologies involve the conversion of photon energy directly into heat energy, chemical energy or electrical energy as well as conversion into electricity through intermediate stages such as conversion into heat and then to electrical energy. The various modes of solar energy conversion and the associated technologies are discussed in the following sub-sections.

2.7.1 Photo-thermal solar energy conversion

This involves the direct conversion of photon energy (solar energy) into heat energy through the use of solar collectors and absorbers. The resulting thermal (heat) energy can then be used directly for example, for drying (as in solar dryers) (Vijay, 2012) and water heating (as in solar water heaters) (Frid et al, 2012) etc. In general, materials employed as absorbers and concentrators for the above class of photo-thermal energy conversion should have desirable properties such as high absorption coefficient over the entire solar spectrum and low thermal emissivity in the infrared region of the solar spectrum (Uhuegbu, 2011) as well as excellent resistance to atmospheric and environmental corrosion. Photo-thermal converters can operate at different temperatures. They can be employed in thermoelectricity generation, magneto-hydrodynamics as well as thermal dissociation of water for the production of hydrogen as another source of fuel. The basic principle of operation of a photo-thermal converter is depicted in figure 2.6.

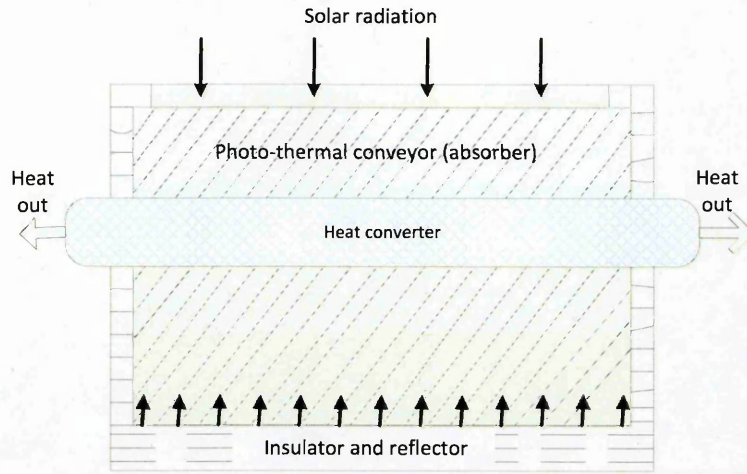


Figure 2.6: Schematic of the basic principle of operation of a photo-thermal converter.

The incident radiation (in the range 0.3 - 2.0 μm) is absorbed by the absorber and converted to heat depending on the design. The absorber therefore becomes transparent to longer wavelength radiation ($>2.0 \mu\text{m}$). These are then reflected back into the absorber. The thermal energy generated is then passed through the conveyor to the point where it is needed for heating application. For improved efficiency, η the incident solar radiation can be concentrated. The collector conversion efficiency of a flat plate solar collector may be given by Equation (3).

$$\eta = \frac{Q_u}{GA_c} \quad (3)$$

where Q_u is the useful energy gain of the solar collector, G is the solar irradiance and A_c is the collector area (Hutchins, 1983).

2.7.2 Thermo-photovoltaic solar energy conversion

In thermo-photovoltaic (TPV) energy conversion, thermal energy is converted into electrical energy. Thermal energy comes from infrared radiation. This infrared radiation (heat) can come from the solar radiation or from the heat in the surrounding. In fact, strictly speaking, since infrared radiation is a part of the broad solar spectrum, thermo-photovoltaic conversion is a special form of photovoltaic energy conversion utilising mainly the infrared radiation. In typical photovoltaic energy conversion using solar cells, the ultraviolet visible and near infrared parts of the solar spectrum are mostly converted into electricity. Conventional solar cells normally contain semiconductors with bandgaps between 1.0 eV and 4.0 eV (Strehlow and Cook, 1973). This automatically makes them

transparent to the infrared radiation corresponding to photons with energies below their bandgaps. In thermo-photovoltaic energy conversion therefore, very narrow bandgap semiconductors are used in the photovoltaic part of the entire process in order to effectively absorb longer wavelength infrared radiation from heat energy generated by an emitter. The thermo-photovoltaic converter therefore consists of thermal emitter and a photovoltaic cell. The thermal emitter is a special material with high thermal emissivity and low thermal absorptivity. Figure 2.7 shows the schematic of the operation of a TPV. The thermal emitter /radiator is a system that is capable of radiating heat energy in a similar way to a black-body radiator. Although the emitter is not a perfect black-body radiator, it can be treated as a black-body radiator to a good approximation so that the principle of black-body radiation governed by Planck's law can be applied to it. In their work, Demichelis et al (1982) considered the emitter as a grey body radiator instead of a black-body radiator and then expressed the energy per unit time emitted by the radiator at a temperature T and incident on the solar cell according to Equation (4).

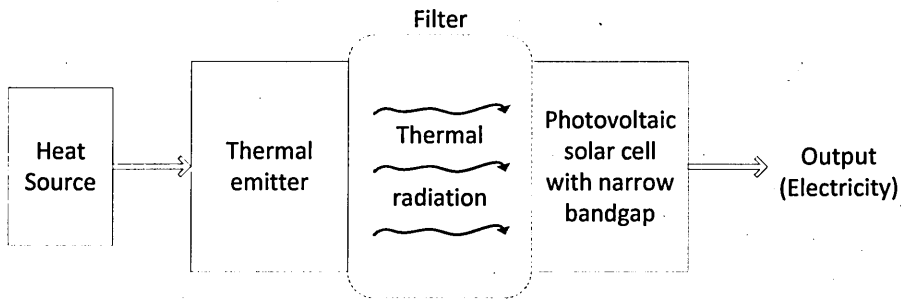


Figure 2.7: Schematic of the operating principle of a TPV. The heat source can be a solar concentrator consisting of a system of lenses with antireflection coatings.

$$P_{inc} = S_{R,C} \int_0^{\infty} \epsilon(\lambda, T) E_n(\lambda, T) \tau(\lambda) d\lambda \quad (4)$$

Where

P_{inc} = Energy per unit time emitted by the radiator,

$S_{R,C}$ = geometric factor of the radiator cell,

$\epsilon(\lambda, T)$ = spectral emittance at wavelength, λ and temperature, T ,

$E_n(\lambda, T)$ = emissive power of a black-body at wavelength, λ and temperature, T ,

$\tau(\lambda)$ = transmittance of the filter between the emitter and the solar cell.

The energy absorbed by the solar cell per unit time (P_{abs}) is then given by

$$P_{abs} = S_{R,C} \int_0^{\infty} A(\lambda) \epsilon(\lambda, T) E_n(\lambda, T) \tau(\lambda) d\lambda \quad (5)$$

where $A(\lambda)$ = absorbance of the cell.

The efficiency of the solar cell is given by

$$\eta_{cell} = \frac{J_{mp} V_{mp}}{J_{ph} V_g} \quad (6)$$

where

η_{cell} = efficiency of the solar cell,

J_{mp} = current density at maximum power point,

V_{mp} = voltage at maximum power point,

J_{ph} = total photo-generated current density,

$V_g = Eg/e$ is the bandgap voltage,

E_g = bandgap energy of the solar cell, and

e = electron charge.

The conversion efficiency η_{TPV} of the thermo-photovoltaic converter then becomes

$$\eta_{TPV} = \frac{J_{ph} V_g}{P_{abs}} A_{cell} \quad (7)$$

where A_{cell} = area of the solar cell.

Equations (4) - (7) show that the efficiency of a TPV depends strongly on the temperature of the emitter and the wavelength of the photons radiated by the emitter. Thermo-photovoltaic energy conversion is therefore a process based on heat/temperature differential between the emitter and the solar cell. Materials that have been used in TPV systems as emitters include erbium oxide (ErO_3) (Hofler et al, 1983), ytterbium oxide (Yb_2O_3) (Hofler et al, 1983; Demichelis, and Minetti-Mezzetti, 1980), molybdenum (Demichelis et al, 1982, Hofler et al, 1983), tungsten (Demichelis et al, 1982; Demichelis and Minetti-Mezzetti, 1980), tantalum (Demichelis et al, 1982) and polycrystalline graphite (Demichelis et al, 1982). Semiconductor solar cells that have been used in TPV systems include germanium solar cells (Hofler et al, 1983), silicon solar cells (Hofler et al, 1983), InGaAsSb/GaSb solar cells (Dashiell et al, 2006), InGaAs/InP solar cells (Waits,

2012), InGaAsP/InP solar cells (Waits, 2012) and InGaAs/InGaAs/InP solar cells (Waits, 2012). Dasheill et al (2006) have obtained a TPV conversion efficiency of 19.7% using InGaAsSb/GaSb solar cell at temperature of ~30°C with an emitter temperature of 950°C.

2.7.3 Photo-chemical solar energy conversion

Photochemical solar energy conversion deals with the conversion of radiant energy of the sun into chemical energy which can further be converted directly into electricity (photo-electrochemical conversion) or stored in the form of hydrogen (through water splitting) (Berberoglu and Pilon, 2010; Babu et al, 2012) or in other forms such as methanol and other hydrocarbons. Photosynthesis is one such way of converting the sun's radiant energy into chemical energy which can be found in nature. The photo-chemical converter is therefore an energy generator as well as an energy storage system. In the case of serving as a storage system, the stored chemical energy can be converted into other desired forms of energy such as heat and electricity for utilisation.

2.7.4 Photovoltaic solar energy conversion

Photovoltaic (PV) solar energy conversion is the direct conversion of solar energy of the sun into electricity using a photovoltaic solar cell. Among all the above discussed solar energy conversion technologies, the photovoltaic technology is the most famous as well as most widely researched and commercialised to date. Unlike the other solar energy conversion technologies, PV technology has provided power for various levels of application ranging from low power applications in the order of 1.0 W as in calculators and wrist watches, to megawatt applications such as in power stations (Wenger et al, 1991). The basic principle of operation of PV solar energy conversion is based on the ability of photons from the solar radiation to break bonds in a photovoltaic (photo-active) material in order to create electron-hole pairs which can then be separated by a built-in electric field (in a fully fabricated photovoltaic device) and collected in an external circuit before they are recombined to produce electricity (McEvoy et al, 2003). The fully fabricated photovoltaic device is a solar cell. Silicon happens to be the most dependable material, as the most widely manufactured solar cells are based on it (Katai, 2011). Silicon based solar cells are of three main types: single crystalline silicon, multicrystalline silicon and amorphous silicon (Nelson, 2004). Single crystal silicon is grown by a number of methods. In the Czochralski

process, a single crystal is slowly pulled out of the melt with interstitial oxygen as the main contaminant present in a concentration of about 10^{18} atom cm^{-3} (Kaiser et al 1956, Bosomworth et al 1970) giving rise to the well-known $9\mu\text{m}$ infrared absorption band. The costly float zone process gradually forms a single crystal from a polycrystalline rod by passing a molten zone through it to produce higher purity material, but may establish present of carbon up to a level of $3 \times 10^{17}\text{ cm}^{-3}$ for infrared absorption band at $16.5\mu\text{m}$ (Newman and Willis 1965, Nozaki 1974). Cz and Fz Multicrystalline silicon used in most commercial silicon solar cell fabrication, is produced by variety of methods such as casting and ribbon growth. The relatively large grains sizes (0.1 - 10 cm) imply that multicrystalline material can yield moderately efficient device if prepared using techniques similar to those used for monocrystalline silicon. The amorphous silicon (a-Si) solar cell has a *p-i-n* junction design due to its short diffusion lengths when doped. Thus, the intrinsic or central undoped region is needed to extend the thickness over which photons can effectively be absorbed. There is charge separation due to electric field created by the built-in bias dropped across the width of the *i* region, provided that the *p* and *n* layer doping levels are high enough, the depletion region is contained almost entirely within the *i* region. In the *p-i-n* diode structure, photocarriers are primarily collected by drift rather than by diffusion. A schematic layer width of *p-i-n* structure is presented in figure 2.8.

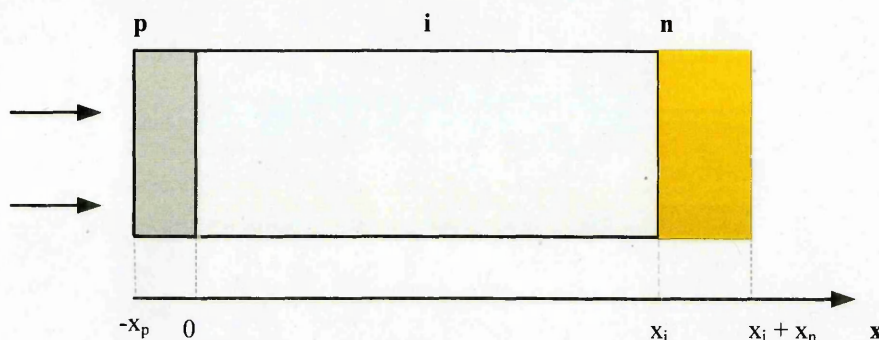


Figure 2.8: Schematic layer widths of p-i-n junction structure for amorphous silicon

A typical crystalline silicon solar cell is an *n-p* junction fabricated in a wafer of *p* type silicon of few hundred microns thick and about 100 cm^2 in area. While the front surface is anti-reflection coated, both front and back surfaces are contacted before encapsulation in a glass covering. The base of the cell, with thickness of about $300 - 500\mu\text{m}$ is formed by the *p* type wafer in order to absorb as much light as possible, and lightly doped ($\sim 10^{16}\text{ cm}^{-3}$) to improve collection in the neutral

base region without limiting the open-circuit voltage. In order to reduce sheet series resistance, the *n* type emitter created by dopant diffusion is heavily doped ($\sim 10^{19} \text{ cm}^{-3}$). Figure 2.9 shows the schematic structure of a basic silicon solar cell.

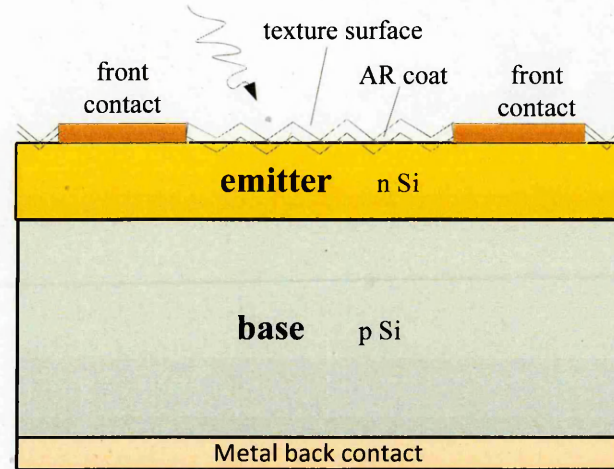


Figure 2.9: Schematic of the structural layer of basic silicon cell

The *n* thin layer should be sufficient to allow as much light as possible to pass through to the base and thick enough to keep series resistance reasonably low as shown in figure 2.10

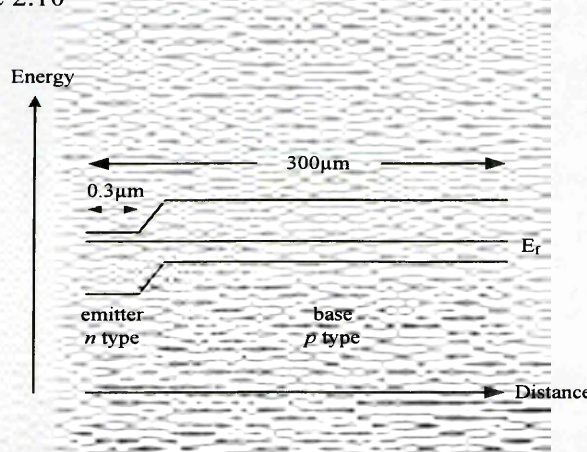


Figure 2.10: Energy diagram of a n-p junction in silicon

The carrier collection from the emitter layer is negligible due to the high recombination as result of the heavily doped layer. The metal back contact is crucial to the operation of the solar cell. The type of metal used here affects the electrical behaviour of the metal/semiconductor interface. This contact can have either ohmic behaviour or a rectifying (Schottky barrier) behaviour. The particular behaviour chosen depends on where the major depletion region in the device is located. If the contact is ohmic, there is no depletion region in semiconductor near

the metal-semiconductor interface. This junction allows current to flow both ways with a voltage-current relationship that comes close to that of a resistor. In general, if a p-n junction type device is intended, then the depletion region is made to exist at the interface between the window layer and the absorber layer. One of these two layers is then a p-type semiconductor and the other is an n-type semiconductor. In this case, the metal back contact should make an ohmic contact with the absorber layer. If a Schottky barrier-type device is intended, then the interface between the metal back contact and the absorber layer is a Schottky (rectifying) interface. In this case, the major depletion region in the device is located at this interface. There may or may not be a depletion region at the interface between the window layer and the absorber layer but the major depletion region is at the Schottky contact. The nature of this metal back contact is therefore crucial in the operation of a photovoltaic solar cell. By definition, an ohmic contact is one that obeys Ohm's law such that similar electrical current passes through it in both directions for a given voltage. On the other hand, a Schottky contact is a rectifying contact which allows electrical current to pass through it in one direction only. In practical devices, there is a very small current that flows in the reverse direction. Because of the large differences (of several orders of magnitude) between the currents in these two directions, the current in the preferred direction is dominant so that the infinitesimal current in the opposite direction is neglected. A p-n junction is also a good rectifying junction. Nevertheless, various techniques have been employed to increase the conversion efficiency of PV solar cells, based on two reasons. One, the silicon band gap (1.1eV) is smaller than the optimum (1.4eV) for terrestrial solar cell conversion, and two, that due to its relatively low absorption, a relatively thick layer of silicon is required to absorb sunlight effectively, making the cell expensive and bulky. These led to number of design that includes the use of solar concentrators (Katai, 2011 and Yang et al, 2013) and multi-junction tandem approach (Keppner et al, 1999). For thin film solar cell (e.g. GaAs, CuInSe₂, CdTe, CdS, ZnTe etc) as alternative, comprehensive reviews of the state of thin film solar cell for different materials are found in Bube (1998) and Archer and Hill (2001) which, will be briefly discussed later in this chapter.

The III-V compound-based solar cells are solar cells that have the group III-V semiconductors as their main absorber materials. The most prominent of these are

GaAs and InP. These have direct bandgaps of 1.42 eV for GaAs (Gurwitz et al, 2012) and 1.35 eV for InP (Ahuja et al, 1997). Both of these also have high carrier mobility (Milnes, 1987 and Joyce and Williams, 1970). Other III-V semiconductors that feature in solar cell fabrication include GaP (direct Eg = 2.78 eV; indirect Eg = 2.40 eV) (Wang et al, 2010), GaSb (Eg = 0.74 eV) (Chin, 1995), InAs (Eg = 0.36 eV) (Bhat et al, 2008), and InSb (Eg = 0.17 eV) (Yang et al, 2007). Sometimes their ternary compound semiconductor variants can be used for the purpose of tailoring the bandgaps. Examples of these ternary III-V compound semiconductors include InGaP, InGaAs, AlGaAs, InAlP etc. Sometimes quartenary semiconductors of the III-V compounds can be formed such as GaInNAs, GaNPAs. The III-V semiconductor-based solar cells are the best option for tandem (multijunction) and concentrated solar cells (Araki et al, 2006, Yamaguchi et al, 2006). The best record efficiencies for this group of solar cells have come from GaAs and InP-based solar cells. These include crystalline InP thin film solar cell with efficiency of 19.1% for a cell area of 4.02 cm² (Keavney et al, 1990), GaAs thin film module with efficiency of 23.5% for a module area of 858.5 cm² (Mattos et al, 2012), GaAs solar cell with efficiency of 27.6% for a cell area of ~ 0.99 cm² (Kayes et al, 2011), GaAs concentrator solar cell with 29.1% efficiency for a cell area of ~ 0.05 cm² as reported by Green et al (2015), InGaP/GaAs/InGaAs multi-junction solar cell with efficiency of 37.9% for a cell area of ~1.05cm² (Sasaki et al, 2013) and GaInP/GaAs:GaInAsP/GaInAs concentrator solar cell with efficiency of 38.5% for a cell area of ~0.20 cm² (McCambridge et al, 2011). Sharp Corporation has also reported record efficiency of 44.4% for a GaAs-based concentrator solar cell (Green et al, 2015).

2.8 Production of solar grade silicon

2.8.1 Siemens/Trichlorosilane (TCS)

The dominant semiconductor silicon technology consists of producing trichlorosilane (TCS) from metallurgical-grade silicon, through purification processes involving several distillation and condensation steps, as well as decomposing it in a thermal chemical vapour deposition (CVD) reactor commonly called a “Siemens reactor” with reference to the firm, which first in the 1960s developed this process, shown on left side of figure 2.11

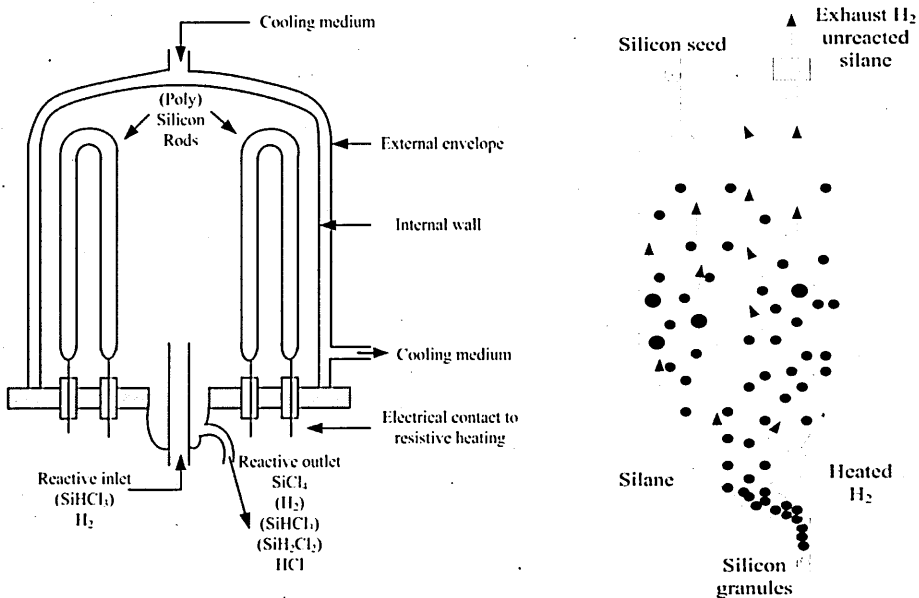
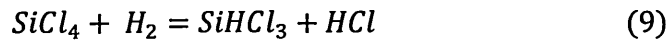


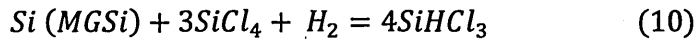
Figure 2.11: Siemens (Trichlorosilane) the dominant polysilicon technology (left) and silane (Fluidized bed reactor) the challenging technology (right)

for semiconductor needs. Approximately 90% of the globally installed polysilicon capacity is produced through this technology. Polysilicon process generates mainly silicon tetrachloride (STC) and other chlorosilanes in significant amounts as by products, which need to be recycled in a closed loop process. Two process strategies are pursued to generate TCS and recycle STC:

- Low pressure (1 - 5 bars) and temperature (300-350°C) hydrochlorination of impure metallurgical grade silicon (MG-Si) by hydrogen chloride for synthesis of TCS and thermal (1300°C) hydrogenation for recycling STC to TCS as given in equation (8), (9) and (10) (Bye and Ceccaroli, 2014)

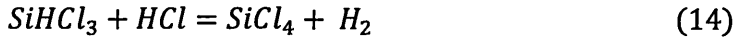


Using high pressure (20-35 bars) and temperature (550°C) hydrochlorination of MG-Si and STC in (10)



The high purity TCS is vaporized and introduced in the Siemens deposition reactor, where the gas is decomposed onto surface of heated silicon seed rods at 1100°C, building large silicon rod of high purity as presented in equation (11), (12), (13) and (14) (Bye and Ceccaroli, 2014)





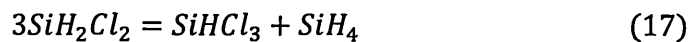
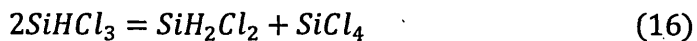
The Siemens process is highly energy consuming as major part of the energy is lost during dissipation. This has led to applying thermal reflector to the inner wall of reactors to reduce lost and wastage in energy.

2.8.2 Silane/ Fluidized bed reactor (FBR)

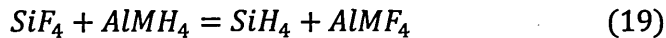
Production of polysilicon in a fluidized bed reactor (FBR) using monosilane/SiH₄/silane as feed-gas seems to be a challenger to the above described TCS/Siemens process. This is due to its strong reduction of energy consumed in the deposition process just by less than 10% of the globally installed polysilicon capacity in magnitude lower than in the Siemens deposition. It stands as a subject of numerous development projects within both incumbent and new producers of polysilicon. FBRs are used in many industrial processes like gasoline production and coal gasification. Silane seems to be the first alternative for a polysilicon process as feed gas as 100% of it can be converted to elementary silicon with hydrogen gas as the only by-product according to equation (15)



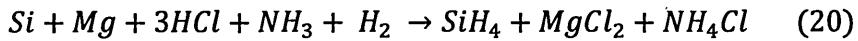
“Seeds”, in the form of fine MG-Si particles, are continuously loaded from the top or the middle of the reactor, whereas introduction of silane gas and hydrogen are near the bottom of the reactor as in the right side of figure 2.11. The gas stream with forces equal those of gravity are ascended with the flowing gas percolating into the particle in bed. Two major challenges of this process when silane is used are its inability to form fine powder and the deposition of silicon on the wall of the reactor. Three of the silane processes are one, using Union carbide that consist of the redistribution of purified trichlorosilane through fixed bed columns filled with quaternary ammonium ion exchange resins acting as catalyst in equation (16) to (20) (Bye and Ceccaroli, 2014)



The second consist of hydrogenation of silicon tetrafluoride SiF_4 by metal hydrides such as lithium aluminium or sodium-aluminium hydrides,



In the third process, silicon and magnesium powder is attacked by silane and ammonium chloride salt,

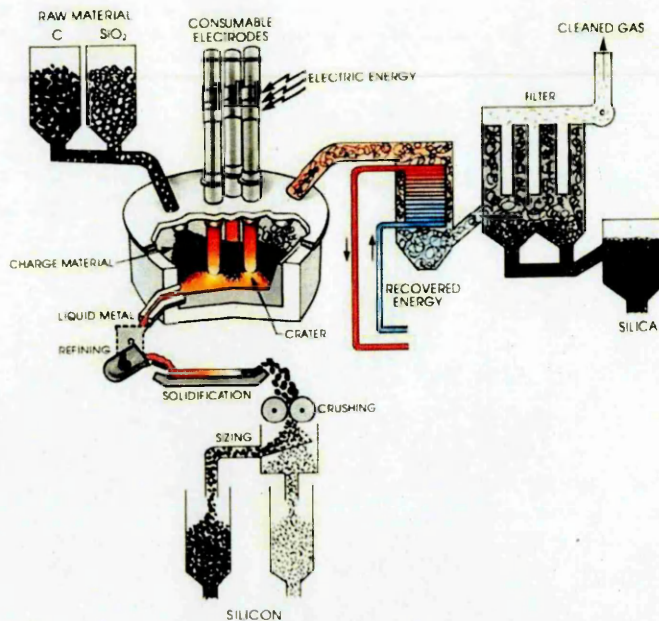


Monosilane and chlorosilanes are volatile silanes which are extremely reactive in the presence of oxygen, water or moisture. They require special care due to their classification as hazardous chemical substances (Ceccaroli and Lohne, 2003).

2.9 Upgrading metallurgical grade silicon (UMG-Si): Emerging technology?

The shortage of high purity silicon feedstock stimulated the launching of numerous projects to refine impure silicon to one with acceptable purity. The single crystal has a continuous and unbroken lattice structure that repeat itself. Poly-crystalline or multi-crystalline materials composed of many small crystals called grains. Metallurgical grade silicon (MG-Si) is multi-crystalline silicon not purified and thus, contains higher concentration of impurities than all other silicon grades. The grains texture is randomly oriented or has a preferential direction. The regions between the grains are called grain boundaries and are considered to be interfacial defects that are detrimental to electrical and thermal conductivity. In the past 8 - 10 years, attempts to make solar cell from metallurgical grade silicon has increased tremendously following the broadly inspired similar attempts during the 70-80s of last century; using those initiatives to research and develop on commercial low cost solar cell (Bye and Ceccaroli, 2014). Different researcher uses different purification process normally based on several steps with each taking care of groups of impurities e.g. donor (p), acceptor (B), transition elements etc. Majority of the processes used are explained in section (2.15). The use of wafers made from solar grade silicon can reduce cost dramatically. Upgraded metallurgical grade silicon (UMG-Si) is produced via leaching and purifying of MG-Si, followed by casting process. Multi-crystalline silicon of about three orders of magnitude less than $\text{S}_0\text{G-Si}$ or 2 - 4N is resulted. Using

special raw materials as rice husk ash for MG-Si produce, boron and phosphorus were found to be in the range of 1 to 4 ppm, while in standard metallurgical grade, B and P range between 7 and 50 ppm. The typical average values being around 25 ppm. The achieved boron level in rice hulls could be as low as 1 ppm. However, phosphorus goes as high as 40 ppm and would request an additional and specific treatment to make use of this source of silicon in solar cells (Ceccaroli and Lohne, 2003).



2.12: Schematic representation of a furnace for production of metallurgical grade silicon (Schei et al, 1998)

2.10 Production of MG-Si silicon from rice husk ash

2.10.1 Silica Preparation from Rice Husk Ash

In nature, the polymorphs of silica are quartz, cristobalite, tridymite, coesite, stishovite, lechatelerite (silica glass) and opal (Velupillai et al, 1997). It is this silica concentrated in the rice husk when it is burnt at a particular temperature over a specific time which makes the ash so valuable unlike every other agricultural waste product.

2.10.2 Thermal Decomposition of Rice Husk

There are two distinct stages in the decomposition of rice husk – carbonization and decarbonization. Carbonization is the decomposition of volatile matter in rice husk at temperature greater than 300°C which releases combustible gas and tar. Decarbonization is the combustion of fixed carbon in the rice husk char at high

temperature in the presence of oxygen (Maeda et al, 2001). The relative proportion of the different silica polymorphs in RHA depends not only upon the combustion temperature and atmosphere but also on the time for which the RH has been burnt. Mehta (1977) obtained totally amorphous silica by keeping the temperature below 500°C for prolonged periods and maintaining oxidizing conditions, while Yeoh (1979) observed that ash remained amorphous at 900°C, when this temperature was maintained for a period less than one hour. It was also noted that ash becomes crystalline silica when heated at 1000°C for more than five minutes. The most common form of crystalline silica found in RHA is quartz, but cristobalite and tridymite are also present as the other forms of crystalline silica, although tridymite and cristobalite are stable at 867-1470°C and 1470-1727°C, respectively, at atmospheric pressure (Heaney, 1994)

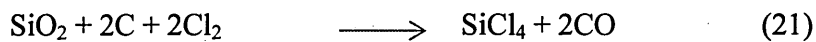
Chopra et al (1981) burnt RH at 700°C, evaluated the ash by X-ray diffraction (XRD) techniques and found that it was amorphous. Further heating of this ash at the same temperature transformed some of it into a quartz crystalline state. This showed the direct effect of time (keeping the temperature constant on the nature of preparation of RHA). The time-temperature relationship in addition to degree of crystallinity simultaneously influence the specific surface i.e. the surface area (cm^2) occupied by one gram of a solid converted to fine particles. It is also a parameter which closely relates to chemical reactivity of the ash. Ankra (1975) showed that the burning environment equally affects the surface area, therefore it must also be considered for efficient RH pyroprocessing. In addition, he studied the effect of chemical treatment and grinding of RH before preparing ash. It was proposed that cellulose and other combustibles should be burnt out without damaging the pore structure of the silica-rich skeleton. He showed that if pyroprocesssing occurs in the range 450°C - 500°C, the residual carbon, though amorphous in nature, cannot be removed on later thermal treatment.

Ikram et al (1984) prepared RHA containing 87% of SiO_2 , to produce polycrystalline silica from it; acid leached RH was heat treated at 300°C to 1200°C for four hours and subjected to extensive XRD studies. The result; revealed that the ash was amorphous below 800°C, with its conversion to crystalline form commenced at 800°C. Tridymite and α -quartz co-existed in comparable quantities at this temperature and the proportion of the latter silica phase increased with

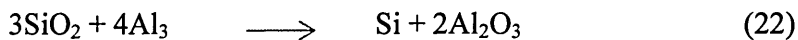
increasing temperature. Pitt (1985), while developing a process for large scale burning of RH, designed a furnace into which RH was sucked using negative pressure maintained by an exhaust fan. The hot gases from furnace, being mixed with ash, were taken to a boiler and finally separated by a multicone separator. In addition, this process had provision to recover the heat produced by combustion of the husk. Similarly, studies were conducted at pilot plant level for fabricating of a low-cost incinerator to produce RHA for cement manufacture. The combustion atmosphere was duly considered while designing and the RH combustion environment controlled by varying the air flow through a central tube (Shah, 2015). Alternatively, a modified Yamamoto paddy drier has been used to produce amorphous ash during field studies (Yeoh et al, 1979). However, the study was later centered round the feasibility of Mehta-Pitt work. The rice grower's co-operative societies also developed a fluidized bed furnace or combustor in which two tons of RH/hour could be burnt to produce amorphous RHA. The heat generated during combustion was high enough to be used in drying citrus pulp.

2.10.3 Rice Husk Ash Utilization

Rice husk ash is obtained by burning of rice husk and chlorinating its silica content to silicon tetrachloride, a raw material for silicon. Theoretically, the direct reduction of SiO_2 sand with carbon to yield Si could be possible but temperature must be more than 2000°C . When SiO_2 in rice husk reacts with chlorine gas in the presence of carbon, the SiO_2 can easily and efficiently change to SiCl_4 at a lower temperature (Basu et al, 1973).



SiCl_4 is purified by distillation because of its boiling point of 57.6°C , and this high purity SiCl_4 is converted to high purity Si by reacting with Zn metal (Okutani, 2009) Silicon metal can be produced by several processes. One of these processes is the reaction of SiO_2 with aluminum (Al) metal as shown below.



Wang et al, (1993) reported that the adiabatic combustion temperature of this reaction is 1760K , and the product Si (melting point, 1683K) is melted.

Banerjee et al (1982) due to the above perspective took energy saving factor and easy availability of reducing agents into consideration thoroughly by evolving a

process which was consequently, a direct reduction with magnesium powder at 600°C-650°C. On the other hand, work was concentrated on leaching RHA and establishing techniques to set optimum carbon/silica ratio for direct reduction (Amick et al, 1982). Ikram and Nazma (1988) prepared RHA at 620°C, reduced it by a metallo-thermic process and the silicon thus obtained was purified subsequently. The total impurity content, after purification was found to be less than 500ppm. Similarly, Hussein et al (2007) utilized RHA for extracting solar grade silicon, depending upon the silica content of prepared RHA. 18:27 (Mg:SiO₂) was found as the most suitable ratio for reduction; resulting silicon powder leached with different acids and evaluated as 99.85% pure. Patel et al, (1987) treated rice husk at temperature up to 1000°C, for different time durations and attempted to retain the amount of rice husk carbon, necessary for carbo-thermic reduction of accompanying SiO₂. Husk was also treated with various acids and bases separately. This experimentation resulted in 99% pure silicon. Rice husk ash has many applications due to its various properties, it is an excellent insulator, thus has applications in industrial processes such as steel foundries. RHA is used by the steel industry in the production of high quality flat steel, typically used for automotive body panels and domestic ‘white goods’ products (Giddel and Jivan, 2007). In the manufacture of insulation for houses and refractory of bricks, it acts as an active pozzolan and has several applications in the cement and concrete industry. A pozzolan is a powdered material which, on addition to the cement mixed with lime in a concrete, reacts to create compounds which improve the strength or other properties of the concrete by released hydration of the cement (King, 2000). It is also highly absorbent, and is used to absorb oil on hard surfaces and potentially to filter arsenic from water during purification. RHA is used in silicon chip manufacture; a company in Michigan is purifying RHA into silica suitable for several industries, including silicon chip manufacture (Tal Materials Inc, 2002). A method of obtaining silicon of 6N (99.9999%) purity by reducing white rice husk ash with magnesium at a temperature of 800°C followed by several successive acid leaching treatments is reported by Barati (2010). The possibility of obtaining silicon of similar purity by direct smelting of purified amorphous silica with carbonaceous reductants in an electric furnace followed by leaching with acids, and repeating the steps about nine times, was also suggested. The method used to analyze the 6N silicon was

not reported. However, the cost of such repeated smelting and leaching would be expected to prohibit use of this method as a low cost alternative to conventional methods. Bose et al (1982) subjected powdered silicon obtained by magnesium reduction of rice husk ash to melting and directional solidification. It was found that boron was the active impurity in the polycrystalline silicon ingot that was obtained. It was also determined that the minority carrier life time of the polycrystalline silicon material was of the order of $1-5\mu\text{s}$, and thus promising for photovoltaic applications. However, it has been subsequently estimated that the minimum carrier lifetime requirement for efficient solar cells fabricated from multicrystalline silicon wafers is $25\mu\text{s}$ (Barati et al, 2012). The formation of crystalline silicon by heating a silicon precursor e.g. silicon dioxide, with an ingredient that will generate an exothermic reaction when heated e.g. magnesium, and isolating crystalline silicon is described in Barati et al (2012).

2.10.4 Ash Analysis

Typically, the ash will contain some unburnt components of the husks. The unburnt component is predominantly carbon. It is typically measured by reheating a sample of ash in an oven. The difference in mass of the sample before and after heating is referred to as the loss on ignition (LOI). The LOI value is normally the same as the carbon content of the ash. The carbon content of RHA varies according to the combustion process. The main aim of converting husk to ash is to utilize its silica for metallurgical-grade silicon; the percentage of silica depends on the source of rice husk, the type of method adopted to ash the husk and the thermal treatment needed. Pyroprocessing of husk is frequently carried out to get RHA with maximum percentage of silica (Onoja et al, 2012). However, production of silica is an exception where certain amount of carbon is retained intentionally (Haxo and Mehta, 1975). This deliberate retention of carbon is difficult to control by researchers. However, proper pyroprocessing may result in RHA with highest percentage of silica. In addition, environment parameter, temperature and time duration are vital in this regard (Khane, 1985)

The results of chemical analysis have shown that the amount of unburnt component estimated as LOI, varied between 2.01% and 9.12% (Nagrale et al, 2012). The results of chemical analysis of RHA prepared in some countries (Swamy et al, 1983) and by Cook et al (1989), have been reproduced in Table 2.1.

Table 2.1: Comparisons of LOI in RHA (Cook et al, 1989) with those of some other locations

	Cook	*Basha	*Tashima	*Bouzoubaa	*Al-Khalaf	*Chandrasekar	*Zhang
Source of RH	Journal	Malaysia	Brazil	India	Iraq	USA	Canada
SiO ₂	92.15	93.10	92.90	90.70	86.80	94.50	94.50
Al ₂ O ₃	0.41	0.21	0.18	0.04	0.40	trace	0.15
Fe ₂ O ₃	0.21	0.21	0.43	0.04	0.19	trace	0.16
CaO	0.41	0.41	1.03	0.04	1.40	0.25	0.55
K ₂ O	2.31	2.31	0.72	2.20	3.84	1.10	3.68
MgO	0.45	0.59	0.35	0.50	0.37	0.23	0.35
Na ₂ O	0.08		0.02	0.10	1.15	0.78	1.12
SO ₃	**	**	0.10	0.10	1.54	1.13	0.24
CuO	**	**	**	**	**	**	**
TiO ₂	**	**	**	**	**	**	**
MnO	**	**	**	**	**	**	**
L.O.I.	2.77	2.36	**	4.80	3.30	**	8.55

Note: ** not reported * on reference

2.11 Effect of Various Impurities in Silicons

It is well known that impurity atoms have a strong effect on the efficiency of silicon as a material for solar cell. It is also known that the effect of impurities can be changed by heat treatments and by exposing the material to gettering atmospheres in which selected elements diffuse into silicon and combine with the impurities (Ceccaroli and Lohne, 2003). The impurity atoms may appear in solid solution as pairs with other elements, for example FeB, or as larger aggregates/precipitates with silicon and/or other elements, for example Fe₂Si. This depends upon the temperature, the concentration and the density of the imperfections (dislocations, grain boundaries). If the temperature or the (chemical) surroundings are altered, it will take some time before a new equilibrium is established. The time to reach equilibrium may depend on parameters such as temperature cooling/ heating rate and chemical composition, grain size, dislocation density etc. When comparing results from literature values in which the specifications of relevant parameters are not defined; it is likely that differences may appear. Most of the impurities in silicon used for solar cells exist at very low concentrations. Since measurements of trace quantities are difficult, much of the progress has occurred when new and better instrumentation has

become available. Over the years many review articles and books dealing with the effect of impurities have been published (Bathey and Cretella, 1982 and Ciftja et al, 2008). Impurities may be incorporated into bulk silicon material via two modes; (i) raw materials from which bulk silicon is produced and (ii) contamination from processing or fabrication of the bulk silicon. The atomic impurities often discussed in the literature with respect to bulk silicon can be classified into: dopants, transition metals, non-metals and other trace elements (Bullis, 1990).

2.11.1 Atoms from Group IIIA (B, Al, Ga...) or VA (P, As, Sb...)

The atoms from group IIIA and VA tend to act as substitutional impurities in silicon. The group IIIA elements substitute for silicon atoms in the crystal lattice resulting in an electron deficient bonding which tends to be supplied by electrons from neighbouring silicon atoms. Accordingly when silicon material is intentionally or otherwise contaminated with group IIIA elements the resulting semiconductor material is called a p-type semiconductor and the Group IIIA elements are termed as acceptor impurities. Group VA elements substitute for silicon atoms in a silicon crystal lattice with an excess electron. The resulting silicon material is termed an n-type semiconductor and donor impurity for the substitute element. Boron and phosphorus represent typical dopant impurities in silicon and are the most problematic impurities in terms of their removal from silicon. Their presence in crystalline silicon tends to modify the semiconductor properties of silicon substantially and they are therefore undesirable impurities beyond specified concentrations as shown below in table 2.2.

2.11.2 Transition metals and non-metals

The transition metals (mainly Ti, Fe, Cr, Ni, V, Co, Mn, and Cu) impurities are known to degrade minority carrier life times and solar cell performance significantly. The minority carrier life time is the average time elapsed before a free electron combines with a hole in the crystal lattice. Fortunately, these transition impurities have relatively low solid solubility in silicon and are thus removed effectively by known crystal growth techniques like acid leaching, directional solidification, slagging etc. Non-metallic impurities such as oxygen, nitrogen, carbon and hydrogen dissolve in silicon mainly as interstitial impurities. The interactive effects of non-metallic impurities and single atom impurities in silicon may facilitate formation of precipitated impurities such as SiC, SiO₂,

silicide etc. The synergetic effects of various impurity groups have been the subject of much ongoing research. The effect of some single metal impurities on the efficiency of a p-type silicon solar cell originally published by Ceccaroli and Lohne (2003) is shown in Figure 2.13 below

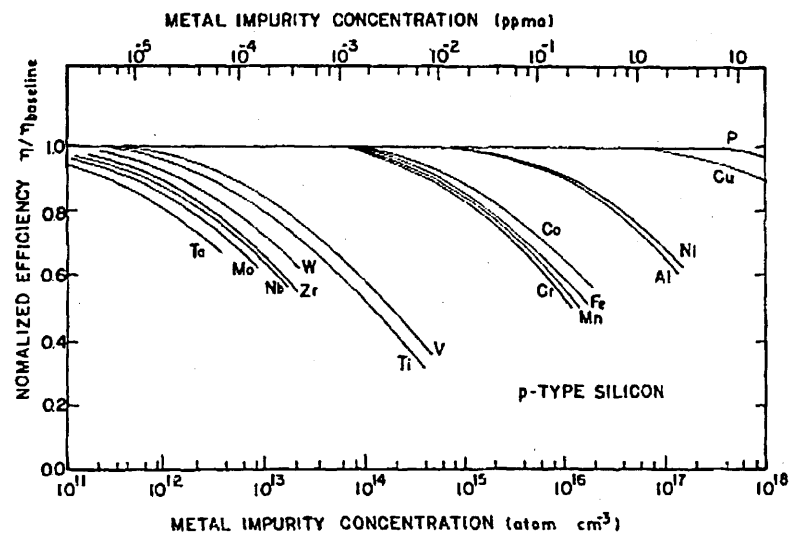


Figure 2.13: Schematic diagram of the effect of metal atom impurities on p-type solar cell efficiency (Ceccaroli and Lohne, 2003)

The metal impurity concentration given in Figure 2.13 is expressed as the number of atoms of impurity per cm^3 . Some impurities like Ta, Mo, W, etc., can reduce cell performance when present in extremely low concentrations; these contaminations produce dramatic changes to the electrical properties of silicon, especially to the minority carrier lifetime through formation of deep-level traps. However, others deep-level impurities, such as Fe, Cu, Cr, and Ni, can be tolerated even at higher concentrations because of their highly mobility with diffusion coefficients close to $10^{-6} \text{ cm}^2 \text{ s}^{-1}$. Ti is also a slow diffuser and easily forms oxide at high temperature. The concentrations of the impurities in Figure 2.3 are much lower than the impurity concentration found in metallurgical-grade silicon (see Table 2.2). Therefore, refining of metallurgical-grade silicon is a necessary step (Pizzini, 2010). However, these impurities are higher than the impurity levels in electronic- (semiconductor-) grade silicon, as shown in Table 2.2. It is from this position that potential exists for the production of less expensive and less pure solar-grade silicon, tailored for the photovoltaic market. It must be noted that solar-grade silicon does not have formal specifications; acceptable concentrations of impurities are usually reported instead. The solar-

grade silicon analyses reported in Table 2.2 provide a guideline rather than a specification for solar-grade silicon.

Table 2.2: Typical chemical analyses of silicon products for the semiconductor

Element	MG-Si (ppm) 2N	Solar-grade silicon (ppm) 6N	Polycrystalline solar-grade silicon (ppm) 7N	Electronic-grade silicon (ppm) 11N
Si*	99	99.999 9	99.999	99.999
Fe	2000-3000	<0.3	99	999 999
Al	1500-4000	<0.1		<0.01
Ca	500-600	<0.1		<0.0008
B	40-80	<0.3		<0.003
P	20-50	<0.1		<0.0002
C	600	<3		<0.0008
O	3000	<10		<0.5
Ti	160-200	<0.01		
Cr	50-200	<0.1		<0.003

* Silicon in mass %

2.12 Factors Influencing RH Ash Properties

2.12.1 Temperature

XRD analysis of RH ash produced over a range of combustion temperatures from 500⁰C to 1000⁰C has shown a change from amorphous to crystalline silica (Shinohara and Kohyama, 2004). In Vietnam, a series of experiment using a laboratory oven under conditions designed to stimulate the combustion from a rural facility were carried out. SEM analysis of the ash found that the globular amorphous silica particles increase in size from 5-10µm to 10–50µm with rising combustion temperature from 500⁰C – 600⁰C with the transition to complete by 900⁰C (Boateng and Skeete, 1990).

2.12.2 Geographical Region

Studies have shown that the physical and chemical properties of RHA are dependent on the soil chemistry, paddy variety, and the climate conditions

(Chandrasekhar et al, 2003). Studies have also shown that differences may also be due to fertilizers applied during rice cultivation (Maeda et al, 2001). However, only one report of a change in the physical and chemical properties of ash influenced by region was found. A variation in colour and trace metal was found in ash from the husks of northern India, resulting in a much darker ash than husks from other places. The colour variation was not related to difference in mineral composition of ash, but can be attributed to the fertilizers applied during rice cultivation, as K₂O found in some ashes could be a consequence of k-rich fertilizers used during the paddy cultivation (Boateng and Skeete, 1990).

2.13 Health Issues

All forms of crystalline silica represent a very serious health hazard as expressed by Occupational Health and Safety Administration (2002). The forms that develop at higher temperatures i.e cristobalite and tridymite are particularly harmful. Exposure to crystalline silica via inhalation can lead to a number of diseases, the most common being silicosis. Amorphous ash does not contain the more harmful forms of silica, but can still be a respiratory hazard, particularly if finely ground. No information specific to RHA is available, and this harmful process applies to crystalline silica from any source.

2.14 Phase transformation diagram of RHA

Based on the phase diagram, rice husk ash show the same transformation characteristics as that of pure silica SiO₂ and occurs in a number of different mineral phases with different crystal structure as shown in Figure 2.14 below. The conversion of husk to ash through thermal treatment may affect the original amorphous nature of RHA silica. This can be detected by XRD technique, i.e, whether the particular sample is in amorphous form or some fraction or whole converted into crystalline modifications (Skoog and West, 1971). On heating, the following mineral transformations are known to occur in silica (Filippov and Kittell, 1975)

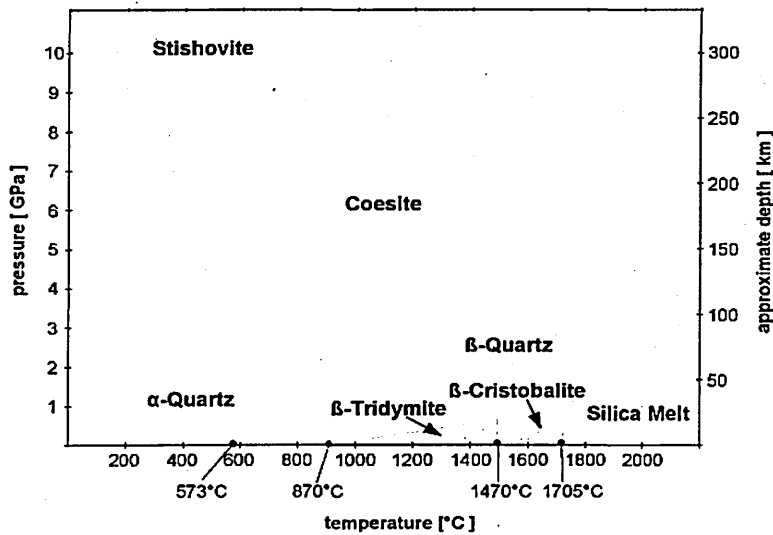


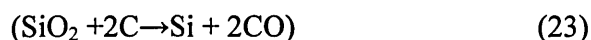
Figure 2.14: Transformation of silica from amorphous state to crystalline state (Hefferan and O'Brien, 2010)

The transformation of silica from amorphous state to crystalline state has been investigated by Boeteng and Skeete (1990). Shackley (2012) found that the transition temperature was about 870°C. The rate of heating is another important factor in controlling the quality of RHA. If the heating rate is high, potassium in rice husks does not volatilize, but instead reacts with silica to form potassium polysilicate combined with carbon. Thus, rapid burning of rice husks causes high residual carbon in the ash (Maeda et al, 2001)

2.15 Purification processes in silicon

The purification processes that are most frequently mentioned in the literature include one of the following technologies or combination. Metallurgical methods are believed to be five times more energy efficient than the conventional Siemens process that uses about 120-200 kWh/kg (Braga et al, 2008). Each of these steps reduces the concentration of a number of impurities by about one order of magnitude. The purification efficiency depends on the physicochemical properties of impurities especially their segregation coefficients. In this research work, some main and relevant techniques to this study for silicon purification will be discussed.

- (a) Reduction of silica by carbon: This process uses the same reaction that is used for manufacturing metallurgical-grade silicon in an arc furnace



The typical purity level in MG-Si manufactured through this process is 98–99% and even 95% because the raw materials used in this process contain high impurity levels. It is possible to obtain much higher degree of purity of silicon at a reasonable cost by using either naturally clean or purified (by leaching) silica or quartz and carbon black or pelletized activated carbon with higher than average purity in specially designed arc furnaces with purified electrodes (Pizzini, 1982).

(b) Acid leaching: This approach calls for pulverizing MG-Si to a powder with 70 μm or less particle size, and then treating this powder with various acids (e.g. aqua regia, hydrochloric acid, hydrofluoric acid) to dissolve metal clusters, which are frequently found in MG-Si at grain boundaries and are exposed during powdering (Amick, 1981). It is possible to obtain silicon with the purity of 99.9–99.97% (Gampel, 1961). The disadvantage of this process is that it is not effective in removing impurities dissolved intra-granularly in high concentrations, e.g., B and P. The efficiency of leaching depends on three main parameters: particle size, time of leaching, and leaching temperature. In a study by Dietl (1987) these parameters were investigated and high purity silicon was achieved as shown in Table 2.3. In order to achieve this level of purity, very fine grinding particle size less than 20 μm is required, which is not ideal in terms of materials handling. Hydrofluoric acid is also a material not easy to handle.

Table 2.3: Purification of silicon by leaching (Dietl, 1987)

	Fe	Ca	Mn	Ti	Al
Before leaching (ppm)	1250	1050	400	290	100
After leaching (ppm)	<1	<2	<1	<0.3	<1

Although leaching has showed success in removing some impurities, not all elements can be removed by this method. Impurities that exist in solid solution or impurities that are trapped as isolated phases within the silicon grains will not be removed. In other words, acid leaching is an effective method to remove the impurities that have already segregated during solidification. The efficiency of the acid leaching can be improved by the addition of calcium. Schei (1985) in study showed silicon containing few percent of calcium was cast, cooled slowly and

crushed into lumps around 5cm in diameter. A CaSi₂ phase formed at the grain boundaries contained most of the impurities due to Ca having high attraction for undesirable impurities (Yoshikawa and Morita, 2012). Exposing the silicon lumps to hydrochloric acid and ferric chloride disintegrated them into silicon crystals of below 2mm. These crystals were further purified by hydrofluoric acid in combination with an oxidizing agent.

(c) Gas blowing through the silicon melt: A purity level of 99.99% can be achieved by blowing gases such as Cl₂, O₂, SiCl₄, wet hydrogen, CO₂, or their combinations (Khattak et al, 2007). These gases react with impurities dissolved in silicon and form volatile compounds which evaporate from the melt. For example, chlorides of many metals and BOH are volatile. This method is effective in removing, e.g., Al, Ca, C, Mg, Fe, B, P, and Ti.

(d) Directional solidification: During crystal pulling from the melt (e.g., Czochralski or float zone growth) or directional solidification of molten silicon (e.g., float zone Si, ingot grown mc-Si) impurities segregate in the melt (Chu et al, 1987). At the end of the growth run, the majority of impurities is found in a thin layer near the top of the directionally solidified ingot or remains in the crucible. Such purification runs can be used to improve the purity of MG-Si. The efficiency of removal of impurities from silicon depends on their segregation coefficients which is the ratio of the element concentrations in silicon in solid state to that in liquid state. Since many elements such as Cu, Fe, Al, Ni etc. have segregation coefficients ranging from 10⁻⁶ to 10⁻¹ (Table 2.4), repeated directional solidifications can reduce impurity levels to a great extent. However, while most of the impurities have low segregation coefficients, P and B have segregation coefficients of about (0.35 and 0.8 respectively) so it is not possible to remove them effectively by directional solidification. Therefore, other purification methods have to be used alongside this method in order to remove P and B efficiently. In general, metals segregate much more effectively than shallow dopants.

Table 2.4: Segregation coefficient of some impurities in metallurgical grade silicon at melting point of silicon (Davis et al, 1980; Trumbore, 1960)

Impurities	Segregation Coefficient
Cu	4×10^{-4}
Zn	1×10^{-5}
B	0.8
P	0.35
Ga	8.0×10^{-3}
In	4×10^{-4}
Al	2.0×10^{-3}
S	10^{-5}
Mn	10^{-5}
Fe	8×10^{-6}
Co	8×10^{-6}
Ni	3.2×10^{-5}
Sb	0.023
Au	2.5×10^{-5}

The advantage of the directional solidification process is that it is an easy process and does not use any chemical reactions. However silicon losses occur since the portion of silicon which solidifies at the last stage should be disposed of because all impurities are concentrated in this section. Another disadvantage is that elements such as phosphorus and boron cannot be removed and an additional process has to be applied in order to make PV-grade silicon, thereby causing extra energy consumption in melting Si multiple times.

(e) Melting and refining of silicon with reactive plasma: A plasma torch is used to melt the near-surface layer of silicon and to activate gases such as argon, hydrogen, oxygen, and water vapour. These gases react with impurities in the melt and form volatile compounds (Nakamura et al, 2003). Both metals and dopants can be removed.

(f) Evaporation of phosphorus from the surface of the silicon melt, heated to boiling temperatures in the near-surface area of a crucible by an electron beam in vacuum (Hanazawa et al, 2003). Removal of phosphorus to very low level was previously thought to be impossible until one of the authors (Maeda) applied

electron beam (EB) melting under 10^{-12} Pa to demonstrate that removal of P could be successful (Sasaki et al, 2013)

(g) “Slagging” or calcium leaching: These approaches are based on mixing silicon with a chemical that has high affinity to undesirable impurities, binds them in a stable compound, and can later be separated from the silicon through deposition on the crucible walls, filtering through the mesh, or acid and solvent leaching. For instance, addition of Ca was successfully used for reduction of Fe, Ti, and P concentrations (Morita et al, 2003). Another example is immersion of crushed silicon in a metal with low melting point, such as aluminum, silver, or zinc (Kotval and Strock, 1980). Silicon may be completely liquefied by forming a Si-Al eutectic at temperatures well below the melting point of Si (such as 1100°C). During cooling, the solubility of Si in Al decreases and silicon precipitates are formed, which are separated from the molten Al by filtering through a mesh. Si pellets are cleaned from Al by acid leaching.

The list above, which is by no means complete, shows that technologies for inexpensive and energy-efficient purification of silicon are readily available.

(h) Post purification process of MG-Si using refining method: This is purification done after the hydrometallurgy process in order to understand the specific behaviour and interaction of certain elements; trace analysis of typical impurities have to be pursued by carrying out different refining stages on the MG-Si being the basic silicon with least purity. A profound analytical characterization of the starting materials, intermediate qualities and final products will have to be looked into as an indispensable task.

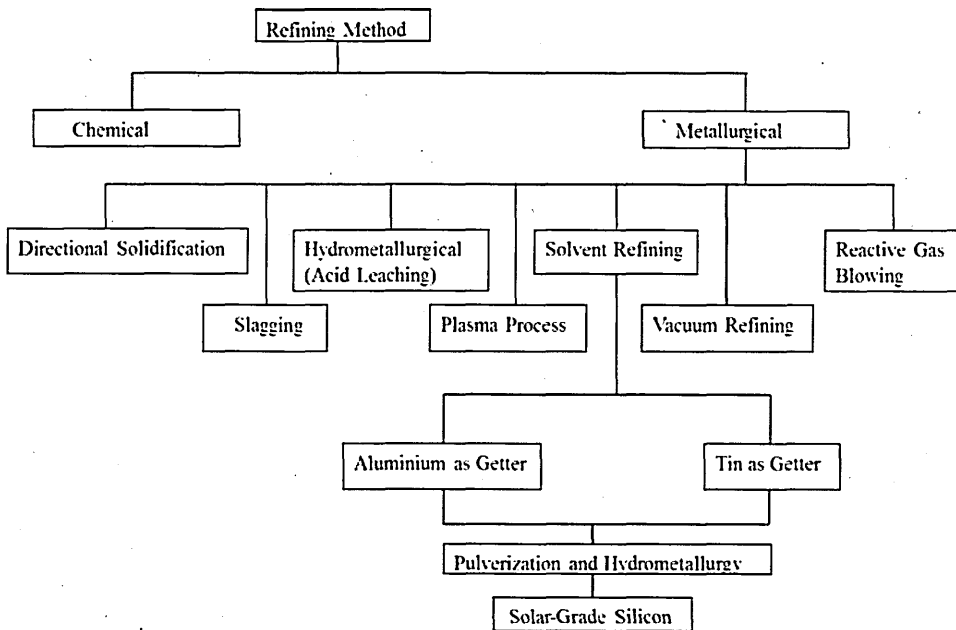


Figure 2.15: Diagram of post purification process

The figure 2.15 shows the post purification methods of MG-Si. However, the alloying process also known as refining process is discussed. It is based on the principle of fractional crystallization. The process involves melting of MG-Si in the presence of a solvent metal which is miscible with silicon in its liquid state, but immiscible in the solid state. Metals such as Mg, Al, Sb, Sn, Zn and Cu can be used for alloying as the impurities present in MG-Si are distributed between the solvent and solute phases according to their distribution coefficients during the melting process. Thus, during solidification of pure silicon crystallizes out from the molten alloy, major portion of impurity elements such as Ni, Fe, Al, Au, Cu and Ti which have low solubility in solid silicon are either retained in the solvent or are deposited at the grain boundaries of the alloy. Pure silicon crystals are separated from the solvent metal by acid leaching of the metal-silicon alloy for removing the solvent metal. The purification of MG-Si by the alloying process has been used by Driole and Bonnier (1971) who alloyed crude silicon with antimony or tin and then applied distillation to remove the solvent metal. Acids leaching process was done to segregated impurities from pure silicon crystals. Thus, this purification route has disadvantage that most of impurities been left behind with residue silicon which always requires the acid treatment to be

removed. Copper refining process is considered superior for the fact that it can easily be removed by acid leaching from silicon. However, not much quantitative results of purification achieved in different stages of the copper alloying process were reported. Among different alloying agents, copper appears to be attractive for: (i) negligible solubility of copper in silicon; (ii) copper is easily recoverable for reuse by aqueous electrolysis; (iii) HF and aqua regia can remove copper even in its oxide form.

2.16 Electrical Characteristics

This section will describe the main principles behind the operation of the solar cell and p-n junctions in semiconductors. First it will discuss carriers in semiconductors, then charge transport in semiconductors, and finally p-n junctions and solar cells.

2.16.1 Semiconductors and p-n junctions

There are two types of charge carriers in semiconductors: electrons and holes. The electron carries a negative charge and the hole (which is always located at the site of a missing electron), behaves as if it is carrying a positive charge. Electrons move in the opposite direction to holes in the presence of an electric field. A pure semiconductor crystal, such as silicon does not have available free electrons for current conduction at zero temperature; that is, the conduction band is empty and the valence band is full. At higher temperatures the thermal energy of the crystal is sufficient to break electron bonds for some conduction to take place. Silicon is of valence 4 and if atoms of valence 5 are added to the silicon crystal, it is easy to ionize the dopant atom creating free electrons; such atoms are referred to as donors. These extra electrons are added to the conduction band and are available for electron conduction as in figure 2.16a.

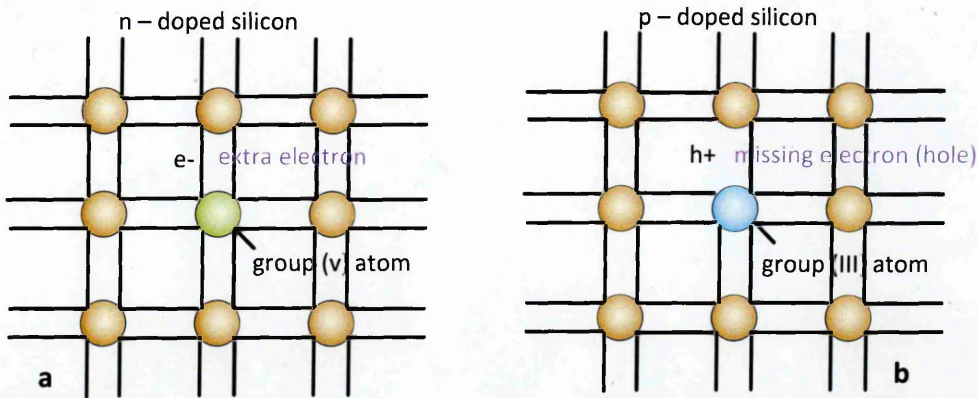


Figure 2.16: Schematic of a silicon crystal lattice doped with impurities to produce n-type and p-type semiconductor material

Similarly, figure 2.16b shows how the addition of atoms of valence 3 to silicon crystals leads to formation of holes. Such atoms are referred to as acceptors. As said before, a hole is a vacant site of an electron in the valence band and when electrons and holes have a close encounter they recombine. An electron-hole pair can be created by removing a bound electron from a neutral atom. In a pure semiconductor, the minimum energy required to create an electron-hole pair is equal to the bandgap energy of the semiconductor. Electron-hole pairs are created by thermal vibrations of the crystal at any non-zero temperature and also by absorption of photons that have energy above the bandgap energy. The latter is the process that is behind the operation of the solar cell. The production rate of electron-hole pairs is proportional to the intensity of the incident light.

Charge carriers can move under two influences: carrier drift, and carrier diffusion. A potential difference between two points in a semiconductor creates an electric field between the two points. The charge carriers, either the electrons or holes, will be drifted or diffused until they hit a scattering center or a trapping center. The carriers will have average drift velocity along the lines of the electric field. How easily the charges can move through the crystal structure in the presence of an electric field is described by a parameter referred to as mobility. Scattering of electrons can affect the transport of charge carriers and therefore the mobility. Two scattering mechanisms are impurity scattering and lattice scattering. Impurity scattering is due to both intentional dopant impurities and unwanted impurities. Lattice scattering is caused by vibrations and imperfections in the crystal lattice. The trapping of charge carriers depends on the energy of the charge carrier at the

trapping/impurity atom. The carrier is trapped if its energy is lower at the trapping site than anywhere else. The electric drift current density in a semiconductor is

$$J_{drift} = (qn\mu_n + qp\mu_p)\varepsilon = \sigma\varepsilon \quad (24)$$

where σ is defined as the conductivity, μ_n and μ_p are the electron and hole mobility respectively, n and p are the carrier concentrations of electrons and holes respectively, q is the electron charge and ε is the electric field strength. Carrier diffusion is due to a carrier concentration gradient in the semiconducting material. The diffusion current density is

$$J_{diff} = qD_n \frac{dn}{dx} - qD_p \frac{dp}{dx} \quad (25)$$

where D_n and D_p are the electron and hole diffusion coefficients respectively. The total current density due to drift and diffusion is

$$J_{total} = J_{drift} + J_{diff} \quad (26)$$

$$= (qn\mu_n + qp\mu_p)\varepsilon + qD_n \frac{dn}{dx} - qD_p \frac{dp}{dx} \quad (27)$$

$$= \left(qn\mu_n\varepsilon + qD_n \frac{dn}{dx} \right) + \left(qp\mu_p\varepsilon - qD_p \frac{dp}{dx} \right) \quad (28)$$

In solar cells, excess carriers are introduced by optical absorption of the semiconductor material, a process often called carrier injection. In this situation, the system is not in thermal equilibrium, that is $pn > n_i^2$, where n_i is the intrinsic carrier concentration. For equilibrium to be regained, minority and majority carriers recombine. When a semiconductor material is illuminated, electron - hole pairs are generated with a rate G_r . At equilibrium, the generation rate is equal to the recombination rate, $G_r = R_r = G_{th}$. The net recombination

rate is $U = R_r - G_{th}$ and is equal to zero at thermal equilibrium. For holes in an n-type semiconductor, the net recombination rate is proportional to the excess minority carrier concentration, or

$$U = \frac{P_n - P_{n0}}{\tau_p} \quad (29)$$

where τ_p is the minority carrier lifetime and is a measure of how fast majority and minority carriers recombine, P_n is the minority carrier concentration and P_{n0} is the minority carrier concentration at thermal equilibrium. The minority carrier lifetime is an important parameter for solar cells so it is used as a measure of the quality of the cell. The minority carrier lifetime can be estimated by illuminating a semiconducting sample and measuring the open-circuit voltage decay. If a short light pulse is used to illuminate an n-type semiconductor, then the minority carrier concentration after the light pulse is turned off is:

$$P_n(t) = P_{n0} + \tau_p G_r \exp(-t/\tau_p)$$

$$\text{at } t = 0, P_n(t) = P_{n0} + \tau_p G_r \quad (30)$$

Figure (2.17) shows a schematic of a p-n junction along with a graph that shows the minority carrier concentration in the n- and p-side of the junction respectively with and without light injection.

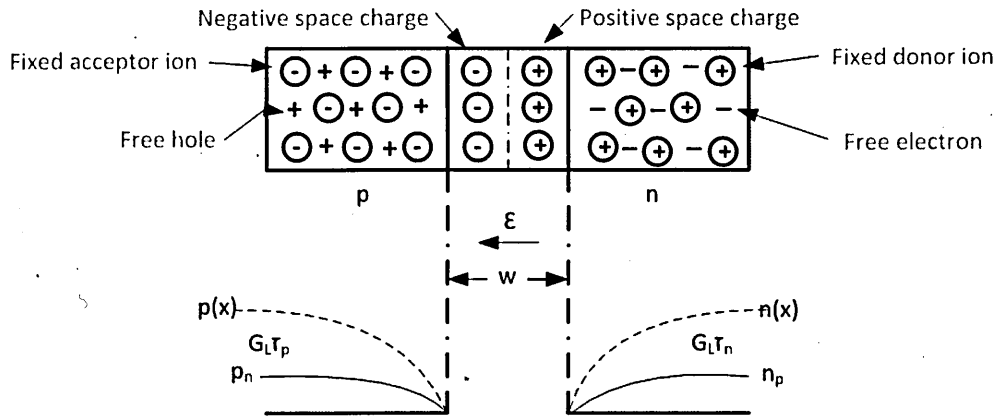


Figure 2.17 Minority carrier concentration in a p-n junction with (dashed line) and without (solid line) light injection

For solar cells, it is important that the recombination does not occur before the carriers reach the p-n junction. The relation between diffusion length L_p of holes in the n-type semiconductor and the minority carrier lifetime is given by

$$L_p \equiv \sqrt{D_p \tau_p} \quad (31)$$

where D_p is the diffusion coefficient of holes and N_a is assumed to be uniform. Similarly, for electrons,

$$L_n \equiv \sqrt{D_n \tau_n} \quad (32)$$

L_n and L_p have the dimension of length and they are called the hole and electron diffusion length. They vary from a few μm to hundreds of μm depending on τ . Equations (31) and (32) are only valid for the minority carriers. The short-circuit current in solar cells can decrease due to the recombination of charge carriers at a boundary (Zook, 1980). As the grain size decreases, electrical parameters such as minority carrier lifetime decrease (Yamazaki et al, 2006).

2.17 Depletion region

A p-n junction of opposite charge carrier types can be created in semiconductors. When this junction is formed, the electrons diffuse to the p-side and holes diffuse to the n-side. This is due to carrier concentration gradients near the junction. Uncompensated donor (N_D) and acceptor (N_A) sites are left behind in the n- and p-side, respectively. Donors on the n-side are ionized and thus positively charged. Similarly, on the p-side, acceptors are ionized and thus negatively charged. This creates an electric field in that region which is called the space-charge region or depletion region. The build-in electric field tends to counteract the inter-diffusion of charge carriers across the junction resulting in an equilibrium condition called thermal equilibrium. This causes the Fermi levels E_F in the semiconductors on both sides of the junction in figure 2.18a to align as shown in 2.18b

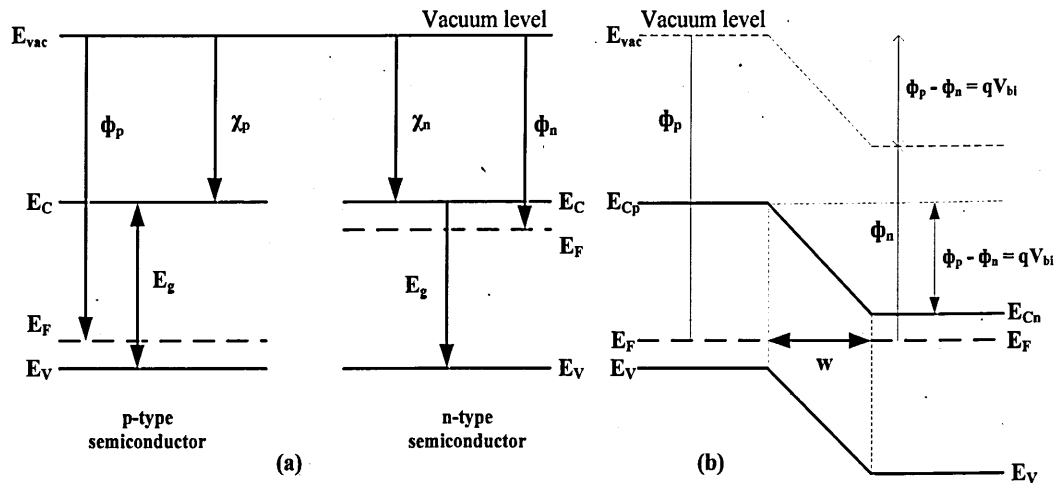


Figure 2.18: A simplified energy band diagram for the formation of p-n junction (a) before junction formation and (b) after junction formation

The potential difference between the n- and p-side is called the built-in potential V_{bi} and is determined by the difference in work functions of n and p type materials, ϕ_p and ϕ_n . The difference in work functions is equal to the difference in

the shift of the fermi levels from the intrinsic potential energy of the semiconductor. χ_p and χ_n are the electrons affinity in n- and p-type materials. A build-in V_{bi} is formed within the depletion region, w due to the electrostatic potential difference between the p-type and the n-type semiconductor on opposite sides of the junction. This build-in potential is then given by equation (33) (Nelson, 2003).

$$V_{bi} = \frac{kT}{q} \ln \frac{N_A N_D}{n_i^2} \quad (33)$$

where q is electronic charge and other symbols have their usual meanings.

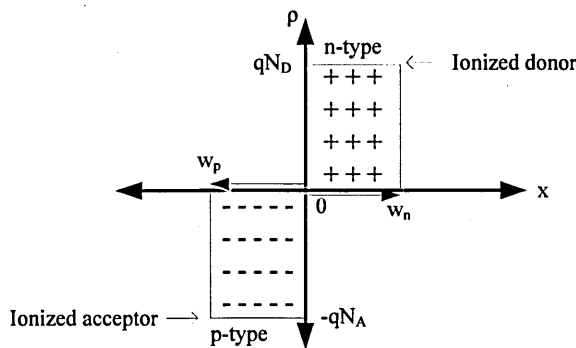


Figure 2.19: Schematic of the space-charge distribution of an abrupt p-n junction in thermal equilibrium

From a well-established theory of p-n junction (Katai, 2011), figure 2.19 shows the schematic of the depletion approximation for space-charge distribution of an abrupt p-n junction in thermal equilibrium with the maximum build-in electric field (E_m) existing at $w = 0$ in the depletion region and is presented in equation (34)

$$|E_m| = \frac{qN_A w_p}{\epsilon_0 \epsilon_s} = \frac{qN_D w_n}{\epsilon_0 \epsilon_s} \quad (34)$$

where w_p and w_n are the distances by which the depletion region extends into the p-type and n-type semiconductor respectively. ϵ_s is the relative dielectric permittivity, also called the dielectric constant of the semiconductor material and ϵ_0 is the dielectric permittivity of free space. The dielectric permittivity of the material in farads/meter is equal to $\epsilon = \epsilon_0 \epsilon_s$, for example $\epsilon_{Si} = 1.04 \times 10^{-10} F/m$.

The maximum electric field in the depletion region is related to the build-in potential according to equation (35)

$$V_{bi} = \frac{1}{2} |E_m| w \quad (35)$$

where $w = w_p + w_n$ is the width of the depletion region given by equation (36)

$$w = \sqrt{\frac{2\epsilon_s \epsilon_0}{q} \left(\frac{1}{N_A} + \frac{1}{N_D} \right) V_{bi}} \quad (36)$$

Equation (36) shows that reducing either the donor or acceptor or both concentration, increases the depletion width of the junction. In a one-sided abrupt junction such as p⁺-n junction, such that $N_A \gg N_D$, the depletion width extends more into the n-side of the junction. Then equation (36) simplifies to equation (37)

$$w = \sqrt{\frac{2\epsilon_s \epsilon_0 V_{bi}}{q N_D}} \quad (37)$$

Equations (33) - (37) are based on thermal equilibrium condition in which case there is no applied external bias across the p-n junction. However, if an external bias voltage V is applied across the junction, then the total electrostatic potential across the junction is modified to $(V_{bi} - V)$ where V takes a positive value for the forward bias and negative value for reverse bias (Choi et al, 2012). Equations (33) - (37) are then modified accordingly.

Under bias condition, the behaviour of the p-n junction changes in response to the applied bias voltage. One can then describe the junction in terms of its current-voltage (I-V) response. Under reverse bias condition in Schottky diodes, the depletion layer capacitance per unit area (C_D) is given for one-sided abrupt junction by equation (38) (Recart and Cuevas, 2006).

$$C_D = \frac{q\epsilon_0 \epsilon_s}{w} = \sqrt{\frac{q\epsilon_s \epsilon_0 N}{2}} (V_{bi} - V)^{-\frac{1}{2}} \quad (38)$$

If equation (38) is rearranged, we can obtain $1/C_D^2$ as in equation (39) (Siad et al, 2004)

$$\frac{1}{C_D^2} = \frac{2}{q\epsilon_s\epsilon_0 a^2 N_{D,A}} (V_{bi} - V) \quad (39)$$

where a is the area of the diode, V the reverse bias voltage, V_{bi} is the built in (diffusion) potential at zero bias and is determined from the extrapolation of the $C^{-2} - V$ plot to the V axis, ϵ_s is the dielectric constant of the silicon material, $N_{D,A}$ is the donor or acceptor concentration of n- or p-type semiconductor. Then, differentiating $1/C_D^2$ with respect to applied bias V gives equation (40)

$$\frac{d\left(\frac{1}{C_D^2}\right)}{dV} = \frac{2}{q\epsilon_s\epsilon_0 N_{D,A}} \quad (40)$$

Equation (40) therefore shows that the graph of $1/C_D^2$ versus V should give a straight line, and from the slope, the doping concentration N , can be obtained. Again, extrapolating the straight line to $1/C_D^2 = 0$, gives the built-in potential, V_{bi} . It should be noted that, it is difficult in practice to obtain the abrupt p-n junction described above for crystalline silicon, as there exist no voltage under which $C^{-2}(V)$ vanishes. The geometrical method used for extraction of the intercept contains high uncertainty and value of the intercept is per se shifted from the real build-in potential (Kim et al, 1993). So, the depletion approximation is not practicable because the approximation considers only the contribution from minority impurity concentration. In a practical device, the majority charge carriers also contribute to the properties of the junction in addition to the contribution from the minority carriers. As a result therefore, the depletion approximation can be modified by replacing the built-in potential, V_{bi} by $(V_{bi} - 2kT/q)$ (Sze and Ng, 2007). The term $2kT/q$ comes from the contribution from the majority carrier electrons in the n-side of the junction and majority carrier holes in the p-side of the junction. In the case of the Schottky diode, this term is given as kT/q since current contribution is mainly by one type of charge carriers. The I-V characteristics of an abrupt p-n junction under bias, is given by the Shockley equation which relates the total current through the p-n junction (which is a diode) to the applied bias according to equation (41) (Sze and Ng, 2007).

$$I = I_s(e^{(qV/nKT)} - 1) \quad (41)$$

where n is the ideality factor and I_s is the reverse saturation current, given by

$$I_s = qA \left(\frac{D_p p_n}{L_p} + \frac{D_n n_p}{L_n} \right) \quad (42)$$

2.18 Solar cell operation

When photon is absorbed by a semiconductor, an electron in the valence band can be excited into the conduction band in a process called photon absorption. This is strongest when the electron can go directly to the conduction band. For a metallized semiconductor material with contacts, investigation has attracted much attention during recent years (Sze, 2006 and Warner et al, 1994). The performance and stability of metal-semiconductor is of great importance to the solar cell devices. The parameters which characterise the contact depend on the fabrication method used; unless, special process leads to some degree of oxidation that generate thin interface oxide layer between the metal and the semiconductor. Thus, such insulating layer at interface may have strong influence on the diode characterisation and lead to bias charged interface states (Akkilic et al, 2003 and Jones et al, 2001), that plays an important role in the determination of Shottky barrier height using the current through a Schottky barrier diode at a forward bias 'V', based on thermionic emission-diffusion theory as determine from the representing of equation 2.32 with equation (2.34) (Sze, 1981; Rhoderick and Williams, 1988; Cova et al, 1998 and Chin et al, 1990):

$$I = aA^{**}T^2 \exp\left(\frac{-q\phi_B}{kT}\right) \left[\exp\left(\frac{qV}{kT}\right) - 1 \right] \quad (43)$$

where q is the electron charge, A^{**} the effective Richardson constant and equals 112 and $32 \text{ A cm}^{-2} \text{ K}^{-2}$ for n- and p-type Si, respectively (Sze, 2006 and Warner et al, 1994), a is effective diode area, T the absolute temperature, k the Boltzmann constant and ϕ_B the barrier height. By comparing equation (41) and (43), it shows that saturated current,

$$I_s = aA^{**}T^2 \exp\left(\frac{-q\phi_{BO}}{kT}\right) \quad (44)$$

assuming barrier height vary linearly with bias, where

$$\phi_B = \phi_{BO} + \beta V \quad (45)$$

where ϕ_{BO} is the barrier height at zero bias and $\beta (= (\partial V)/(\partial \phi))$ is the change in effective barrier height with bias voltage, substituting equation. (45) into equation. (44) becomes.

$$I = I_s \exp\left(-\beta \frac{qV}{kT}\right) \left[\exp\left(\frac{qV}{kT}\right) - 1 \right] \quad (46)$$

By introducing a parameter n such that $1/n = 1 - \beta$, equation. (46) can be written as

$$I = I_s \exp\left(\frac{qV}{nkT}\right) \left[1 - \exp\left(\frac{-qV}{kT}\right) \right] \quad (47)$$

For forward bias $V > 3kT/q$, the second term in equation (47) becomes insignificant and the parameter n is call the ideality factor of a schottky diode for I-V relations. This factor can be calculated from the slope of a linear region of the forward bias of $\ln(I) - V$. The barrier height ϕ_{BO} is determined from extrapolated I_s and given by the relation;

$$\phi_{BO} = \frac{kT}{q} \ln\left(\frac{aA^{**}T^2}{I_s}\right) \quad (48)$$

For silicon semiconducting materials with an indirect bandgap, lattice vibrations are required to assist in the process. The absorption coefficient α describes the ability of the material to absorb photons, as the semiconductor is transparent and the absorption coefficient is zero below the bandgap energy E_g

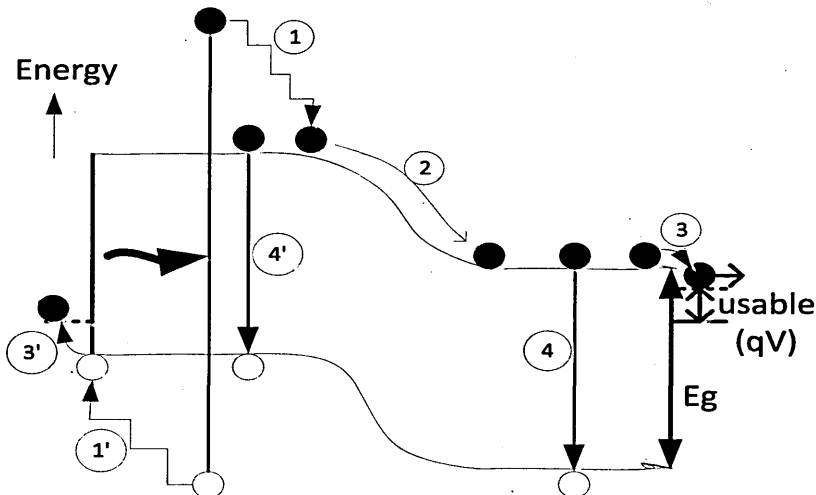


Figure 2.20: Efficiency loss processes in a p-n junction solar cell: (1) thermalisation loss; (2) junction loss; (3) contact loss and (4) recombination loss

Similarly, above a specific cutoff wavelength, λ_c the absorption coefficient is zero. It is given by

$$\lambda_c = \frac{1.24}{E_g} \quad (49)$$

where E_g is in eV and λ_c is in μm . The band gap energy of silicon is 1.12eV at room temperature. Therefore photons with energy less than the bandgap energy of silicon are not absorbed. Photon energies higher than 1.12eV correspond to wavelengths less than $1.11\mu\text{m}$ and therefore silicon absorb light from the near-infrared to the ultra-violet region. When photons of energy larger than the band gap energy of the semiconductor hit the surface of a semiconductor, electron-hole pairs are generated. Photons of energy that is much larger than the bandgap energy of the semiconductor lose part of their energy as heat. For absorbed photons in the semiconductor, the carrier generation rate is

$$G_r = \frac{\alpha P_{op}}{\hbar\omega} = \alpha J_{ph}(x) \quad (50)$$

where $J_{ph}(x)$ is the photon flux, P_{op} is optical power per unit area, α is the absorption coefficient and $\hbar\omega$ is the photon energy. This is referred to as photoconductivity. The responsivity of the semiconductor to incoming photons is given by

$$R_{ph} = \frac{J_L}{P_{op}} \quad (51)$$

where J_L is the resulting photocurrent density. The absorption coefficient α for direct bandgap materials is typically a factor of 100 higher than for indirect bandgap materials (Singh, 2007).

A p-n junction solar cell in principle composed of a p-n junction near the surface of the diode (shallow junction) and ohmic contacts to the front and back of the diode. The schematic diagram of a solar cell is shown in Figure 2.21. The ohmic contacts on the front surface are called bus bars and are used to provide ohmic contacts with minimum series resistance and without shadowing the incoming radiation. The junction must be near the surface of the grown film for most of the minority carriers to be able to reach the junction before they recombine with the majority carriers. If a minority carrier reaches the junction, it is swept across the junction by the electric

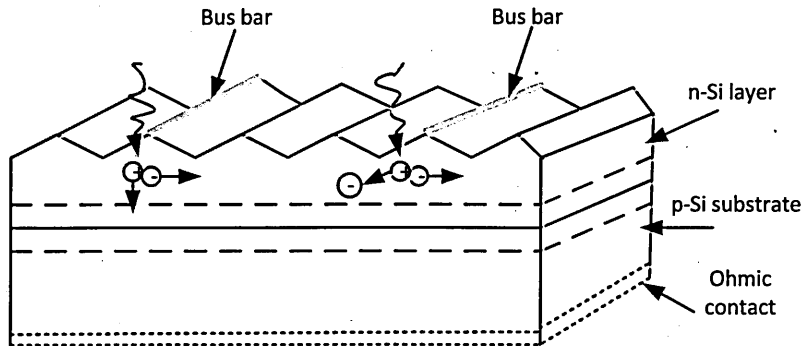


Figure 2.21: A schematic of a p-n junction solar cell along with the front and back ohmic contacts. On the left an incoming photon generates an electron-hole pair; the hole diffuses across the junction and contributes to the current. On the right, is hole from the generated electron-hole pair trapped by an impurity and does not contribute to the current

field resulting in an electric current. The texturing of the front surface is to reduce net reflection of light (by scattering all admitted or reflected light isotopically) and increase the optical depth of the cell, while shading of front surface by metal contacts reduces the surface area available to the incident light by as much as 10%. The diffusion length of the minority carriers is a measure of how far they diffuse before recombining. Therefore it is required that the diffusion length is larger than the distance from where they are created to the junction. The power solar cells can convert is proportional to the power of the incident light and the area of the cell. High doping is sometime needed in the emitter to reduce the series resistance, thereby increasing V_{bi} , to in turn increase V_{oc} . In silicon, the influence of doping on V_{oc} is limited by the shrinkage of the bandgap due to the introduction of tail states (Nelson, 2003).

2.18.1 Creation of an active layer

p-n junctions are typically fabricated by diffusion of impurities or dopants into a bulk material which can be silicon. This can be done in various ways, for example by placing a silicon wafer inside a chamber along with a gas that contains an impurity that would act as an acceptor or a donor and thus give the appropriate doping. By annealing for specific amount of time, the dopant diffuses a certain distance into the substrate. One disadvantage of this method is that the p-n junction will be graded instead of abrupt. In addition, if the substrate is polycrystalline, the dopants will diffuse faster along the grain boundaries, creating channels of dopants. Consequently, the depth of the junction and the thickness of

the solar cell will be relatively large which will lower the efficiency due to recombination of electrons and holes.

Another method is ion implantation, in which the dopant ions are accelerated into the grown silicon film. A disadvantage of this method is that the surface gets damaged during the ion bombardment. This can be partially fixed by annealing the substrate which in turn drives the junction deeper into the substrate, which is a disadvantage for solar cells because the junction has to be close to the surface in order for the charge carriers to reach the junction before they recombine.

This research work will apply a liquid-liquid refining process on MG-Si derived from rice husk ash containing minimum amount of B to produce SoG-Si grown on a silicon wafer. An Ohmic contact will be made to the rear face and schottky contact to the front face in order to produce a solar cell for evaluation.

2.19 Summary

This chapter presented a literature review that discussed silicon, silicon solar cells and silicon solar cell technology. The subsequent sections of the chapter presented the current issues on energy supply and consumption. The need for alternative sustainable, renewable as well as affordable clean energy supply for various applications was also presented. Reduction of greenhouse gases that largely contribute to the current issue of global warming was identified as the ultimate benefit of renewable and alternative clean energy supply. Rice husk ash (biomass/agricultural waste material), several renewable energy sources and the corresponding technologies to meet this need were reviewed with special emphasis on solar energy conversion for the purpose of this thesis. The review suggested well advance technologies as the conventional siemens and Silane chemical purification processes used for the refinement of silicon and an upgrading inexpensive emerging technology that uses metallurgical route which emerged due to the difficulty in producing solar grade silicon for solar grade cell application via this route that uses mineral quartz that consumed energy, time and money. A section discussed rice husk and its thermal decomposition into RH ash silica which is used in this work as an inexpensive emerging technology material for solar grade silicon material, an alternative source of silica that can be processed at more economical means to remove problematic boron, phosphorus

and other impurity elements before reduction. It reviewed the impurities in RH and their effects, the factors influencing RHA silica properties, the health issues involved, the phase transformation of RHA silica and the RHA silica purification processes. The sequence of process steps and process parameters such as temperature, time, type of reductants, type and concentrations of leaching reagent and optimization in order for this approach to solar grade silicon to be technically and economically feasible. Various refining technique that can be applied to reduce MG-Si in order to reach the solar grade silicon was also discussed. The chapter also discussed electrical characterization, semiconductors and p-n junctions, depletion region, solar cell operation and the creation of active layers.

It is as a result of motivation from the above summary that I have decided to use this research work to investigate the possibility of producing low-cost solar grade silicon from rice husk.

References

- Abdel Hamid, Z., Abdel Aal, A., & Schmuki, P. (2008). Nanostructured black cobalt coatings for solar absorbers. *Surface and Interface Analysis*, 40(11), 1493-1499.
- Adams W.G., Day R.E. (1877), *Proc. Roy. Soc. London A* 25 113.
- Ahuja, R., Auluck, S., Wills, J. M., Alouani, M., Johansson, B., & Eriksson, O. (1997). Optical properties of graphite from first-principles calculations. *Physical Review B*, 55(8), 4999.
- Akkilic, K., Türüt, A., Cankaya, G., & Kiliçoglu, T. (2003). Correlation between barrier heights and ideality factors of Cd/n-Si and Cd/p-Si Schottky barrier diodes. *Solid state communications*, 125(10), 551-556.
- Al-ferov Z .I., Andrew V. M., Kagan M. B., Protasov I.I., Trofim V.G. (1971), Sov. Phys. Semicond. 4 2047.
- AL-Khalaf, Moayad N. and Yousif, Hana A. (1984). Use of rice husk ash in concrete. *International journal of cement composites and lightweight concrete*, 6 (4), 241-248.
- Alonso, D. M., Bond, J. Q., & Dumesic, J. A. (2010). Catalytic conversion of biomass to biofuels. *Green Chemistry*, 12(9), 1493-1513.
- Amick, J., A. (1982). Purification of rice hulls as a source of solar grade silicon for solar cells. *Journal of the electrochemical society*, 129 (4), 864-866.
- Ankra, K. (1975). *Studies of black silica produced under varying conditions* (Doctoral dissertation, University of California, Berkeley).
- Araki, K., Kondo, M., Uozumi, H., Ekins-Daukes, N. J., Egami, T., Hiramatsu, M., & Yamaguchi, M. (2006). Packaging III-V tandem solar cells for practical terrestrial applications achievable to 27% of module efficiency by conventional machine assemble technology. *Solar energy materials and solar cells*, 90(18), 3320-3326.

Archer, M. D., & Green, M. A. (Eds.). (2014). Clean electricity from photovoltaics (Vol. 4). World Scientific.

ASTMG-173-03, (2014). Solar Spectral Irradiance:Air Mass 1.5, [Online]. Available at: <http://rredc.nrel.gov/solar/spectra/am1.5/> (Retrieved 21/02/2014).

Avila-García, A., & Morales-Ortiz, U. (2006). Thermally and air-plasma-oxidized titanium and stainless steel plates as solar selective absorbers. *Solar energy materials and solar cells*, 90(15), 2556-2568.

Banerjee, H. D, Sen, S. and Acharya, H. N. (1982). Investigations on the production of silicon from rice husks by the magnesium method. *Materials science and engineering*, 52 (2), 173-179.

Barati, M. et al. (2011). *Production of high purity silicon from amorphous silica*, WO Patent 2,011,022,817.

Basha, E. A, et al. (2005). Stabilization of residual soil with rice husk ash and cement. *Construction and building materials*, 19 (6), 448-453.

Basu, Prabir K., King, C. Judson and Lynn, S. (1973). Manufacture of silicon tetrachloride from rice hulls. *AICHE journal*, 19 (3), 439-445.

Becquerel A.E, Acad C. R., (1839). *Sci. Paris*, 9, 561.

Bhat, R., Dutta, P. S., & Guha, S. (2008). Crystal growth and below-bandgap optical absorption studies in InAs for non-linear optic applications. *Journal of Crystal Growth*, 310(7), 1910-1916.

Bird, R. E. (1982). Terrestrial solar spectral modeling. *Solar Cells*, 7(1-2), 107-118.

Bird, R., Hulstrom, R., & Riordan, C. (1985). Normalization of direct beam spectral irradiance data for photovoltaic cell performance analyses. *Solar Cells*, 14(2), 193-195.

Boateng, A. A and Skeete, D. A (1990). Incineration of rice hull for use as a cementitious material: The guyana experience. *Cement and concrete research*, 20 (5), 795-802.

Booth, D. C., Allred, D. D., & Seraphin, B. O. (1979). Stabilized CVD amorphous silicon for high temperature photothermal solar energy conversion. *Solar Energy Materials*, 2(1), 107-124.

Bose, D. N, Govindacharyulu, P. A and Banerjee, H. D (1982). Large grain polycrystalline silicon from rice husk. *Solar energy materials*, 7 (3), 319-321.

Bosomworth, D. R., Hayes, W., Spray, A. R. L., & Watkins, G. D. (1970). Absorption of oxygen in silicon in the near and the far infrared. In *Proceedings of the Royal Society of London A: Mathematical, Physical and Engineering Sciences* (Vol. 317, No. 1528, pp. 133-152). The Royal Society.

Bouzoubaâ, N. and Fournier, B. (2001). Concrete incorporating rice-husk ash: Compressive strength and chloride-ion penetrability. *Materials technology laboratory, CANMET, dept.of natural resources, canada*, , 1-16.

BP Energy Review (2015), <http://www.bp.com/statisticalreview> (Retrieved 11/01/2016).

Braga, A.F.B, et al. (2008). New processes for the production of solar-grade polycrystalline silicon: A review. *Solar energy materials and solar cells*, 92 (4), 418-424.

Bube, R. H., & Bube, R. H. (1998). Photovoltaic materials (Vol. 1). Amsterdam: *Imperial College Press*.

Bui, D.D. Hu J. and Stroeven, P. (2005). 'Particle Size Effect on the strength of Rice Husk Ash Blended Gap-graded Portland Cement Concrete; Cement and Concrete Composites. 357.

Bullis, W. M. (1990). Silicon material properties. *Handbook of semiconductor silicon technology*, 347-450.

Bye G., and Ceccaroli, B. (2014). Solar grade silicon: Technology status and industrial trends. *Solar Energy Materials and Solar Cells*, 130, 634-646.

Caballero, L. J. (2010). Contact definition in industrial silicon solar cells. *Solar energy*, 375-398.

Cain F., (2012) Life of the Sun, Universe Today, March 10.www.universetoday.com/18847/life-of-the-sun (Retrieved 24/11/2013).

Ceccaroli, B and L, Otto (2003). Solar grade silicon feedstock. *Handbook of photovoltaic science and engineering*, , 153-204.

Chandrasekhar, S., et al. (2003). Review processing, properties and applications of reactive silica from rice husk—an overview. *Journal of materials science*, 38 (15), 3159-3168.

Chin, V. W., Green, M. A., and Storey, J. W. (1990). Evidence for multiple barrier heights in P-type PtSi Schottky-barrier diodes from IVT and photoresponse measurements. *Solid-state electronics*, 33(2), 299-308.

Chin, V. W. L. (1995). Electron mobility in GaSb. *Solid-state electronics*, 38(1), 59-67.

Choi, P. H., Kim, H. J., Baek, D. H., & Choi, B. D. (2012). A study on the electrical characteristic analysis of c-Si solar cell diodes. *J Sem Tech Sci*, 12(1), 58-65.

Chopra, S. K, Ahluwalia, S. C and Laxmi, S. (1981). Technology and manufacture of rice-husk ash masonry (RHAM) cement. In: *Proceedings of ESCAP/RCTT Workshop on Rice-Husk Ash Cement, New Delhi*.

Chu, T. L., Chu, S. S., Kelm, R. W., & Wakefield, G. W. (1978). Solar Cells from Zone-Refined Metallurgical Silicon. *Journal of the Electrochemical Society*, 125(4), 595-597.

Ciftja, A (2008). Refining and recycling of silicon: A review.

Cook, D.J., Joseph, S., Baweja, D. and Crookham, G.D. (1989). Production and Utilization of Rice Husk Ash – Preliminary Investigation. Third CANMET/ACI International Conference on Fly ash, Silica fume, slag and natural Pozzolans in concrete, Trondheims Nonsay, June 18-23, 861-878.

Cova, P., Singh, A., Medina, A., & Masut, R. A. (1998). Effect of doping on the forward current-transport mechanisms in a metal–insulator–semiconductor contact to InP: Zn grown by metal organic vapor phase epitaxy. *Solid-State Electronics*, 42(4), 477-485.

Christiana, H and Stuart, B (7 2 2014), <http://www.pveducation.org/pvcdrom/pn-junction/doping>

Cramarossa, F., & Pio, C. (1983). Deposition techniques and applications of amorphous silicon films. *Materials Chemistry and Physics*, 9(1-3), 213-233.

Dashiell M. W., Beausang J. F., Ehsani H., Nichols G. J., Depoy D. M., Danielson L. R., Talamo P., Rahner K. D., Brown E. J., Burger S. R., Fourspring P. M., Topper W. F. Jr and Turner G. W., (2006) IEEE Transactions on Electron Devices 53 (12) 2879 - 2891.

Davis J. R, et al. (1980). Impurities in silicon solar cells. *Electron devices, IEEE transactions on*, 27 (4), 677-687.

Demichelis, F., & Minetti-Mezzetti, E. (1980). A solar thermophotovoltaic converter. *Solar Cells*, 1(4), 395-403.

Demichelis, F., Minetti-Mezzetti, E., Agnello, M., & Perotto, V. (1982). Bandpass filters for thermophotovoltaic conversion systems. *Solar Cells*, 5(2), 135-141.

Dietl, J. (1983). Hydrometallurgical purification of metallurgical-grade silicon. *Solar Cells*, 10(2), 145-154.

Dietl, J. (1987). Metallurgical ways of silicon meltstock processing. *Silicon processing for photovoltaics II*, 2, 285.

Dincer, I. (2000). Renewable energy and sustainable development: a crucial review. *Renewable and Sustainable Energy Reviews*, 4(2), 157-175.

Driole, J., & Bonnier, E. (1971). Herstellung von Silizium mit hohem Reinheitsgrad. *Metallwiss. Tech*, 25, 2-7.

Filippov, S. I and Kittell, G. (1975). *The theory of metallurgical processes*. Mir.

Fischer, G., & Schrattenholzer, L. (2001). Global bioenergy potentials through 2050. *Biomass and bioenergy*, 20(3), 151-159.

Foster, R., Ghassemi, M., and Cota, A. (2009). *Solar energy: renewable energy and the environment*. CRC Press.

Frid, S. E., Mordynskii, A. V., & Arsatov, A. V. (2012). Integrated solar water heaters. *Thermal Engineering*, 59(11), 874-880.

Fritts, C. E. (1883). On a new form of selenium cell, and some electrical discoveries made by its use. *American Journal of Science*, (156), 465-472.

Gay-Lussac, J. & Thenard, L. (1809). Mémoires de Physique et de Chimie de la Société d'Arcueil, 2, 339.

Goetzberger, A. and Hebling, C. (2000). Photovoltaic materials, past, present, future. *Solar energy materials and solar cells*, 62 (1), 1-19.

Green M. A., (1990) *Photovoltaics of age; Conference on Record, 21st IEEE Photovoltaic Specialists Conference, Kissimimee, May*, pp. 1-7.

Green, M.A., (1993). Silicon solar cells: evolution, high-efficiency design and efficiency enhancements. *Semiconductor science and technology*, 8(1), p.1.

Green, M. A. (2002). Photovoltaic principles. *Physica E: Low-dimensional Systems and Nanostructures*, 14(1), 11-17.

Green, M. A. (2009). The path to 25% silicon solar cell efficiency: History of silicon cell evolution. *Progress in Photovoltaics: Research and Applications*, 17(3), 183-189.

Green, M. A., Emery, K., Hishikawa, Y., Warta, W., & Dunlop, E. D. (2015). Solar cell efficiency tables (Version 45). *Progress in photovoltaics: research and applications*, 23(1), 1-9.

Giddel, M. R., & Jivan, A. P. (2007). Waste to wealth, potential of rice husk in India a literature review. In *International Conference on Cleaner Technologies and Environmental Management PEC, Pondicherry, India* (Vol. 2, pp. 4-6).

Gueymard, C. A., Myers, D., & Emery, K. (2002). Proposed reference irradiance spectra for solar energy systems testing. *Solar energy*, 73(6), 443-467.

Gueymard, C. A. (2004). The sun's total and spectral irradiance for solar energy applications and solar radiation models. *Solar energy*, 76(4), 423-453.

Gurwitz, R., Tavor, A., Karpeles, L., Shalish, I., Yi, W., Seryogin, G., & Narayananamurti, V. (2012). Bandgap and band discontinuity in wurtzite/zincblende GaAs homomaterial heterostructure. *Applied Physics Letters*, 100(19), 191602.

Hanazawa, K., Yuge, N., Hiwasa, S., & Kato, Y. (2003). Evaporation of phosphorus in molten silicon with electron beam irradiation method. *Journal of the Japan Institute of Metals*, 67(10), 569-574.

Haxo J. R, and Mehta, P. K (1975). Ground rice-hull ash as a filler for rubber. *Rubber chemistry and technology*, 48 (2), 271-288.

Heaney, P. J. (1994). Structure and chemistry of the low-pressure silica polymorphs. *Reviews in mineralogy and geochemistry*, 29 (1), 1-40.

Hefferan, K., & O'Brien, J. (2010). *Earth materials*. John Wiley & Sons.

Heinimo J. and Junginger M. (2007) Production and trading of biomass for energy - An overview of the global status, *15th European Biomass Conference & Exhibition*, 7 - 11 May, Berlin Germany.

Höfler, H., Würfel, P., & Ruppel, W. (1983). Selective emitters for thermophotovoltaic solar energy conversion. *Solar cells*, 10(3), 257-271.

- Hoogwijk, M., Faaij, A., Van Den Broek, R., Berndes, G., Gielen, D. and Turkenburg, W. (2003). Exploration of the ranges of the global potential of biomass for energy. *Biomass and bioenergy*, 25(2), 119-133.
- Horowitz, D. (2005). Jimmy Carter and the Energy Crisis of the 1970s: *A Brief History with Documents*. Bedford/St. Martins.
- Hulstrom, R., Bird, R., and Riordan, C. (1985). Spectral solar irradiance data sets for selected terrestrial conditions. *Solar Cells*, 15(4), 365-391.
- Hussein, A. M., EL-Saied, Houssni and Yasin, Mohamed H. (2007). Bioconversion of hemicelluloses of rice hull black liquor into single-cell protein. *Journal of chemical technology and biotechnology*, 53 (2), 147-152.
- Hutchins, M. G. (1983). Selective thin film coatings for the conversion of solar radiation. *Surface technology*, 20(4), 301-320.
- Ikram, N., Hussain, K. and Akhter, M. (1984). Preparation of Polycrystalline Silicon Dioxide from Rice Husk Ash. *J. Natur. Sci. and Maths.*, 24, 261-268.
- Ikram, N and Akhter, M. (1988). X-ray diffraction analysis of silicon prepared from rice husk ash. *Journal of materials science*, 23 (7), 2379-2381.
- Jones, F. E., Daniels-Hafer, C., Wood, B. P., Danner, R. G., & Lonergan, M. C. (2001). Current transport at the p-InP| poly (pyrrole) interface. *Journal of Applied Physics*, 90(2), 1001-1010.
- Joyce, B. D., & Williams, E. W. (1970). The preparation and photo-luminescent properties of high purity vapour grown indium phosphide layers'. In Proceedings of the international symposium on GaAs and related compounds, Aachen, W. Germany (pp. 57-63).
- McKendry, P. (2002). Energy production from biomass (part 1): overview of biomass. *Bioresource technology*, 83(1), 37-46.

Kaiser, W., Keck, P. H., & Lange, C. F. (1956). Infrared absorption and oxygen content in silicon and germanium. *Physical Review*, 101(4), 1264.

Kapur T., Kandpal T. C. and. Garg H. P (1996) Electric generation from rice husk in Indian rice mills: potential and financial viability. *Biomass Bioenergy* 10: 393 - 403

Kasten, F. (1993). Discussion on the relative optical air mass. *Lighting Research and Technology*, 25(3), 129-130.

Kayes, B. M., Nie, H., Twist, R., Spruytte, S. G., Reinhardt, F., Kizilyalli, I. C., and Higashi, G. S. (2011). 27.6% conversion efficiency, a new record for single-junction solar cells under 1 sun illumination. In Photovoltaic Specialists Conference (PVSC), 37th IEEE (pp. 000004-000008). IEEE.

Keavney, C. J., Haven, V. E., & Vernon, S. M. (1990, May). Emitter structures in MOCVD InP solar cells. In Photovoltaic Specialists Conference, 1990. Conference Record of the Twenty First IEEE (pp. 141-144). IEEE.

Keppner, H., Meier, J., Torres, P., Fischer, D. and Shah, A. (1999). Microcrystalline silicon and micromorph tandem solar cells. *Applied physics A*, 69(2), 169-177.

Khattak, C. P., et al. (1999). Production of solar-grade silicon by refining of liquid metallurgical-grade silicon. In: AIP Conference Proceedings, 731.

Khattak, C.P., Joyce D.B. and Schmid, F. (2007). Conference Record of the 29th IEEE Photo Voltaic Specialists Conference 2002, IEEE, Piscataway, NY, USA, 364

King, B. (2000). A brief introduction to pozzolans. *Alternative construction-contemporary natural building methods*.

Kitai, A. (2011). Principles of solar cells, LEDs and diodes: the role of the PN junction. *John Wiley & Sons*.

Koch, A., McBratney, A., Adams, M., Field, D., Hill, R., Crawford, J. and Angers, D. (2013). Soil security: solving the global soil crisis. *Global Policy*, 4(4), 434-441.

Kotval P. S and Strock H.B. (1980). US patent 4,193,975.

Larbi, K.K., Roy, R., Barati, M., Lakshmanan, V.I., Sridhar, R. and McLean, A (2012). Use of rice husk for emission neutral energy generation and synthesis of solar-grade silicon feedstock. *Biomass conversion and biorefinery*, 2 (2), 149-157.

Licastra, P.H. (1974). Profitable uses of Rice Hulls, Col. Engr. Univ. Engg. California, Berkeley. 2

Lide, D. R. (2009). CRC handbook of chemistry and physics 2009-2010: A ready reference book of chemical and physical data.

Maeda, N., et al. (2001). Development of a new furnace for the production of rice husk ash. *Aci special publications*, 199 (2), 835-852.

Masterson, K. D. (1977). Selective surfaces for solar-thermal conversion. *Journal of Solid State Chemistry*, 22(1), 41-49.

Matson, R. J., Emery, K. A., & Bird, R. E. (1984). Terrestrial solar spectra, solar simulation and solar cell short-circuit current calibration: a review. *Solar cells*, 11(2), 105-145.

Mattos, L. S., Scully, S. R., Syfu, M., Olson, E., Yang, L., Ling, C., and He, G. (2012). New module efficiency record: 23.5% under 1-sun illumination using thin-film single-junction GaAs solar cells. In *Photovoltaic Specialists Conference (PVSC)*, 2012 38th IEEE (pp. 003187-003190). IEEE.

McCambridge, J. D., Steiner, M. A., Unger, B. L., Emery, K. A., Christensen, E. L., Wanlass, M. W., and Ashmead, J. W. (2011). Compact spectrum splitting photovoltaic module with high efficiency. *Progress in Photovoltaics: Research and Applications*, 19(3), 352-360.

McEvoy, A., Markvart, T., and Castaner, L. (Eds.). (2003). Practical handbook of photovoltaics: *fundamentals and applications*. Elsevier.

Mehta, P. K. (1977). Properties of blended cements made from rice husk ash. In: *ACI Journal Proceedings*, ACI.

Mendoza B., (2005) Advances in Space Research, 35 882 - 890.

Miles, R. W., Zoppi, G. and Forbes, I. (2007). Inorganic photovoltaic cells. *Materials today*, 10(11), 20-27.

Milnes, A. G. (1983). Impurity and defect levels (experimental) in gallium arsenide. *Advances in electronics and electron physics*, 61, 63-160.

Morita, K., Kongoli, F.K., Thomas B.G. and Sawamipkakali W. (2003). proceedings of modeling, control and optimization in Ferrous and Non-ferrous Industry Symposium, Minerals, Metals and Mater. Soc. Warrendale, PA, USA, 49

Nakamura, N., Baba, H., Sakaguchi Y., Hiwasa, S. and Kato, Y. (2003). *J. Jpn. Inst. Met.* 67 583

Nagrale, S. D, Hajare, H and Modak, P. R. (2012). Utilization of rice husk ash. *Carbon*, 2 (6), 42.

Nelson, J (2003). The physics of solar cells. World Scientific. 57, 182.

Nelson, J (2004). The physics of solar cells. London, imperial college press.

Newman, R. C., & Willis, J. B. (1965). Vibrational absorption of carbon in silicon. *Journal of physics and chemistry of solids*, 26(2), 373-379.

Nozaki, T., Yatsurugi, Y., Akiyama, N., Endo, Y., & Makide, Y. (1974). Behaviour of light impurity elements in the production of semiconductor silicon. *Journal of Radioanalytical Chemistry*, 19(1), 109-128.

Occupational Health and Safety Administration. (2002). Regulations for Mineral Dusts. Standard 1910.1000 Table Z-3

Ohl R.S., (1941) Light-sensitive device including silicon, US Patent No. 2,443,542, 27th May.

Okutani, T (2009). Utilization of silica in rice hulls as raw materials for silicon semiconductors. *Journal of metals, materials and minerals*, 19 (2), 51-59.

Onojah, A., Amah, A. N and Ayomanor B. O. (2012) Comparative studies of silicon from rice husk ash and natural quartz. *Am. J. Sci. Ind. Res.*, 3(3), 146-149

Patel, M., Karera, A. and Prasanna, P. (1987). Effect of thermal and chemical treatments on carbon and silica contents in rice husk. *Journal of materials science*, 22 (7), 2457-2464

Pitt, M (1985). *J. Mater. Sci.*, 20, 4387

Pizzini, S. (1982). Solar grade silicon as a potential candidate material for low-cost terrestrial solar cells. *Solar energy materials*, 6(3), 253-297.

Pizzini, S (2010). Towards solar grade silicon: Challenges and benefits for low cost photovoltaics. *Solar energy materials and solar cells*, 94 (9), 1528-1533.

Ranjan, S., Balaji, S., Panella, R. A., & Ydstie, B. E. (2011). Silicon solar cell production. *Computers & Chemical Engineering*, 35(8), 1439-1453.

Recart, F., and Cuevas, A. (2006). Application of junction capacitance measurements to the characterization of solar cells. *IEEE transactions on electron devices*, 53(3), 442-448.

Rhoderick, E. H. (1988). RH Williams Metal–semiconductor contacts 2nd Ed. *Clerendon: Oxford*.

Riordan, C. J. (1986). Spectral solar irradiance models and data sets. *Solar cells*, 18(3), 223-232.

Salmi, J., Bonino, J. P., & Bes, R. S. (2000). Nickel pigmented anodized aluminium as solar selective absorbers. *Journal of materials science*, 35(6), 1347-1351.

Sanyal, I., Chattopadhyay, K. K., Chaudhuri, S., & Pal, A. K. (1991). Grain boundary scattering in CuInSe₂ films. *Journal of applied physics*, 70(2), 841-845.

Sasaki, K., Agui, T., Nakaido, K., Takahashi, N., Onitsuka, R., & Takamoto, T. (2013, September). Development of InGaP/GaAs/InGaAs inverted triple junction concentrator solar cells. In *9th International Conference On Concentrator Photovoltaic Systems: Cpv-9* (Vol. 1556, No. 1, pp. 22-25). AIP Publishing.

Sasaki, H., Kobashi, Y., Nagai, T., & Maeda, M. (2013). Application of electron beam melting to the removal of phosphorus from silicon: toward production of solar-grade silicon by metallurgical processes. *Advances in Materials Science and Engineering, 2013*.

Schei, A. (1985). High purity silicon production. In: *Proceedings of the International Seminar on Refining and Alloying of Liquid Aluminum and Ferro-Alloys, Trondheim, Norway*, 73-89.

Schei, A., Tuset, J. K., & Tveit, H. (1998). *Production of high silicon alloys* (pp. 284-291). Trondheim, Norway: Tapir.

Schultz, O., Glunz, S. W., & Willeke, G. P. (2004). ACCELERATED PUBLICATION: Multicrystalline silicon solar cells exceeding 20% efficiency. *Progress in photovoltaics: Research and Applications, 12*(7), 553-558.

Seraphin, B. O. (1982). Thin films in photothermal solar energy conversion. *Thin Solid Films, 90*(4), 395-403.

Shackley, S., Carter, S., Knowles, T., Middelink, E., Haefele, S., Sohi, S., and Haszeldine, S. (2012). Sustainable gasification–biochar systems? A case-study of rice-husk gasification in Cambodia, Part I: Context, chemical properties, environmental and health and safety issues. *Energy Policy, 42*, 49-58.

Shah, P. R. (2015). Study the Effects of Rice Bran Oil Methyl Ester on Performance and Emission Characteristics of Agriculture Diesel Engine. *International Research Journal of Engineering and Technology [IRJET]*, vol. 2., pp. 2467 - 2472.

Shakun, J. D., Clark, P. U., He, F., Marcott, S. A., Mix, A. C., Liu, Z., & Bard, E. (2012). Global warming preceded by increasing carbon dioxide concentrations during the last deglaciation. *Nature, 484*(7392), 49-54.

Siad, M., Keffous, A., Mamma, S., Belkacem, Y., & Menari, H. (2004). Correlation between series resistance and parameters of Al/n-Si and Al/p-Si Schottky barrier diodes. *Applied surface science*, 236(1), 366-376.

Singh, J. (2007). *Semiconductor devices: basic principles*. John Wiley & Sons.

Skoog, D. A and West, D. M (1971). Principles of instrumental analysis, holt, reinhart, and winston. *Inc.printed in USA*, 232 .

Spitz, J. (1977). Selective surfaces for high temperature solar photothermal conversion. *Thin Solid Films*, 45(1), 31-41.

STAT, FAO (2012). FAOSTAT-statistical database, 2012.

STAT, FAO (2015). FAO(Food and agriculture Organisation); Rice market monitor;

http://www.fao.org/fileadmin/templates/est/COMM_MARKETS_MONITORING/Rice/Images/RMM/RMM_APRL15.pdf

Strehlow, W. H., & Cook, E. L. (1973). Compilation of energy band gaps in elemental and binary compound semiconductors and insulators. *Journal of Physical and Chemical Reference Data*, 2(1), 163-200.

Sun, J., & Liu, H. (2011). Selective hydrogenolysis of biomass-derived xylitol to ethylene glycol and propylene glycol on supported Ru catalysts. *Green Chemistry*, 13(1), 135-142.

Sundquist, E. T. (1993). The global carbon dioxide budget. Science-New York then Washington, 259, 934-934.

Swamy, R. N., ALI, Sami A. R. and Theodorakopoulos, D. D. (1983). Early strength fly ash concrete for structural applications. *Journal of the american concrete institute*, 80 (5), 414-423.

Sze, S. M., & Ng, K. K. (2006). *Physics of semiconductor devices*. John wiley & sons. New York.

Sze, S. M., and Kwok, K. N. (2007). Physics of semiconductor devices 3rd edition.
John Wiley & Sons, Inc., New Jersey, United States of America.

Tal Materials Inc. (2002) <http://www.talmaterials.com/ricehull.htm>

Tashima M. M., Da Silva, C. A. R. and Akasaki, J. L., (2004). 'The Possibility of Adding RHA to Concrete' Civil Engineering Department
<http://congress.cimne.upc.es/rilem04/admin/files/filepaper/p282.pdf>, FEIS/UNESP Brazil.

The 1970's Energy Crisis, <http://cr.middlebury.edu/es/altenergylife/70's.htm>
(Retrieved 04/10/2014).

The Free Online Dictionary, www.thefreedictionary.com/nonrenewable
(Retrieved 04/10/2014).

Trumbore, F. A. (1960). This Week's citation Classic_. *Bell syst.tech.J*, 39 , 205-233.

Uhuegbu, C. C. (2011). Photo-thermal solar energy conversion device. Journal of Emerging Trends in Engineering and Applied Sciences (JETEAS), 2(1), 96-101.

U. S. Department of the Interior, Bureau of Reclamation, (2005) Hydroelectric Power.Power Sources Office, www.usbr.gov/power/edu/pamphlet.pdf.

Velupillai, L., Mahin, D. B., Warshaw, J. W., & Wailes, E. J. (1997). A study of the market for rice husk-to-energy systems and equipment. Louisiana State University Agricultural Center, USA.

Ranko, G. (2012). A review of solar drying technologies. *Renewable and Sustainable Energy Reviews*.

Voronkov, M. G. (2007). Silicon era. *Russian Journal of Applied Chemistry*, 80(12), 2190-2196.

Wahlund, B., Yan, J., & Westermark, M. (2004). Increasing biomass utilisation in energy systems: a comparative study of CO₂ reduction and cost for different bioenergy processing options. *Biomass and Bioenergy*, 26(6), 531-544.

Wang, L.L, Munir, Z.A and MAXIMOV, Y.M (1993). Thermite reactions: Their utilization in the synthesis and processing of materials. *Journal of materials science*, 28 (14), 3693-3708.

Wang, B. P., Zhang, Z. C., & Zhang, N. (2010). Fabrication and optical properties of gallium phosphide nanoparticulate thin film. *Solid State Sciences*, 12(7), 1188-1191.

Waits, C. M. (2012). Thermophotovoltaic Energy Conversion for Personal Power Sources (No. ARL-TR-5942). *Army Research Lab Adelphi Md Sensors and Electron Devices Directorate*.

Wenger, H. J., Schaefer, J., Rosenthal, A., Hammond, B., & Schlueter, L. (1991, October). Decline of the Carrisa Plains PV power plant: the impact of concentrating sunlight on flat plates. In *Photovoltaic Specialists Conference*. Conference Record of the Twenty Second IEEE (pp. 586-592). IEEE.

Werner, J. H., & Rau, U. (1994). Schottky contacts on silicon. In *Silicon-Based Millimeter-Wave Devices* (pp. 89-148). Springer Berlin Heidelberg.

Woditsch, P and Koch, W (2002). Solar grade silicon feedstock supply for PV industry. *Solar energy materials and solar cells*, 72 (1), 11-26.

www.usatoday.com/story/weather/2013/09/27/global-warmingreportintergovernmental-panel-on-climate-change/ 2878853/ (Retrieved 24/11/2013).

Xakalashe, B.S. and Tangstad, M. (2012). Silicon processing: From quartz to crystalline silicon solar cells. *Chemical technology*

Yamazaki, T. et al. (2006). Dependence of solar cell performance on electronic properties at grain boundaries in polycrystalline silicon thin films deposited by atmospheric pressure chemical vapor deposition. *Japanese journal of applied physics*, 45 , 6342.

Yamaguchi, M., Takamoto, T., & Araki, K. (2006). Super high-efficiency multi-junction and concentrator solar cells. *Solar Energy Materials and Solar Cells*, 90(18), 3068-3077.

Yang, Y., Yang, W., Tang, W., & Sun, C. (2013). High-temperature solar cell for concentrated solar-power hybrid systems. *Applied Physics Letters*, 103(8), 083902.

Yang, Y., Li, L., Huang, X., Li, G., & Zhang, L. (2007). Fabrication and optical property of single-crystalline InSb nanowire arrays. *Journal of materials science*, 42(8), 2753-2757.

Yasuda, K and Okabe, T. H. (2010). Solar-grade silicon production by metallothermic reduction. *Jom*, 62 (12), 94-101.

Yeoh, A.K, et al. (1979). The relationship between temperature and duration of burning of rice-husk in the development of amorphous rice-husk ash silica. In: *Proceedings of UNIDO/ESCAP/RCTT, Follow-Up Meeting on Rice-Husk Ash Cement, Alor Setar, Malaysia*, .

Yoshikawa, T, A, K and Morita, K (2005). Boron removal by titanium addition in solidification refining of silicon with si-al melt. *Metallurgical and materials transactions B*, 36 (6), 837-842.

Yoshikawa, T and Morita, K (2003). Removal of phosphorus by the solidification refining with Si-Al melts. *Science and technology of advanced materials*, 4 (6), 531-537.

Yoshikawa, T and Morita, K (2005). Removal of B from si by solidification refining with si-al melts. *Metallurgical and materials transactions B*, 36 (6), 731-736.

Zhang, L, XU, C. C., and Champagne, P. (2010). Overview of recent advances in thermo-chemical conversion of biomass. *Energy conversion and management*, 51 (5), 969-982.

Zhao, J., Wang, A., Altermatt, P., & Green, M. A. (1995). Twenty-four percent efficient silicon solar cells with double layer antireflection coatings and reduced resistance loss. *Applied Physics Letters*, 66(26), 3636-3638.

Zhao, J., Wang, A., Green, M. A., & Ferrazza, F. (1998). 19.8% efficient "honeycomb" textured multicrystalline and 24.4% monocrystalline silicon solar cells. *Applied Physics Letters*, 73(14), 1991-1993.

Zook, J. D (1980). Effects of grain boundaries in polycrystalline solar cells. *Applied physics letters*, 37 (2), 223-226.

3 EXPERIMENTAL TECHNIQUES

3.1 Introduction

The use of sophisticated analytical instruments for determining all major areas of fundamental research is almost now a routine process for modern chemical laboratories. This has been a vast expanding area of knowledge as the instrument and computer manufacturers are producing analytical machines which are continuously increasing in power and scope. Further, all manual techniques of analytical studies had steadily been transferred to the automated techniques. Thus, chemical analysis can be divided into three broad categories as listed below. They are almost invariably applied to major areas such as fundamental research, product development, product quality control, Medical and Clinical studies, etc:

- Qualitative analysis: This is chemical analysis that identifies one or more species present in a sample.
- Quantitative analysis: This is chemical analysis that finds out the total amount of particular species present in a sample.
- Structural analysis: This is chemical analyses that help in finding the spatial arrangement of atoms in a molecule and the position or presence of certain organic functional groups contained in a given compound.
- 'Surface analysis', plays a very vital role in obtaining surface related physical properties such as the topography, depth profiling, orientation of molecules etc. in material study

3.1.1 Classification of analytical techniques used in characterisation

The various techniques employed in the characterisation of materials and semiconductor materials in general are classified as follows: analysis through spectroscopy, analysis through chromatography, analysis through thermal energy, analysis through x-ray techniques, analysis through microscopy, analysis through electrochemical techniques and analysis through miscellaneous techniques. The techniques used in this research will therefore be discussed in this chapter.

3.2 Compositional characterisation

Some properties of many compound semiconductors depend largely on the elemental (or atomic) composition of those materials. As an example, the electrical conductivity of silicon solar cell is seriously affected by the amounts B, P and some other trace element atoms in the material. For reasons such as this, it

becomes important to know the exact or at least, the approximate atomic composition of these silicon or semiconductor materials in order to use them properly for specific applications. In carrying out compositional analysis of silica, silicon or semiconductor material a number of techniques are used. These mainly include X-ray fluorescence (XRF) (Onojah et al, 2012), energy dispersive X-rays (EDX) (Rohrich et al, 2004) and secondary ion mass spectroscopy (SIMS) (Guryanov et al, 2006). In this research project however, only XRF and EDX was used for compositional characterisation of the silica and silicon material due to unavailability and lack of easy access to other techniques.

3.2.1 X-Ray Fluorescence (XRF)

The ashes produced from the RH samples at different temperatures were taken to MERI laboratory for chemical analysis. The Philip X-ray fluorescence spectrometer was used to run the samples i.e the ashes obtained. X-Ray Fluorescence Spectrometry (XRF) is a non – destructive analysis technique used to identify and determine concentrations of elements present in solid, powdered and liquid samples. XRF is capable of measuring all elements from Beryllium (Be) to Uranium (U) and beyond at trace levels often below part per million (ppm) and up to 100%. XRF is applied to industrial and research work because of its ability to carry out accurate and reproducible analyses at very high speed. Samples for XRF analysis should be presented to the spectrometer in a homogenous reproducible form. When a high-energy X-ray is incident on the atom of an element, an electron can be ejected from an inner shell of this atom thus rendering the atom unstable. In order to return to stability, an electron from an outer energy shell can fall into this lower energy level electron vacancy to occupy it, thereby losing the excess energy in form of X-ray photon. This manner of production of radiation (light) is called X-ray fluorescence and the XRF technique is based on this principle. The wavelength of this emitted radiation is characteristic of the atoms of the particular element involved and is related to the atomic number, Z of the element according to Equation (3.1) (Jenkins and Meyers, 2000).

$$\frac{1}{\lambda} = K(Z - \sigma)^2 \quad 3.1$$

where K is a constant depending on the spectral series and σ is a shielding constant whose value is < 1 . The emitted wavelengths therefore indicate the elements present. The XRF system uses computer programs to plot the

wavelength dispersion of these emitted radiations and therefore identify the various elements in the sample being studied. The intensity of the spectral lines actually shows the amount (concentration) of atoms of each element present. In this way, a quantitative mapping of the atomic composition of the elements making up a test sample is obtained. Figure 3.1 illustrates the basic principles of X-ray fluorescence. The energy (ΔE) of the emitted X-ray photon is related to its wavelength by Equations (3.2) and (3.3) (Jenkins and Meyers, 2000).

$$\lambda_{(\mu m)} = \frac{1.24}{\Delta E} \quad 3.2$$

where

$$\Delta E = E_1 - E_0 \quad 3.3$$

where E_0 and E_1 are the corresponding energies of the K and L shells as shown in figure 3.1

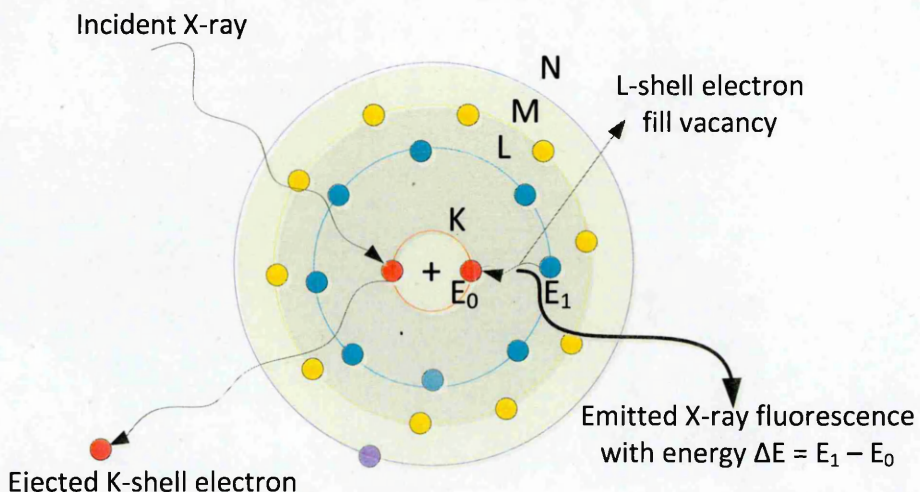


Figure 3.1: Illustration of the basic principle of x-ray fluorescence

3.2.2 Energy dispersive X-ray (EDX)

The EDX process is similar to the XRF process. A major difference is that, while the XRF uses an X-ray beam as incident beam, the EDX uses an electron beam. It is for this particular reason that the EDX detector is usually attached to the SEM system so that common source of electron beam is used for both the SEM and the EDX operations. The emitted characteristic X-rays are also used to generate an energy dispersion spectrum of atoms of the elements in the sample by means of the software programs incorporated into the equipment. From this spectrum the approximate atomic composition of the sample can be obtained. In addition to production of X-rays by EDX process, a continuum of white light and other

radiations are also produced (Van Grieken and Markowicz, 2001). This actually causes interference when determining the atomic composition of the specimen. Thus, the EDX technique is not as accurate as the XRF techniques for quantitative analysis of atomic composition (Van Grieken and Markowicz, 2001). All EDX measurements reported in this thesis were carried out using EDX detector (Oxford Instruments, UK) attached to FEG NOVA NANO SEM equipment (FEI Company, The Netherlands). The EDS is used to measure the energies of x-ray and analyse characteristic spectra. When the semiconductor detector received x-ray emitted from the specimen, electron-hole pairs is generated whose energy corresponds to the energy of x-ray; the detector is cooled by liquid nitrogen, in order to reduce the electric noise while the electric current measurement enables we obtain values of the x-ray energy.

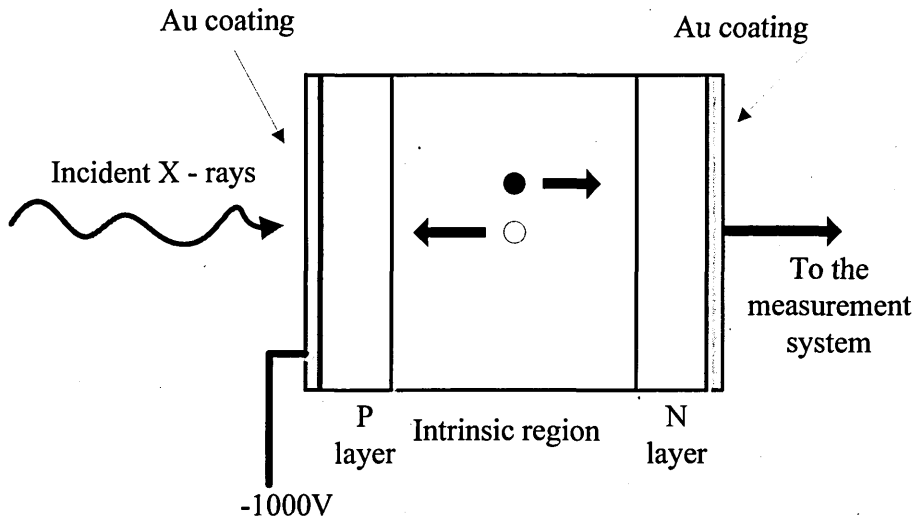


Figure 3.2: illustration of the basic principle of energy dispersive X-ray

The EDS measures with a small probe current and short-time acquisition of spectra. The EDS X-ray spectra enable qualitative analysis that identifies what elements are present in a sample area when irradiated with an electron beam. Point analysis to obtain a spectrum from a point irradiated with electron beam, line analysis that give a one-dimensional distributions of elements of interest on specified line and Mapping that display two-dimensional distributions of elements of interest in specified area are the three available analysis mode. Mapping also called area analysis is a qualitative analysis performed while the electron probe is scanned over a chosen area. For EDS, the detection limit is a few thousand ppm.

In order to obtain the specific elements in the derived MG-Si, the electron probe scan were scanned over a chosen area to acquire its characteristic X-rays with specific energies. The X-ray map shows the distribution of continuous X-rays and not the distributions of elements of interest. In addition, should energies of characteristic x-rays from elements not of interest come very close to those of the elements of interest; x-ray maps might show elements not of interest. This is because the energy resolution of the spectrometer is equal to the differences between the element not of interest and the element of interest.

3.3 Structural characterisation

Structural characterisation of semiconductor materials involves the study and determination of structural properties such as crystal structure and phases of species present in the materials. X-ray diffraction (XRD) measurement is usually applied for this purpose. One can then determine the particular crystal system present in the semiconductor material. Apart from determining the crystal system present in a material, the amount of atoms as well as the preferred orientation of atoms or crystallites making up the material can as well be known by identifying the crystal lattice planes of those atoms. Each crystal lattice plane is denoted by a set of three numbers (Miller indices) in brackets denoted by (hkl) (Kittel, 2005).

3.3.1 Powder X-ray diffractometer (XRD):

The physical properties (Crystalline or Amorphous nature) of the samples were ascertained by making use of diffraction of x-ray from these powders. XRD pattern of an unknown compound and a standard one was compared and their chemical identity found. X-ray was generated by bombarding high speed electrons on some suitable target, thus when the x-ray beam strikes the RHA surface at definite angle, the interaction between its resultant electric vector and the electron on matter results in scattering of incident rays. The angle of diffraction (θ) relates to the atomic spacing of the x-ray bombarded crystals through Bragg's equation. The condition for constructive interference of these scattered rays in order to produce the needed diffraction pattern is governed by Bragg's law (Kittel, 2005). Bragg's law states that, for constructive interference to occur, the path difference between the two interfering waves (which is equal to $2dsin\theta$ from figure (3.3) must be equal to a whole number, n of the wavelength, thus giving rise to Equation (3.4).

$$n\lambda = 2d \sin \theta \quad (3.4)$$

where λ is the wavelength of the x – rays used d is the interplanar spacing within the investigated material.

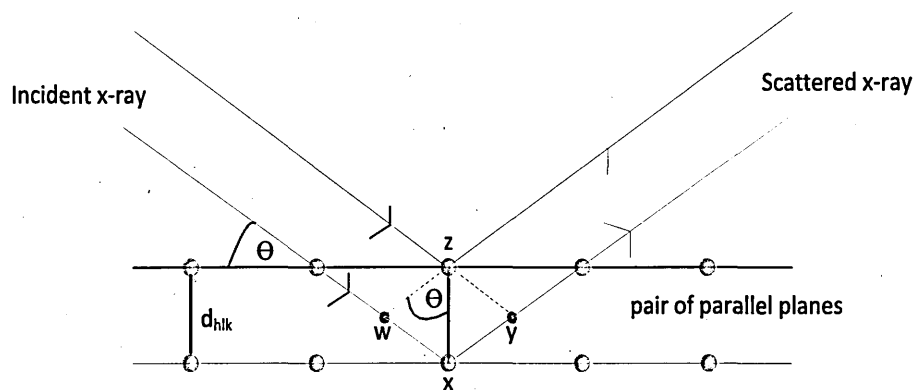


Figure 3.3: The scattering of x-ray from a set of planes

In order to observe useful data from the X-ray experiment, the scattered x-ray beam from the points x and z must produce diffracted beams which are in phase as shown in figure 3.3 above. This is only possible if the extra distance travelled by the x-ray photon from w to x and x to y is an integral number of wavelengths. The path difference is dependent on both the lattice spacing d_{hkl} and the angle of incidence of the x-ray beam, θ

$$\text{path difference} = wx + xy = 2d_{hkl} \sin \theta = n\lambda \quad (3.5)$$

A systematic diagram of a powder diffractometer is shown in figure 3.4 below. The x-ray produced by the x-ray tube is aligned to fall on the sample through a slit and are scattered in all directions. By scanning the detector around the sample along the circumference of a circle, it is made to cut through the diffraction maxima. The x-ray diffraction pattern displays intensity as a function of the detector angle 2θ .

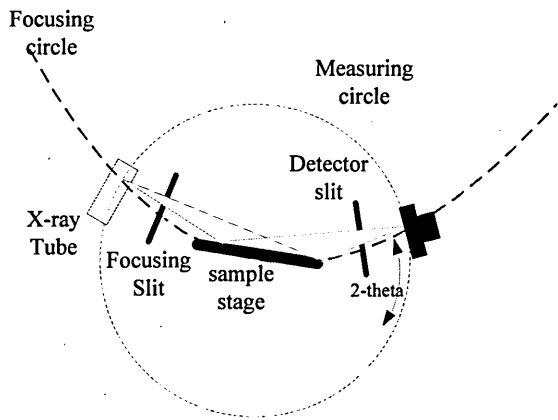


Figure 3.4: Systematic X-Ray Powder Diffractometer

The reflection geometry of powder diffractometers enable slits close to the detector remove noise and leads to well-resolved data, where the sample behaves like a mirror which focuses the beam on to the detector. Factors which affect the intensity and number of peaks (reflections) include:

- i. crystal class
- ii. lattice type
- iii. symmetry
- iv. unit cell parameter
- v. the distribution and type of atoms in the unit cell.

Since the X-ray wavelength, λ is constant, determination of the diffraction angle (2Θ)

will help to determine the d-spacing (inter-planar spacing) of the lattice planes using Equation (3.4) or (3.5), where n is unity for successive lattice planes. From the resulting peaks of the X-ray diffractogram, some other crystalline properties of the material can be determined. These include finding the Miller indices of the various crystal planes (orientations) in the samples, obtaining the lattice constants of the crystal structures present in the material and estimating the sizes of the crystallites in the material. Equations (3.4) - (3.5) (Kittel, 2005 and Patterson, 1939) are the relevant equations employed in the analysis of XRD results of crystalline materials such as semiconductors.

$$a = d\sqrt{h^2 + k^2 + l^2} \quad (3.6)$$

$$D = \frac{k\lambda}{\beta \cos\theta} \quad (3.7)$$

$$\beta = 4\mathcal{E} \tan \theta \quad (3.8)$$

where α is the lattice constant, D is crystallite size, k is Scherer constant, β is full width at half maximum (FWHM) of the particular XRD peak (usually the most intense peak) under consideration and \mathcal{E} known as a strain in the crystal lattice is a measure of the distribution of lattice constant emerging from crystal imperfection such as grain boundary or lattice dislocation. The deviation from perfect crystallinity leads to a broadening of the peaks (Yogamalar, 2009). The FWHM is the full width of the XRD peak (in radians) at half the peak intensity as shown in figure 3.5.

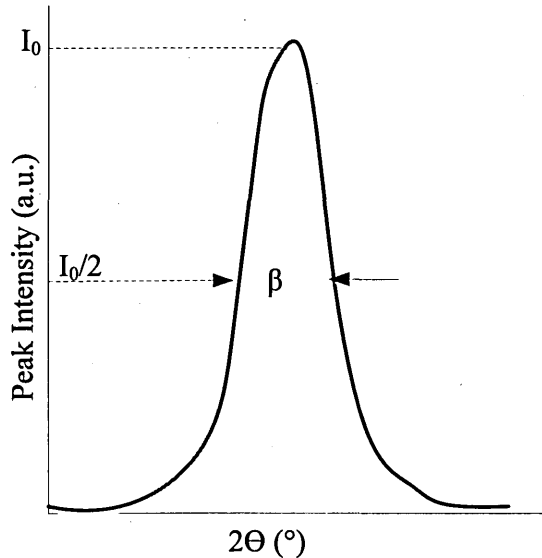


Figure 3.5: XRD peak showing FWHM

The XRD equipment used in the project reported in this thesis was the Philips X'Pert Pro diffractometer (Philips Analytical, Almelo, the Netherlands) using Cu-K_α radiation with excitation wavelength of 1.5406 nm at source tension and current of 40 kV and 40 mA respectively.

3.3.2 Thermogravimetric Analysis (TGA)

One most common techniques used to investigate thermal events and kinetics during pyrolysis of biomass is TGA (Hatakeyama and Quinn, 1999; Nassar, 1999; Mansaray and Ghaly, 1999; Caballero et al., 1997; Helsen and Van den Bulck, 2000; Kastanaki et al., 2002). It provides a measurement of weight loss of the sample as a function of time and temperature. The kinetics of these thermal events has been determined by the application of the Arrhenius equation corresponding

to the separate slopes of constant mass degradation (Nassar, 1999; Mansaray and Ghaly, 1999). TGA which is an essential laboratory tool used for material characterization uses a technique in which mass of the substance is monitored as a function of temperature or time when it is subjected to a controlled temperature program in a control atmosphere. It means that TGA is simply a measurement of a sample weight as it is being heated or cooled in a furnace. The instrument can quantify loss of water, loss of solvent, loss of plasticizer, decarboxylation, pyrolysis, oxidation, decomposition, weight of filler, amount of metallic catalytic or carbon nanotube and weight percentage of ash. TGA could be used as a tool for providing comparison of kinetic data of various reaction parameters such as temperature and heating rate. Other advantages include only a single sample, and few data are required for obtaining kinetics over an entire temperature range in a continuous manner. Nassar (1999) identified two thermal events during the pyrolysis of both bagasse and rice straw by assuming a pseudo first-order reaction. Mansaray and Ghaly (1999) investigated the behaviour of rice husks in a similar manner and two thermal events were identified in the firing process. TG data can be obtained from the following rate expression (Hatakeyama and Quinn, 1999):

$$\frac{d\alpha}{dt} = \frac{A}{\phi} e^{-\frac{E(1)}{R(T)}} (1 - \alpha)^n \quad 3.9$$

where α is the conversion of reactant, t (min) is the time, A (min^{-1}) is the pre exponential factor (frequency factor), ϕ is the heating rate ($^{\circ}\text{C}$), E (J/mol) is the activation energy, R (J/mol/K) is the universal gas constant (8.314), T (K) is the temperature, n is the reaction order. Eq. (3.9) relates the fraction of material consumed with time in the form of an Arrhenius expression comprising of activation energy (E), pre-exponential factor (A) and reaction order (n). The logarithmic form is given in equation (3.10)

$$\ln(d\alpha/dt) = \ln(A/\phi) - E/RT + n \ln(1 - \alpha) \quad 3.10$$

by differentiating with respect to $\ln(1 - \alpha)$, the above equation will simplifies to:

$$\frac{d \ln \left[\left(\frac{d\alpha}{dt} \right) \right]}{d[\ln(1 - \alpha)]} = n - \frac{E}{R} \frac{d \left(\frac{1}{T} \right)}{d[\ln(1 - \alpha)]} \quad 3.11$$

The data from the TGA on measured mass loss with time for the tested samples was used to determine the left and right hand parameters of Eq. (3.11) for different time intervals. The resultant plot $d \left[\ln \left(\frac{d\alpha}{dt} \right) \right] / d[\ln(1 - \alpha)]$ versus

$d\left(\frac{1}{T}\right)/d[\ln(1 - \alpha)]$ of Eq. (3.11) for several time intervals should provide a straight line with an intercept of n and a slope of $(-E/R)$, thus enabling determination of kinetic parameters (E and n). After determining activation energy and order of reaction for a given temperature range, Eq. (3.9) was employed in conjunction with the data of T , $d[\ln(d\alpha/dT)]/d[\ln(1 - \alpha)]$ versus $d(1/T)/d[\ln(1 - \alpha)]$ and $d[\ln(d/dT)]/d[\ln(1 - \alpha)]$ versus $d(1/T)/d[\ln(1 - \alpha)]/dT$ to determine the frequency factor A . The basic principle of TGA is that when a sample is heated, its mass changes. This change can be used to determine the composition of a material or its thermal stability, up to 1000°C. Usually, a sample loses weight as it is heated up due to decomposition, reduction or evaporation. A sample could also gain weight due to oxidation or absorption. While in use, the TGA machine tracks the change in weight of the sample via a microgram balance as shown in figure 3.6. Temperature is monitored via a thermocouple. The TGA can also track change in weight as a function of time. Data can be graphed as weight percent or time vs temperature (°C). Using data produced from the laboratory graphed for weight percent vs temperature, TGA output curves can be analysed in a number of ways. If the material in question is stoichiometric, the molar weight of the component being burned off can be ascertained based on the weight percent lost and the total molar weight of the material.

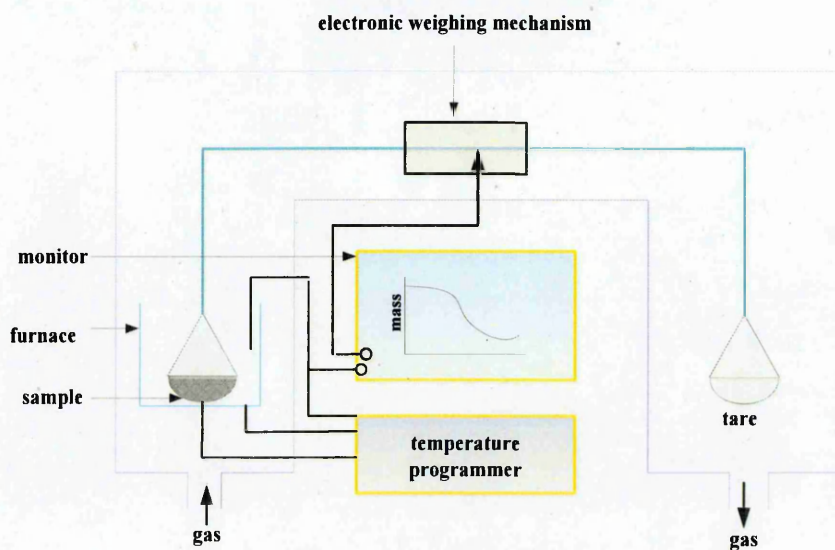


Figure 3.6: Schematic drawing of a Thermogravimetric Analyzer

3.4 Morphological characterisation

Morphological characterisation of silica, silicon and silicon solar cell reveals the pattern of arrangement of grains in the sample as well as surface morphology of the sample. The size of the grains, the boundaries between them (grain boundaries) and the surface roughness are therefore known. These morphological characteristics are of importance in semiconductor devices fabrication. For instance in making metal contacts to solar cell semiconductor materials or devices, the nature (size) of the grain boundaries becomes important as large grain boundaries can result in short-circuit between the two metals on opposite sides of the device. Again proper coverage of silicon surface by an evaporated metal contact or by another semiconductor grown on top of it depends on the surface roughness of the silicon or semiconductor substrate. A semiconductor with high surface roughness will require a thicker metal or semiconductor layer on top of it in order to completely cover the surface of the semiconductor substrate. A good knowledge of the nature and amount of grain boundaries in a semiconductor also helps to understand the extent of grain boundary scattering of charge carriers.

In carrying out morphological characterisation of semiconductors, atomic force microscopy (AFM), scanning electron microscopy (SEM) and transmission electron microscopy (TEM) are typically used. Whereas the AFM uses the force on a cantilever to produce images of the sample surface, both SEM and TEM used in this research work uses electrons to produce images of the samples surface being studied unlike ordinary microscopes where photons (light) are rather used to form the images of the sample surface. All three microscopes however, have differences in their principles of operation as well as in versatility. For example, whereas the SEM is limited in resolution and versatility, the TEM is more complex to prepare samples (Williams and Carter, 1996).

3.4.1 Scanning electron microscopy (SEM)

SEM was used to analyse the morphology, topography and composition of the RHA. The SEM was invented soon after the TEM but took longer to be developed into a practical tool for scientific research. Today, SEM is used in many fields, such as medical and materials research, semiconductor industry, and forensic-science labs. The scheme of SEM operation is illustrated in figure 3.7 which consists of electron gun as electron source, two condenser lenses, scanning coils,

which facilitates the deflection of electron beam in x and y directions, objective lens, and detectors for backscattered and secondary electrons. SEM operates in vacuum chamber with high-energy electron source (2-25kV) and a wide range of magnifications is possible, from about 10 times (about equivalent to that of a powerful hand-lens) to more than 500,000 times, about 250 times the magnification limit of the best light microscopes. Condenser lenses focus the electron beam into a diameter of less than 1nm. The reflected electron from the sample, backscattered or secondary electrons, are collected by detector to provide an image of the sample. In many cases, the backscattered electrons reflected from the sample are used in analytical SEM due to the relation of intensity and atomic number of materials (Egerton, 2006).

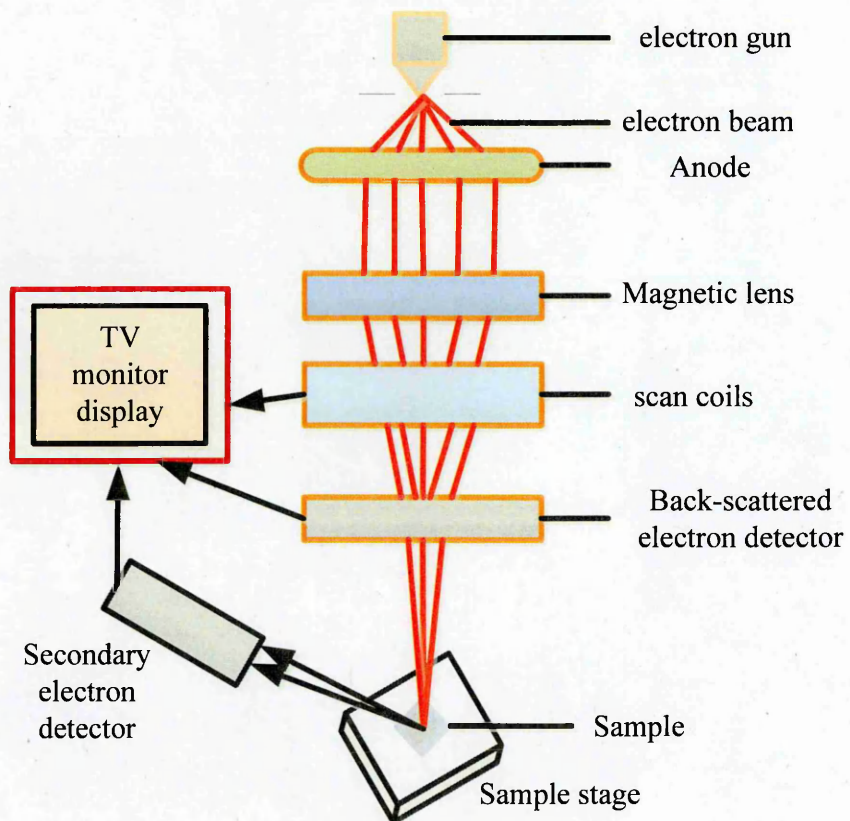


Figure 3.7: Schematic operation of SEM

3.4.2 Transmission Electron Microscopy

Transmission Electron Microscopy (TEM) is similar to SEM technique. However, energy of the electron beam is typically higher for the TEM (with order of 50 – 400 kV) when compared to the SEM makes a major difference. TEM technique

that involves electron beam interaction as it passes through a specimen was applied on the MG-Si from RH ashed at 1000°C to look beyond the SEM. The electrons emitted by a source are focused and magnified by a system of magnetic lenses. The geometry of TEM is shown in figure 3.8. The electron beam is confined by the two condenser lenses which also control the brightness of the beam, passes the condenser aperture and “hits” the sample surface. The electrons that are elastically scattered consist of the transmitted beams, which pass through the objective lens. The objective lens forms the image display and the following apertures, the objective and selected area aperture are used to choose of the elastically scattered electrons that will form the image of the microscope. Finally, the beam goes to the magnifying system that is consisted of three lenses, the first and second intermediate lenses which control the magnification of the image and the projector lens. The formed image is shown either on a fluorescent screen or in monitor or both and is printed on a photographic film.

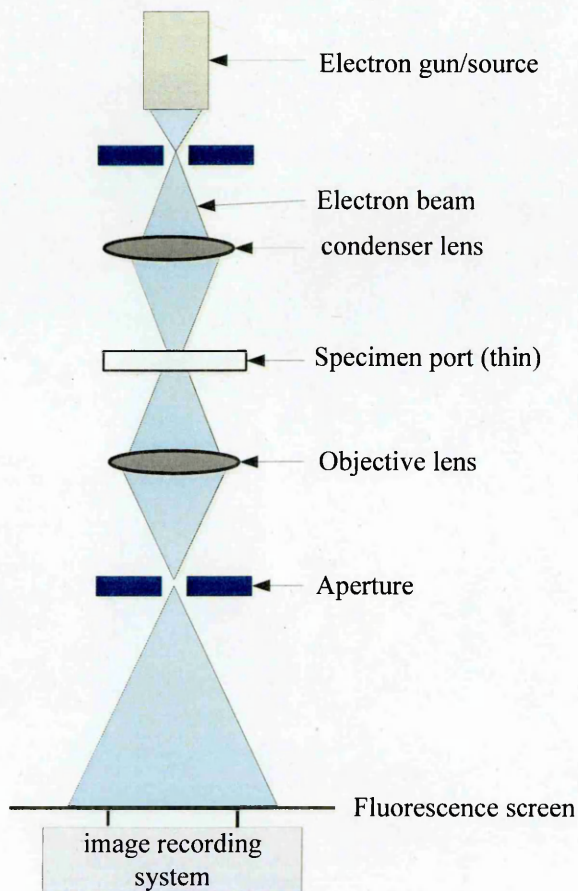


Figure 3.8: Schematic operation of TEM

The operation of TEM requires an ultra-high vacuum and a high voltage. Today TEMs constitute arguably the most efficient and versatile tools for the

characterization of materials over spatial ranges from the atomic scale through the ever-growing 'nano' regime (from < 1nm to ~ 100nm) up to nanometer level and beyond (Egerton, 2006).

3.5 Optical Characterisation

A good knowledge of the optical properties of the semiconductors used in solar cell fabrication is of paramount importance as a silicon solar cell is essentially an optoelectronic device in micro-electronics applications (Ferrieu et al, 1992). These devices consist of films with thicknesses of about 1 μm and it is important to know the refractive index and absorption coefficient as function of wavelength to predict the photoelectric behaviour of the cell device. Two major semiconductor layers employed in the fabrication of silicon solar cells are the window layer and the absorber layer. These are so-called because of the part they play in the solar cell when light is incident on it. The window layer basically acts as a "window" through which light (photons) enters the active junction or junctions of the solar cell. Its optical properties should therefore reflect this function namely; it should have high transparency (transmittance), low absorbance and low reflectance. On the other hand, very high absorbance and nil transmittance are desirable in the absorber layer whose function is mainly to absorb the incident light and create electron-hole pairs. In fact the amount of photocurrent produced by a solar cell is a strong function of these parameters. It therefore becomes imperative that these semiconductors are properly characterised for their optical properties (Bouhafs et al, 1998).

3.5.1 Raman Spectroscopy

Raman Spectroscopy is a method to determining modes of molecular motions, especially vibrations of materials. This was used on the MG-Si from RH ashed at 1000°C . It is predominantly applicable to the qualitative and quantitative analyses of covalently bonded molecules. It characterizes regions for different groups as in IR. It is useful for a variety of samples, organic, inorganic & biological identification of phases, molecular and crystalline symmetries, and identification of crystalline polymorphs and measurement of stress. The Raman technique was named after the Indian scientist Sir C. V. Raman who is the first to observed in practice the inelastic scattering of light in 1928, He won the Nobel Prize in physics in 1930 for his discovery (Turrell et al, 1989)

When a high intense light source is coupled into and propagates along a substance, its photons interact with the molecules of the material. The electron orbits in molecules of the substance are perturbed periodically at a frequency that is same as the source light. The perturbation of these electron orbits result in a periodic separation of charge within the molecules, which is called an induced dipole moment. The oscillating induced dipole moment is manifest as a source of Electromagnetic (EM) radiation, thereby resulting in scattered light. The majority of the scattered light is emitted at a frequency identical to the frequency of the source light, a process referred to as elastic scattering. However, additional light is scattered at different frequencies, a process referred to as inelastic scattering (Hahn, 2007).

The Raman effect occurs when light impinges upon a molecule and interacts with the electron cloud and the bonds of that molecule. For the spontaneous Raman effect which is a form of light scattering, a photon excites the molecule from the ground state to a virtual energy state. When the molecule relaxes, it emits a photon and it returns to a different rotational or vibrational state. The difference in energy between the original state and this new state leads to a shift in the emitted photon's frequency away from the excitation wavelength. The Raman effect which is a light scattering phenomenon, should not be confused with absorption (as with fluorescence) where the molecule is excited to a discrete (not virtual) energy level. If the final vibrational state of the molecule is more energetic than the initial state, then the emitted photon will be shifted to a lower frequency in order for the total energy of the system to remain balanced. This shift in frequency is designated as a Stokes shift. If the final vibrational state is less energetic than the initial state, then the emitted photon will be shifted to a higher frequency, and this is designated as an anti-Stokes shift. Raman scattering is an example of inelastic scattering because of the energy transfer between the photons and the molecules during their interaction as shown in figure 3.9. The amount of the polarizability change will determine the Raman scattering intensity. The pattern of shifted frequencies is determined by the rotational and vibrational states of the sample as in figure 3.9.

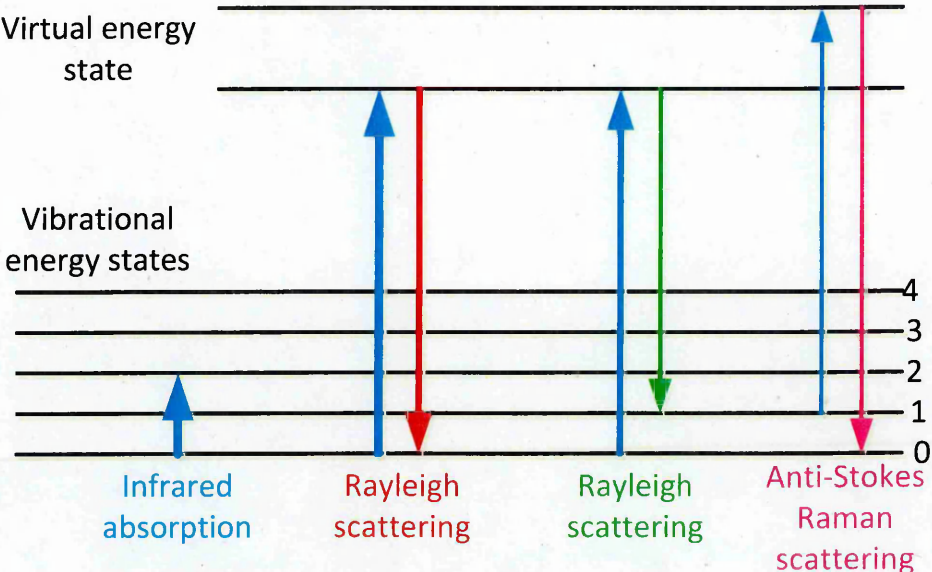


Figure 3.9: Schematic illustration of Raman energy levels

A change in the molecular polarization potential or amount of deformation of the electron cloud with respect to the vibrational coordinate is required for a molecule to exhibit a Raman effect.

3.5.2 Fourier Transform Infrared Spectrometer (FTIR)

"Fourier spectroscopy" is a general term that describes the analysis of any varying signal into its constituent frequency components. The mathematical methods named after J.B.J. Fourier are extremely powerful in spectroscopy and have been discussed in detail (Rui 2006, Harper 1993 and Arfken et al 2013). Fourier spectrometers utilizing interferometers are thus faster by a factor equal to the number of resolvable elements in the spectrum. Fourier-based methods are used over a wide spectral range (Lee and Comisarow, 1987; Banwell and McCash, 1999; Steward, 1983, and Guelachvili 1981). Different FT-IR spectrometers use different interferometers, such as the Michelson interferometer, lamellar grating interferometer, and Fabry-Perot interferometer. The spectrometers utilizing Fabry-Perot interferometers have low resolving power as compared to the two beam interferometers, namely the Michelson and lamellar grating interferometers. Practical FTS began to come into its existence only in the late 1940s. Interferometers were used to measure light from celestial bodies and scientists produced the first Fourier transform spectrum in 1949. By this time, it was possible to calculate the necessary Fourier transforms, however, it remained a

laborious and time-consuming task. At this point, besides Michelson interferometer, researchers had developed different types of interferometers, namely lamellar grating and Fabry-Perot interferometers (Weisstein, 1996). Figure 3.10 represents a basic Michelson interferometer.

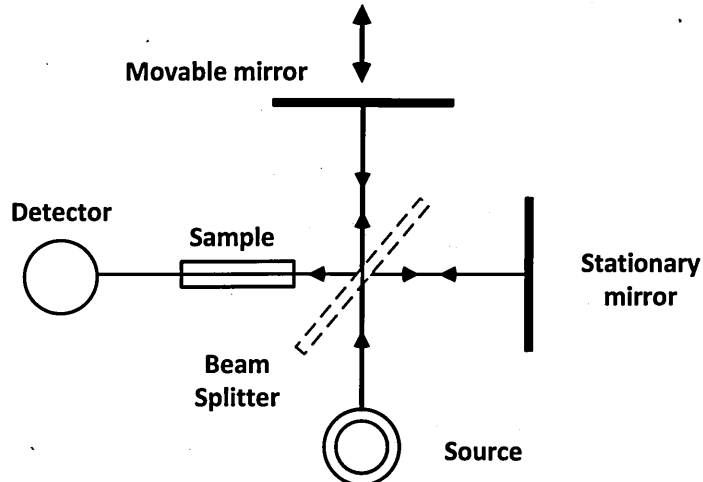


Figure 3.10: Schematic diagram of Michelson interferometer

When molecules are irradiated with IR, the IR with the same wavelength resulting from the frequency of the vibration or other modes of the molecular bonds will be absorbed, and an absorption peak will appear at this wavelength or wave number. If we consider that the characteristic bonds of molecules are wavelength absorber, each absorber can absorb a characteristic wavelength to show an absorbance peak at the corresponding wavelength when an IR wave passes through the sample. Therefore, IR spectroscopy can be used to

1. Identify a known component present in an unknown sample.
2. Study the formation of new chemical bonds or substitutions.
3. Perform quantitative analysis for a component of interest.

Among sampling techniques used by FTIR spectroscopists, attenuated total reflectance (ATR) is probably becoming the most popular as it is quick, relatively non-destructive and requires only minimal or no sample preparation. This method involves contact sampling of a crystal with a high refractive index and excellent IR transmitting properties (Larkin, 2011). In ATR-FTIR spectroscopy, IR beam is directed onto an ATR crystal which is reflected on the internal surface in contact with the sample. When IR strike boundary at an angle greater than the crystal critical angle, it creates an evanescent wave that extends beyond the surface of the crystal into the sample. Absorption of some IR radiation of the evanescent wave

occurs in the sample, while the remaining radiated towards the detector are collected by the detector after it exits the crystal (Fig. 3.11). Since the evanescent wave penetrates only a few microns ($0.5 - 5 \mu\text{m}$) into the sample there must be good contact between the crystal and the sample to assure a constant penetration depth of light into the sample. Furthermore, this technique is mainly for surface measurement. A very wide range of sample types can be measured by ATR. The samples can be organic or inorganic, liquids, solids or gases, and analysed over a wide range of temperatures.

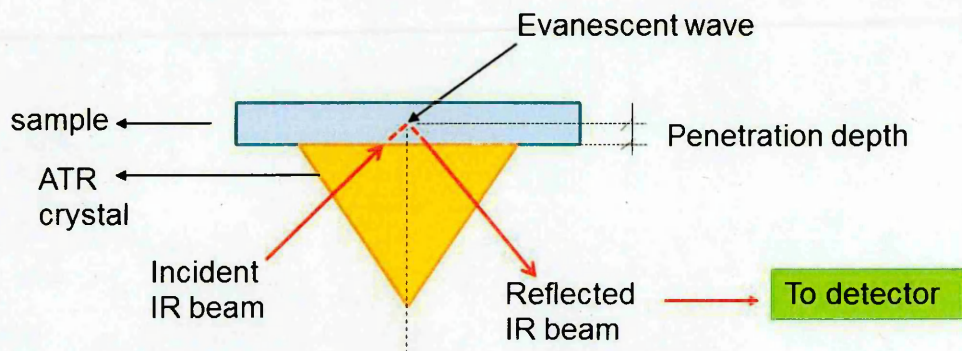


Figure 3.11: Schematic of an ATR-FTIR system

In this study, a Thermo Nicolet NEXUS spectrometer equipped with a mercury cadmium telluride (MCT) detector which is cooled by liquid nitrogen was used for all the FTIR analysis. A single reflection diamond ATR cell (Graseby Specac, UK) was used, which has the trade name "Golden gate". RHA samples were pressed on top of the diamond ATR crystal and their spectra were collected using OMNIC software (version 7.3).

3.6 Device characterisation Techniques

The ultimate aim of growing semiconductors is to use them in fabricating semiconductor devices, and the basic building block of any semiconductor device is the diode. The solar cell is therefore essentially a diode. In order to characterise these devices in general, two major measurements are used. These are current - voltage (I-V) and capacitance - voltage (C-V) (Siad et al, 2004; Singh and Cohen, 1980; Li et al, 2013 and Christoforou et al, 1989). These two techniques characterise the current and capacitance responses of the devices when an external

voltage bias is applied. For a solar cell however, an additional technique is involved, and this is spectral response technique. This is used to characterise the charge carrier collection behaviour of the solar cell over a given range of photon wavelength or photon energy (Field, 1999 and Sopori, 1987). This work therefore discusses these three major device characterisation techniques bearing in mind the solar cell.

3.7 Electrical characterisation

The electrical properties of semiconductors are extremely important in the fabrication of semiconductor devices, as they largely control the behaviour of such devices. For examples, the speed of switching devices depends on the charge carrier mobility whereas the storage capacity of memory devices depends largely on the proper capacitive behaviour of such devices (Choi et al, 2012). Again, the conductivity type of semiconductor materials are extremely important in deciding the types of junctions that will exist in devices made with such semiconductors. This section therefore discusses the common techniques used in determining the electrical properties that characterise semiconductor materials.

3.7.1 Conductivity measurement - Direct current (DC)

Current-Voltage (I-V) characterisation is used principally to determine the electrical conductivity (σ) and resistivity (ρ) of semiconductor materials by applying Ohm's law. In order to do this, two ohmic contacts must be made to the semiconductor. Varying DC voltages are then applied across the two terminals in both directions and the corresponding DC currents flowing through the material are recorded using an ammeter. Figure 3.12 illustrates the principle of this process.

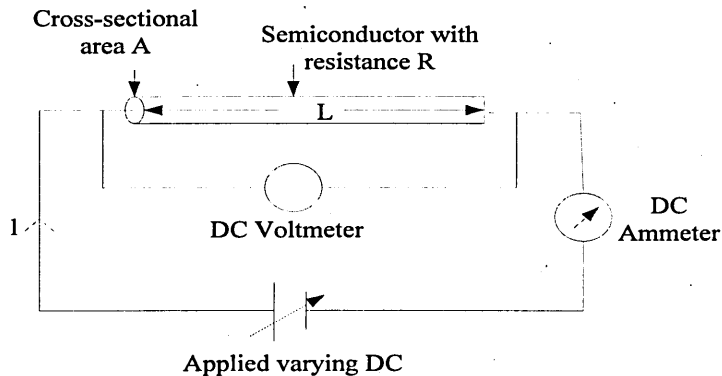


Figure 3.12: Schematic of circuit arrangement to illustrate I-V measurement of a semiconductor with resistance, R

A graph of current vs. voltage for the arrangement in figure 3.12 gives a straight line, whose slope is used to determine the resistance of the semiconductor by applying Ohm's law. All I-V measurements reported in this thesis were carried out using a computerized Keithley 619 Electrometer-Multimeter (Keithley Instruments Inc., OH, USA). Figure 3.13 shows a typical I-V characteristic of a semiconductor for the determination of resistance. Equation (3.12) gives the resistance (R) of the semiconductor as well as its resistivity (ρ) which is the resistance per unit length per unit cross-sectional area.

$$R = \frac{\Delta V}{\Delta I} = \rho \frac{L}{A} \quad 3.12$$

where L and A are the thickness and cross-sectional area of the semiconductor respectively, as shown in figure 3.12.

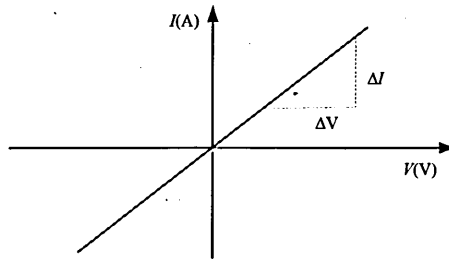


Figure 3.13: Schematic illustration of a typical I-V characteristic of a semiconductor for the determination of resistance

Equations (3.13) and (3.14) (Sze and Ng, 2007) are then used to obtain the resistivity and conductivity of the material respectively.

$$\rho = \frac{RA}{L} \quad 3.13$$

$$\sigma = \frac{1}{\rho} \quad 3.14$$

3.7.2 Hall Effect measurement

The Hall Effect technique is used to determine the type of conductivity in semiconductors as well as obtain their carrier concentration and carrier mobility. It depends principally on Lorentzian force on a charge carrier flowing in a semiconductor, confined in a magnetic field (Sze and Ng, 2007). Assume a piece of semiconductor with a current (I) flowing along it in the x-direction (from left to right). If an external magnetic field vector B is applied perpendicular to the direction of current flow in the z-direction (upward) as shown in figure 3.14, then a Hall voltage will develop along the y-

axis. If an n-type semiconductor is used, the electrons are pushed towards the end of the semiconductor (towards the reader) setting up an electric field E_y also towards the reader. A Hall voltage V_H therefor develops in the direction perpendicular to I and B . If a p-type semiconductor is used, the holes are still pushed towards the end of the semiconductor (towards the reader) but an electric field E_y is set up into the paper which in turn sets up Hall voltage with an opposite sign to that due to the n-type semiconductor. From the Hall voltage data obtained and the known values of the magnetic field intensity and the applied current, the Hall mobility, carrier concentration and conductivity type of the particular semiconductor involved can be obtained using Equations (3.15) - (3.21) (Sze and Ng, 2007).

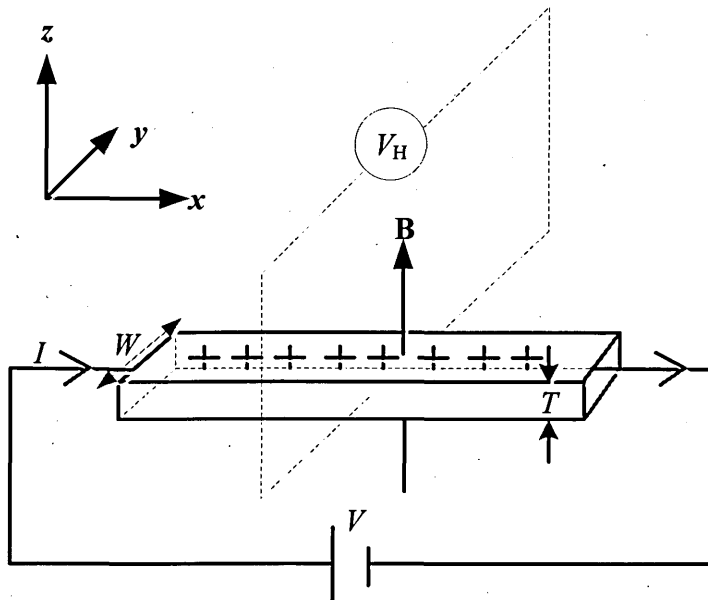


Figure 3.14: Illustration of Hall Effect in a semiconductor carrying a current I in a magnetic field B perpendicular to the direction of current flow. A Hall voltage V_H is developed perpendicular to I and B

$$n = -\frac{r_H}{R_H q} \quad 3.15$$

$$p = \frac{r_H}{R_H q} \quad 3.16$$

where R_H is the Hall coefficient (which is positive for p-type material and negative for n-type material) and q is electronic charge. The constant r_H is the Hall factor given by Equation (3.17).

$$r_H = \frac{\langle \tau^2 \rangle}{\langle \tau \rangle^2} \quad 3.17$$

where τ is the mean free time between collisions.

The Hall coefficient can be obtained from the measured Hall voltage, applied current, applied magnetic field and thickness of the semiconductor used according to Equation (3.18).

$$R_H = \frac{V_H}{J_X B_Z t} \quad 3.18$$

where J_X is the magnitude of x-component of the applied current density, B_z is the z-component of the applied magnetic field and t is the thickness of the sample.

The conductivity (σ) is obtained from the applied current density and electric field by Equation (3.19).

$$\sigma = \frac{J_X}{E_X} \quad 3.19$$

Thus, the Hall mobility (μ_H) is obtained from Equation (3.20).

$$\mu_H = |R_H| \sigma \quad 3.20$$

The drift mobility (μ) is related to the Hall mobility by Equation (3.21).

$$\mu_H = r_H \mu \quad 3.21$$

If equations (3.14) and (3.20) are combined, the resistivity can be obtained.

3.8 Current-Voltage (I - V) characterisation

The I-V characterisation shows how the current through a diode responds to applied bias voltage. Figure 3.15 shows the equivalent of a sample diode.

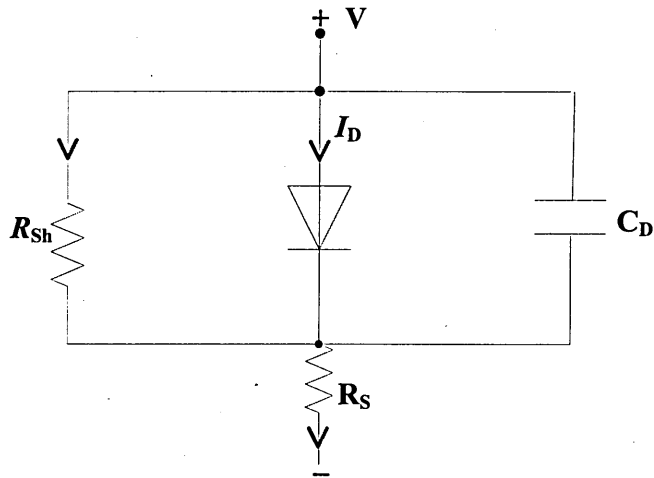


Figure 3.15: Schematic illustration of equivalent circuit of a diode showing shunt resistance (R_{sh}), series resistance (R_s) and depletion capacitance (C_D)

The I-V characterisation of a diode in general only reflects the effects of R_s and R_{sh} . The effect of C_D is only seen in a capacitance-voltage measurement. The equations governing the behaviour of a diode are presented in chapter two specifically for solar cells. All I-V measurements carried out in this work were done using a computerised Keithley 619 Electrometer/Multimeter (Keithley Instruments Inc., USA).

3.8.1 I-V Characteristics under dark condition

Under dark condition (i.e. without illumination), the I-V characteristics of a diode in general, can be presented in log-linear form or in linear-linear form. In the log-linear form, the current through the diode is presented in logarithmic scale while the applied bias voltage is presented in linear scale. Figure 3.16 shows typical log-linear I-V characteristics of a diode.

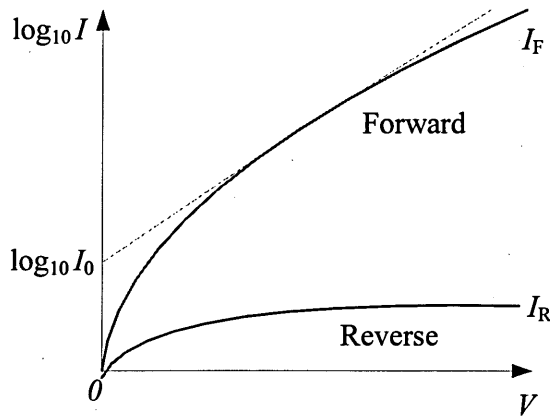


Figure 3.16: Typical log-linear I-V characteristics of a diode showing both forward current (I_F) and reverse current (I_R). Here both forward and reverse characteristics are plotted to be in the same quadrant for convenience, by changing the sign of the reverse bias voltage to positive from negative.

Figure 3.16 is very useful in obtaining a number of parameters that characterise the diode under dark condition. The parameters that can be obtained from this figure include; diode rectification factor (R.F.), diode ideality factor (n), reverse saturation current (I_o) and potential barrier height (ϕ_B).

The R.F. is defined as the ratio of forward current to reverse current at a bias voltage of 1-V as shown in Equation (3.22).

$$\text{R.F.} \approx \left(\frac{I_F}{I_R} \right)_{v=1} \quad 3.22$$

The R.F. is a measure of the rectifying quality of the diode. A rectification factor of about three orders of magnitude (R.F. $\sim 10^3$) is enough to make a good diode (Dharmadasa, 2012). In order to obtain the diode ideality factor from figure 3.16, equation 2.12 is used and re-presented here as equation (3.23) for convenience.

$$I = I_o \left[\exp \left(\frac{qV}{nkT} \right) - 1 \right] \quad 3.23$$

For an applied forward bias of $V > 0.75$ V, the exponential term in Equation (3.23) becomes sufficiently large (Siad et al, 2004) such that

$$\exp \left(\frac{qV}{nkT} \right) \gg 1 \quad 3.24$$

Then Equation (3.23) simplifies to Equation (3.25), thus

$$I = I_o \exp\left(\frac{qV}{nkT}\right) \quad 3.25$$

Taking the natural logarithm of both sides of Equation (3.25), and rearranging, yields

Equation (3.26).

$$\ln I = \frac{qV}{nkT} + \ln I_o \quad 3.26$$

Re-writing Equation (3.26) in common logarithmic form for convenience then gives

$$0.434 \log_{10} I = \frac{qV}{nkT} + 0.434 \log_{10} I_o \quad 3.27$$

Dividing Equation (3.27) by 0.434 gives

$$\log_{10} I = \left(\frac{q}{2.303nkT}\right)V + \log_{10} I_o \quad 3.28$$

Equation (3.28) shows that the graph of $\log_{10} I$ vs V gives a straight line, with slope of $q/2.303nkT$. Therefore from the slope of the forward current in figure 3.16, the value of n can be obtained since q , k and T are all known. The value of n is very useful in understanding the current transport mechanism in a diode. In an ideal diode where thermionic emission takes place only, the current transport is over potential barrier with the value of n as unity. If current transport is dominated by recombination and generation (R & G) mechanism, then $n = 2.00$. If both mechanisms are present as is the case in a practical diode, n takes a value between 1.00 and 2.00. In a practical diode series resistance is present. This also has an effect on the value of n . In fact, if R_s is large the situation becomes more complicated and the value of n can be greater than 2.00. Equation (3.28) shows that the intercept of straight line portion of the forward current with the highest gradient in figure 3.16 on the $\log_{10} I$ axis, gives $\log_{10} I_o$. Therefore, the reverse saturation current (I_o) is obtained from this value. I_o is also a measure of the degree of rectification of the diode. If the diode rectification is high, then I_o is low. Again I_o will be low for a diode with large barrier height. Once I_o is obtained, the barrier height ϕ_B can be determined from I_o extrapolation from existing diode of equation 2.15 re-presented as;

$$I_o = A^* T^2 \exp\left(-\frac{q\phi_B}{kT}\right) \quad 3.29$$

Re-arranging Equation (3.29) will then give

$$\phi_B = \frac{kT}{q} \ln\left(\frac{A^* T^2}{I_o}\right) \quad 3.30$$

If the dark I-V characteristics are rather plotted in linear-linear scale as shown in figure 3.17, another set of device parameters can be obtained. These parameters include; R_s , R_{sh} , threshold (or cut-in) voltage (V_T) and reverse breakdown voltage (V_{BD}).

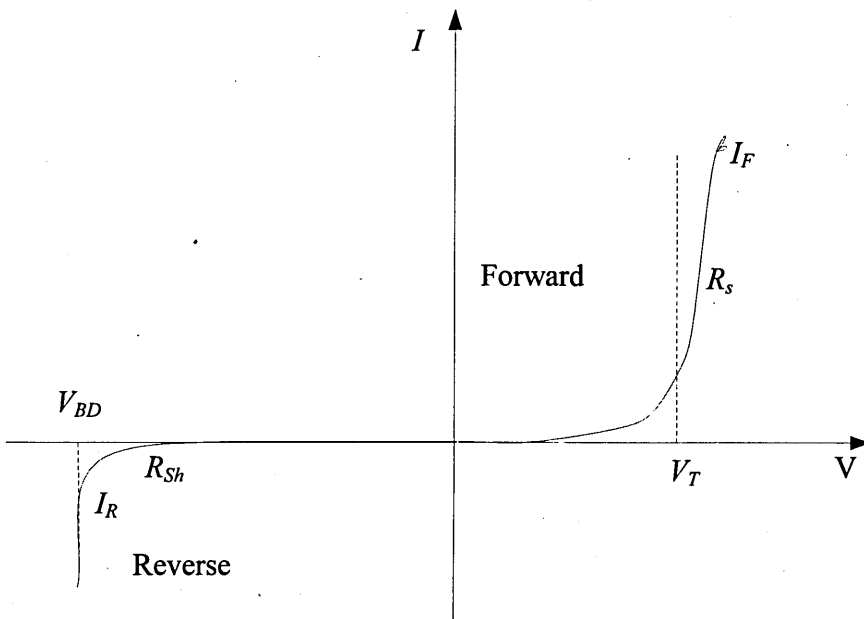


Figure 3.17: Typical linear-linear I-V characteristics of a diode under dark condition

The series resistance is obtained by finding the slope ($\Delta I / \Delta V$) of the straight line portion of the high forward current and applying Ohm's law, so that R_s is obtained from Equation 3.31.

$$R_s = \frac{1}{(\Delta I / \Delta V)} \quad 3.31$$

A low value of R_s is desirable for a good device in which case the forward current has highest possible slope ($\Delta I / \Delta V$) (Sze, 2007). In a practical diode however, a high value of R_s can arise due to two major reasons. One of these is the presence

of resistive oxide layer between the semiconductor and the metal contact (forming an MIS structure). This resistive interfacial layer can arise due to oxidation caused by the etching process preceding the metal contact formation, or due to high density of surface states and therefore high surface recombination velocity (Siad, 2004 and Keffous et al, 2003). Another reason for high series resistance is the use of semiconductor materials with high bulk resistivity (Siad, 2004 and Keffous et al, 2003). This is because, at sufficiently high forward bias, the current through the diode increases rapidly so that the series resistance of the diode is controlled by both bulk resistance of the semiconductor material used, and the contact resistance at the two metal/semiconductor interfaces (Sharma, 1996). At such high series resistance, the slope of the forward I-V curve decreases substantially. For an ideal diode, $R_s = 0$; so that the slope of the forward current $\rightarrow \infty$.

From the reverse I-V curve, the shunt resistance R_{sh} is obtained by determining the slope ($\Delta I / \Delta V$) as in the case of R_s . The value of R_{sh} is indicative of the presence of current leakage paths in the diode. For a good diode, a high value of R_{sh} is desirable (Sze and Ng, 2007; Sharma, 1996), while for an ideal diode, $R_{sh} \rightarrow \infty$. With low R_{sh} value, substantial leakage current (I_0) flows in the diode under reverse bias. During the forward biasing of a diode, very small current flows through the diode as bias voltage increase gradually from 0 V up to a certain minimum voltage. Beyond this voltage, the current through the diode rises rapidly. This minimum voltage is known as the threshold voltage (V_T) or cut-in voltage or turn on voltage of the particular diode involved (Sze and Ng 2007; Sharma 1996 and Wu et al 2010) as shown in figure 3.17. Ge and Si diodes have typical threshold voltages of about 0.2 V and 0.7 V respectively (Sharma, 1996). In order for a diode to operate, a forward bias $> V_T$ must be applied. The threshold voltage also represents the built-in potential of a diode. Under reserve bias, a negligible current flows through the diode. However, at a certain high reserve bias, a large reverse current suddenly begins to flow through the diode as shown in figure 3.17. The reverse bias voltage at which this happens is known as the peak inverse voltage, or simply, the breakdown voltage (V_{BD}). This is so-called because, beyond this point, the diode breaks down and is permanently damaged (Sze and Ng, 2007; Sharma, 1996) as a result of the large reserve current that flows through it. Various breakdown conditions and mechanisms in diodes are well-known and

are discussed in standard text books (Sze and Ng 2007; Mehta and Mehta 2008 and Sharma 1996).

3.8.2 I-V characterisation under illumination

All the I-V characterisations discussed so far apply to all diodes under dark conditions, including the solar cell (which is essentially a photodiode). The solar cell is designed to operate naturally under illumination. It therefore becomes imperative to discuss the features of the I-V characteristics of a diode (solar cell) under illuminated conditions. Since the solar cell is a current source under illumination, the relevant diode equations discussed so far under dark conditions are modified accordingly and the diode equivalent circuit of figure 3.15 is also modified to reflect the current generating property of the solar cell. If an ideal solar cell is considered first, in which case $R_s = 0$ and $R_{sh} = \infty$, then one obtains the ideal equivalent circuit under illumination as shown in figure 3.18.

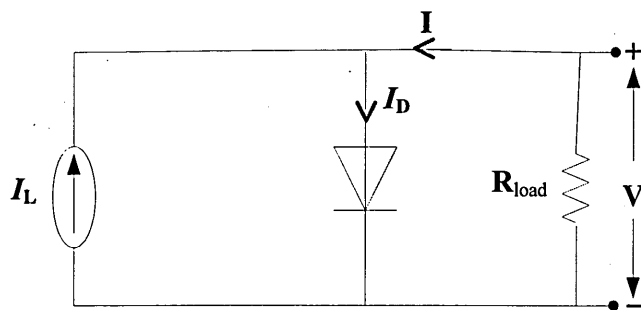


Figure 3.18: Ideal equivalent circuit of a solar cell under illumination

When light is shone on the solar cell under forward bias, photocurrent (J_L) is generated which also flows through the diode in a direction opposite to J_D . The total current (J) in the device then becomes (Sze and Ng, 2007),

$$J = J_o - J_L = J_o \left[\exp\left(\frac{qV}{nkT}\right) - 1 \right] - J_L \quad 3.32$$

When these two currents (J_D and J_L) are equal, the total current through the solar cell becomes zero. Then the V_{oc} is obtained from Equation 3.32 by setting $J = 0$ and $J_L = J_{sc}$, thus yielding Equation 3.33.

$$V_{oc} = \frac{nkT}{q} \ln\left(\frac{J_{sc}}{J_o} + 1\right) \quad 3.33$$

The graph of J or I vs. V in Equation 3.32 yields the result in figure 3.19 for a solar cell.

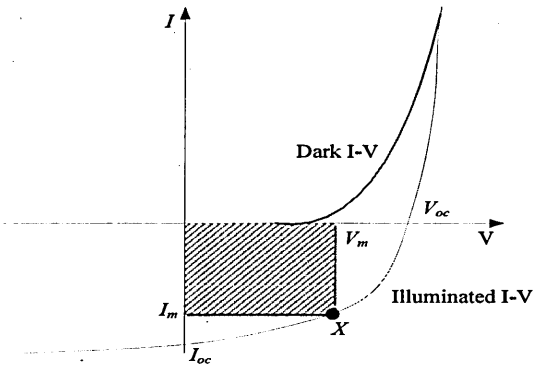


Figure 3.19: I-V characteristics of a solar cell under dark and illumination conditions

The shaded rectangular area in the graph is the power rectangle which gives the maximum output power (P_m) from the solar cell. The corresponding quantities I_m and V_m are respectively the current and voltage at the maximum output power, so that

$$P_m = I_m V_m \quad 3.34$$

The maximum power point is also defined according to Equation 3.35 (Sze and Ng, 2007).

$$P_m = I_m V_m = FF \times I_{sc} \times V_{oc} \quad 3.35$$

where FF is the fill factor which defines the "squareness" of the I-V curve. Thus

$$FF = \frac{I_m V_m}{I_{sc} V_{oc}} \quad 3.36$$

Then the conversion efficiency, η is defined as the ratio of the maximum output power to the total input power (P_{in}) as given in equation 3.27 (Nelson, 2004).

$$\eta = \frac{P_m}{P_{in}} = \frac{I_m V_m}{P_{in}} = \frac{I_{sc} V_{oc} FF}{P_{in}} \quad 3.37$$

where P_{in} is the solar power density of the incident light, which for the AM 1.5, is 100 Wcm^{-2} . For a practical solar cell, the effects of R_s and R_{sh} are brought into Equation 3.32 accordingly by replacing V with $(V - IR_s)$. R_s is more influential than

R_{sh} since it directly affects the fill factor. The equivalent circuit of a real practical solar cell is then given in figure 3.20.

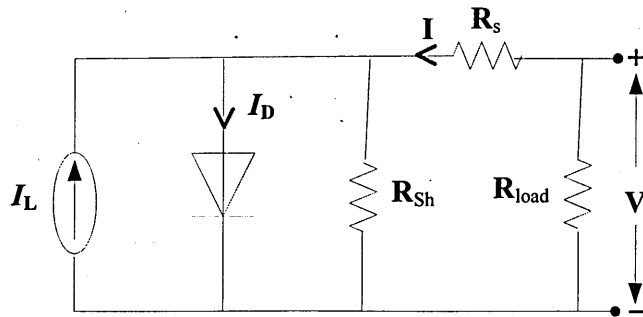


Figure 3.20: Equivalent circuit of a practical solar cell showing the presence of R_s and R_{sh}

From figure 3.19 therefore, the solar cell parameters under illumination can be obtained. The J_{sc} (or I_{sc}) and V_{oc} can be read directly from the graph. The FF can be obtained by drawing the largest possible rectangle through the maximum power point (X), and reading directly, I_m and V_m as shown, and then applying Equation 3.25. Using Equation 3.26 the conversion efficiency, η is then obtained by substitution. R_s and R_{sh} under illumination are also obtained just in the same way as in the dark I-V graph described previously.

3.9 Capacitance-Voltage (C-V) characterisation

Every diode has a depletion region of a certain width, w . This depletion region is the heart of the diode and where all the major activities in the diode take place. All the equations describing the behaviour of a diode under various conditions actually show what happens in the depletion region. The description of the formation of a rectifying junction given in chapter 2 simply shows that the depletion region of a diode can be approximated to a parallel plate capacitor with a separation of w between the two oppositely charged plates. The capacitance of this capacitor (called depletion capacitance, C_D) is given by Equations (38) and (39) which have the same form for both p-n junction diode and Schottky barrier diode. They are also the same for a solar cell under dark condition. These two equations are re-presented here as Equation 3.38.

$$C_D = \frac{\epsilon_s \epsilon_0}{w} = \sqrt{\frac{q \epsilon_s \epsilon_0 N}{2} (V_{bi} - V)^{-1/2}} \quad 3.38$$

where C_D is the capacitance per unit area here.

Thus, it implies

$$\frac{1}{C_D^2} = \frac{2}{q\epsilon_s\epsilon_0 N} (V_{bi} - V) \quad 3.39$$

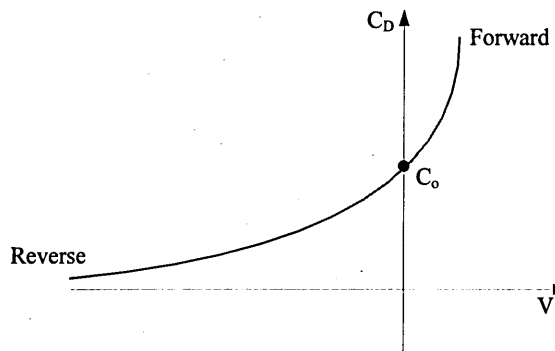


Figure 3.21: Schematic illustration of C_D vs V characteristics of a diode under forward and reverse bias conditions

Now, a graph of C_D vs. V using Equation (3.38) under bias, gives a curve of the form shown in figure 3.21. The value of C_D at zero bias ($V = 0$) gives the actual depletion capacitance per unit area (C_o) of the junction (Sze and Ng, 2007). With this capacitance, the width of the depletion region can be determined, using Equation (3.38). Instead of plotting C vs. V for the depletion region, I/C vs. V can be plotted using Equation (3.39). For an ideal diode, this should give a straight line of the form shown in figure 3.22, and is called the Schottky-Mott plot (Sze and Ng, 2007).

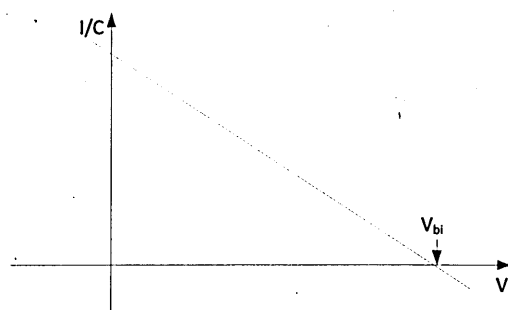


Figure 3.22: Schottky-mott plot of an ideal diode.

The slope of the Schottky-Mott graph gives the quantity, $(2/q\epsilon_0 N)$ and the intercept on V-axis gives the built-in potential, V_{bi} , of the device (Bagnoli and

Nannini, 1987). From the slope, the carrier concentration N of the diode can be obtained, since ϵ_s and q are known. Recall that N represents the resultant uncompensated carrier density in the device. If the dominant dopants in the diode material are donors, then $N = N_D - N_A$, but if the dominant dopants are acceptors, then $N = N_A - N_D$. From the above discussion, the C-V technique becomes a very important technique for determining important electrical properties of a semiconductor diode in general.

It is important to mention here that the C-V measurement is usually carried out at relatively high frequencies up to 10 MHz. The reason for this is to eliminate from the result, the effect of defects present in the device. This is because the defects are known to be slow traps. At high frequencies therefore, they are unable to follow the current through the diode and therefore cannot easily trap the charge carriers (Sarangi et al, 2010). This idea is used to determine the density of defects (traps) in a diode using C-V measurement. In this case, the C-V measurement is carried out at high frequency (say, 1 MHz) and then at a low frequency (say, 10 Hz). The difference in the capacitance obtained from the low frequency and high frequency measurements gives the concentration of impurities or defects in the device (Sarangi et al 2010). At low frequencies, the traps are more active and contribute to the capacitance of the junction by introducing diffusion capacitance to the normal depletion capacitance. At high frequencies however, the slow traps cannot follow the fast ac signal and the diffusion capacitance effect can be ignored (Sarangi et al, 2010). The equipment used for all the C-V measurements reported in this thesis was a Hewlett Packard 4284A 20 Hz - 1 MHz Precision LCR Meter (Yokogawa Hewlett Packard, Japan) with a Keithley 6517A Electrometer/High Resistance Meter (Keithley Instruments, OH, USA).

3.10 Spectral response (SR) characterisation

Spectral response (SR) characterisation is very important for solar cells since light of certain wavelengths must be absorbed by the solar cell in order to create electron-hole pairs and subsequently produce photocurrent. The spectral response is therefore useful in determining the total current deliverable by a solar cell (Sze and Ng 2007; Hartman and Lind; 1982 and Gummel and Smits, 1964) and the range of wavelengths of photons that are absorbed and are converted to current by the solar cell. There are three types of spectral response used in characterising

solar cells. These include; spectral responsivity (*S*) external quantum efficiency (*EQE*) and internal quantum efficiency (*IQE*) (Hartman and Lind, 1982). All of these are also related and are wavelength dependent.

Spectral responsivity is the amount of current that is delivered by a solar cell per unit incident photon power. The unit is therefore given as amperes per watt (A/W) (Field, 1999).

External quantum efficiency is defined as the ratio of the number of charge carriers in the current delivered by a solar cell to the number of incident photons of a given energy. The *EQE* is actually derived from the spectral responsivity (Sze and Ng, 2007 and Hartman and Lind, 1982) so that

$$EQE = \frac{\text{output current}/(\text{charge per electric})}{\text{total input photon power}/(\text{energy per photon})} \quad 3.40$$

or

$$EQE(\lambda) = \frac{J(\lambda)}{q\phi(\lambda)} \quad 3.41$$

where λ is incident photon wavelength, $J(\lambda)$ is the photocurrent at a given wavelength, q is electronic charge and $\phi(\lambda)$ is the number of photons per unit area per unit time per unit bandwidth of wavelengths. Since *EQE* is derived from spectral responsivity, the equation for *EQE* can alternatively be written as

$$EQE(\lambda) = \frac{S(\lambda)}{\lambda} \cdot \frac{hc}{q} \quad 3.42$$

EQE is usually expressed in percentage.

Internal quantum efficiency is a more complicated spectral response since it involves the actual number of photons absorbed by the solar cell in order to produce photocurrent. It is clear that not all the incident photons are absorbed by the solar cell. Some of these photons are reflected at the point of incidence on the solar cell. Some are transmitted through the solar cell while the rest are absorbed. In determining the *IQE* using the total incident photon flux therefore, the amount of photons reflected and those transmitted should be put into consideration. This is the major point of difference between *IQE* and *EQE*. If one assumes zero

transmission for a solar cell with sufficient thickness and high absorption coefficient, then IQE can be written as in Equation (3.42) (Sze and Ng, 2007 and Yang et al, 2008) by modifying Equation (3.40)

$$IQE(\lambda) = \frac{J(\lambda)}{q\phi(\lambda)[1 - R(\lambda)]} \quad 3.42$$

where $R(\lambda)$ is the fraction of the photons reflected by the solar cell at the point of incidence Comparing Equations (3.40) and (3.42), one therefore sees that for any given solar cell, IQE is higher than EQE . The IQE result can give information on the loss mechanisms in the solar cell for absorbed photons with energies higher than the bandgap of the solar cell material (Hartman and Lind, 1982). From the foregoing, it is also obvious that once the spectral response is known, the current deliverable by a solar cell can be obtained by integrating over all wavelengths from zero to the bandgap wavelength, as can be inferred from Equations (3.40) and (3.42).

3.11 Summary

Various rice husk silica and its silicon derived characterisation techniques are presented and discussed in this chapter. These techniques vary in their fundamental principles and in the particular properties or characteristics of the materials they are used to study. They generally range from structural characterisation to morphological, compositional and optical characterisation techniques etc. The importance of each technique is to understand the nature of the materials before producing other materials or devices with them. Although many characterisation techniques are available, only a selected few were employed in characterising the materials used in producing low cost silicon in the course of this research for obvious reasons such as availability, cost and time scale.

The characterisation of semiconductor devices (including solar cells) was presented in this chapter. The various characterisation techniques employed for this purpose, were discussed to include, I-V, C-V and spectral response techniques. Each technique is seen to be unique in nature and in the manner they are carried out yielding different results that help to understand the behaviour of the devices under study. I-V characterisation is seen to reveal the behaviour of the electrical current through the diode (device) under external bias. C-V characterisation reveals the response of the depletion region capacitance of diodes under different

bias conditions. Both I-V and CV characterisation techniques also help to understand the nature of defects (impurities) present in the device. Spectral response measurements are particularly useful for characterising solar cells. Since the solar cell must absorb incident light (photons), the particular useful range of wavelengths of the incident photons is known through these measurements. In addition, the result of the spectral response measurement can help obtain the total current deliverable from the solar cell as well as help in understanding the possible loss mechanisms that come into play in the solar cell.

Reference

- Arfken, G. B., Weber J. H and Harris E. F (2012) Mathematical Methods for Physicists. *ScienceDirect*. 7th ed; pp. 935 - 962.
- Bagnoli, P. E., & Nannini, A. (1987). Effects of interfacial states on the capacitance-voltage characteristics of Pd/SiO₂/n-Si Schottky diodes. *Solid-state electronics*, 30 (10), 1005-1012.
- Bayhan, H., & Kavasoglu, A. S. (2007). Exact analytical solution of the diode ideality factor of a pn junction device using Lambert W-function model. *Turkish Journal of Physics*, 31(1), 7-10.
- Bohne, W., Röhrich, J., Schöpke, A., Selle, B., Sieber, I., Fuhs, W., and González-Díaz, G. (2004). Compositional analysis of thin SiO_xN_y:H films by heavy-ion ERDA, standard RBS, EDX and AES: a comparison. *Nuclear Instruments and Methods in Physics Research Section B: Beam Interactions with Materials and Atoms*, 217(2), 237-245.
- Caballero, J.A., Marcilla, A., Conesa, J.A., (1997). Thermogravimetric analysis of olive stones with sulphuric acid treatment. *J. Anal. Appl. Pyrol.* 44, 75–88.
- Choi, P. H., Kim, H. J., Baek, D. H., and Choi, B. D. (2012). A study on the electrical characteristic analysis of c-Si solar cell diodes. *J Sem Tech Sci*, 12(1), 58-65.
- Christoforou, N., Leslie, J. D., & Damaskinos, S. (1989). Current-voltage, capacitance-voltage, and capacitance-temperature measurements on CdS/CuInSe₂ solar cells. *Solar Cells*, 26(3), 215-225.
- Dharmadasa, I. M. (2012). Advances in thin-film solar cells. *Pan Stanford publishing, Pte. Ltd*, Boulevard, Singapore.
- Egerton, R. F. (2006). *Physical principles of electron microscopy: an introduction to TEM, SEM, and AEM*. Springer Science & Business Media.
- Ferrieu, F., Halimaoui, A., and Bensahel, D. (1992). Optical characterisation of porous silicon layers by spectrometric ellipsometry in the 1.5–5 eV range. *Solid state communications*, 84(3), 293-296.

Field, H. (1998). UV-VIS-IR Spectral responsivity measurement system for solar cells. In *AIP Conference Proceedings* (pp. 629-635). IOP INSTITUTE OF PHYSICS PUBLISHING LTD.

Gummel, H. K., and Smits, F. M. (1964). Evaluation of solar cells by means of spectral analysis. *Bell System Technical Journal*, 43(3), 1103-1121.

Guryanov, G., Clair, T. S., Bhat, R., Caneau, C., Nikishin, S., Borisov, B., & Budrevich, A. (2006). SIMS quantitative depth profiling of matrix elements in semiconductor layers. *Applied surface science*, 252(19), 7208-7210.

Hahn, D.W., (2007). Raman scattering theory. *Department of Mechanical and Aerospace Engineering, University of Florida*.

Harper, C. (1993) Introduction to Mathematical Physics, *Prentice-Hall of India Private Ltd.* New Delhi.

Hartman, J. S. and Lind, M. A. (1982). Spectral response measurements for solar cells. *Solar cells*, Vol.7(1), pp.147-157

Hatakeyama, T., Quinn, F. X., (1999). Thermal analysis—Fundamentals and applications to polymer science. *John Wiley & Sons*, Chichester.

Helsen, L., Van den Bulck, E., (2000). Kinetics of the low-temperature pyrolysis of chromated copper arsenate-treated wood. *J. Anal. Appl. Pyrol.* 53, 51–79.

Jenkins, R. and Meyers, R.A., (2000). Encyclopedia of Analytical Chemistry. *John Wiley & Sons Ltd*, pp.13269 -13288.

Kastanaki, E., Vamvuka, D., Grammelis, P., Kakaras, E., (2002). Thermogravimetric studies of the behaviour of lignite-biomass blends during devolatilization. *Fuel Process. Technol.* 77–78, 159–166.

Keffous, A., Siad, M., Mamma, S., Belkacem, Y., Chaouch, C. L., Menari, H., & Chergui, W. (2003). Effect of series resistance on the performance of high resistivity silicon Schottky diode. *Applied surface science*, 218 (1), 337-343.

Kittel C, (2005). Introduction to Solid State physics, 8th edition, *John Wiley & Sons, Inc.*, New Jersey, United States of America

Larkin, P. (2011). Infrared and Raman spectroscopy; *principles and spectral interpretation*. The United States: Elsevier.

Li, Y., Huang, W., Huang, H., Hewitt, C., Chen, Y., Fang, G., & Carroll, D. L. (2013). Evaluation of methods to extract parameters from current–voltage characteristics of solar cells. *Solar Energy*, 90, 51-57.

Mansaray, K.G., Ghaly, A.E., (1999). Kinetics of the thermal degradation of rice husks in nitrogen atmosphere. *Energy Sources* 21, 773–784.

Marton, L., (1968). Early History of the Electron Microscope. *San Francisco Press*. San Francisco, California.

Mehta v. K. and Mehta R. (2008), Principles of Electronics. 11th ed., New Delhi, S. Chand

Nassar, M. N., (1999). Thermal analysis of kinetics of Bagasse and Rice Straw. *Energy Sources* 21, 131–137.

Nelson, J. (2003). *The physics of solar cells*. London: Imperial college press.

Onojah, A., Amah, A.N. and Ayomanor, B.O., 2012. Comparative studies of silicon from rice husk ash and natural quartz. *Am. J. Sci. Ind. Res.*, 2012, 3(3): 146-149.

Rui N., (2006). Fourier Series and Their Applications. [online].
<https://dspace.mit.edu/bitstream/handle/1721.1/78574/18-100c-spring-2006/contents/projects/niu.pdf>

Sarangi, S. N., Adhikari, P. K., Pandey, D., & Sahu, S. N. (2010). Current–voltage and capacitance–voltage studies of nanocrystalline CdSe/Au Schottky junction interface. *Journal of Nanoparticle Research*, 12(6), 2277-2286.

Sharma, A. K. (1996). *Semiconductor Electronics*. New Age International (P) Ltd, New Delhi, india.

Siad, M., Keffous, A., Mamma, S., Belkacem, Y., & Menari, H. (2004). Correlation between series resistance and parameters of Al/n-Si and Al/p-Si Schottky barrier diodes. *Applied surface science*, 236(1), 366-376.

Singh, J., & Cohen, M. H. (1980). Capacitance-voltage measurements in amorphous Schottky barriers. *Journal of Applied Physics*, 51(1), 413-418.

Sopori, B. L. (1987). A spectral response measurement system for large-area solar cells. *Solar cells*, 22(4), 287-294.

Sze, S. M., & Ng, K. K. (2007). Photodetectors and solar cells. *Physics of semiconductor devices*, 663-742.

Turrell, G., Gardiner, D.J. and Graves, P.R., (1989). Practical Raman Spectroscopy. *Gardiner, DJ*, pp.13 - 54.

Van Grieken, R., & Markowicz, A. (Eds.). (2001). *Handbook of X-ray Spectrometry*. CRC Press.

Williams, D. B. and Carter, C. B. (1996). The transmission electron microscope. In *Transmission electron microscopy* (pp. 3-17). Springer US.

Wu, I. W., Chen, Y. H., Wang, P. S., Wang, C. G., Hsu, S. H., & Wu, C. I. (2010). Correlation of energy band alignment and turn-on voltage in organic light emitting diodes. *Applied Physics Letters*, 96(1), 013301.

Yang, W. J., Ma, Z. Q., Tang, X., Feng, C. B., Zhao, W. G., & Shi, P. P. (2008). Internal quantum efficiency for solar cells. *Solar Energy*, 82(2), 106-110.

Yogamalar, R., Srinivasan, R., Vinu, A., Ariga, K., & Bose, A. C. (2009). X-ray peak broadening analysis in ZnO nanoparticles. *Solid State Communications*, 149(43), 1919-1923.

4 MATERIALS AND METHOD

4.1 Source of Materials

4.1.1 Rice Husk (RH)

Rice husk collected from Nasarawa L.G.A in Nasarawa state of Nigeria was used as source of raw materials for preparation of rice husk silica. The rice husk labelled batches A, B and C were collected from local rice milling industry at three different sites and times. While batch A was purely rice husk, batch B contained very small particles of rice and batch C contained some dirt from the rice husk dumping site. Figure 4.1 shows the representation of RH.



Figure 4.1: Schematics of rice husk

4.2 Methodology/ Procedure

Rice husk ash when not properly prepared by controlling the burning temperature consists of comparatively higher percentage of unburnt carbon and lower silica. It has already been mentioned that the RHA produced at 1000°C is less reactive due to its crystalline nature. Here, the procedure involved is to produce RHA that contains minimum amount of residual carbon and maximum amorphous silica at below 800°C and crystalline silica above that temperature. The procedures are as follow:

a) Pre-treatment of RH

Sufficient stock amount of RH (500g) for the three different batches were weighed and washed with 20 litres each of hot de-ionized water in cleaned stainless steel beaker. Several washings were done to remove the adhering clay particles and the water decanted off after every washing was observed carefully; the process continued until washing mediums contained almost no dust particles on visual inspection. The thoroughly washed RH was oven dried at about 42°C (average temperature) for five hours.



Figure 4.2: Schematic of rice husk ash

b) Ash production

Rice husk for batches A, B and C were weighed and each put into ceramic crucibles and annealed in furnace at different temperatures of 700°C, 800°C, 900°C and 1000°C. Batch A was annealed for 700°C, 800°C and 900°C for 5 hours. Batch B was annealed for each of the temperature for 5 hours and batch C annealed at all mentioned temperature above for 12 hours. When done at those temperatures, the recovered whitish RHA samples were weighed and transferred to desiccators to cool for about 24hrs. It was then weighed again and readings tabulated in table 4.1 - 4.3.

Table 4.1: Rice husk ash produced batch A

S/No.	Mass of RH(g)	Temp(°C)	Mass of RHA(g)	Ash(%)	Ashing time
1	85.88	700	15.82	18.42	5hrs
2	135.82	800	24.67	18.16	5hrs
3	137.26	900	26.28	19.15	5hrs

Table 4.2: Rice husk ash produced batch B

S/N	Mass of RH(g)	Temp(°C)	Mass of RHA(g)	Ash(%)	Ashing time
1	70.00	700	9.70	13.86	5hrs
2	100.00	800	13.81	13.81	5hrs
3	93.00	900	13.37	14.38	5hrs
4	100.00	1000	13.57	13.57	5hrs

Table 4.3: Rice husk ash produced batch C

S/N	Mass of RH(g)	Temp(⁰ C)	Mass of RHA(g)	Ash(%)	Ashing time
1	100.00	700	19.26	19.26	12hrs
2	100.00	800	20.10	20.10	12hrs
3	100.00	900	19.17	19.17	12hrs
4	100.00	1000	19 .44	19.44	12hrs

4.3 Ash Analysis

Techniques applied to the rice husk ash produced at 700⁰C, 800⁰C, 900⁰C and 1000⁰C for 5hrs or 12hrs for batches A, B and C included x-ray diffraction, x-ray fluorescence, energy dispersive x-ray, scanning electron microscopy, Fourier transform infrared spectroscopy, transmission electron microscopy and thermogravimetric analysis. This research project is mostly based on the above mentioned instruments because major properties of rice husk depend largely on their elemental (or atomic) composition.

4.4 Rice Husk Ash Quantitative and Qualitative Evaluation

XRF, XRD, SEM, TEM, FTIR and ICP were used to analyse the RHA prepared at different temperatures. A comparatively high percentage of the RHA annealed (SiO_2) was achieved for each samples for all ashing temperature with some trace elements present.

4.5 Purification of Rice Husk Ash Silica

Rice husk ash Samples containing chemical compositions were subjected to upgradation/purification by carrying out the procedures below:

4.5.1 Treatment with an oxidant

The induced oxidation of RH carbon to CO₂ is expected to improve the silica content. Hence, the following treatment was given to RHA specimens of different temperature and natural coarse particle size. 15g of each RHA was added 0.8cm³ of 16M HNO₃, and heated in an electric furnace at 700⁰C for one hour. The coarse particles of all RHA specimens were seen to have pulverized, and particle sizes reduced. The resulting ashes were further treated by alkali leaching.

4.5.2 Alkali leaching

Alkalies in RHA might be present in free or combined state. In order to eliminate their water soluble fractions, 13g of each oxidant treated RHA were boiled in 500ml de-ionize water for 1hour so as to leach out the sodium and potassium impurity that are soluble in boiling water. The residues were dried at 100°C in an oven till constant weights are weighed.

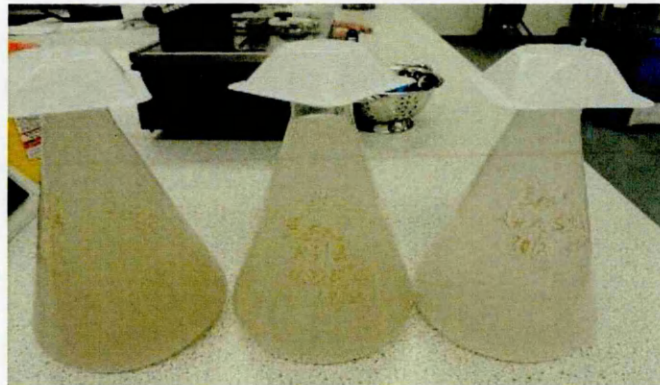


Figure 4.3: Schematic of RHA leaching with deionized water

4.5.3 Digestion of RH ash in dilute hydrochloric acid

Exactly 11g of RHA specimens from alkali leach RHA were digested in 500ml of 5M hydrochloric acid on hot plate, giving constant agitation of 300 rpm by magnetic stirrer. Figure 4.4 represent RHA acid digestions carried out separately for 120 minutes at 95°C. The residues of digested samples were filtered using Whitman paper and then dried in an oven for 1hr at 110°C.

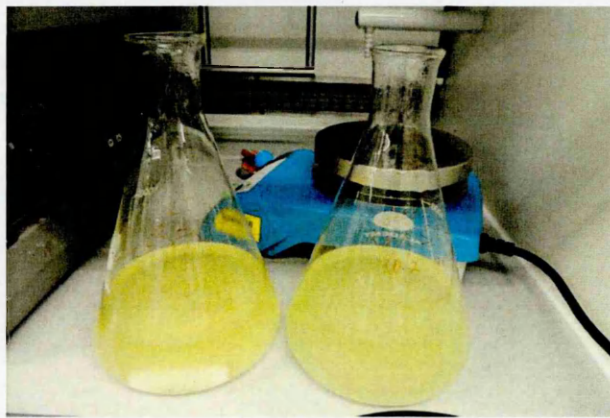


Figure 4.4: Schematic of RHA digested in HCl (colour changes to yellow colour)

4.5.4 Neutralization of HCl acid digested samples

9.5g of each sample was weighed and transferred to a conical flask. 1000ml of deionized water were added to each flask containing a sample with the aid of

magnetic stirrer to stir continuously at 300rpm. The flasks were transferred to hot plates to heat up for 1hr at 85°C before dropping to cool down for 12hrs. The acidic solution was decanted carefully with the solution temperature and pH reading taken. The processes were repeated; but this time, 2hrs settling time before decanting of solution after dropping from the hot plate. The acidic solution is observed to be pure (have a pH = 7.0 - 7.4) before filtering and oven drying.

4.5.5 Dry thermal treatment

Physical elimination of residual carbon without mineralogical phase transformation of silica was attempted to upgrade the silica content. The samples, each weighing 8.0g of chemically purified RHA were put in alumina crucibles and heated in electric furnace at 700°C for 4 hours.

4.6 Production of Metallurgical-Grade Silicon

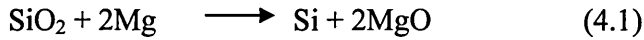
The rice husk ash samples after passing through various solid-liquid extractions; were then dried in an oven at 110°C for 2hrs before allowing cooling down for 24 hours. The samples of RHA silica were pulverized and thoroughly mixing with magnesium powder in a mortal at a ratio of RHAs: Mg (1.0g: 1.0g) to form magnesium and silica mixture. 4.0g of each sample were transferred from the mortal to alumina crucibles for heating in an electric furnace with a controlled atmosphere at a temperature of 800°C for 5 hours before cooling down to room temperature. By heating the mixture of treated RHA (silica) and magnesium powder in a crucible, the magnesium reduces the silica to elemental silicon as represented in figure 4.5.



Figure 4.5: Schematic of derived MG-Si from rice husk ash

A mixture of magnesium, magnesium oxide, magnesium silicide and silicon resulted, which were transferred to a desiccators and left to cool down for 72

hours before leaching in HCl acid. The powder that falls to the bottom of the flask is chemically purified by boiling in molarity HCl for 1 hour (Gray, 2005), filtered and the residues oven dried for 1 hour before thermally treated exclusively for minimizing residual carbon or temperature resistant organic matter; forming metallurgical-grade silicon.



The samples powder were preserved for XRF, XRD, SEM, TEM, FTIR and Ramam Spectroscopy quantitative and qualitative analysis. The charts showing all the various stages are presented in figure 4.6 below.

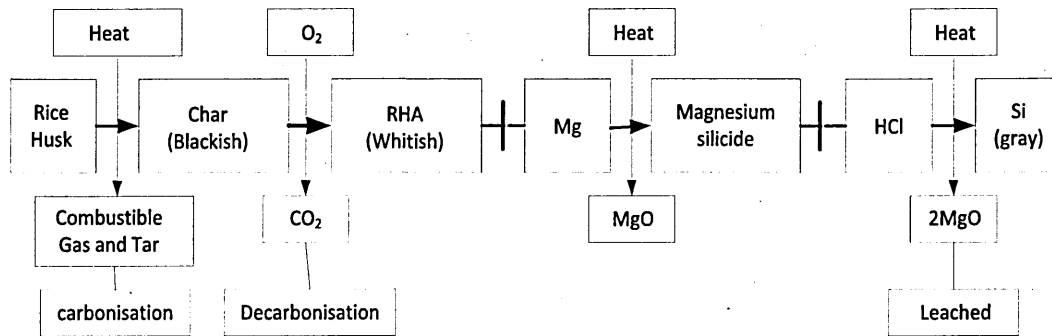


Figure 4.6: Diagram of the processes from RH to thermal decomposition of RH to metallurgical-grade silicon

Metallurgical-grade silicon derived is the least quality silicon from the categories of silicon quality. It seems to contain high percentage impurity concentrations in their crystal growth, this can perturb by inclusions, precipitates, or defects which may finally cause structural breakdown. The illustration of the various categories of silicon quality which covers about eight orders of magnitude from metallurgical-grade silicon to hyperpure silicon is shown in figure 4.7. In a reduction process, impurities from rice husk ash (silica) carbon mixtures and other auxiliary materials contaminate the crude metallurgical-grade silicon to an amount of one to two and half percent silicon. This requires a very efficient purification methods ranging from hydrometallurgy refinement based on solid-liquid extraction in which, such parameters as the type and concentration of acid mixtures, the duration and temperature of the leaching procedure to the solvent refining process as shown in figure 2.15 can almost eliminate impurities with

favourable segregation coefficients down to concentration of very low weight parts per million range, thus, upgrading the silicon from its previous basic category to high purity silicon category within the quality ranges of different silicon products of figure 4.7.

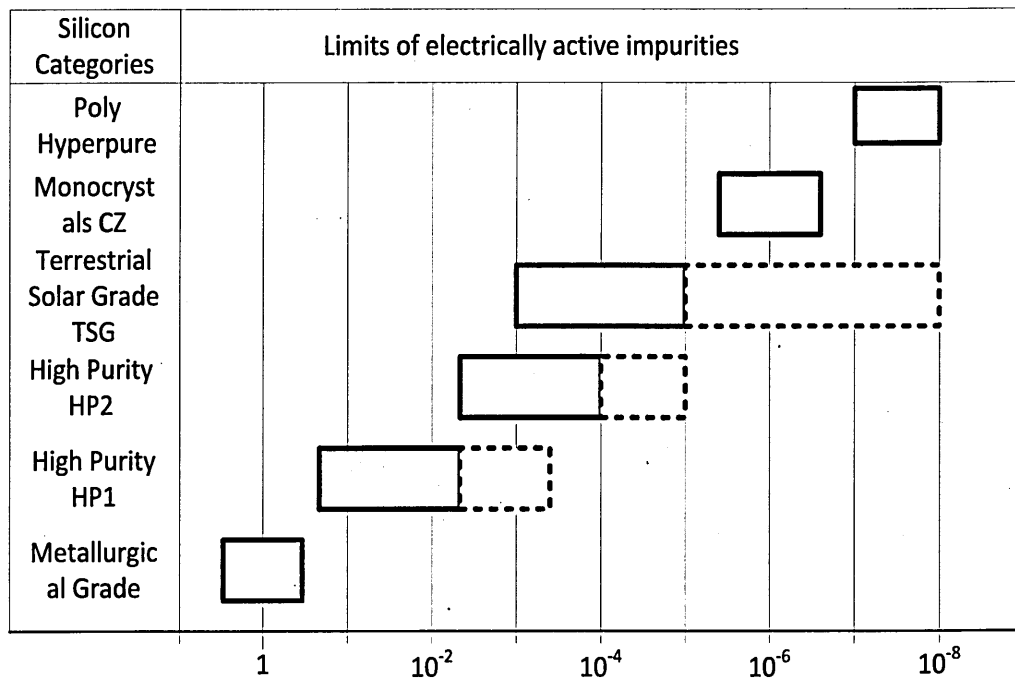


Figure 4.7: Quality ranges of different silicon products: Basic stage of refining, metallurgical-grade; HP1, high purity; HP2, high purity, advance stage of refining; Terrestrial solar grade; CZ, Czochralski and Polycrystals hyperpure, final stage of refining (Sirtl et al, 1979)

4.7 Post purification of metallurgical-grade silicon by alloying process

Metallurgical-grade silicon derived from RHA of batch C1000 was replicated from a 99.99% commercial grade Si powder with ~ 325 mesh particle size purchased from Sigma Aldrich, UK. This was to test run the alloying process due to insufficient amount (0.5g) of derived MG-Si remaining after leaching processes. This was done by contaminating 10.85g Si with 35mg NaCl, 31.5mg Mg, 17.5mg Al and 7.1mg FeB all of analytical purity and thoroughly mixed in a mortar. 29.58g of tin powder with 4.0g replica Si powder was thoroughly mixed and then put in a 20.71cm³ alumina crucibles inside a fume hood. The crucible and its contents was introduced into a furnace programmed to holding temperature of 1200°C at 3.5°C/min heating rate for 3hrs before it start cooling down to room temperature at 2°C/min.



Figure 4.8: Schematic of solidified Si-Sn alloy

Figure 4.8 shows the solidified Si-Sn alloy removed from furnace and crucible crushed with a G-clamp. The crushed Si-Sn was separated from the crucible and further ground to powder using Retsch Vibratory Disc Mill RS 200, German product grinding machine.

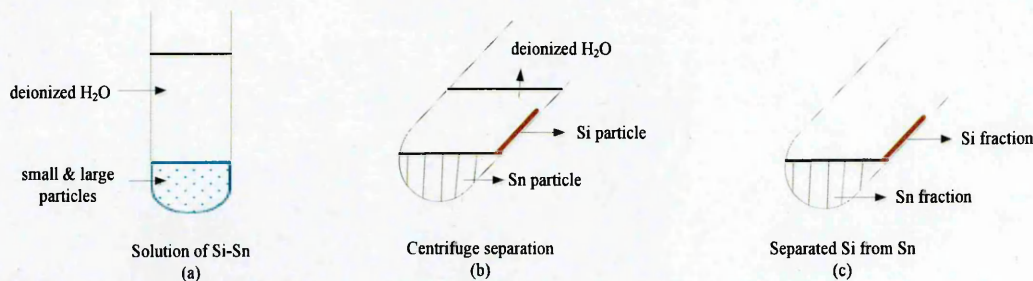


Figure 4.9: Sketch of grind Si-Sn alloyed powder separation process (a, b and c).

Figure 4.9 shows the sketch of 2g of grind Si-Sn alloy powder placed in the rotor plastic container with deionized water added and put in the rotor at room temperature for separation. The Sorvall RC6 centrifuge, UK product was started and the rotate speed regulated to 600 rpm and held for 5 minutes. The sample container was taken out and deionized water decanted. Sample of separated silicon was taken for SEM and EDS analysis.

4.8 Summary

This chapter discussed the source of raw material used for production of silica which was labelled in batches of silica. The chapter also discussed the reduction of this silica into MG-Si material needed for production of solar grade silicon. In this research work, the methods/procedures applied were also discussed. The analysis from RH ash silica was tabulated and the production of MG-Si and its post purification process explained.

Reference

Gray, T. (2005). Making Silicon from Sand. Popular Science 267(4), 116.

Van Overstraeten, R., & Palz, W. (Eds.). (1979). *2nd EC Photovoltaic Solar Energy Conference: proceedings of the international conference, held at Berlin (West), 23-26 April 1979.* D. Reidel.

5 RESULTS AND DISCUSSIONS

5.1 Processing and pyroprocessing of rice husk

5.1.1 Rice husk ash content

The results reported below are limited to rice husk collected from rice milling company in Nasarawa L.G.A. of Nasarawa state, Nigeria. The contents of rice husk ashed at different temperature are presented in Table-5.1, 5.2 & 5.3.

Table 5.1: Silica content in rice husk ash heated for 5 hours at different temperature for batch A

S/No.	Temperature (°C)	Silica ash contents (wt %)
A700	700	18.42
A800	800	18.16
A900	900	18.15
Mean		18.24
Standard deviation		0.15

The statistical computation for batch A gives a low standard deviation of 0.15 which is an indication that all RH ash contents derived at different temperature of ashing have values that are very close to their mean value of 18.24 wt %. This inferred that there are no much differences in derived RHA silica quantity due to temperature difference.

Table 5.2: Silica content in rice husk ash heated for 5 hours at different temperature for batch B

S/No.	Temperature (°C)	Silica ash contents (wt %)
B700	700	13.86
B800	800	13.81
B900	900	14.38
B1000	1000	13.57
Mean		13.91
Standard deviation		0.34

The statistical computation for batch B gives a low standard deviation of 0.34. This is an indication that all RH ash contents derived at different temperature of ashing have values that are very close to their mean value of 13.91 wt %. It inferred that there are no much differences in derived RHA silica quantity due to temperature difference.

Table 5.3: Silica content in rice husk ash heated for 12 hours at different temperature for batch C

S/No.	Temperature (°C)	Silica ash contents (wt %)
C700	700	19.26
C800	800	20.10
C900	900	19.17
C1000	1000	19.44
Mean		19.49
Standard deviation		0.42

The statistical computation for batch C gives a low standard deviation of 0.42 which is an indication that all RH ash contents derived at different temperature of ashing have values that are very close to their mean value of 19.49 wt %. It inferred that there are no much differences in derived RHA silica quantity due to temperature difference.

The average rice husk ash content of the different temperature from the above tables are 18.58, 13.91.and 19.49%. Houston (1972) reported that ash content varies from 16.00 to 26.00 percent. On the other hand, Ikram and Akhter (1988) showed in their study that ash amounted to 17.06 percent. Similarly, it is determined by Mehta (1977) as 20.00 percent. The results obtained in this study indicate that batch A and C lies within the wide range reported in literatures, while batch B is below due to the quantity of raw rice contained within the rice husk. It was also observed from table 5.1, 5.2 and 5.3 that the standard deviation for table 5.1 has the lowest value and as such gives the best rice husk ash yield. Thus, it therefore shows that it might not be necessary ashing RH for more than 5 - 6 hours.

5.1.2 Rice husk ash silica

The main aim of converting husk to ash is to utilize its silica for metallurgical-grade silicon whose percentage usually varied from source to source. It depends on the type of method adopted and conditions of given thermal treatment. Pyroprocessing of husk is frequently carried out to get RHA with maximum percentage of silica. However, production of silica is an exception where certain amount of carbon is retained intentionally (Haxo and Mehta, 1975). This last factor is difficult to control by researchers. However, proper pyroprocessing may result in RHA with highest percentage of silica. In addition, environment

parameter, temperature and time duration are vital in this regard (Khane, 1985).

Samples of the RHA were analysed by XRF, XRD, TGA and SEM.

5.2 Characterization of RHA

The various batches of RHA were characterised for their structural, optical, morphological and compositional properties using XRF, ICP-OES, XRD, ATR-FTIR, TGA, SEM and EDX measurements. This was done in order to further understand the behaviour, quantity and quality of these materials.

5.2.1 X-ray fluorescence spectrometry (XRF)

Table 5.4: Batch A chemical analysis of RHA using X-ray fluorescence spectrometry (XRF)

Compounds	A700 (wt %)	A800 (wt %)	A900 (wt %)
SiO ₂	97.42	98.03	97.48
K ₂ O	0.36	0.38	0.37
CaO	0.37	0.35	0.35
MnO	0.02	0.03	0.03
FeO ₃	0.07	0.05	0.06
P ₂ O ₅	0.15	0.16	0.39
Na ₂ O	0.48	0.30	0.32
MgO	0.11	0.00	0.26
AS ₂ O ₃	0.33	0.29	0.29
Al ₂ O ₃	0.18	0.19	0.25
ZrO ₂	0.02	0.02	0.02
SO ₃	0.20	0.20	0.18
Total Impurities	2.29	1.97	2.52

Looking at XRF results of batch A RHA presented in table 5.4, it showed that while A800 RHA contained the highest silica content of 98.03 wt % with least average impurity of 1.97wt %, A900 produced the next highest silica with 97.48%. However, A900 contained highest quantity of impurities with 2.52 wt % when compared with A700 that contained the least silica content of 97.42 wt %, but with impurity of 2.29 wt %. Thus, the result showed there are no much quantitative value difference in RHA silica due to temperature and time of roasting.

Table 5.5: Batch B chemical analysis of RHA using x-ray fluorescence spectrometry (XRF) and inductively coupled plasma (ICP)

Compounds	B700 (wt %)	B800 (wt %)	B900 (wt %)	B1000 (wt %)
SiO ₂	95.24	95.67	95.73	96.03
K ₂ O	1.04	0.83	0.96	0.86
CaO	0.75	0.77	0.73	0.68
Mn ₃ O ₄	0.12	0.12	0.11	0.11
FeO ₃	0.11	0.1	0.11	0.08
P ₂ O ₅	1.09	1.09	1.01	0.85
Na ₂ O	0.09	0.08	0.11	0.08
MgO	0.69	0.69	0.66	0.59
Al ₂ O ₃	0.12	0.11	0.18	0.09
TiO ₂	0.02	0.01	0.02	0.02
SO ₃	0.36	0.33	0.25	0.25
B	0.27	0.48	0.22	0.23
Total impurities	4.66	4.61	4.36	3.84

Looking at XRF results of batch B RHA presented in table 5.5, it showed that while B1000 RHA contained the highest silica content with 96.03 wt % and a least average impurity of 3.84 wt %, it was followed in descending order by B900, B800 and B700 with 95.73, 95.67 and 95.24 wt % respectively. The impurity however, showed the direct opposite pattern as that of the RHA silica content with B1000 having the least impurity of 3.84 wt %, followed in ascending order by B900, B800 and B700 with 4.36, 4.61 and 4.66 wt % respectively. Thus, the result showed there are no much quantitative value difference in RHA silica due to temperature and time of roasting.

Table 5.6: Batch C chemical analysis of RHA using x-ray fluorescence spectrometry (XRF) and inductively coupled plasma (ICP)

Compounds	C700 (wt %)	C800 (wt %)	C900 (wt %)	C1000 (wt %)
SiO ₂	94.86	96.41	95.29	96.59
K ₂ O	0.43	0.27	0.49	0.25
CaO	0.48	0.44	0.50	0.48
Mn ₃ O ₄	0.05	0.08	0.06	0.05
Fe ₂ O ₃	0.15	0.13	0.24	0.10
P ₂ O ₅	1.03	0.74	1.11	0.80
Na ₂ O	0.16	0.08	0.20	0.22
MgO	1.20	0.50	0.64	0.58
Al ₂ O ₃	0.68	0.33	0.44	0.24
TiO ₂	0.04	0.03	0.08	0.02
SO ₃	0.40	0.42	0.37	0.44
B	0.52	0.57	0.58	0.23
Total impurities	5.14	3.59	4.71	3.41

Looking at XRF results of batch C RHA presented in table 5.6, it showed that while C1000 RHA contained the highest silica content with 96.59 wt % and a least average impurity of 3.41 wt %, it was followed by C800 in silica content and low impurity by 96.41wt % and 3.59 wt % respectively. C900 with silica content of 95.29 wt % and impurity of 4.71 wt % was next. C700 with the least silica content of 95.29 wt % contains the highest impurity of 5.14 wt %. Thus, the result shows there are no much quantitative value difference in RHA silica due to temperature and time of roasting.

5.2.2 X-ray diffraction (XRD) of RHA

The XRD analysis results presented in figure 5.1 diffractogram showed peaks that are representation of corresponded peaks to those of close Inorganic Crystal

Structure Database (ICSD). The spectrum of batch A RH sample ashed at 700°C for 5hrs revealed that the RHA consisted mainly of amorphous silica as shown in the blue spectrum of the diffractogram of figure 5.1. The XRD spectrum of RH ashed at 800°C contains three peaks belonging to quartz, while the RH ashed at 900°C (green spectrum) contains all 3 allotropes of silica. This implies that silica with amorphous or crystalline nature can be produced from RHA. The appearances of peaks in the XRD spectrum of RH ashed at 800°C matching ICSD peaks with reference code 00-033-1161 indicate conversion of amorphous to crystalline quartz silica with temperature difference. Whereas, the spectrum of the RH ashed at 900°C displays silica peaks of crystalline with phases A, C and Q for anorthite, cristobalite, and quartz respectively matching ICSD quartz low peaks with reference code 01-085-0335 and cristobalite alpha/ cristobalite peaks with reference code 01-082-1403/ 01-082-0512 respectively. All XRD data for the above reference code allotropes are given in appendix 1.

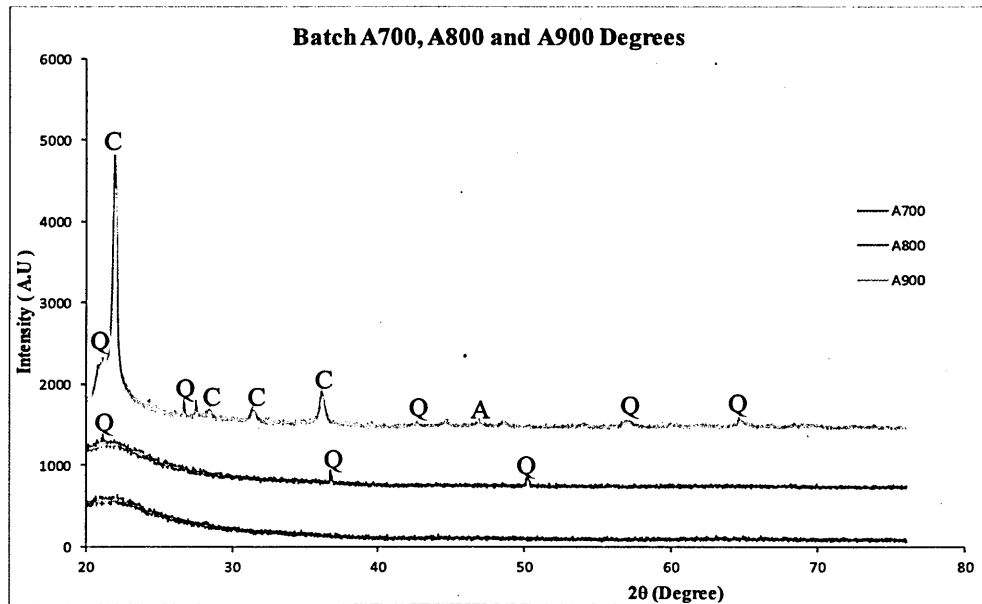


Figure 5.1: Offset XRD diffractograms of RHA. (Symbols Q, A and C means peak positions of Quartz, Anorthite and Cristobalite respectively).

Figure 5.2 shows sample of figure 5.1 silica after been left at room temperature for a year before another XRD analysis was done. It was seen from the diffractogram that all three spectra indicated that the atoms tends to have arranged themselves in such a way that resembles that of a crystal atoms. Thus, the RH A700 ashed at 700°C has showed few quartz peaks that match ICSD with

reference code 01-083-2465. RH A800 ashed at 800°C showed more pronounced quartz peaks comparable to A900 RH ashed at 900°C, which has also acquired some more peaks compared to A900 in figure 5.1; The ICSD reference codes for A800 and A900 peaks in figure 5.1 were same as for figure 5.2. The diffractogram of figure 5.3 XRD shows the results of the year old RHA after leaching in hot deionized water. The three spectra show peaks similar to those in figure 5.1 except that for A900, the peaks were more pronounced due to further crystallized formation and anorthite decomposition. All peak in figure 5.3 spectra were matched with the ICSD reference code mentioned above.

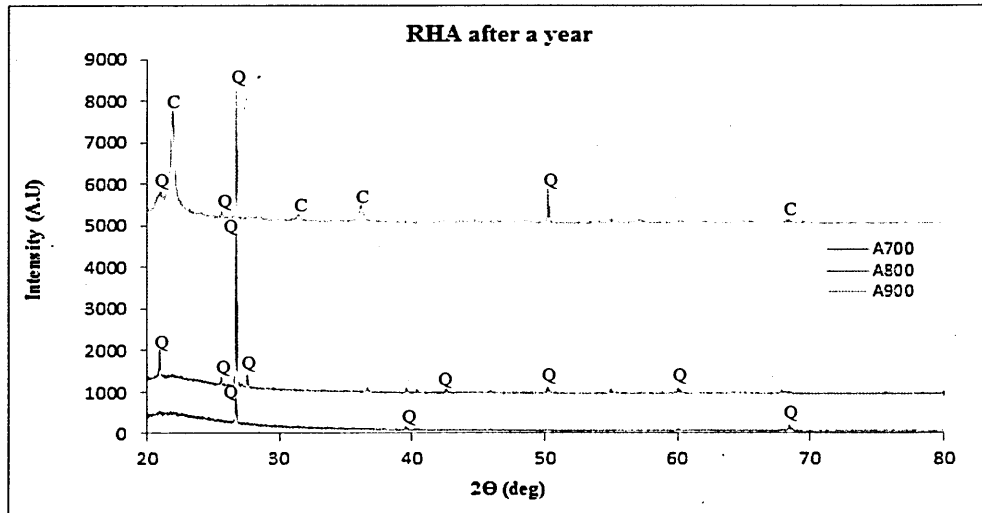


Figure 5.2: Offset XRD diffractograms of RHA twelve months after ashing (Symbols Q and C means peak positions of Quartz and Cristobalite respectively)

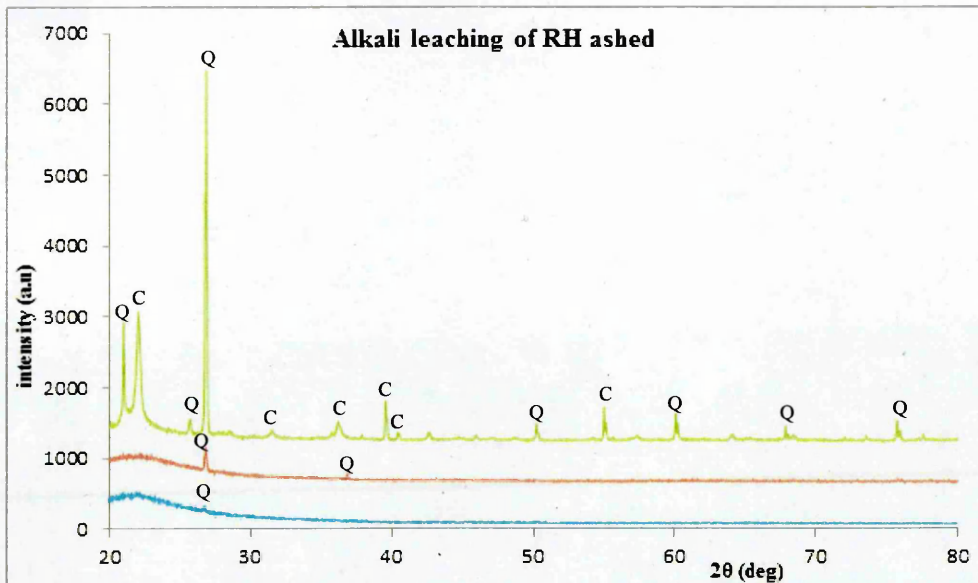


Figure 5.3: Offset XRD diffractograms of leached figure 5.1. (symbol Q and C means peak positions of Quartz and Cristobalite respectively)

It was observed from the diffractograms in figure 5.4 that ashing batch B rice husk sample at 700°C, 800°C and 900°C for 5hrs produced only amorphous silica, whereas the same batch RH ashed at 1000°C converted into crystalline quartz and cristobalite silica that matches those of ICSD reference code 01-085-0335 and 01-082-0512 peak list respectively as shown on the diffractogram spectra peak. The lack of crystalline silica after ashing at 800°C and 900°C may be due to the inclusion of raw rice particles in batch B rice husk, which introduced a greater proportion of amorphous cellulosic materials, thereby influencing the arrangement of the RH ash molecules.

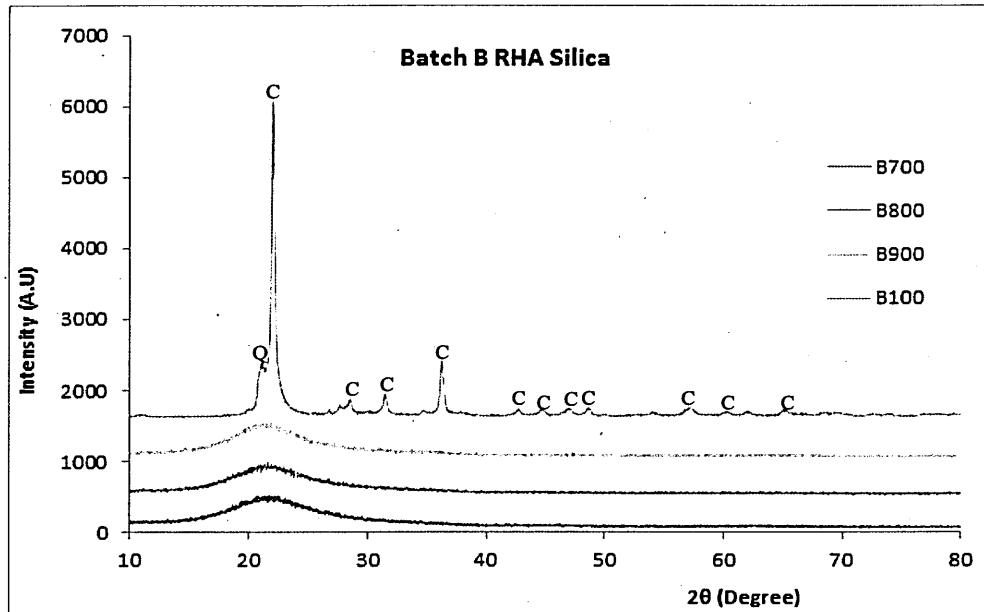


Figure 5.4: Offset XRD diffractograms of RHA derived from batch B sample. (Symbols Q and C means peak positions of Quartz and Cristobalite respectively).

It was observed from batch C XRD analysis results shown in Figure 5.5 that the sample of RH ashed at 700°C , 800°C 900°C and 1000°C for 12 hours consist of quartz and cristobalite, but with a significant proportion of sample being amorphous. RHA has been reported to be amorphous at ashing temperature of 500°C - 700°C with crystalline silica forming at temperature equals to or greater than 800°C (Agrawal, 1989). The appearance of peaks due to quartz and cristobalite in the diffractograms reveal that, in sample C, a small quantity of crystalline silica is found after ashing at 700°C , in contradiction of Agrawal's findings. However Chopra et al (1981) reported that some of the amorphous silica in RHA transformed to crystalline quartz after heating for up to 12 hours at 700°C . The very high peak on RH ashed at 800°C must have occurred as a result of diffraction due to the crystalline transformation of the material into quartz. However, the dirt blended with batch C initial RH must have contributed to RHA silica of formation of crystalline silica. All spectra peaks in figure 5.5 matches the ICSD reference codes: 01-083-2465, 01-033-1161 and 01-085-0335 of silicon dioxide. See appendix 1 for used reference code.

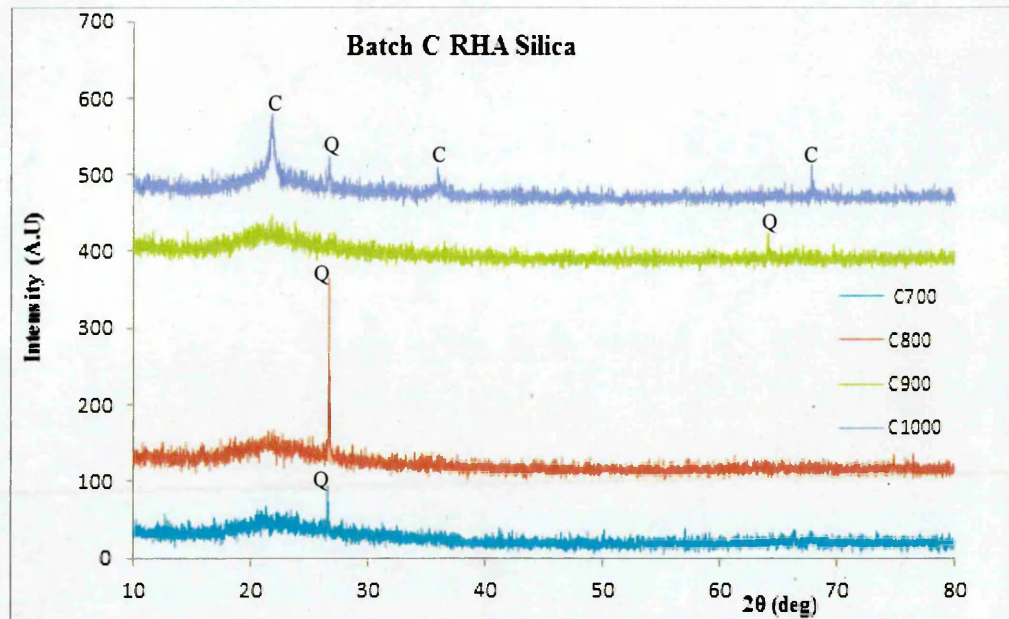


Figure 5.5: Offset XRD Diffractogram of RHA. (Symbols Q and C means peak positions of Quartz, Amorphous and Cristobalite respectively).

5.2.3 Thermal analysis on RHA

Samples of rice husk (both as-produced and ground) underwent thermogravimetric (TG) analysis using a TGA/DSC1 Gas Controller GC100 Mettler Toledo at heating rate of $10^{\circ}\text{C}/\text{min}$. Two starting states were used to investigate the effect of initial particle size on the ashing process. In all samples, volatile organic substances (cellulose, hemicellulose and lignin) contained in the RH started to be driven off at 40°C ; the process was completed at 117°C , as shown in Fig. 5.6. It was seen that 4.60% and 4.98% (0.50mg and 0.66mg) of the substance lost in the process for "raw" rice husk and ground rice husk respectively. Carbonization occurs between 117°C and 300°C to yield black rice husk ash with very little loss in mass. Decarbonization occurs rapidly between 300°C and 500°C with very high percentage weight lost up to 63% (7.06mg) and 56% (7.47mg) for "raw" RH and ground RH respectively.

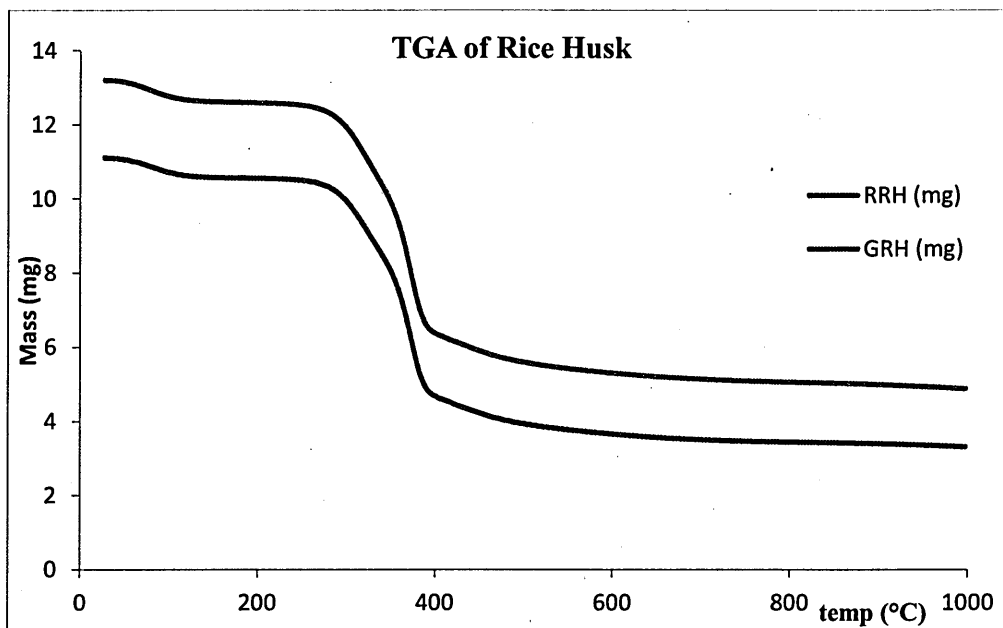


Figure 5.6: Thermogravimetric analysis offset curves of raw rice husk (RRH) and ground rice husk (GRH).

These results show that a greater proportion of carbon and volatile organic substances are removed from the "raw" rice husk. I postulate that this is impact due to the release of some volatile organic compounds as result of increase in exposed surface from grinding. The settling of the finer particles may also reduce the penetration of oxygen to some of the sample resulting in incomplete combustion

5.2.4 Scanning electron microscopy (SEM)

The Secondary electron images obtained using FEI Nova Nano SEM 200 reveals in Fig. 5.7 some selected forms and microstructures of RHA independent of batch temperature and time. It was observed from Fig. 5.8a that undamaged RH after ashing between 700 and 1000°C possesses a finger-like shape made up of inner honeycombed structure as in Fig. 5.8b and a thick outer surface skin-like well-organized corrugated structure in nature as shown in the micrographs of Figure 5.8c surface morphology. These observations are in agreement with those made by Ikram and Akhter (1988). The porosity shown in Fig. 5.8d with honeycombed structure of the RHA is responsible for its high specific surface area; the increased reactivity that is a consequence of the high specific surface area reduces the time needed for leaching process to be effective and highly suitable for hydrometallurgical purification.

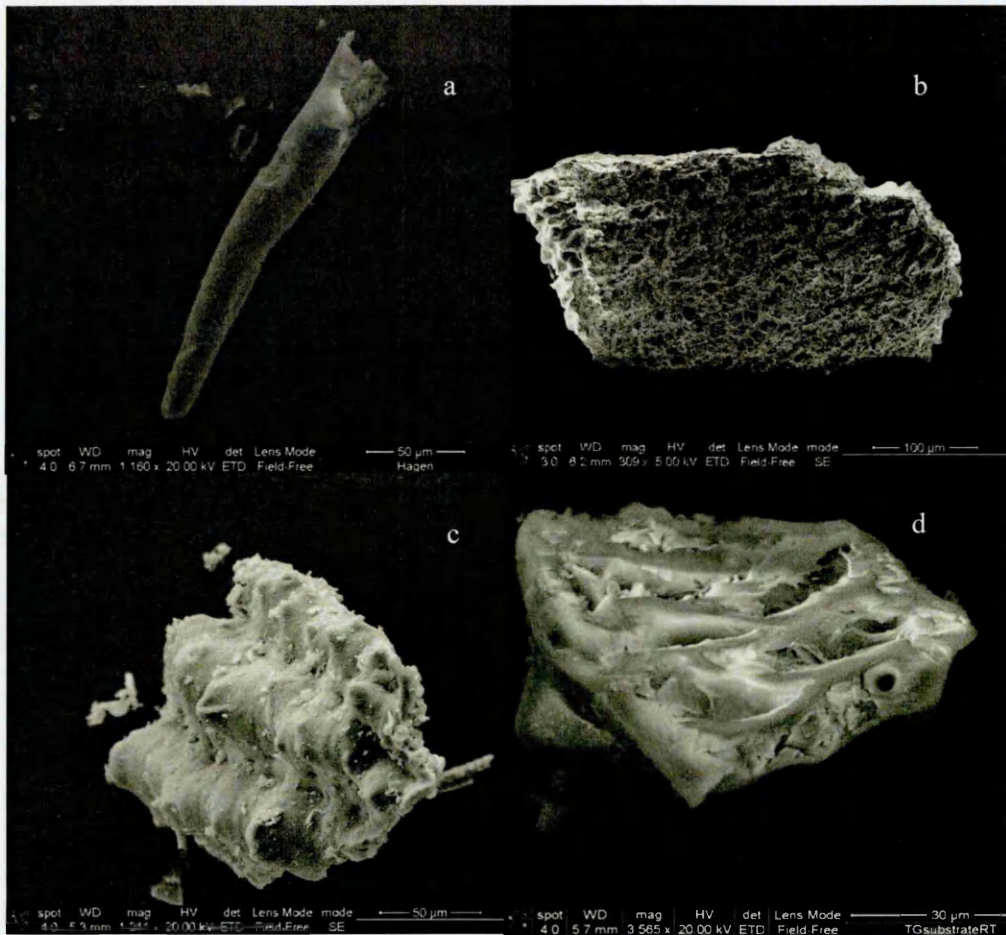


Figure 5.7: Typical micrograph of 900°C for 5hrs (a) RHA undamaged finger-like structure, (b) porous, honeycomb-like structure, (c) well-organized outer corrugated structure, (d) the structure with many residual pores of large internal surface area.

5.2.5 Attenuated total reflection Fourier transform infrared (ATR-FTIR) spectroscopy

Samples of rice husk and rice husk ash underwent ATR-FTIR analysis using a single reflection diamond ATR cell (Graseby Specac, UK), which has the trade name “Golden gate”. Samples of RH and RHA were pressed on top of the diamond ATR crystal and their spectra were collected. To collect and analyse the spectra, OMNIC software (version 7.3) was used. Fig. 5.8 shows the resulting ATR spectra for the samples of raw RH and the ash silica for batch C heated at 700, 800, 900 and 1000°C (in order to see the differences, spectra were off-set). As can be seen, there are strong absorption peaks at $\sim 789 \text{ cm}^{-1}$ and 1040 cm^{-1} , just as those from commercial grade silica, indicating the presence of silica which slightly varied from that of the rice husk with 789 and 1030 cm^{-1} . For the various heating rates, the ATR spectrum shows no significant changes in the peak position. However, the intensity of the peaks for 700 and 800°C (amorphous silica) were

higher and almost of same intensity compared to that of crystalline silica (900°C), indicating that the amorphous silica yield decreased with increasing heating rate above 800°C. The intensity later increase with increase heating to 1000°C which is consistent with the results of reaction characteristic analysis, as indicated by some XRD diffractogram. This inferred that sample is almost entirely crystalline in nature.

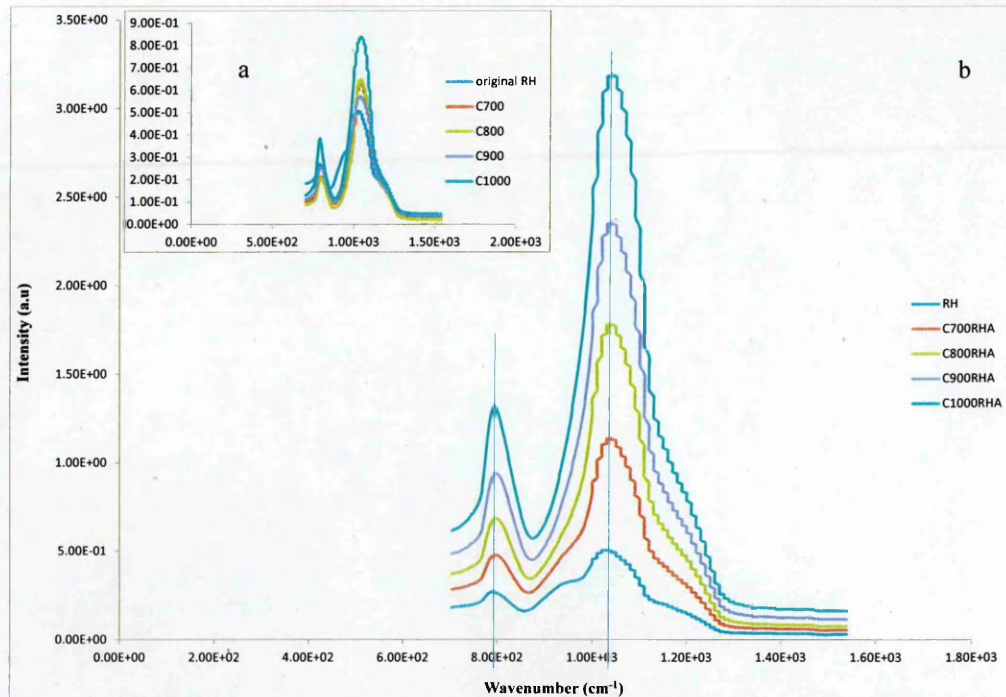


Figure 5.8: ATR spectrogram of RH and RHA. (a) original spectra, (b) off-set spectra.

5.3 Impurities evaluation using XRF and ICP

Looking at the XRF results of RHA batch A impurities represented in table 5.7 as extracted from table 5.4, it showed quantitative evaluation of some major elemental contaminants of metallic impurities contained in rice husk silica such as; Na₂O, MgO, P₂O₅, Al₂O₃, SO₃, K₂O, CaO, Mn₃O₄ and Fe₂O₃ present in their compound form in weight percentage for different heated temperature.

Table 5.7: Impurities in batch A

Compounds	wt %	A700	A800	A900
K ₂ O	%	0.36	0.38	0.37
CaO	%	0.37	0.35	0.35
MnO	%	0.02	0.03	0.03
Fe ₂ O ₃	%	0.07	0.05	0.06
P ₂ O ₅	%	0.15	0.16	0.39
Na ₂ O	%	0.48	0.30	0.32
MgO	%	0.11	0.00	0.26
AS ₂ O ₃	%	0.33	0.29	0.29
Al ₂ O ₃	%	0.18	0.19	0.25
ZrO ₂	%	0.02	0.02	0.02
SO ₃	%	0.20	0.20	0.18
total impurity	%	2.29	1.97	2.52
standard deviation	%	0.1555	0.1425	0.1389

The batch A impurity represented results showed individual impurity quantity with K₂O, CaO, Na₂O, Al₂O₃, SO₃ and AS₂O₃ contributing bulk of the impurity, MnO, FeO₃ and ZrO₂ are at trace level. Looking at the total impurity of A700, A800 and A900 and their standard deviation, A900 having highest impurity of 2.59 wt % seems to have the least standard deviation of 0.1389 wt % compare to total impurities of 1.97 wt % and 2.29 wt % for A800 and A700 with standard deviation of 0.1425 and 0.1555 wt % respectively. This infers that A900 has a better estimated silica impurity than for A700 and A800.

Table 5.8: Impurities in batch B

Compounds (wt %)	B700	B800	B900	B1000
K ₂ O	1.04	0.83	0.96	0.86
CaO	0.75	0.77	0.73	0.68
Mn ₃ O ₄	0.12	0.12	0.11	0.11
Fe ₂ O ₃	0.11	0.10	0.11	0.08
P ₂ O ₅	1.09	1.09	1.01	0.85
Na ₂ O	0.09	0.08	0.11	0.08
MgO	0.69	0.69	0.66	0.59
Al ₂ O ₃	0.12	0.11	0.18	0.09
TiO ₂	0.02	0.01	0.02	0.02
SO ₃	0.36	0.33	0.25	0.25
B (ICP)	0.27	0.48	0.22	0.23
Total impurities	4.66	4.61	4.36	3.84
standard deviation	0.3983	0.3737	0.3702	0.3379

The XRF of batch B RHA impurity results represented in table 5.8, showed individual impurity quantity with K₂O, CaO, Na₂O, Al₂O₃, FeO₃, Mn₃O₄, P₂O₅, SO₃, Al₂O₃ and B contributing bulk of the impurity and TiO₂ appears in trace level. Looking at the total impurity of B700, B800, B900 and B1000 with their standard deviation, it shows that B1000 has the least average impurity and standard deviation of 3.84 and 0.3379 wt % respectively, followed in descending order by B900, B800 and B700 with 4.36/0.3702, 4.61/0.3737 and 4.66/0.3983 wt % respectively. These indicates that B1000 produces rice husk with least impurity and better impurity distribution compared to B900, B800 and B700 in descending order. This may be due to reaction of the raw rice presence with temperature during ashing.

Table 5.9: Impurities in batch C

Compounds (wt %)	C700	C800	C900	C1000
K ₂ O	0.43	0.27	0.49	0.25
CaO	0.48	0.44	0.50	0.44
Mn ₃ O ₄	0.05	0.04	0.06	0.05
Fe ₂ O ₃	0.15	0.13	0.24	0.10
P ₂ O ₅	1.03	0.74	1.11	0.70
Na ₂ O	0.16	0.08	0.20	0.22
MgO	1.20	0.50	0.64	0.58
Al ₂ O ₃	0.68	0.33	0.44	0.24
TiO ₂	0.04	0.03	0.08	0.02
SO ₃	0.36	0.33	0.25	0.25
ZrO ₂	0.20	0.19	0.20	0.20
BaO	0.01	0.01	0.02	0.02
B (ICP)	0.52	0.57	0.58	0.51
Total impurities	5.31	3.66	4.81	3.58
standard deviation	0.3766	0.2658	0.3060	0.2596

The XRF of batch C RHA impurity results represented in table 5.8, showed individual impurity quantity with Mn₃O₄, K₂O, CaO, Al₂O₃, Fe₂O₃, P₂O₅, SO₃, Al₂O₃ MgO, ZrO₂ and B contributing bulk of the impurity. Na₂O, TiO₂ and BaO appear in trace level. Looking at the total impurity of C700, C800, C900 and C1000 with their standard deviation, it shows that C1000 has the least average impurity and standard deviation of 3.58 and 0.2596 wt % respectively, followed by C800 with 3.66 and 0.2658 wt %, next by C900 with 4.81 and 0.3060 before C700 with highest average impurity and standard deviation of 5.31 and 0.3766 wt % respectively. This indicates that C1000 produced silica with the least and best estimated impurity. Observation from table 5.7, 5.8 and 5.9 showed that RH produces silica impurity can be as low as 1.97 wt % for clean RH as batch A800 and up to 5.31 Wt % for unclean RH as C700.

5.4 Purification process

In order to remove these major metal impurities above, a low cost process known as hydrometallurgy leaching treatment involving addition of 0.8cm^3 of 16M HNO_3 to 15g RHA and heating at 700°C for 1hr was used. All processing was carried out in fume cupboards to minimize the health risk associated with crystalline silica. The products were rinsed using deionized water, filtered and dried. The samples then underwent a digestion using 5M HCl acid for 120 minutes at 95°C on hot plate with constant agitation from a magnet rotated at 300 rpm. The residues of digested samples were filtered using Whitman paper and then dried in an oven for 1hr at 110°C . The material was rinsed in deionized water until the rinse water had a pH of between 7 and 7.4. The residue was filtered and dried in an oven for 1hr at 110°C . The purity obtained is tabulated in table 5.10 (batch B) and 5.11 (batch C).

Table 5.10: Impurities after leaching batch B

Compounds	B700	B800	B900	B1000
K_2O	0.03	0.17	0.2	0.17
CaO	0.06	0.08	0.13	0.16
Mn_3O_4	0.04	0.03	0.05	0.08
FeO_3	0	0.01	0.02	0.02
P_2O_5	0.14	0.09	0.12	0.12
Na_2O	0.01	0.04	0.02	0.02
MgO	0.12	0.15	0.27	0.34
Al_2O_3	0.02	0.02	0.02	0.04
SO_3	0.34	0.24	0.26	0.36
B	0.06	0.11	0.18	0.4
Total impurities	0.82	0.94	1.27	1.71

It is clearly seen that the RHA silica C700 was the purest with silica up to 99.51% pure; while C800 was next in purity by 99.28%, C1000 was least with 98.79% which is only 0.30% less pure than C900. These results are due to the fact that C700 silica is more amorphous in nature and more chemically reactive than C1000 that is least chemically reactive. This implies that the chemically reactivity decreases with increase crystallinity in RHA silica and is in agreement with (Mehta, 1977). Looking at the XRF leached impurity results of batch B presented in table 5.10, the statistical computation of its impurities mean, impurities

standard deviation and impurities standard error showed that while B700 has least average impurity of 0.0820 wt %, B800 however has the least impurity standard deviation and impurities standard error of 0.0747 and 0.0236 respectively. This indicates that although B700 silica was highest in purity after leaching, B800 has the best leached individual impurities compared to B700, B900 and B1000. From the XRF and ICP leached RH silica results of batch C presented in table 5.11, it was observed that C700 has the least average impurity, impurity standard deviation and impurity standard error of 0.0445, 0.0611 and 0.0193 wt % after leaching respectively. This indicates that apart from C700 silica being the purest for batch C, its individual impurity compound reaction to leached treatment was the best compared to C800, C900 and C1000 respectively.

Table 5.11: Impurities after leaching batch C

Compounds (wt %)	700	C800	C900	C1000
K ₂ O	0.00	0.03	0.03	0.04
CaO	0.01	0.03	0.03	0.04
Mn ₃ O ₄	0.01	0.01	0.01	0.01
FeO ₃	0.00	0.00	0.01	0.02
P ₂ O ₅	0.12	0.12	0.14	0.2
Na ₂ O	0.00	0.01	0.02	0.02
MgO	0.02	0.05	0.06	0.09
Al ₂ O ₃	0.09	0.16	0.18	0.16
TiO ₂	0.00	0.01	0.01	0.01
SO ₃	0.18	0.18	0.18	0.18
B	0.06	0.11	0.18	0.4
Total impurities	0.49	0.71	0.85	1.17

5.4.1 pH Neutralization

In order to neutralize the acidity of the treated RHA silica contained from the leaching techniques discussed in chapter 4.5.1 - 4.5.5, the leachates were rinsed in 1000ml deionized water and filtered for batches A, B and C samples. The rinsing process was repeated until pH of water indicates 7 - 7.4. Figure 5.8 shows the pH of the rinse after each rinse for batch C. Data from other batches showed similar trends.

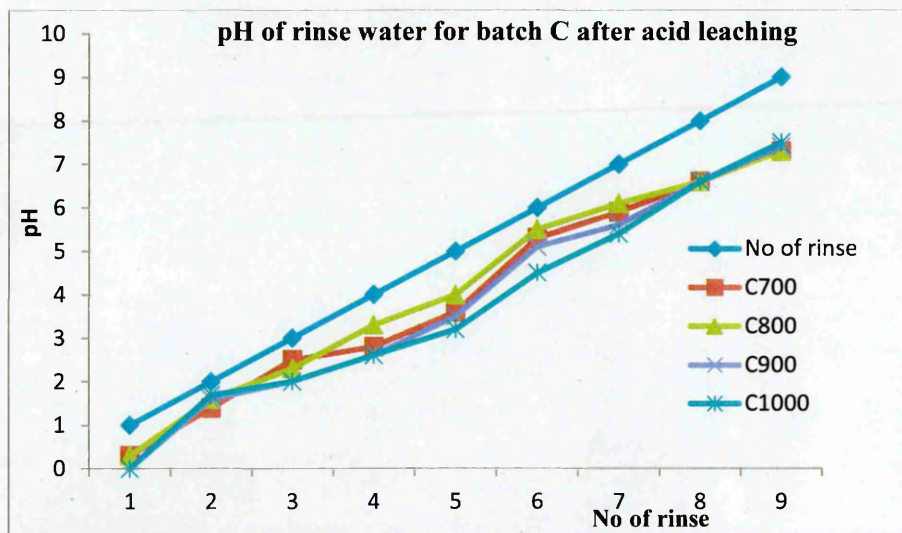


Figure 5.9: pH neutralization of batch C acid leached RHA

5.4.2 Effect of individual processing steps

The diffractograms in figures 5.10 - 5.13 show the effect of the different purification steps on the crystallinity of batch C samples. It was seen from the diffractograms that amorphous rice husk ash leached on hot plate with deionised water for 120 minutes through constant stir with a magnetic stirrer yield a spectrum with crystalline nature. In this respect, the presence of water or moisture makes structures of amorphous cellulose samples become unstable and usually later form partial crystalline material. Most cellulose materials like rice husk consist of crystalline and amorphous domains in varying proportions depending on source (Ciolacu et al, 2010). The physical properties, chemical behaviour and reactivity of contained cellulose strongly influences the arrangement of the molecules with respect to each other. The addition of nitric acid to the leachate was seen to increase the reflectivity of the chemically reactive RH silica ash at 700 and 800°C as well as boost the peaks intensity, especially the strongest peak.

The nitric acid seems not to have effect on the samples ashed at 1000°C nor change the phases of its original RHA or leached crystal phases.

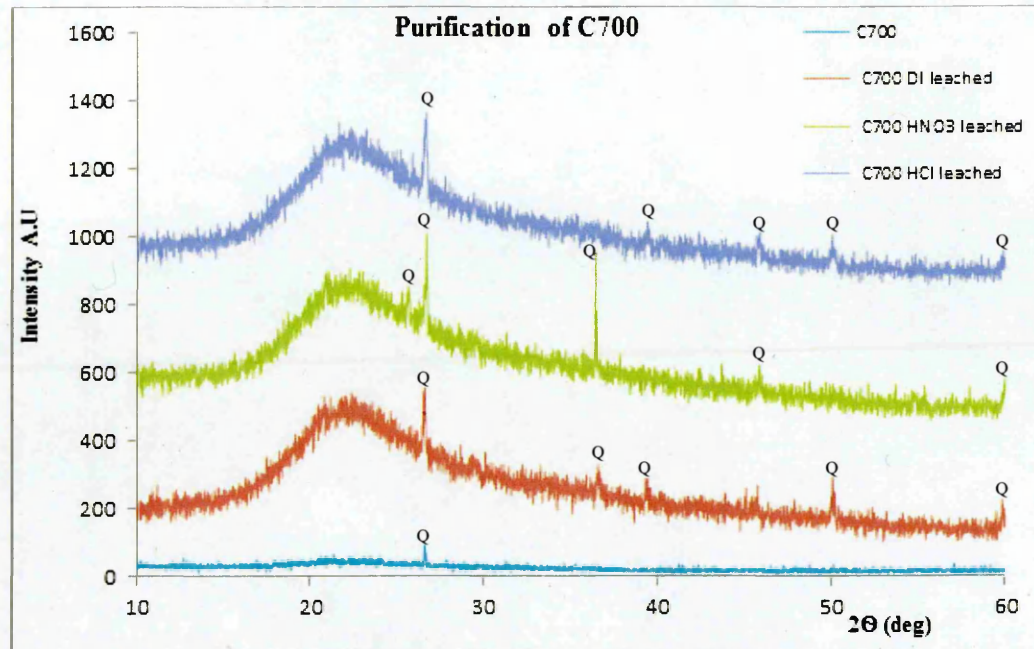


Figure 5.10: Offset XRD diffractograms of C700 during different steps of purification process. (symbol Q means peak position of quartz). ICSD reference code 01-083-2465 used

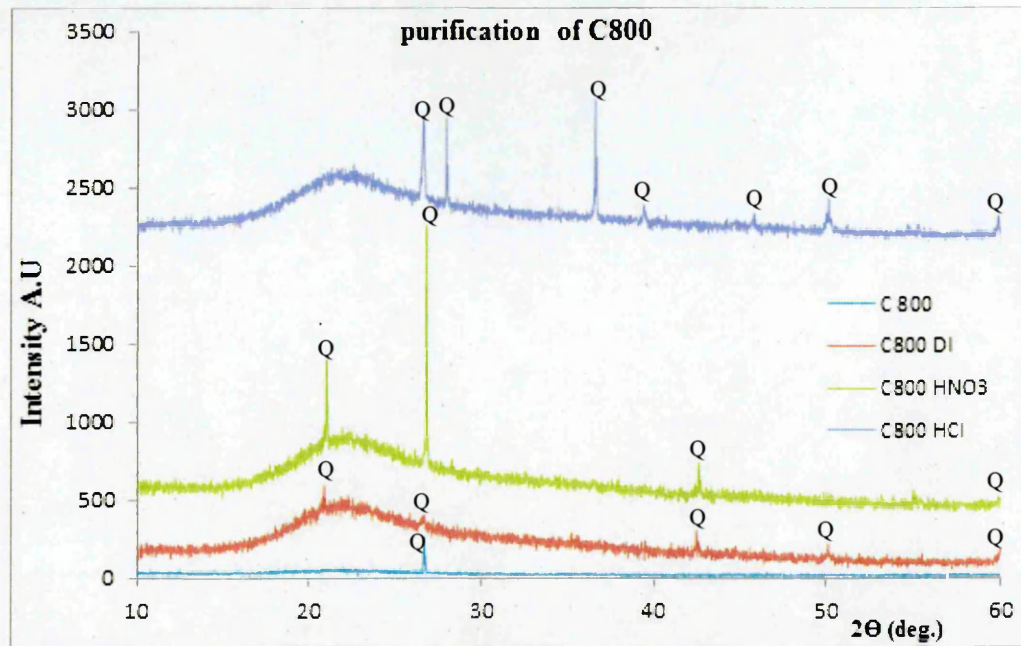


Figure 5.11: Offset XRD diffractograms of C800 during different steps of purification process. (Symbols Q mean peak positions of Quartz). ICSD reference code 01-033-1161 used.

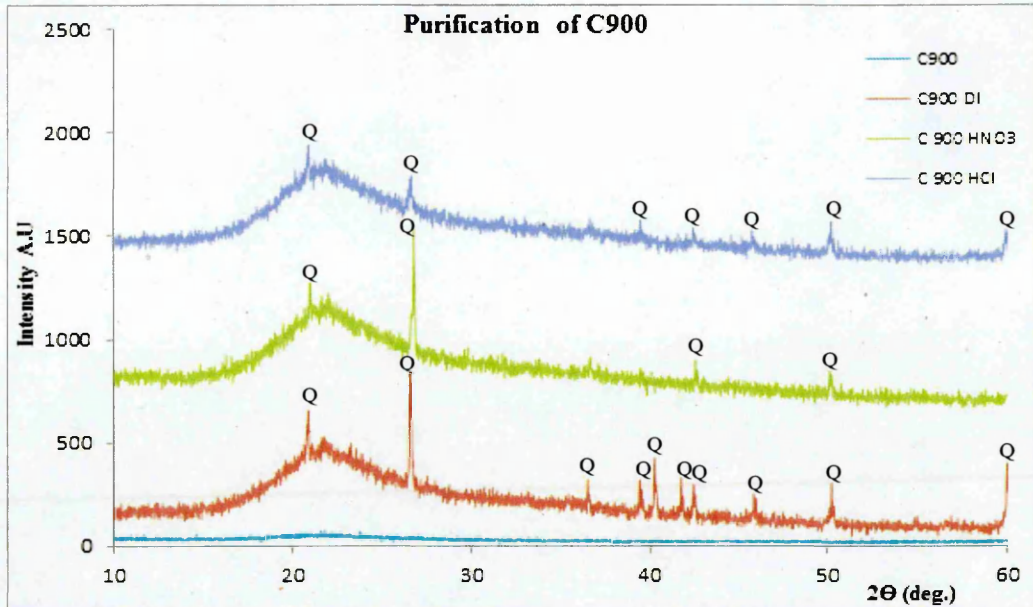


Figure 5.12: Offset XRD diffractograms of C900 during different steps of purification process. (Symbols Q and C means peak positions of Quartz and Cristobalite respectively). ICSD reference code 01-085-0335 used

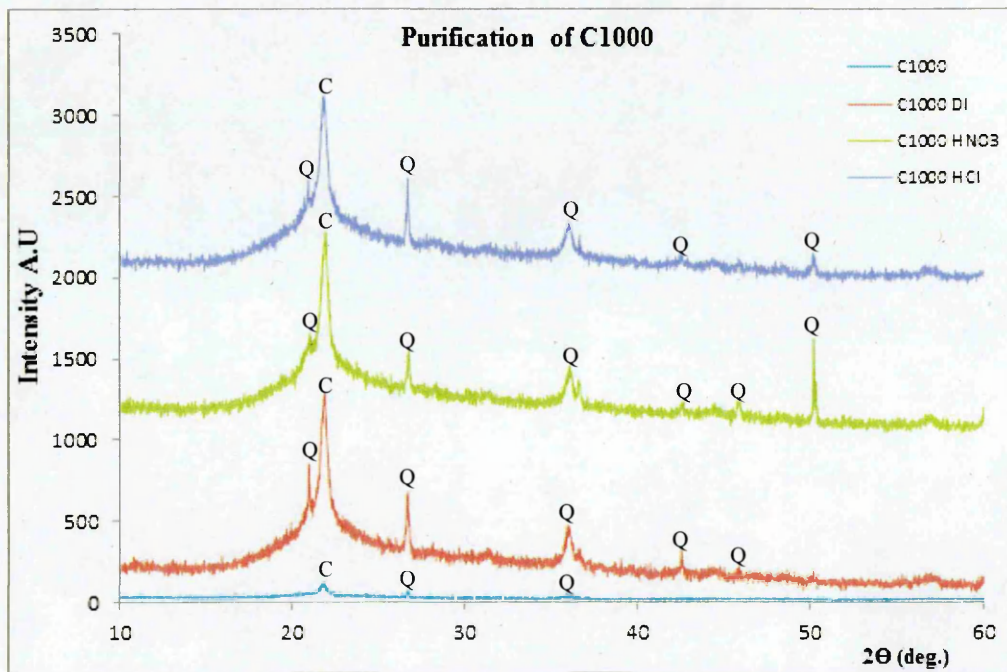


Figure 5.13: Offset XRD diffractograms of C1000 during different steps of purification process. (Symbols Q and C means peak positions of Quartz and Cristobalite respectively). ICSD reference code 01-085-0335 and 01-082-0512 used

5.4.3 Effect of leaching on RHA

The concentration of major metallic contaminants identified by XRF and ICP analysis are listed in tables 5.7, 5.8 and 5.9. The hydrometallurgical leaching for each step of purification process were also analysed using XRF and ICP. Batches B and C were plotted with the results presented in figure 5.14a-e as a fraction of the initial impurity level.

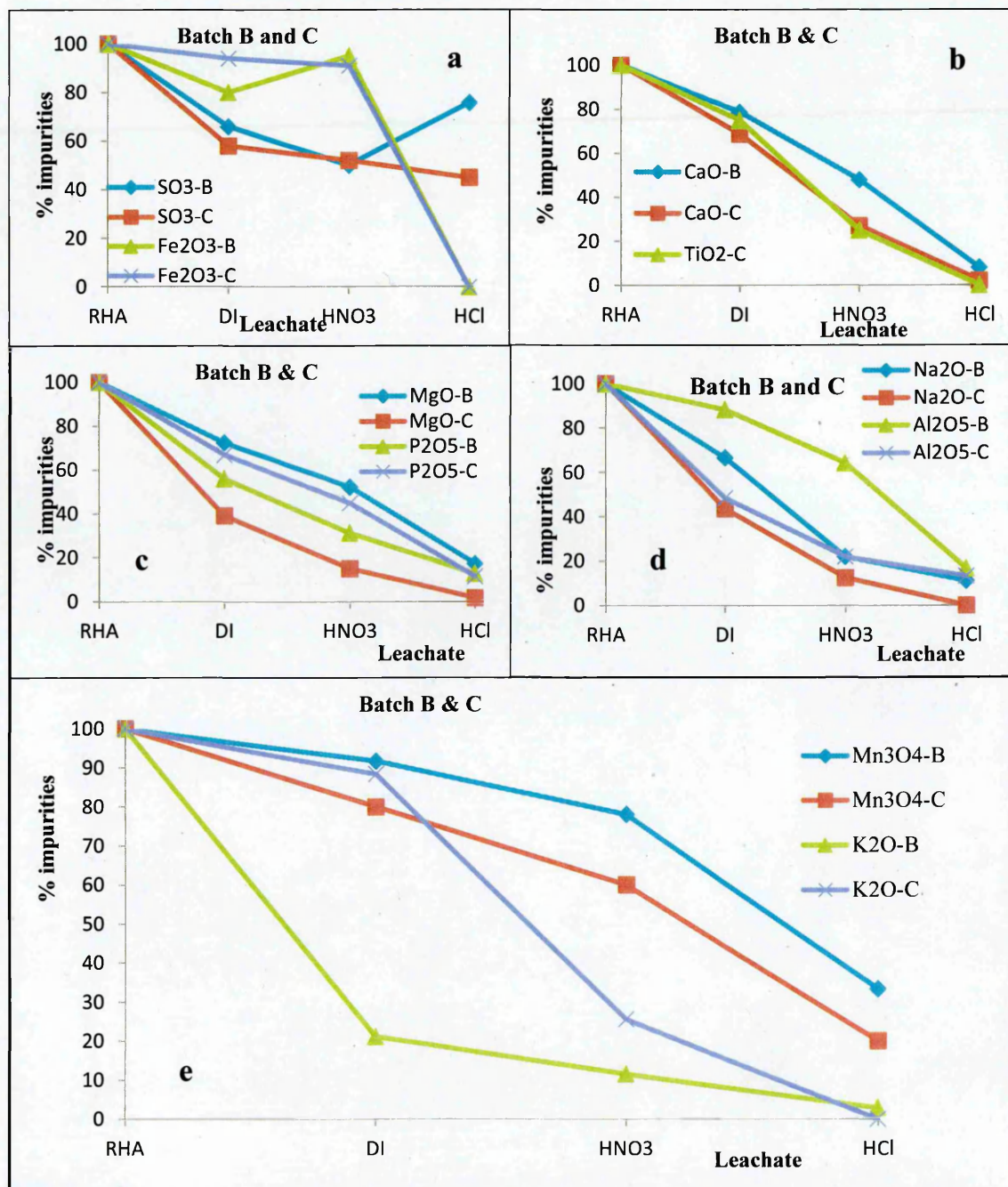


Figure 5.14: graphs of impurity content for each purification steps. (Symbols a, b, c, d and e represents graph of purification steps for SO₃-Fe₂O₃, CaO-TiO₂, MgO-P₂O₅, Na₂O-Al₂O₅ and Mn₃O₄-K₂O for batches B and C RHA respectively)

Figures 5.14a-e illustrate near total removal of some major impurities such as TiO_2 , Fe_2O_3 , K_2O , Na_2O , MgO and CaO . Between 80 and 90% of the P_2O_5 , Al_2O_3 and Mn_3O_4 were removed. The removal of SO_3 was least (55%) which might be detrimental to SoG silicon. Figure 5.15a-d illustrates the leaching steps and partial removal of boron (a dopant element) from batch B and C with high percentage purities as a result from treatment to rice husk ash. The removal of boron in figure 5.15a plotted graph shows the possibility that 79% elimination of boron is achievable from derived rice husk silica material for silicon preparation. Figure 5.15b plotted graph of rice husk ash at 800°C next RH ash at 700°C with 75% boron removal. The crystalline silica materials from rice husk ash at 900°C and 1000°C yield least purity of 70% and 73% for batch B and C as shown in figure 5.15c and 5.15d respectively.

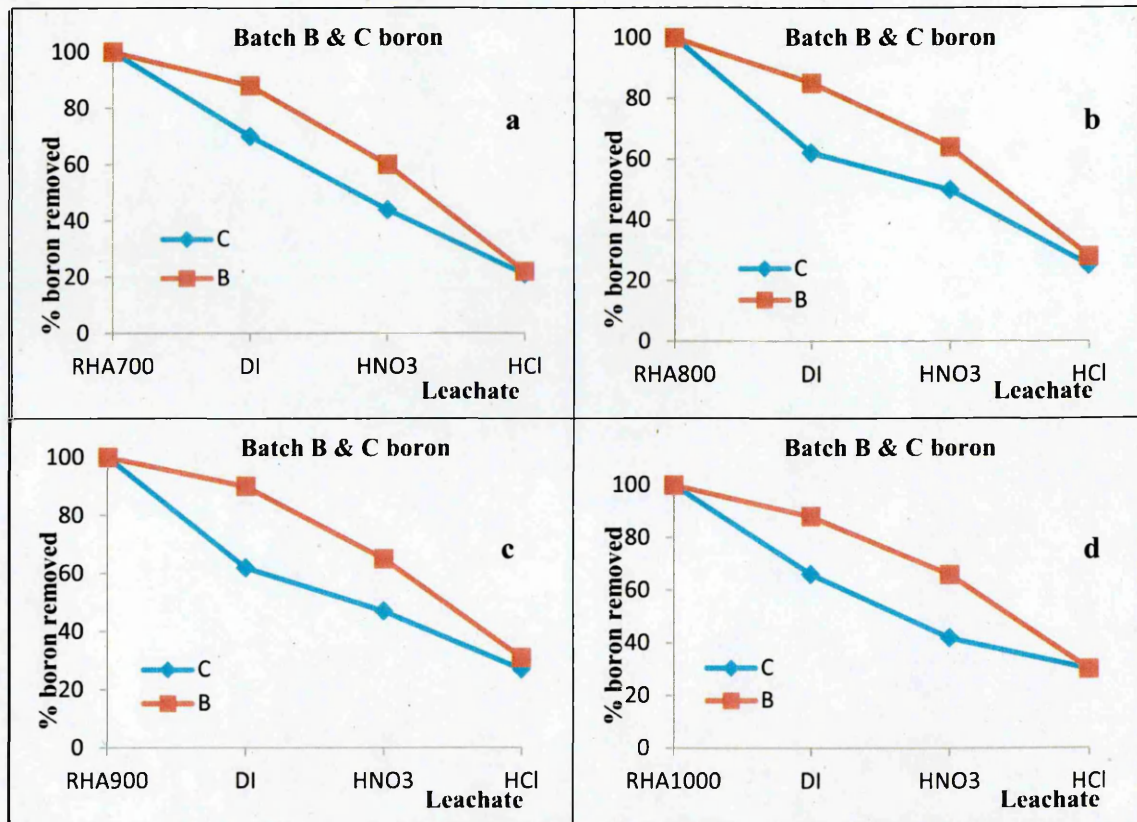


Figure 5.15: Graphs of boron impurity content at each leaching step normalised to initial boron concentration

Effect of each leaching processing steps on RHA purification

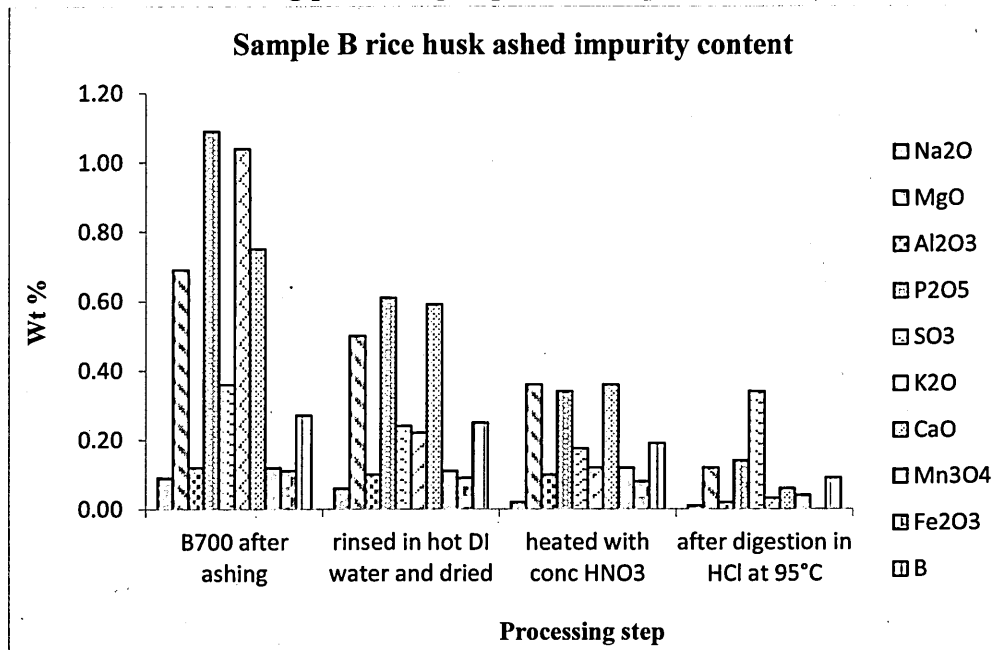


Figure 5.16: Effect of each processing step on the removal of impurities in batch B RHA as determined by X-ray Fluorescence analysis

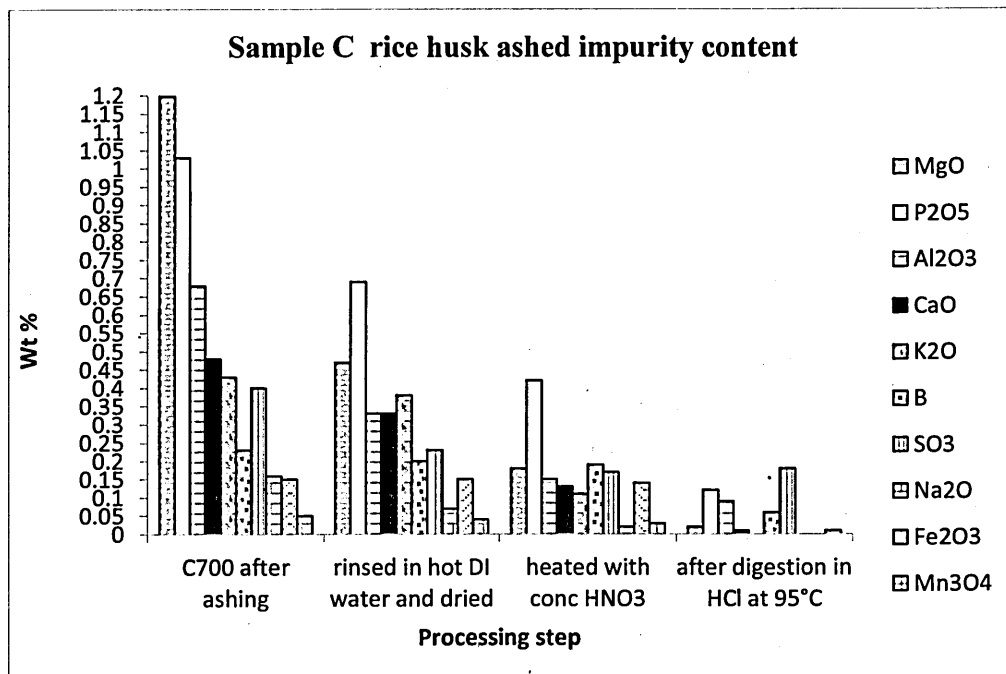


Figure 5.17: Effect of each processing step on the removal of impurities in batch C RHA as determined by X-ray Fluorescence analysis

It was seen that DI water heated at 95°C for an hour can remove up to 50% of Na₂O and K₂O impurity while this seems to have very small or no effect on removing Fe₂O₃. Thus, it implies Na₂O and K₂O are soluble in water. The

addition of 0.8ml conc HNO₃ to 11g dried RHA sample was to enable impurities not soluble in hot DI water but rather soluble in conc NHO₃ be removed after reheated at 700°C in furnace before re-leaching in HCl and then given repeated rinsing and then drying. The effect from analysis results of figure 5.16 and 5.17 shows that further reduction of impurities in almost all trace elements present was achievable. The RHA purification processes yield 99.18% and 99.51% of silica for batch B and C respectively. removal of many metallic trace impurities is significant: MgO (98.33%), Al₂O₃ (96.77%), Mn₃O₄ (80%), SO₃ (55%), CaO (97.92%), B (73.91%) and P₂O₅ (88.34%) are removed by leaching for batch C. Impurities such as Na₂O, Fe₂O₃ and K₂O are almost completely leached out beyond detection of the XRF as shown in figure 5.16 after the final processing step.

5.4.4 Effect of heat on mass of ash silica

Sample of RH ash at 700°C underwent thermogravimetric (TG) analysis using a TGA/DSC1 Gas Controller GC100 Mettler Toledo at a heating rate of 10°C/min up to 1000°C. The observed thermal behaviour of rice husk ash and leached rice husk ash during pyrolysis performance in argon atmosphere is shown in figure 5.18a-d.

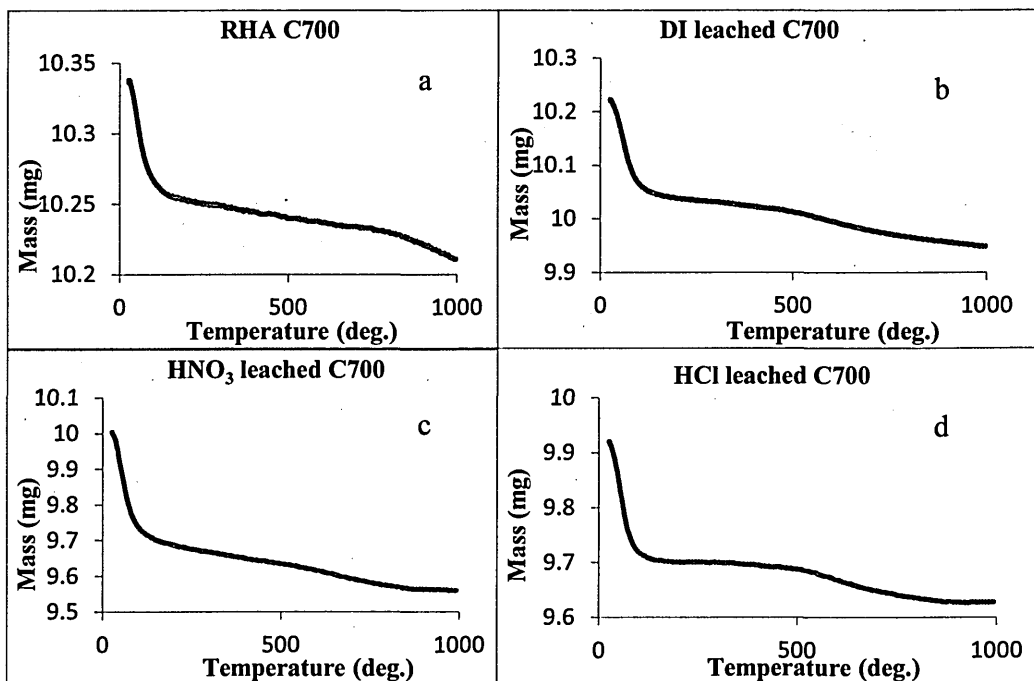


Figure 5.18: present residual unburnt carbon. a) C700 RHA. b) C700 leached RHA. c) C700 HNO₃ leached RHA and d) C700 HCl leached RHA

The plotted graphs for a, from investigation shows that the ashed silica still contains volatiles which constitute approximately 11.33% between 28°C and 115°C for unleached RHA, this volatiles reduces to 2.83% after using the leaching steps in figure b, c and d. Thus, the unburnt carbon component estimated as loss on ignition (LOI) for the unleached RHA was seen to have reduced farther by approximately 0.06mg during combustion between 500°C and 900°C as shown in b, c and d leaching process.

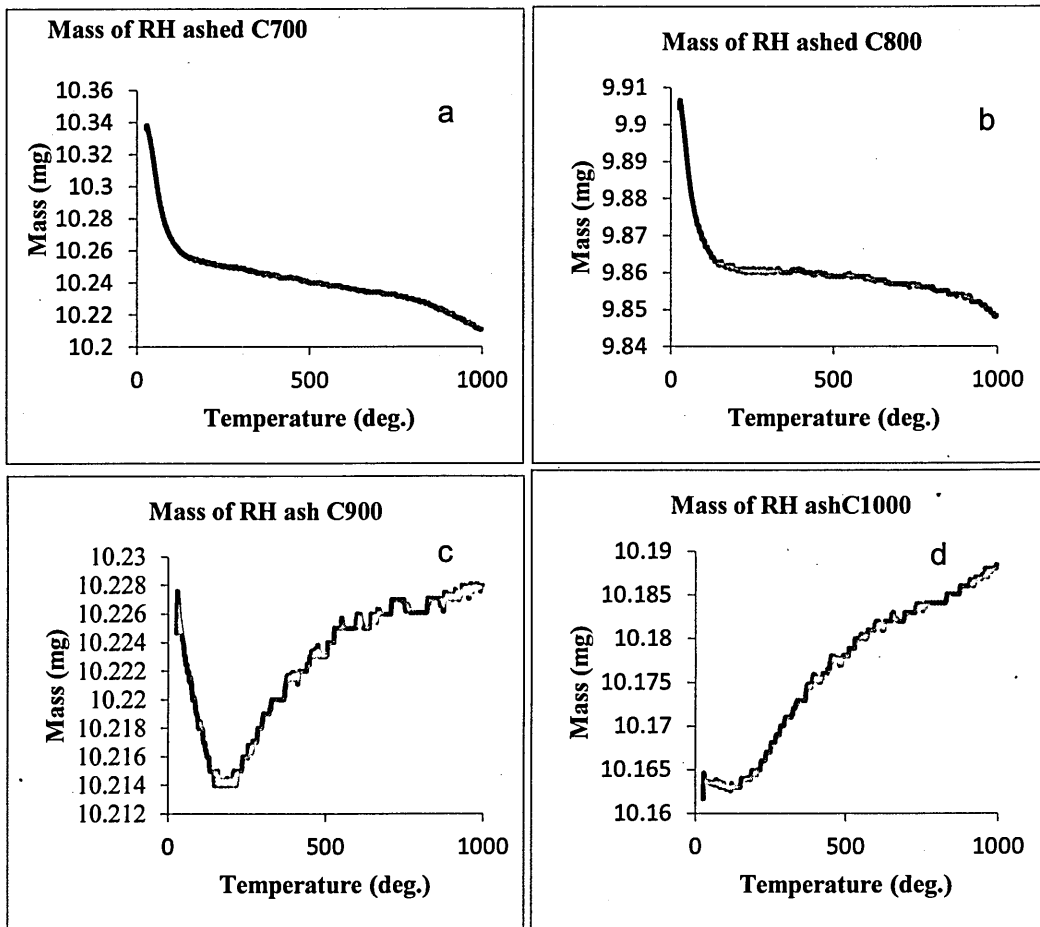


Figure 5.19: Present residual mass versus temperature after leaching. a) C700 is mass loss, devolatilization and slow combustion of RHA. b) C800 is mass loss, devolatilization and slow combustion of RHA. c) C900 is devolatilization and mass gain of RHA and d) C1000 is mass gain RHA.

The batch C RH ashed at 700, 800, 900 and 1000°C was pyrolyzed using the TG analysis at a heating rate of 10°C/min up to 1000°C as shown in figure 5.19a and 5.19b. It shows that the RH ashed at 700 and 800°C still possessed some volatile contents as well as unburnt carbon on reheating. At 900°C, figure 5.19c shows that at a temperature of 159°C pyrolysis, the mass of RH ash was observed to have released all volatile and the mass of RH silica increases by a very small

fraction. The RH ashed at 1000°C when pyrolyzed using TGA, was observed to have very little or no volatile released, before the mass of RH silica underwent slight increase of 0.025mg with temperature change. This change or increase in mass might be due to change in momentum of RHA particle with temperature rise. Thus, Temperature is found to influence the surface area or size of RHA silica as show in figure 5.20.

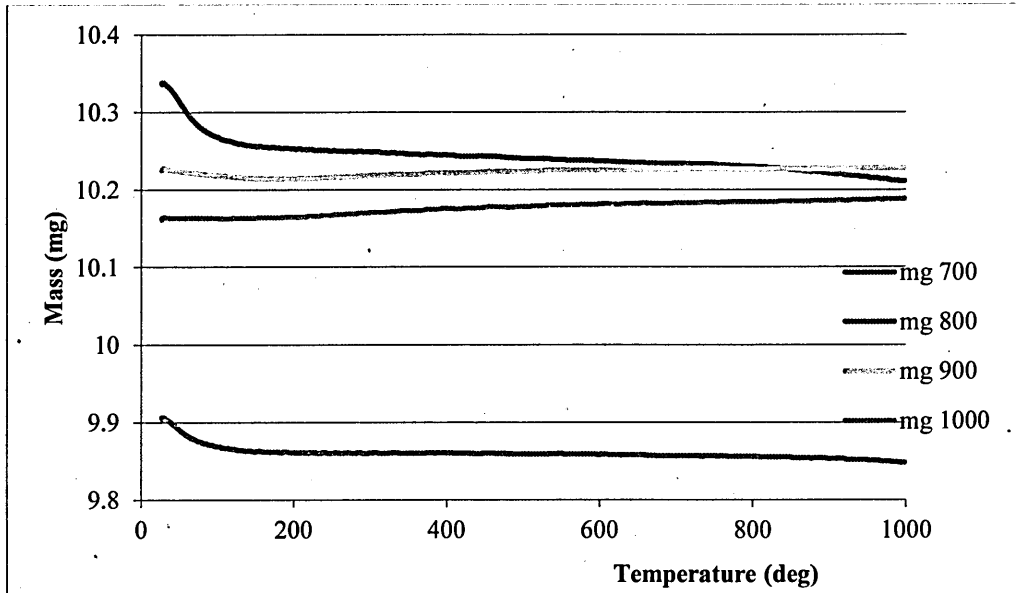


Figure 5.20: Present mass loss (removal of moisture), release of organic volatile matters (devolatilization), oxidation of fixed carbon (slow combustion) and mass gain

5.5 Summary

This chapter presented the source of utilised RH and discussed the physical and chemical compositions of the RHA contents obtained from analytical techniques such as XRD, XRF and ICP. Observed impurities in samples was purified and analysed to determine the effect of individual leaching steps on impurity removal. ATR-FTIR spectroscopy was used in this chapter to discuss effect of temperature on rice husk silica nature. Mass and LOI were also determined from TG analysis results.

6 METALLURGICAL GRADE SILICON (MG-Si) DERIVED FROM RHA

6.1 Processing and Pyroprocessing of MG-Si from RHA

The purified rice husk ash for batches A, B and C ashed at 700, 800, 900 and 1000°C after various solid-liquid extractions processes were dried in oven at 110°C for 2hrs before allowing to cool down for 24 hours. The batch A700 and B700 was reduced in air at Sheffield Hallam University while batch C samples were taken to Xera Carb for pyrolytic reduction with magnesium powder in an atmosphere controlled furnace. At Xera Carb, the RHA silica was pulverized and thoroughly mixed with magnesium powder in a mortar at a ratio of RHA: Mg (1.0g: 1.0g) to form mixture of magnesium and silica powder. 4.0g of each sample were transferred from the mortar to alumina crucibles for heating in an Ar gas electric furnace at a temperature of 800°C for 5 hours before cooling down to room temperature. The samples were removed from furnace and taken to the chemical laboratory in Sheffield Hallam University for hydrometallurgy treatment.

At this stage the samples are described as MG-Si.

6.2 Hydrometallurgy process of MG-Si

Two days later 3g of derived MG-Si from RHA was measured into a mortar and 0.4cm³ HNO₃ added and heated in a furnace at 300°C for 1hrs. It was allowed to cool down to room temperature before digested in 500ml of diluted 5M HCl in a conical flask, given rotation of 300rpm with magnetic stirrer for 2 hrs at 95°C on hotplate. The MG-Si was filtered and dried using the Whitman filter paper. 2g of digested sample was leached in hot DI water given rotation of 300rpm with magnetic stirrer for 1 hr at 85°C on hotplate, the residue from a Whitman filter paper was dried at 110°C for 1hr before rinsing in a conical flask containing 1000ml of DI water. The rinsing was done continuously for evening filtering until a pH of 6.5 was obtained. The elemental silicon residue from the final solution with pH 6.5 was dried at 110°C for 1 hr in an oven and then transferred to a desiccator to cool down for 72 hours before taken for analysis. The results from XRF, XRD, SEM, Raman, TEM, ICP-OES etc. are tabulated or presented below.

6.3 MG-Si derived from RHA Results and Discussions

Results reported below are limited to derived MG-Si from rice husk prepared at the Sheffield Hallam University, Sheffield, United Kingdom. The chemical composition of this MG-Si was analysed by XRF available at MERI, SHU and

ICP-OES at Element Materials private laboratory in Sheffield. These data are summarized in Tables 6.1, 6.2 and 6.3. The example actual experimental data print-out for batch C is given in appendix 2.

Table 6.1: Quantitative analysis of highest purity batch A700 derived MG-Si using X-ray fluorescence (XRF).

Elements	MG-Si _{A700} (wt %)
Si	98.45
Al	0.11
K	0.09
Ca	0.06
Ti	0.03
Fe	0.11
Cu	0.02
Mg	1.13
total impurity	1.55

Table 6.2: Quantitative analysis of highest purity batch B700 derived MG-Si using X-ray fluorescence (XRF) and Inductive couple plasma optical emission spectrometry (ICP-OES) technique

Elements	MG-Si _{B700} (wt %)
Si	98.66
Al	0.12
K	0.1
Ca	0.06
P	0.12
Fe	0.11
Cu	0.02
Mg	0.59
B	0.22 by ICP-OES
total impurity	1.34

The XRF analysis results for MG-Si derived from RHA batch A700 and B700 after leached are presented in table 6.1 and 6.2. The results indicate a Si yield of 98.45 and 98.66 wt % respectively, which is in agreement with the required value for metallurgical-grade silicon (Pizzini, 1982). Looking at the impurities detected in batch A, Al, K, Ca, Ti, Fe, Cu and Mg were observed using XRF. B is too light for detection with this technique. Apart from P and B which are dopant elements and are difficult to remove, the high amount of Al and Mg are due to Al

introduction into the sample from alumina crucible during heating and reacting of Si with excess of Mg during reduction process respectively. Table 6.3 showed XRF and ICP extracted results from appendix 2, represented as batch C MG-Si derived from RH ashed at 700, 800, 900 and 1000°C with the last column showing results for commercial grade silicon (Si_{com}) powder of ~325 mesh particle size purchase from Sigma Aldrich, UK. The results indicate that all derived silicon are metallurgical-grade. None of the RHA derived material reached the purity of Si_{com} (99.72 wt %). The MG- $\text{Si}_{\text{C}700}$ derived silicon has highest purity of 98.82 wt %, followed in ascending order of temperature by MG- $\text{Si}_{\text{C}800}$ with 98.77 wt %, next by MG- $\text{Si}_{\text{C}900}$ with 98.64 wt % and the least MG- $\text{Si}_{\text{C}1000}$ with 98.63 wt %. The major impurities are Na, Mg, Al, Cl, Fe and B. It was observed that P for all batches C MG-Si was reduced below the detection limit of XRF except for MG- $\text{Si}_{\text{C}800}$ with 0.01 wt %. S was not detected. The high value of Al, Mg and Cl are due to used alumina crucible, excess Mg during silica reduction and HCl leaching process respectively.

Table 6.3: Batch C Quantitative analysis of all obtained elements in MG-Si derived from C700, C800, C900 and C1000 using X-ray fluorescence (XRF) and Inductive couple plasma optical emission spectrometry (ICP-OES) techniques for B only

Element (%)	MG- $\text{Si}_{\text{C}700}$	MG- $\text{Si}_{\text{C}800}$	MG- $\text{Si}_{\text{C}900}$	MG- $\text{Si}_{\text{C}1000}$	MG- Si_{com}
Si	98.82	98.77	98.64	98.63	99.72
Na	0.2	0.18	0.29	0.22	0.09
Mg	0.29	0.26	0.21	0.31	ND
Al	0.23	0.15	0.24	0.16	ND
P	ND	0.01	ND	ND	ND
S	ND	ND	ND	ND	ND
Cl	0.17	0.28	0.22	0.33	0.07
Fe	0.07	0.1	0.1	0.08	0.02
B	0.22	0.25	0.3	0.27	0.1
total impurity	1.18	1.23	1.36	1.37	0.28

ND: not detected

6.3.1 Qualitative analysis of derived MG-Si from RHA and Commercial grade Si using X-ray diffraction (XRD)

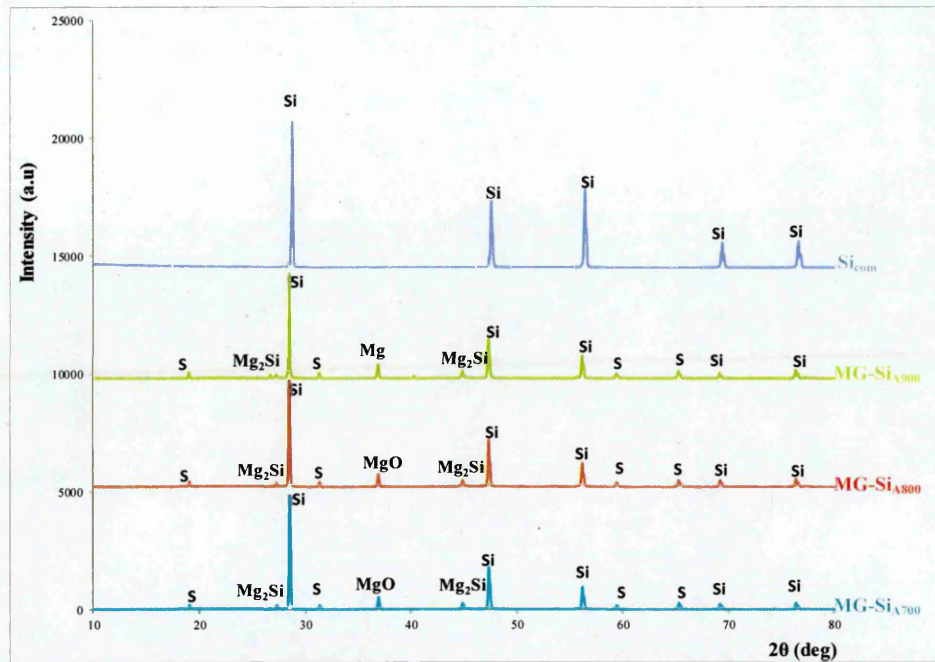


Figure 6.1: Offset X-Ray diffractograms for batch A RHA reduced with magnesium and a commercial grade Si (symbols Si, Mg₂Si, MgO and S: Peak positions of silicon, silicide, Magnesium oxide and spinel respectively).

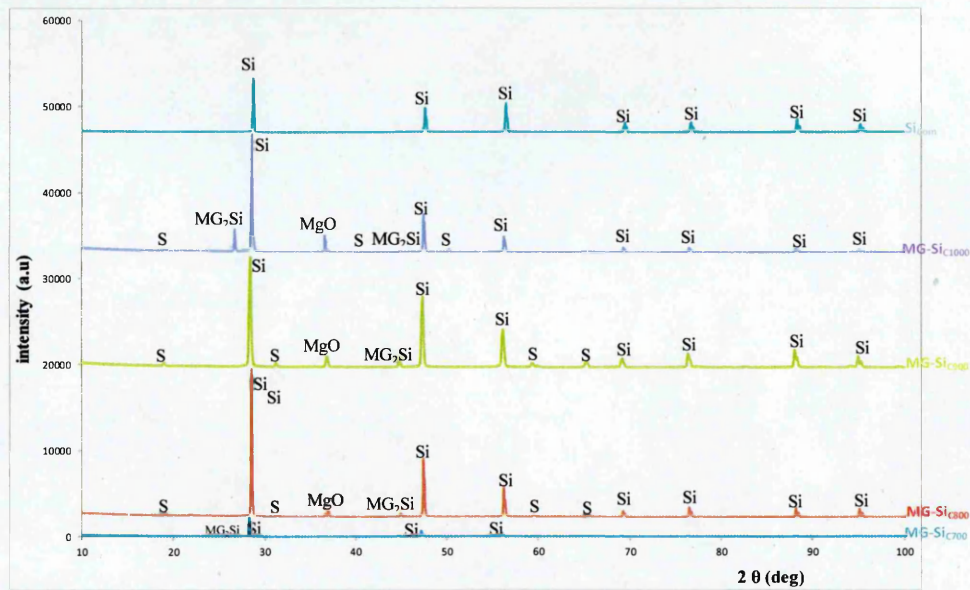


Figure 6.2: Offset X-Ray diffractograms for batch C RHA reduced with magnesium and a commercial grade MG-Si (symbols Si, Mg₂Si, MgO and S: Peak positions of silicon, silicide, Magnesium oxide and spinel respectively).

The XRD pattern in figure 6.1 and 6.2 showed the typical phases identified in the MG-Si derived from metalloceramic process of rice husk silica reduced with magnesium powder and some by-products other than silicon. The reaction products observed apart from silicon are magnesium silicide (Mg_2Si) and spinel ($MgAl_2O_4$). These by-products irrespective of their amounts presented in the phases of diffractogram spectra have detrimental effect on silicon yield. Grinding of RHA before reduction and acid leaching, increase the exposed surface of derived RHA MG-Si. This help in enhancing material purification.

6.3.2 Qualitative analysis of derived MG-Si for B1000 using transmission electron microscopy (TEM)

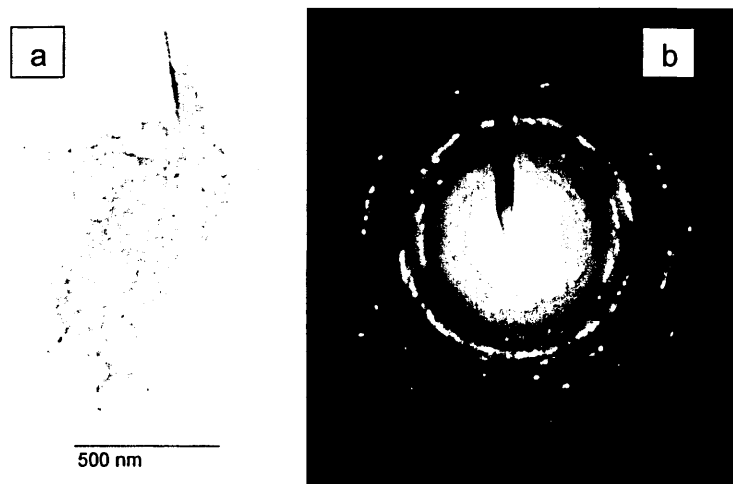


Figure 6.3: (a) Bright-field TEM micrograph of a particle of RHA-derived silicon. (b) Ring diffraction pattern obtained from selected area of particles of RHA-derived silicon

The micrograph of figure 6.3a shows that the RHA MG-Si is in agglomerate of tiny flakes up to $0.5\mu m$ in diameter. The ring diffraction from figure 6.3b shows that the RHA MG-Si consists of fine polycrystalline material with no obvious texture. Some of the crystallites within the RHA MG-Si are as small as 20nm in diameter, which is in agreement with the calculated results in appendix 3a-e that showed nano-particle sizes of RHA-derived Si for batch C using Scherrer's formula to evaluate their XRD parameters.

6.3.3 Morphology of MG-Si from RHA

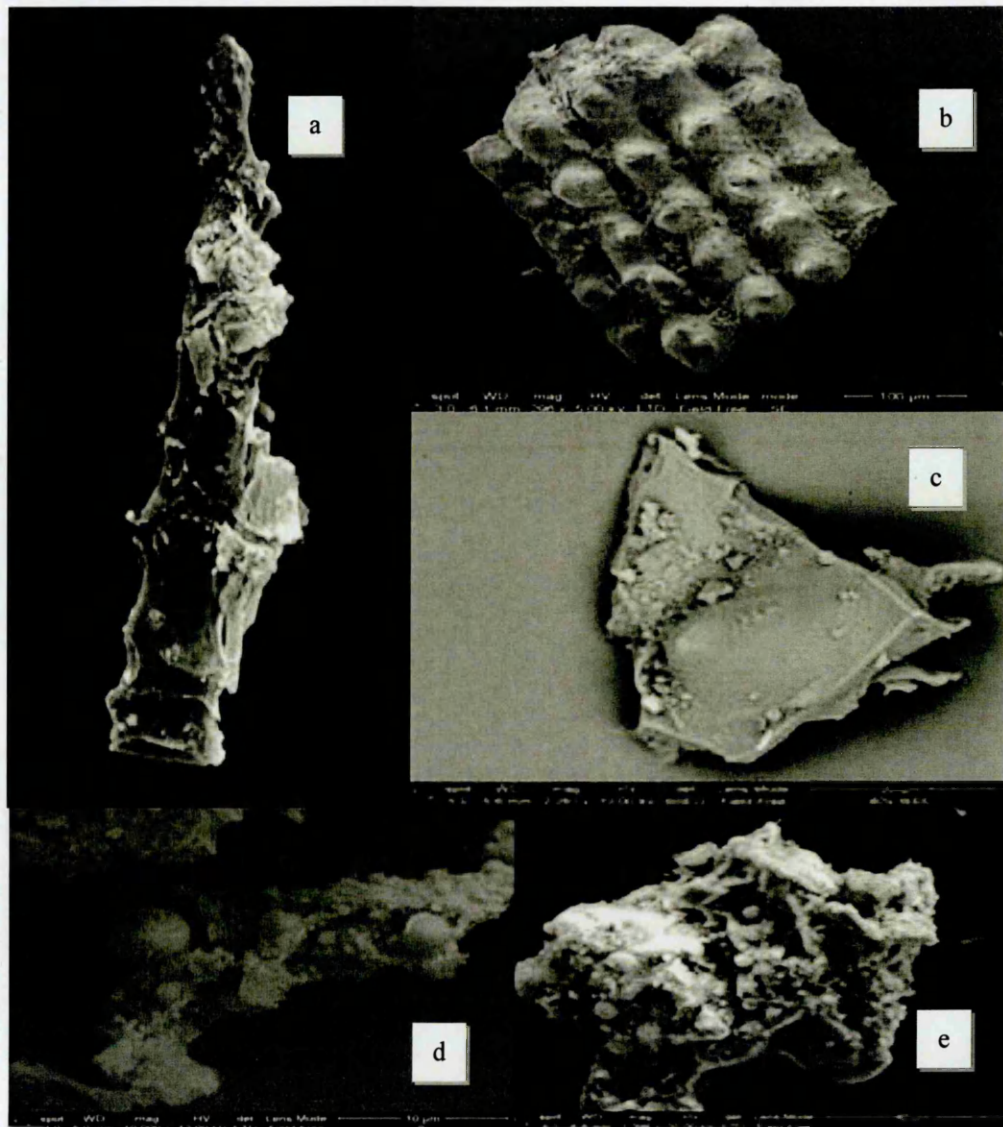


Figure 6.4: Micrographs of the outer and inner surfaces of MG-Si from RHA. (a) Finger-like shape MG-Si with asperities and cracks. (b) Corrugated outer epidemic of MG-Si with asperities. (c) A thick skin-like outer surface of MG-Si with deposit of leached off debris. (d) & (e) Aggregated, multiphase MG-Si particle.

The micrographs of figure 6.4 show that the roughness of outer and inner surface of batch C700 have undergone no significant change during the reduction process. The slight change that occurred is due to RHA pulverization, reduction to silicon and HCl acid digestion treatment that increased the brittleness and weaken the particle, thereby causing wearing of asperities on the outer particle surface as well as cracking presented in the micrographs a, b and d. Figure c and e showed that the derived MG-Si had due to combustion and reaction aggregated, multiphase

and develop relatively small-size particle. The micrograph c and e are similar morphology for C700 and C800 respectively.

6.3.4 X-ray Mapping using Energy Dispersive X-ray Spectrometer (EDS) of MG-Si

In order to understand the spatial distribution of specific elements in batch B and C of derived MG-Si, the micrographs presented in figure 6.5(a) → 6.9(a) are results to show that energy dispersive x-ray spectroscopy was used to generate composition maps for Mg, Si, Al and O using K_{a1} lines, these maps are illustrated in figure 6.5(b) →e for B700 and 6.6(b) →d for C700 to C1000 respectively.

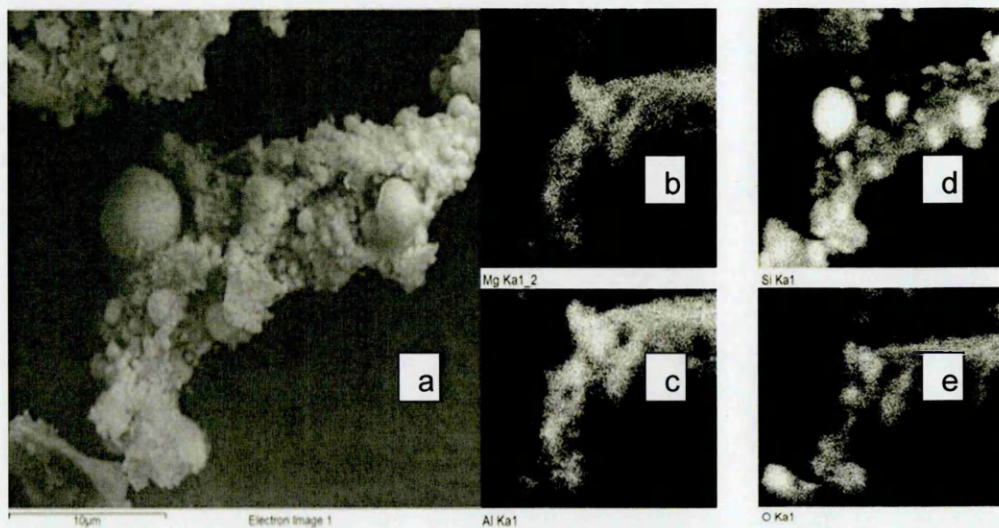


Figure 6.5: X-ray mapping of B700 MG-Si. (a) EDS micrograph of Si sample derived from RHA. (b) Mg mapping of Si sample. (c) Si mapping of Si sample. (d) Al mapping of Si sample. (e) O mapping of Si sample.

the EDS analysis of derived MG-Si for batch C700 →C1000 confirmed the present of Al and Mg impurities in all samples of batch C MG-Si. Hu et al (2013) reported that Al, Mg, Ca and P impurities were detected in the microstructure phase of their refined silicon after their refining process and that P was removed in the microstructure phase after the refined work. The EDS results of this work further confirmed XRF non detection of P in all batch C derived silicon. Zhao et al (2011) reported that MG-Si impurities P and B are solidly dissolved inside the Si matrix and even when crushed and acid leached, P cannot be removed except by solvent refining and B is too light to be detected by XRF. So, I have mainly concentrated on P within the refining process. Contrary to Zhao et al (2011), none

of the EDS mapping impurity phase or analysis spectra for B700 or C700 →1000 showed the presence of P in this work. This indicate that P impurity in MG-Si derived from rice husk ash can be removed beyond SEM and EDS detection limit.

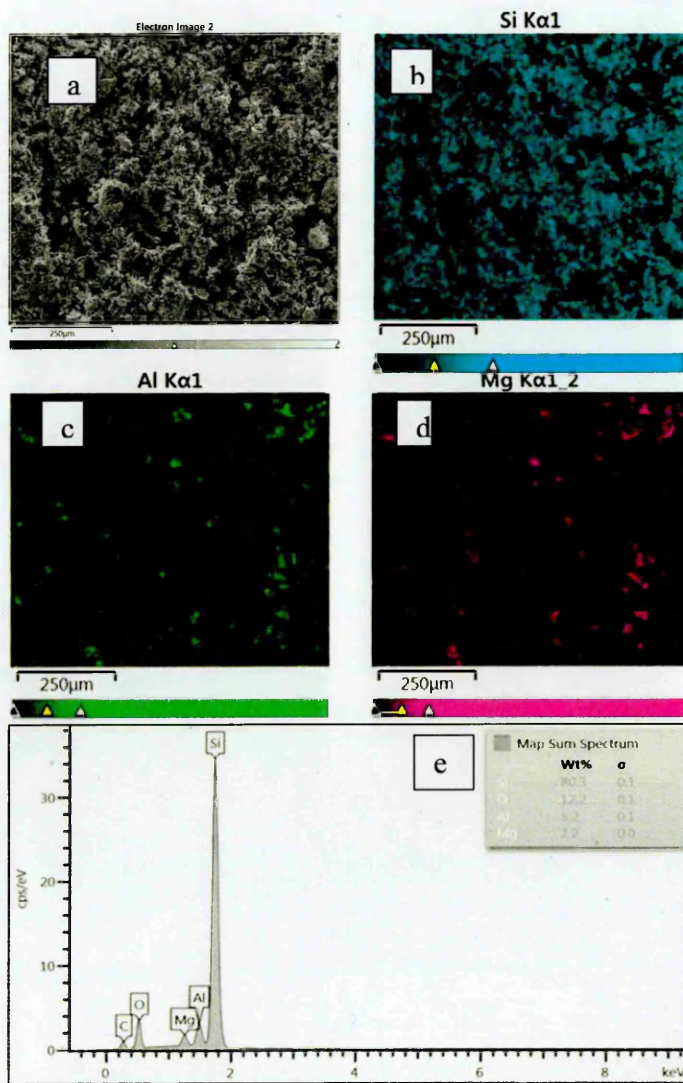


Figure 6.6: X-ray mapping of an impurity phase in batch C700 derived MG-Si (a, b, c and d) and EDS analysis e

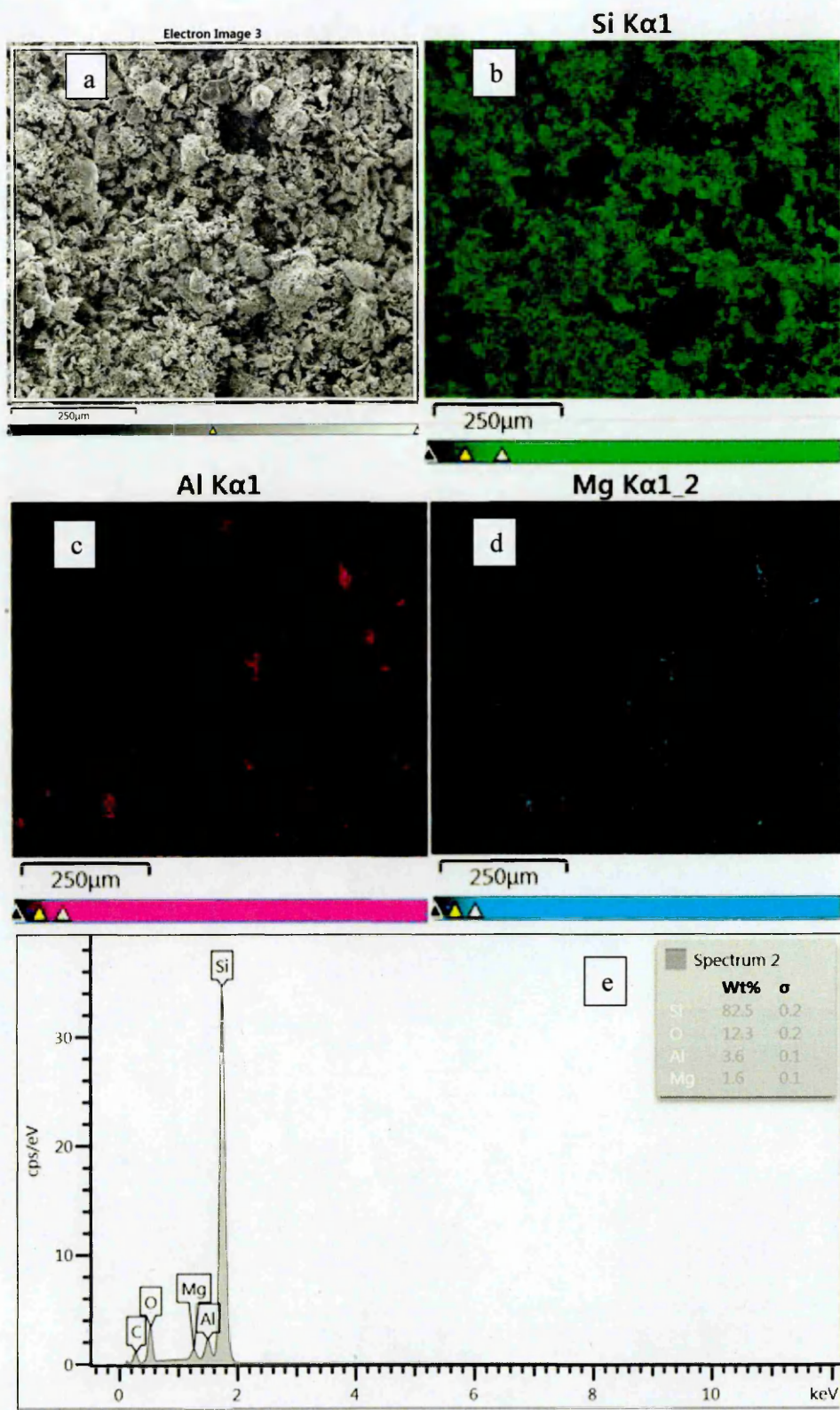


Figure 6.7: X-ray mapping of an impurity phase in batch C800 derived MG-Si (a, b, c and d) and EDS analysis e

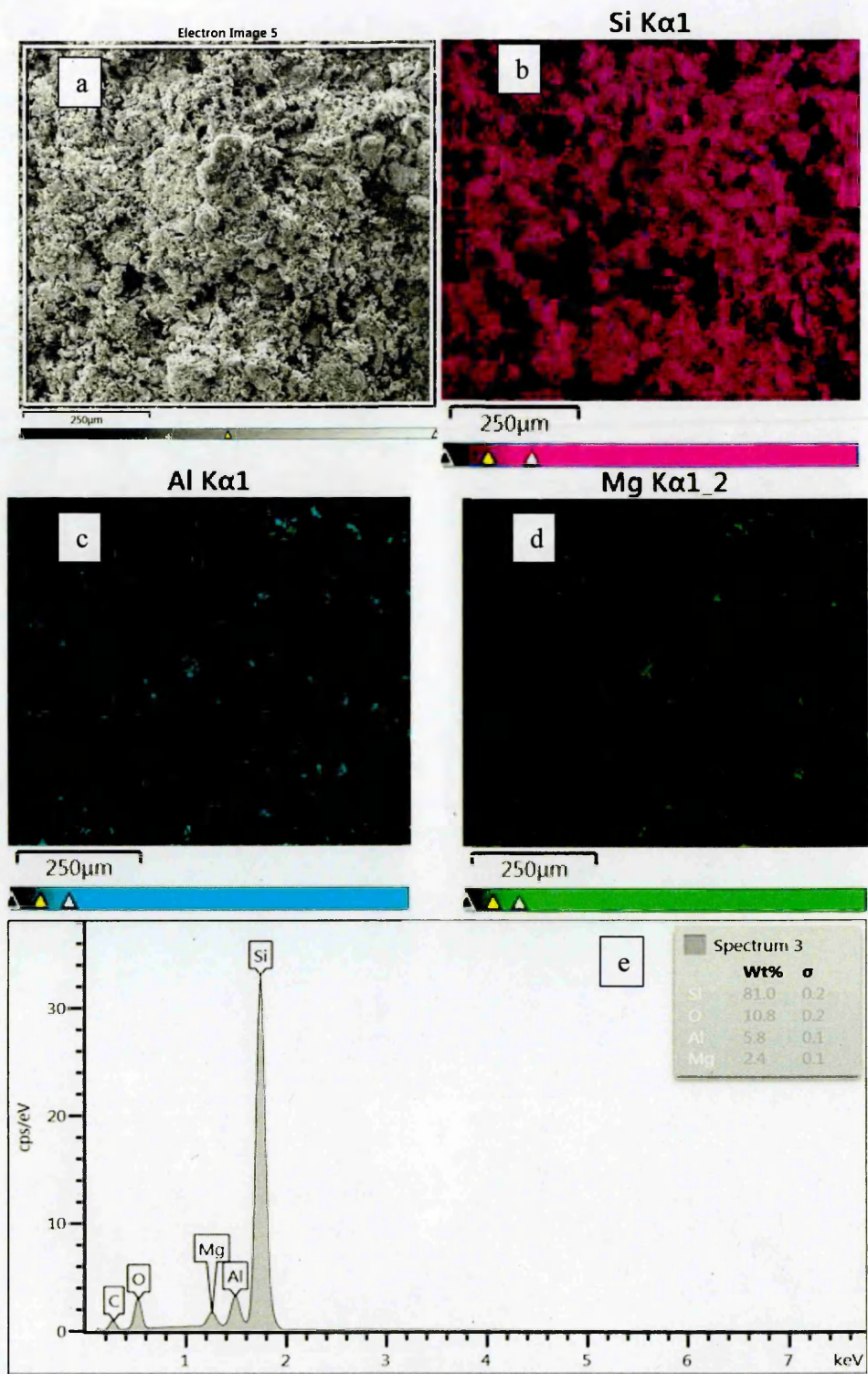


Figure 6.8: X-ray mapping of an impurity phase in batch C900 derived MG-Si (a, b, c and d) and EDS analysis e.

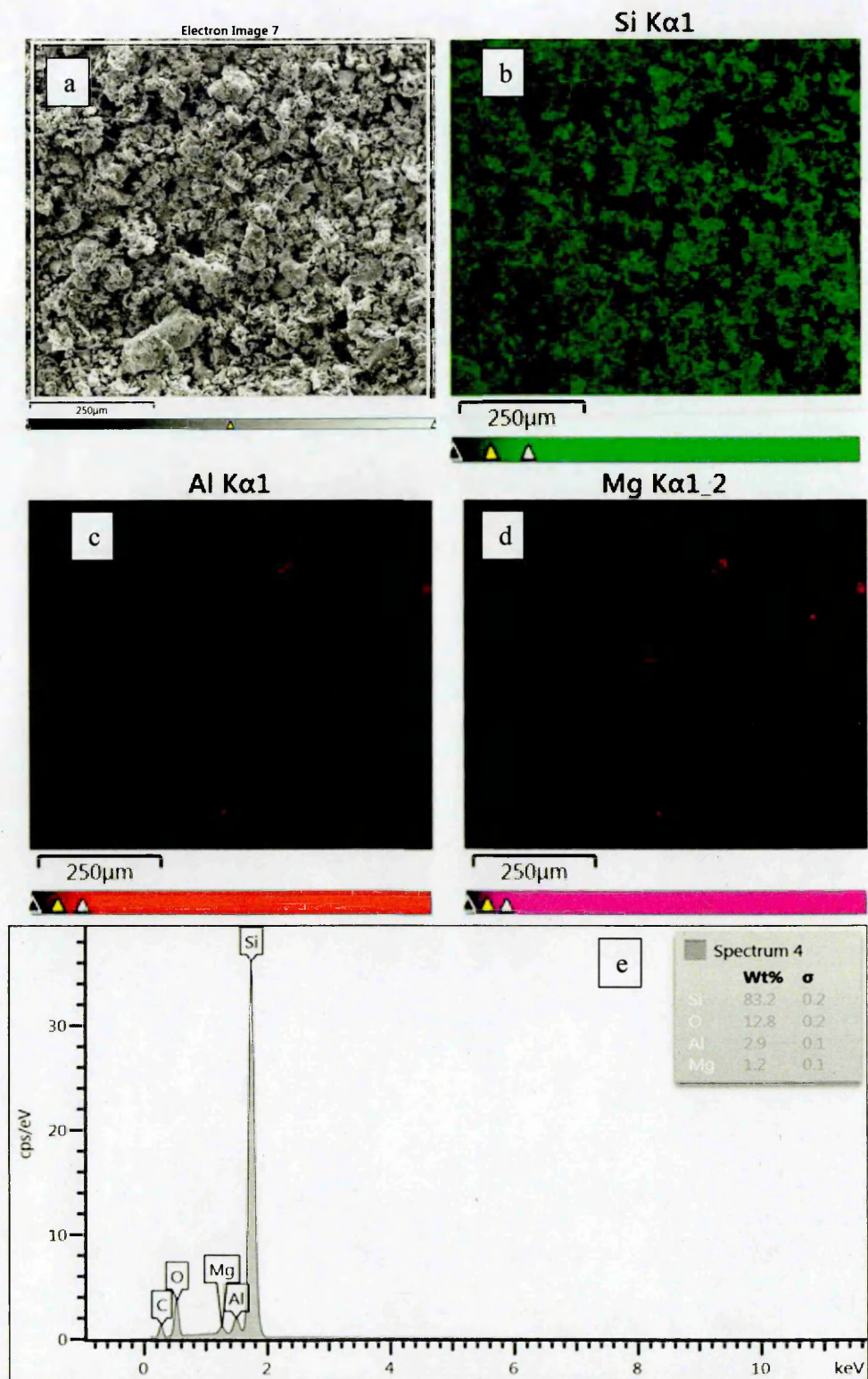


Figure 6.9: X-ray mapping of an impurity phase in batch C1000 derived MG-Si (a, b, c and d) and EDS analysis e.

6.3.5 Thermal effect on MG-Si

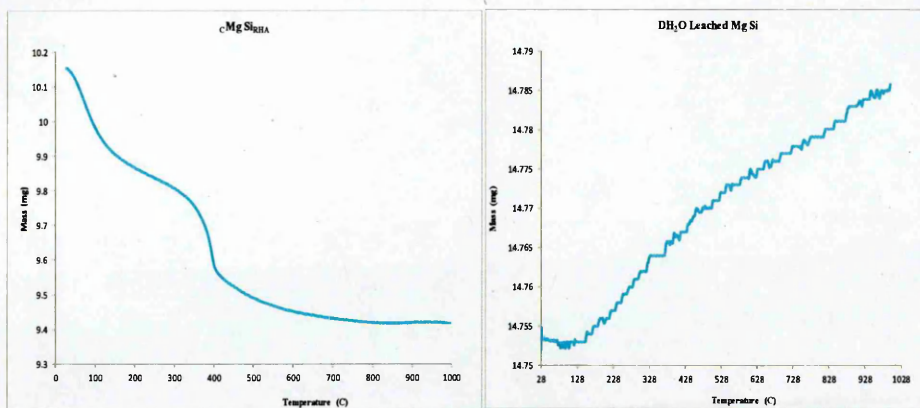


Figure 6.10: Present derived MG-Si residual mass versus temperature. (left) mass loss and devolatilization of MG-Si. (right) Slow combustion and mass gain

The observed thermal behaviour of derived MG-Si for C700 leached and pyrolysed under argon atmosphere of TG instrument. The results shown in figure 6.10 represent the plotted graphs for the MG-Si and its leached and dried product. The graph on the left showed that the MG-Si contains volatiles and moisture which constitute approximately 0.74mg. However, the volatiles and moisture tends to reduce to 0 after all applied leaching steps. Thus, the leached MG-Si graph on the right showed very little or no farther reduction between room temperature and 148°C. Thereafter, an increase in mass of the Si by approximately 0.03mg during combustion between 148°C and 1000°C.

6.3.6 Particle size effect on MG-Si

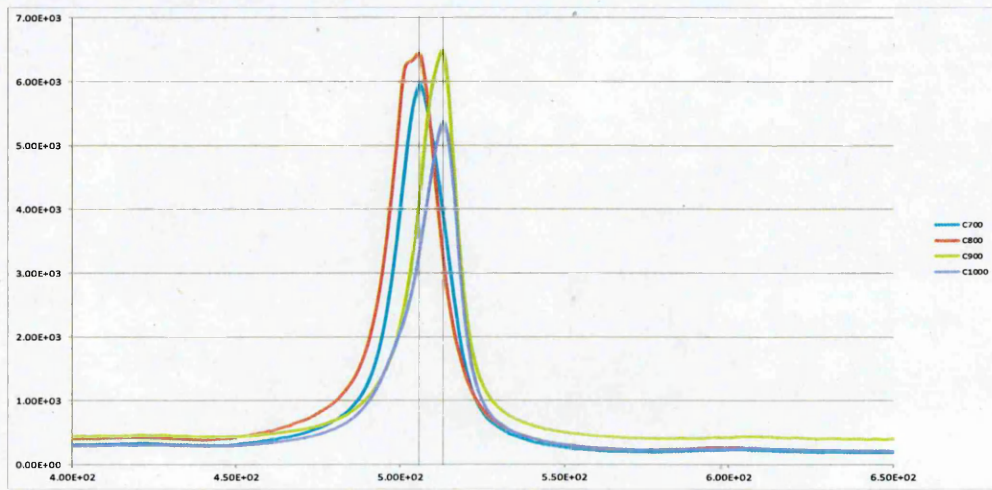


Figure 6.11: Raman spectra of polycrystalline silicon derived from RHA batch C at different temperature. Using laser power of 5mW and wavelength of 532nm

The figure 6.11 show a set of representative Raman spectra run under same conditions for all samples of batch C silicon produced under different temperature. The Raman instrument used is Thermo Scientific, DXR2 Raman Microscope, USA product. It was observed that C700 and C800 silicon powder shift farther away from the frequency of single crystal silicon value 520 cm^{-1} toward amorphous silicon of lower frequency value 480 cm^{-1} and become more broaden than the crystalline silicon. The line that passes through C700 and C800 of the spectra peak occurs at frequency value 505 cm^{-1} indicating C900 and C1000 with frequency value 513.5 are more crystalline in nature then the latter. The downshift of frequency and spectral broadening are indicative of small crystallite size smaller than $\sim 300\text{ \AA}$. These observations are in agreement with those made by Campbell and fauchet (1986), Iqbal et al (1981).

6.4 Refined silicon composition

The concentration of different impurities in ground refined Si-Sn powder and centrifuged sample was analyzed with SEM and EDS. The result for the ground refined Si-Sn powder showed in figure 6.12 and 6.13 indicate the present of Sn in the alloyed powder sample whereas, the result of centrifuged alloyed powder presented in figure 6.14 and 6.15 indicated that Si was successfully separated from Sn

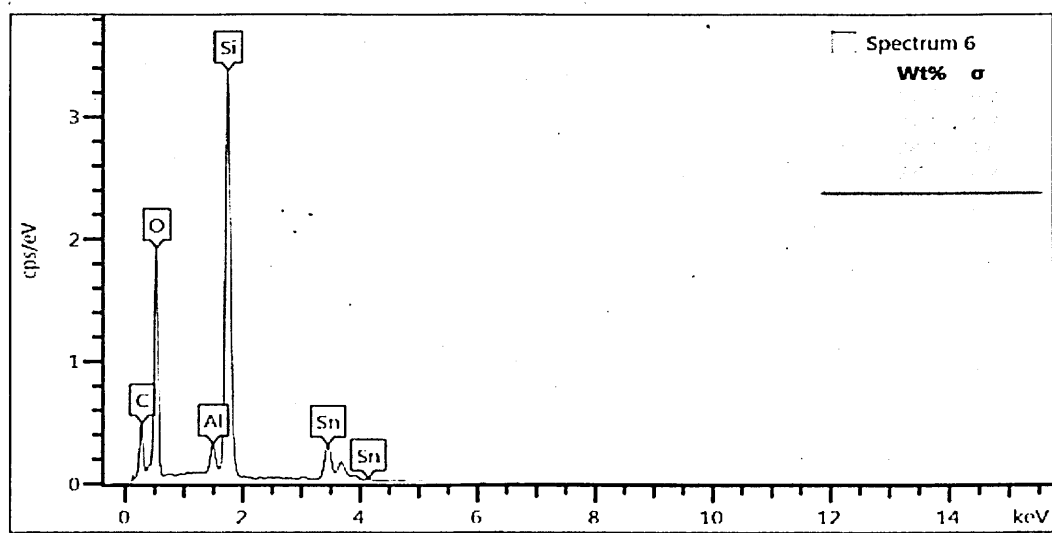


Figure 6.12: The EDS analysis of impurities in Si-Sn refined alloy powder.

Electron Image 11

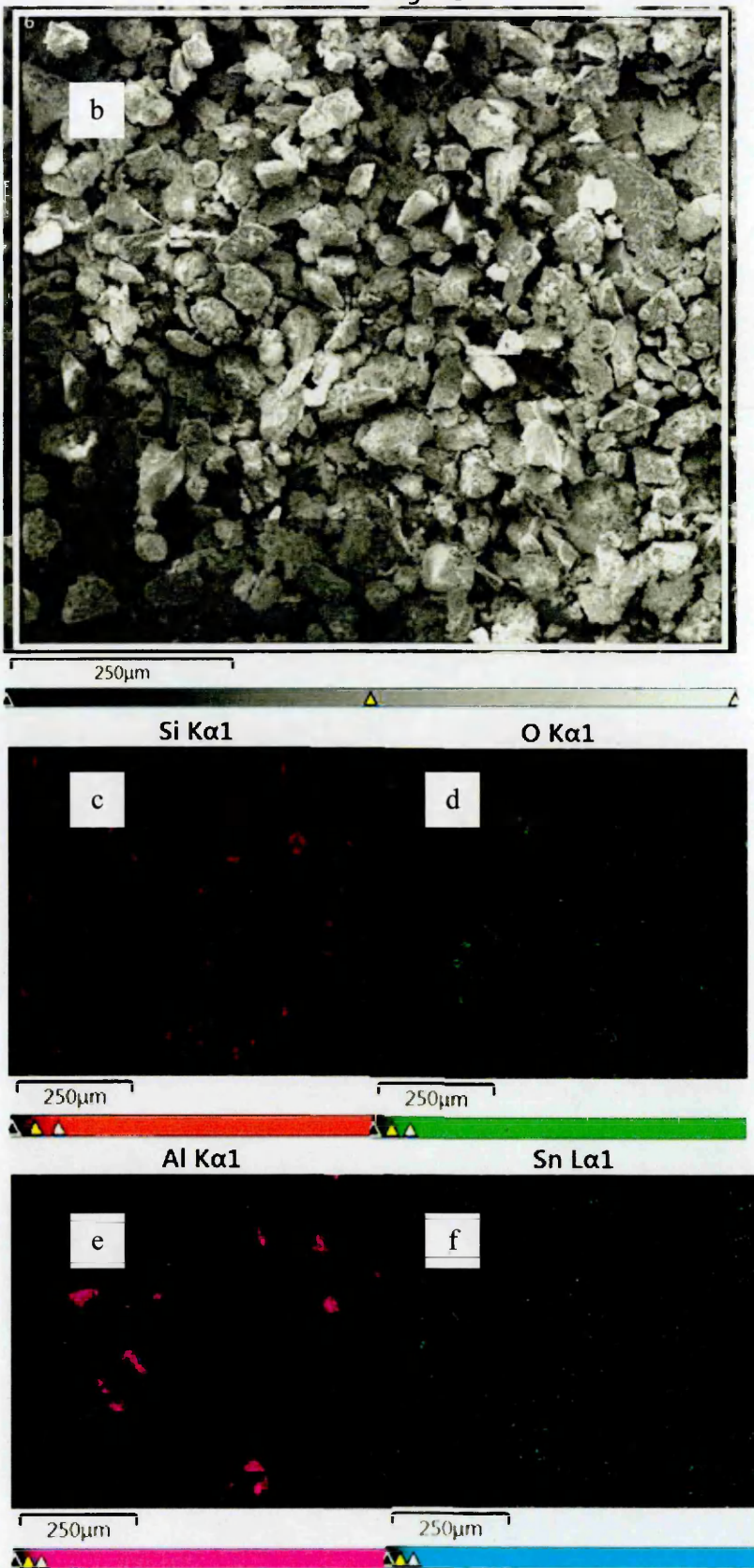


Figure 6.13: The microstructure of impurity phases in refined Si-Sn alloyed powder

Electron Image 9

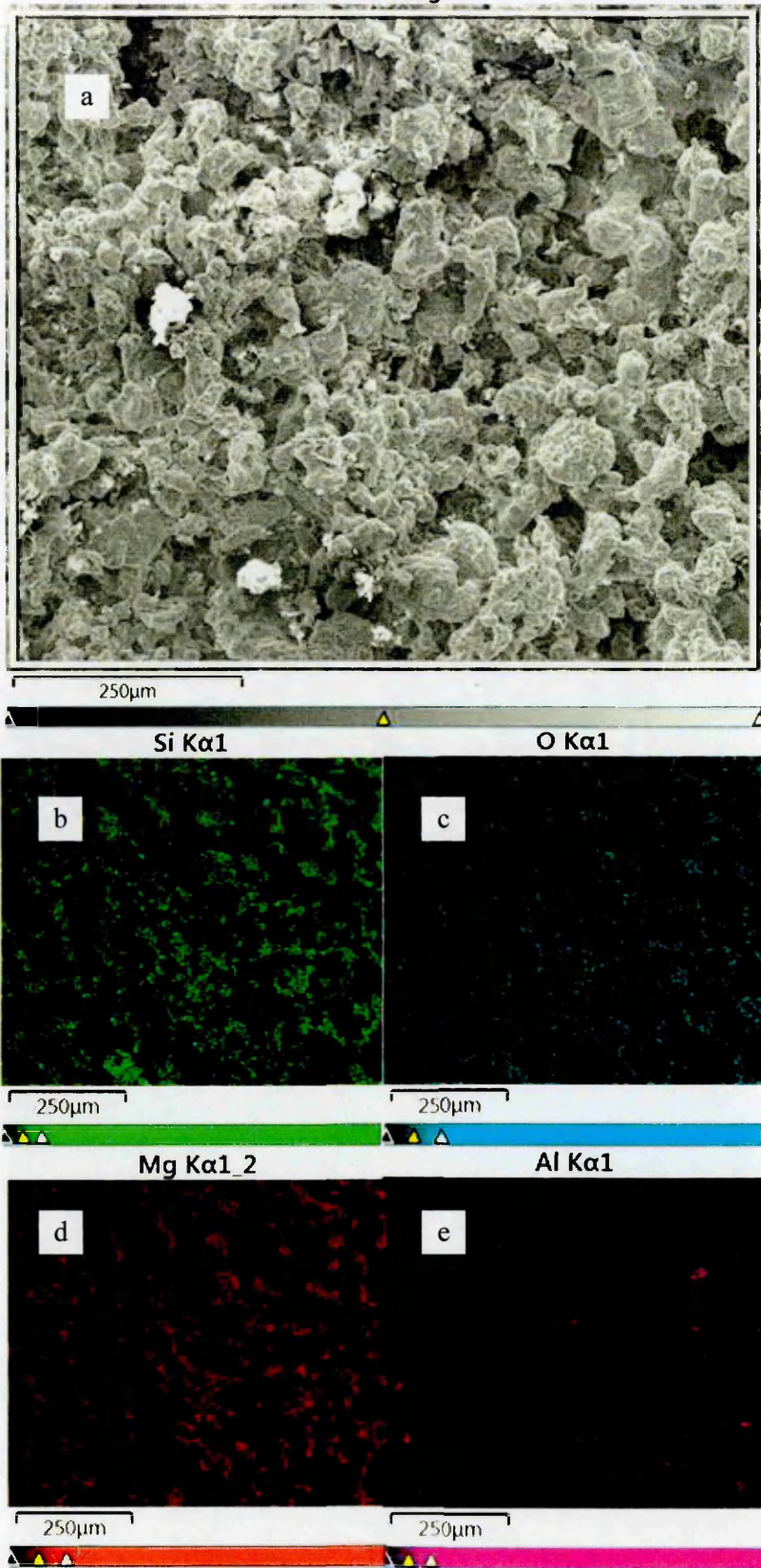


Figure 6.14: The microstructure of impurity phases in centrifuged refine Si-Sn alloyed powder

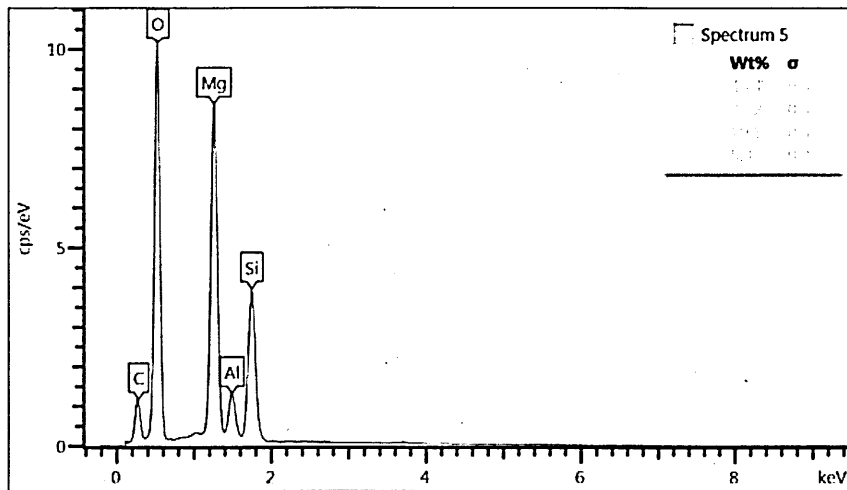


Figure 6.15: The EDS analysis of impurities in Si refined from Si-Sn alloy powder.

6.5 Summary

This chapter demonstrated that reduction of RHA silica to MG-Si was achievable using magnesium metal as a preferred selected metal for metallocermic reduction. Hydrometallurgy leaching process was also discussed and the results presented show a noticeable removal of impurities in MG-Si. The total amount of MG-Si obtained after leaching process was about 1g; it implied that a bit over 90% was used for analysis or loss during decanting or filtering of leached solution. The chapter finally presented and discussed the X-ray mapping technique results of refined Si-Sn alloy powder as well as the result of its centrifuged separation.

Reference

- Campbell, I. H., & Fauchet, P. M. (1986). The effects of microcrystal size and shape on the one phonon Raman spectra of crystalline semiconductors. *Solid State Communications*, 58(10), 739-741.
- Hu, L., Wang, Z., Gong, X., Guo, Z., & Zhang, H. (2013). Impurities removal from metallurgical-grade silicon by combined Sn-Si and Al-Si refining processes. *Metallurgical and Materials Transactions B*, 44(4), 828-836.
- Iqbal, Z., Vepřek, S., Webb, A. P., & Capezzuto, P. (1981). Raman scattering from small particle size polycrystalline silicon. *solid state communications*, 37(12), 993-996.
- Pizzini, S. (1982). Solar grade silicon as a potential candidate material for low-cost terrestrial solar cells. *Solar energy materials*, 6(3), 253-297.
- Zhao, L. X., Zhi, W. A. N. G., Guo, Z. C., & Li, C. Y. (2011). Low-temperature purification process of metallurgical silicon. *Transactions of Nonferrous Metals Society of China*, 21(5), 1185-1192.

7 Conclusion

The work demonstrated that a low-energy and economically viable technological purification process to purify RHA silica at a temperature below 300°C is achievable due to its high reactivity using leaching in HNO₃, dilute HCl and hot water. This is contrary to earlier work on RH or SiO₂. The energy required for industrial scale purification of RHA is estimated at 5KWh Kg⁻¹ for final silicon material produced, greatly less than the 65KWh Kg⁻¹ of current Siemens chlorination plant (Doe 2012, Feldman 2014 and Pizzini 2012).

The work shows that dopant impurity B was reduced using hydrometallurgy process. Results from other works showed that the dopant elements removal without solvent refining process is not possible. Furthermore, P impurity was also seen to be reduced beyond the limit of XRF detection using mere acid leaching, which means that it is feasible to eliminate B and P.

The work shows that it is feasible for amorphous or crystalline silica to be reduced by magnesium metal at much lower temperatures below 800°C, as low as 550°C (Banerjee et al, 1982), than the conventionally used temperatures.

The work also shows that it is feasible for S to be removed alongside other impurities during reduction process.

The work demonstrated from comparison of the purity of commercial grade silicon and purify of the derived MG-Si from rice husk ash that the impurities present in the MG-Si is probably due to excess magnesium from the magnesium metal used and Aluminum from the alumina crucible used.

The work shows that it is feasible to separate Si from ground refined Si-Sn alloy using a centrifuge machine. Looking at the purity achieved from the work, the availability of rice husk as raw material, the low cost and low energy required to produce high purity MG-Si from RHA silica; I can conclude that although the produced silicon may not meet solar grade silicon requirements, its purity are higher than MG-Si and might require very little improvement to achieved solar grade silicon needed for solar cell production.

7.1 Challenges encountered and Future work

7.1.1 Introduction

The cleansing of raw rice husk before ashing has always been a serious business, as it demands a very good start to remove all mud and unwanted substance on the surface of the husk. More demanding yet is the ashing process that requires time and temperature control, not properly ashed rice husk will produce blackish rice husk ash due to the presence of large amount of carbon. The impurities within the ash required different processing steps for removal. To produce high purity Si, special techniques, such as alkali treatment, oxidation, digestion, leaching, etc., and equipment (aquabath, controlled atmosphere furnace ICP-OES, etc.) are required. Carrying out ashing, purification, metallothermic reduction and refining processes without these equipment was therefore a very difficult task. This chapter highlight the challenges encountered during the course of the research work. The corresponding measures taken to overcome these difficulties are also presented. Because the business of solar grade silicon is not an easy one, not all the desired work and results with respect to the solar grade silicon were achieved within the time available for this research work. The remaining work required in order to achieve these targets are also presented in this chapter as part of future work.

7.2 Challenges encountered in the course of this research

This section discussed several challenges encountered at different levels of the research work that resulted to this thesis

7.2.1 Drying of RH material

In the course of trying to dry washed rice husk (the start material) used for the research work, I have to use household gas cooker oven because of lack of sunlight in Sheffield or oven in the laboratory for the purpose. The husk was supposed to be dried at 35 to 40°C, instead it was dried at unknown temperature.

7.2.2 Ashing of RH material

In the course of thermal treatment to produce RHA for its silica contents, furnace with controlled atmosphere is very important to prevent oxidation and external impurities from the materials been prepared. SHU clean room and the furnace with controlled atmosphere were no longer in use when I started my research. Thus, it took me over six months to get a normal furnace for the research and

about 18 months before I got access to an Ar gas controlled atmosphere furnace. This means that all work involving furnace wasn't done under controlled atmosphere except for batch C reduction

7.2.3 Boron analysis

SHU had XRF instrument for elemental analysis. Unfortunately, boron was too light to be detected by it and as such all batch A produce were done and analyzed using the XRF. Boron analysis of batches B and C were done at Element Material Company in Sheffield.

7.3 Future work

In future, due to shortage of purified derived MG-Si while research wasn't yet completed, it is advisable to produce up to 100g of RHA and to start its purification process with at least 50% in order to avoid the situation of running into shortage of material at any stage.

Future work will need completion of the solvent refining process started in this work by using Sn as the gettering metal for any remaining B and P impurity. This is to enable the removal of dopant impurity B or P that dissolved inside the Si and to ease transfer into the molten Si-Sn alloy. Thus, recrystallized Si leaves the impurities in the liquid Sn. There are known or novel techniques for the separation of Si from Sn or Si-Sn liquid. Other metal as Al, Fe and Ca that has high affinity for impurities could be tried. Slagging or directional solidification technique can also be tried in future.

Future work will need the formation of RH MG-Si thin film or RH silicon ingot for solar grade silicon. An ohmic contact made to the rear face and Schottky contact to the front face to produce a solar cell will further boost the value of RH. If possible, during refining process, the recrystallizing Si from the alloy metal could be allowed to grow on an FTO glass by using a vacuum heat treatment furnace suitable for internal manipulation. The grown FTO/SoG-Si can be given Schottky contact on the front surface in order to characterize and evaluate if the electrical properties suit that of a solar cell.

Reference

Banerjee, H. D., Sen, S., & Acharya, H. N. (1982). Investigations on the production of silicon from rice husks by the magnesium method. *Materials Science and Engineering*, 52(2), 173-179.

DOE, U. (2012). Sunshot vision study. *US DOE, Washington, DC*.

Feldman, D. (2014). Photovoltaic (PV) pricing trends: historical, recent, and near-term projections.

Pizzini, S. (2012). *Advanced silicon materials for photovoltaic applications* (pp. 311-353). John Wiley & Sons.

Appendix 1: XRF data for C700, batch C

Materials Research Institute
Sheffield Hallam University
Howard Street, Sheffield S1 1WB

C:\UQ4\Steel\JOB\JOB.784 2016-01-22
Ben 700

2400 Rh 60kV LiF220 Ge111 TlAP
C:\UQ4\Steel\ASC\Kdata.asc 2002-05-29 ..\ChData.asc 2001-11-06
Calculated as : Elements Matrix (Shape & ImpFc) : 1 Teflon
X-ray path = Vacuum Film type = No supporting film
Case number = 3 Unknown Dilution
Eff.Diam. = 23.0 mm Eff.Area = 415.3 mm²
KnownConc = 0 %
Rest = 0 % Viewed Mass =
2200.000 mg
Dil/Sample = ? Binder Sample Height = 2.20 mm
< means that the concentration is < 100 mg/kg
<2e means wt% < 2 StdErr. A + or & means: Part of 100%

	Z	wt%	StdErr	Z	wt%	StdErr	Z
	wt%	StdErr					
<hr/>							
11+Na	0.201	0.053	29+Cu	<			52 Te
12+Mg	0.29	0.07	30+Zn	<			53 I
13+Al	0.23	0.10	31+Ga	0.0128	0.0037	55 Cs	<
14+Si	98.82	0.05	32 Ge	<			56 Ba
0.073	0.093		33 As	<2e	0.020	SumLa..Lu	<
15 P			34 Se	<			72 Hf
<2e	0.010						
15+Px	<		35 Br	<			73 Ta
16 Sx	<		37 Rb	<			74+W
0.0135	0.0043						
16 S			38 Sr	<			75 Re
17+Cl	0.17	0.012	39 Y	<			76 Os
18 Ar	<		40 Zr	<			77 Ir
19+K	0.0247	0.0048	41 Nb	<2e	0.0060	78+Pt	<
0.0316	0.0066						
20+Ca	0.0516	0.0044	42 Mo	<			79+Au
0.0222	0.0065						
21 Sc	<		44 Ru	<			80 Hg
22+Ti	0.0184	0.0016	45 Rh	<			81 Tl
23 V	<		46 Pd	<			82 Pb
24+Cr	0.0163	0.0028	47 Ag	<			83 Bi
25+Mn	0.0340	0.0020	48 Cd	<			90 Th
26+Fe	0.0673	0.0050	49 In	<			92 U
27 Co	<		50+Sn	0.0146	0.0059	94 Pu	<
28+Ni	<		51 Sb	<			95 Am
<hr/>							
==== Light Elements =====		==== Noble Elements =====		<hr/>			
Lanthanides =====				<hr/>			
SumBe..F	0.12	0.10	44 Ru	<			57 La
4 Be			45 Rh	<			58 Ce

5 B		46 Pd	<	59 Pr	
6 C		47 Ag	<	60 Nd	<
7 N		75 Re	<	62 Sm	<
8 O		76 Os	<	63 Eu	<
9 F	<2e	0.10	77 Ir	<	64+Gd
0.0248	0.0069		78+Pt	0.0316	0.0066
0.0360	0.0066		79+Au	0.0222	0.0065
				66 Dy	<
				67 Ho	<
				68 Er	<
				69 Tm	<
				70 Yb	<
				71 Lu	

KnownConc= 0

REST= 0

D/S=12.80

Binder

LOI = 99.2% of original sample, as calculated from $100 * (1 - 0.100 / 12.800)$

Appendix 1: XRF data for C800, batch C

Materials Research Institute
Sheffield Hallam University
Howard Street, Sheffield S1 1WB

C:\UQ4\Steel\JOB\JOB.785 2016-01-22

Ben 800

2400 Rh 60kV LiF220 Ge111 TlAP

C:\UQ4\Steel\ASC\Kdata.asc 2002-05-29 ..\ChData.asc 2001-11-06

Calculated as : Elements Matrix (Shape & ImpFc) : 1 Teflon

X-ray path = Vacuum Film type = No supporting film

Case number = 3 Unknown Dilution

Eff.Diam. = 23.0 mm Eff.Area = 415.3 mm²

KnownConc = 0 %

Rest = 0 % Viewed Mass =

765.154 mg

Dil/Sample = ? Binder Sample Height = 1.07 mm

< means that the concentration is < 50 mg/kg

<2e means wt% < 2 StdErr. A + or & means: Part of 100%

sum

Z	wt%	StdErr	Z	wt%	StdErr	Z
wt%	StdErr					
			29+Cu	0.0075	0.0021	52 Te
<2e	0.034					
11+Na	0.18	0.069	30+Zn	0.0118	0.0017	53 I
12+Mg	0.26	0.08	31+Ga	0.0133	0.0050	55 Cs
<2e	0.070					
13+Al	0.15	0.11	32 Ge	<2e	0.0052	56 Ba
14+Si	98.77	0.06	33 As	<		SumLa..Lu
0.08	0.12					
15 P			34 Se	<2e	0.0068	72 Hf
0.030	0.014					
15+Px	0.0122	0.0015	35 Br	<2e	0.0077	73 Ta
16 Sx	<		37 Rb	<		74+W
0.0158	0.0054					
16 S			38 Sr	<		75 Re
<2e	0.0072					
17+C1	0.28	0.018	39 Y	<		76 Os
<2e	0.0071					
18+Ar	0.0146	0.0064	40 Zr	<2e	0.015	77 Ir
19+K	0.0231	0.0045	41+Nb	0.032	0.016	78+Pt
0.0222	0.0097					
20+Ca	0.0605	0.0050	42 Mo	<		79 Au
<2e	0.010					
21 Sc	<		44 Ru	<		80 Hg
22+Ti	0.0158	0.0018	45 Rh	<		81 Tl
23 V	<		46 Pd	<		82 Pb
<2e	0.011					
24+Cr	0.0215	0.0034	47 Ag	<2e	0.013	83 Bi
<2e	0.013					
25+Mn	0.0099	0.0026	48 Cd	<		90 Th
26+Fe	0.0164	0.0069	49 In	<		92 U

27 Co	<	50+Sn	0.044	0.020	94 Pu
<2e	0.012				
28+Ni	0.0083	0.0022	51 Sb	<	95 Am
<2e	0.012				
===== Light Elements =====			===== Noble Elements =====		
Lanthanides =====					
SumBe..F	0	0.12	44 Ru	<	57 La
4 Be			45 Rh	<	58 Ce
5 B			46 Pd	<	59 Pr
6 C			47 Ag	<2e	60 Nd
<2e	0.010				
7 N			75 Re	<2e	62 Sm
8 O			76 Os	<2e	63 Eu
9 F	<		77 Ir	<	64 Gd
<2e	0.0078		78+Pt	0.0222	0.0097
0.0334	0.0077		79 Au	<2e	65+Tb
				0.010	66 Dy
					67 Ho
					68 Er
					69 Tm
					70 Yb
<2e	0.0061				71 Lu

KnownConc= 0 REST= 0 D/S=16.32

Binder

LOI = 99.4% of original sample, as calculated from $100 * (1 - 0.100 / 16.321)$

Appendix 1: XRF data for C900, batch C

Materials Research Institute
Sheffield Hallam University
Howard Street, Sheffield S1 1WB

C:\UQ4\Steel\JOB\JOB.786 2016-01-22
Ben 900

2400 Rh 60kV LiF220 Ge111 TlAP
C:\UQ4\Steel\ASC\Kdata.asc 2002-05-29 ..\ChData.asc 2001-11-06
Calculated as : Elements Matrix (Shape & ImpFc) : 1 Teflon
X-ray path = Vacuum Film type = No supporting film
Case number = 3 Unknown Dilution
Eff.Diam. = 23.0 mm Eff.Area = 415.3 mm²
KnownConc = 0 %
Rest = 0 % Viewed Mass =
2200.000 mg
Dil/Sample = ? Binder Sample Height = 2.20 mm
< means that the concentration is < 50 mg/kg
<2e means wt% < 2 StdErr. A + or & means: Part of 100%
sum

	Z	wt%	StdErr	Z	wt%	StdErr	Z	
	wt%	StdErr						
11+Na	0.29	0.061		29+Cu	0.0133	0.0018	52 Te	<
12+Mg	0.21	0.09		30+Zn	<		53 I	<
<2e	0.023			31+Ga	0.0102	0.0037	55 Cs	
13+Al	1.24	0.13		32 Ge	<		56 Ba	<
14+Si	98.64	0.06		33 As	<		SumLa..Lu	
0.06	0.12			34 Se	<		72+Hf	
15 P				35 Br	<		73 Ta	<
0.041	0.010			37 Rb	<2e	0.0046	74 W	<
16+Sx				38 Sr	<		75 Re	<
16 S				39 Y	<		76+Os	
17+Cl	0.215	0.015		40 Zr	<2e	0.0063	77 Ir	<
0.0147	0.0045			41 Nb	<		78+Pt	
18+Ar	0.0114	0.0056		42 Mo	<		79+Au	
19+K	0.0125	0.0025		44 Ru	<2e	0.0039	80 Hg	<
0.0232	0.0072			45 Rh	<		81 Tl	<
20+Ca	0.0107	0.0040		46 Pd	<		82 Pb	
0.0223	0.0075			47 Ag	<		83 Bi	
21 Sc	<			48 Cd	<		90 Th	<
22+Ti	0.0213	0.0019		49 In	<		92 U	
23 V	<			50+Sn	0.0151	0.0067	94 Pu	
<2e	0.0055			51 Sb	<		95+Am	
24+Cr	0.0200	0.0030						
<2e	0.0078							
25+Mn	0.0133	0.003						
26+Fe	0.0958	0.0068						
27 Co	<							
<2e	0.0050							
28+Ni	<							
0.0104	0.0049							

===== Light Elements =====			===== Noble Elements =====			=====	
Lanthanides =====							
SumBe..F	0.05	0.11	44 Ru	<2e	0.0039	57 La	<
4 Be			45 Rh	<		58 Ce	<
5 B			46 Pd	<		59 Pr	
6 C			47 Ag	<		60 Nd	<
7 N			75 Re	<		62 Sm	<
8 O			76+Os	0.0147	0.0045	63 Eu	<
9 F	<2e	0.11	77 Ir	<		64 Gd	<
			78+Pt	0.0232	0.0072	65+Tb	
0.0424	0.0071		79+Au	0.0223	0.0075	66 Dy	
<2e	0.0093					67 Ho	<
						68 Er	<
						69 Tm	<
						70 Yb	
<2e	0.0052					71 Lu	

KnownConc= 0

REST= 0

D/S=14.49

Binder

LOI = 99.3% of original sample, as calculated from $100 * (1 - 0.100/14.491)$

Appendix 1: XRF data for C1000, batch C

Materials Research Institute
 Sheffield Hallam University
 Howard Street, Sheffield S1 1WB

C:\UQ4\Steel\JOB\JOB.788 2016-01-22
 Ben 1000

2400 Rh 60kV LiF220 Ge111 T1AP
 C:\UQ4\Steel\ASC\Kdata.asc 2002-05-29 ..\ChData.asc 2001-11-06
 Calculated as : Elements Matrix (Shape & ImpFc) : 1 Teflon
 X-ray path = Vacuum Film type = No supporting film
 Case number = 3 Unknown Dilution
 Eff.Diam. = 15.8 mm Eff.Area = 196.1 mm²
 KnownConc = 0 %
 Rest = 0 % Viewed Mass =
 2200.000 mg
 Dil/Sample = ? Binder Sample Height = 0.88 mm
 < means that the concentration is < 100 mg/kg
 <2e means wt% < 2 StdErr. A + or & means: Part of 100%

sum

	Z	wt%	StdErr	Z	wt%	StdErr	Z
	wt%	StdErr					
				29+Cu	0.0117	0.0026	52 Te <
11+Na	0.22	0.063		30+Zn	0.0115	0.0021	53 I <
12+Mg	0.31	0.06		31+Ga	0.0132	0.0057	55 Cs <
13+Al	0.16	0.08		32 Ge	<		56 Ba <
14+Si	98.63	0.05		33 As	<2e	0.029	SumLa..Lu
0.15	0.14						
15 P				34+Se	0.0125	0.0059	72 Hf
0.047	0.017						
15 Px	<			35 Br	<		73 Ta <
16 Sx	<			37 Rb	<		74+W
0.0165	0.0065						
16 S				38 Sr	<		75 Re <
17+C1	0.35	0.021		39 Y	<		76+Os
0.0166	0.0066						
18+Ar	0.0166	0.0077		40 Zr	<		77 Ir <
19+K	0.0209	0.0041		41 Nb	<		78 Pt
<2e	0.010						
20+Ca	0.0441	0.0053		42 Mo	<		79 Au
<2e	0.011						
21 Sc	<			44 Ru	<		80 Hg <
22+Ti	0.0231	0.0024		45 Rh	<		81 Tl <
23 V	<			46 Pd	<		82 Pb <
24+Cr	0.0155	0.0042		47 Ag	<		83 Bi <
25+Mn	<			48 Cd	<		90 Th <
26+Fe	0.0799	0.0058		49 In	<		92 U
27 Co	<			50 Sn	<		94 Pu <
28+Ni	0.0104	0.0028		51 Sb	<		95 Am <

==== Light Elements ==== ===== Noble Elements =====
 Lanthanides =====

SumBe..F	0	0.11	44 Ru	<	57+La		
0.0194	0.0079		45 Rh	<	58 Ce	<	
4 Be			46 Pd	<	59 Pr		
5 B			47 Ag	<	60 Nd		
6 C							
<2e	0.012						
7 N			75 Re	<	62 Sm	<	
8 O			76+Os	0.0166	0.0066	63 Eu	
<2e	0.022						
9 F	<		77 Ir	<	64 Gd	<	
			78 Pt	<2e	0.010	65+Tb	
0.060	0.010						
			79 Au	<2e	0.011	66 Dy	<
						67 Ho	<
						68 Er	<
						69 Tm	<
						70 Yb	<
						71 Lu	

KnownConc= 0

REST= 0

D/S= 6.67

Binder

LOI = 98.8% of original sample, as calculated from $100 * (1 - 0.100 / 6.674)$

Appendix 1: XRF data for Commercial grade Si

Materials Research Institute
Sheffield Hallam University
Howard Street, Sheffield S1 1WB

C:\UQ4\Steel\JOB\JOB.783 2016-01-22

Ben silicon

2400 Rh 60kV LiF220 Ge111 TlAP

C:\UQ4\Steel\ASC\Kdata.asc 2002-05-29 ..\ChData.asc 2001-11-06

Calculated as : Elements Matrix (Shape & ImpFc) : 1 Teflon

X-ray path = Vacuum Film type = No supporting film

Case number = 3 Unknown Dilution

Eff.Diam. = 23.0 mm Eff.Area = 415.3 mm²

KnownConc = 0 %

Rest = 0 % Viewed Mass =

765.154 mg

Dil/Sample = ? Binder Sample Height = 0.37 mm

< means that the concentration is < 100 mg/kg

<2e means wt% < 2 StdErr. A + or & means: Part of 100%

sum

Z	wt%	StdErr	Z	wt%	StdErr	Z
---	-----	--------	---	-----	--------	---

wt%	StdErr
-----	--------

29+Cu	<	52 Te
-------	---	-------

<2e	0.036
-----	-------

11+Na	0.09	0.088	30 Zn	<	53 I	<
-------	------	-------	-------	---	------	---

12 Mg	<		31 Ga	<	55 Cs	<
-------	---	--	-------	---	-------	---

13 Al	<		32 Ge	<	56 Ba	<
-------	---	--	-------	---	-------	---

14+Si	99.72	0.05	33 As	<2e	0.027	SumLa..Lu
-------	-------	------	-------	-----	-------	-----------

0.193	0.097
-------	-------

15 P			34 Se	<	72 Hf
------	--	--	-------	---	-------

0.031	0.012
-------	-------

15 Px	<		35 Br	<2e	0.0066	73 Ta	<
-------	---	--	-------	-----	--------	-------	---

16+Sx	<		37 Rb	<		74+W
-------	---	--	-------	---	--	------

0.0131	0.0044
--------	--------

16 S			38 Sr	<2e	0.0095	75+Re
------	--	--	-------	-----	--------	-------

0.0119	0.0048
--------	--------

17+Cl	0.07	0.022	39 Y	<		76 Os	<
-------	------	-------	------	---	--	-------	---

18+Ar	0.0267	0.0070	40+Zr	0.028	0.012	77 Ir	<
-------	--------	--------	-------	-------	-------	-------	---

19 K	<		41+Nb	0.054	0.014	78 Pt	<
------	---	--	-------	-------	-------	-------	---

20+Ca	0.01	0.0050	42 Mo	<		79 Au	<
-------	------	--------	-------	---	--	-------	---

21 Sc	<		44+Ru	0.025	0.012	80 Hg	<
-------	---	--	-------	-------	-------	-------	---

22 Ti	<		45 Rh	<		81 Tl	<
-------	---	--	-------	---	--	-------	---

23 V	<		46 Pd	<2e	0.014	82 Pb	<
------	---	--	-------	-----	-------	-------	---

24 Cr	<		47 Ag	<		83 Bi
-------	---	--	-------	---	--	-------

<2e	0.0097
-----	--------

25 Mn	<		48 Cd	<2e	0.013	90+Th
-------	---	--	-------	-----	-------	-------

0.049	0.013
-------	-------

26+Fe	0.0215	0.0029	49 In	<		92 U
-------	--------	--------	-------	---	--	------

27 Co	<		50+Sn	0.059	0.022	94 Pu	<
-------	---	--	-------	-------	-------	-------	---

28 Ni	<		51 Sb	<		95 Am	<
-------	---	--	-------	---	--	-------	---

==== Light Elements ==== ===== Noble Elements =====

Lanthanides =====

SumBe..F	0	0.12	44+Ru	0.025	0.012	57 La	<
4 Be			45 Rh	<		58 Ce	<
5 B			46 Pd	<2e	0.014	59 Pr	
6 C			47 Ag	<		60 Nd	
<2e	0.0095						
7 N			75+Re	0.0119	0.0048	62 Sm	<
8 O			76 Os	<		63+Eu	
0.091	0.011						
9 F	<		77 Ir	<		64+Gd	
0.0254	0.0076						
0.0381	0.0073		78 Pt	<		65+Tb	
<2e	0.0091					66 Dy	
			79 Au	<			
						67 Ho	<
						68 Er	<
						69 Tm	<
						70 Yb	<
						71 Lu	

KnownConc= 0

REST= 0

D/S=18.71

Binder

LOI = 99.7% of original sample, as calculated from $100 * (1 - 0.100 / 18.708)$



Sheffield Hallam University
Materials & Engineering
Howard Street
Sheffield, S1 1WB

Report No: 14063169
Issue Date: 18/06/2014
Order No: A3 119 783
Test Date: 17/06/2014
Element No: 14E06352

Analysis Report

Results:

Test No	Sample ID	Boron mg/Kg
Units		
F3270	HCl 01 900	20
F3271	HCl 700	9
F3272	HCl 800	8
F3273	HCl 1000	19
F3274	DI H ₂ O leach 800	48
F3275	H ₂ O leached 900	22
F3276	700°C DI- Hot	27
F3277	1000°C DI- Hot	23
F3278	RHA 700°C	19
F3279	RHA 800°C	18
F3280	RHA 900°C	22
F3281	BRH 1000	20
F3282	MG Si B	39

Tested in accordance with in house procedure(s) for ICP OES techniques.

Issued by:

J.C. Hastings
Manager
Analytical

This certificate is issued in accordance with the laboratory accreditation requirements of the United Kingdom Accreditation Service. It provides traceability of measurement to recognised national standards, and to units of measurement realised at the National Physical Laboratory or other recognised national standards laboratories. If, upon reproduction, only part of this report is copied, Element will not bear any responsibility for content, purport and conclusions of that reproduction. This report has legal value only when printed on Element paper and furnished with an authorised signature. Digital versions of this report have no legal value. The Terms & Conditions of Element (to be found at www.element.com) are applicable on all services provided by Element.

Sheffield Hallam University **Report No.** 16040269
 Birch Road **Element Ref.** 16E04175
 Sheffield **Report Date** 13/04/2016
 S9 3XL **Order No** A3189957
Test Date 13/04/2016

Sample Description: Commercial Grade Silicon
Given Material Specification: Not Given

Chemical Analysis

ICP Chemical Analysis - Nominated Elements - (ICP OES)

Test No. D0649

Element	Units: ppm
B	10

uthorised Signatory:



Name: Alan Beadsley
 Alan Beadsley

Position: Senior Analytical
 TechnicianSenior Analytical
 Technician

ny tests marked with a * are not on our UKAS schedule of accreditation.

here appropriate, the results reported herein provide traceability of measurement to recognised national standards, and to units of measurement realised at the National Physical Laboratory or other recognised national standards laboratories. Any opinions or interpretations given herein fall outside the scope of our schedule of accredited testing. If, upon reproduction, only part of this report is copied, Element will not bear responsibility for content, purport and conclusions of that reproduction. Original reports issued by Element, either in electronic or physical form have legal value only when furnished with an authorised signature. Any subsequent digital or physical copies of this report have no legal value unless authorised by Element. The Terms & Conditions of Element, available upon request, are applicable on all services provided by Element. NB: Results given in this report relate only to the items received and tested.

Results Checked: CH MEC CORR MET

SHEFFIELD HALLAM UNIVERSITY
CITY CAMPUS
HOWARD STREET
SHEFFIELD
S1 1WB

Report No: 16030012SC
 Issue Date: 09/03/2016
 Order No: A3189957
 Test Date: 08/03/2016
 Specification: N/A
 Element No: 16E03011

Analysis Report

Results:

Test No	Sample Identification	Boron ppm
C0038	Mg-Si 700	116
C0039	Mg-Si 800	137
C0040	900	124
C0041	1000	157

Tested in accordance with in house procedure(s) for ICP OES techniques.
 This report is issued supplementary to and replaces certificate 16030012.

Issued by :



A.Beadsley
 Senior
 Technician
 Analytical

This certificate is issued in accordance with the laboratory accreditation requirements of the United Kingdom Accreditation Service. It provides traceability of measurement to recognised national standards, and to units of measurement realised at the National Physical Laboratory or other recognised national standards laboratories. If, upon reproduction, only part of this report is copied, Element will not bear any responsibility for content, purport and conclusions of that reproduction. This report has legal value only when printed on Element paper and furnished with an authorised signature. Digital versions of this report have no legal value. The Terms & Conditions of Element, available upon request, are applicable on all services provided by Element.



SHEFFIELD HALLAM UNIVERSITY
CITY CAMPUS
HOWARD STREET
SHEFFIELD
S1 1WB

Report No: 14100668
Issue Date: 23/10/2014
Order No: Mr Benedict Ayomanor
Test Date: 23/10/2014
Specification: See Below
Element No: 14E10545

Analysis Report

Results:

Test No	Sample Identification	Boron Mg/Kg
K0823	BATCH C HNO3 700	52
K0824	BATCH C HN03 800	45
K0825	BATCH C HN03 900	18
K0826	BATCH C HN03 1000	46
K0827	NATURAL QUARTZ HCL	13
K0828	BATCH C RHA 1000 HCL	40
K0829	XRD BATCH C RHA 1000°C	49
K0830	XRD BATCH C RHA@900°C 0.4g	23
K0831	12/08/14 BATCH C RHA@800°C 0.4g XRD	11
K0832	BATCH C RHA@700°C 0.4g XRD	6
K0833	BATCH C RHA 700 D1	38
K0834	BATCH C RHA@700°C 0.4g	32
K0835	BATCH C RHA@800°C HCL	30
K0836	BATCH C RHA@900°C D1	34
K0837	BATCH C RHA 1000°C D1	51
K0838	BATCH C RHA 800 D1	57
K0839	BATCH C RHA 900 HCL	58

Tested in accordance with in house procedure(s) for ICP OES techniques.

Issued by:

A.Beadsley

Senior

Technician

Analytical

This certificate is issued in accordance with the laboratory accreditation requirements of the United Kingdom Accreditation Service. It provides traceability of measurement to recognised national standards, and to units of measurement realised at the National Physical Laboratory or other recognised national standards laboratories. If, upon reproduction, only part of this report is copied, Element will not bear any responsibility for content, purport and conclusions of that reproduction. This report has legal value only when printed on Element paper and furnished with an authorised signature. Digital versions of this report have no legal value. The Terms & Conditions of Element, available upon request, are applicable on all services provided by Element.

Name and formula

Reference code: 00-027-1402

Mineral name: Silicon, syn

PDF index name: Silicon

Empirical formula: Si

Chemical formula: Si

Crystallographic parameters

Crystal system: Cubic

Space group: Fd3m

Space group number: 227

a (Å): 5.4309

b (Å): 5.4309

c (Å): 5.4309

alpha (°): 90.0000

beta (°): 90.0000

gamma (°): 90.0000

Calculated density (g/cm^3): 2.33

Volume of cell (10^6 pm^3): 160.18

8.00

RIR: 4.70

Subfiles and Quality

Subfiles: Inorganic
Mineral
Alloy, metal or intermetallic
Common Phase
Educational pattern
Forensic

Quality: Star (S)

Comments

Color: Gray

General comments: Reflections calculated from precision measurement of a_0 .
 a_0 uncorrected for refraction.

Sample source: This sample is NBS Standard Reference Material No. 640.

Additional pattern: To replace 5-565 and 26-1481.

Temperature: Pattern taken at 25(1) C.

References

Primary reference: *Natl. Bur. Stand. (U.S.) Monogr.* 2513, 35, (1976)

Peak list

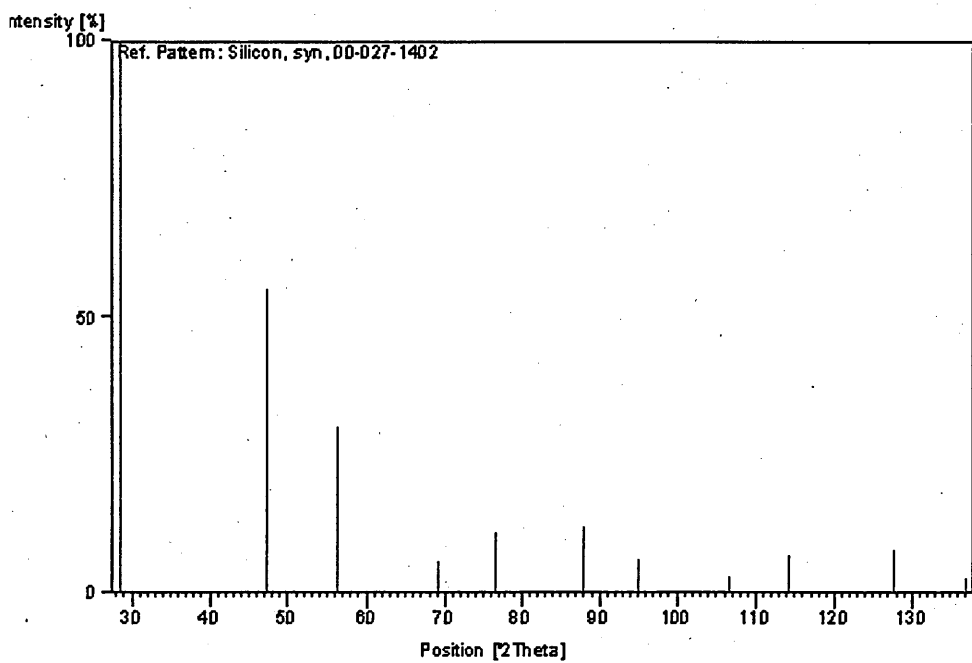
No.	h	k	l	d [Å]	2Theta[deg]	I [%]
1	1	1	1	3.13550	28.443	100.0
2	2	2	0	1.92010	47.304	55.0
3	3	1	1	1.63750	56.122	30.0
4	4	0	0	1.35770	69.132	6.0

5	3	3	1	1.24590	76.380	11.0
6	4	2	2	1.10860	88.029	12.0
7	5	1	1	1.04520	94.951	6.0
8	4	4	0	0.96000	106.719	3.0
9	5	3	1	0.91800	114.092	7.0
10	6	2	0	0.85870	127.547	8.0
11	5	3	3	0.82820	136.898	3.0

Structure

No.	Name	Elem.	X	Y	Z	Biso	sof	Wyck.
Si1	SI		0.00000	0.00000	0.00000	0.0000	1.0000	16c

Stick Pattern



Name and formula

Reference code: 01-082-0512
 Mineral name: Cristobalite
 CSD name: Silicon Oxide
 Empirical formula: O₂Si
 Chemical formula: SiO₂

Crystallographic parameters

Crystal system: Tetragonal
 Space group: P41212
 Space group number: 92
 a (Å): 4.9970
 b (Å): 4.9970
 c (Å): 7.0700
 alpha (°): 90.0000
 beta (°): 90.0000
 gamma (°): 90.0000
 Calculated density (g/cm³): 2.26
 Volume of cell (10⁶ pm³): 176.54
 Z: 4.00
 RIR: 5.35

Subfiles and Quality

Subfiles: Inorganic
 Mineral
 Alloy, metal or intermetallic
 Corrosion
 Modelled additional pattern
 Quality: Calculated (C)

Comments

CSD collection code: 074530
 Test from ICSD:
 No R value given.
 At least one TF missing.

References

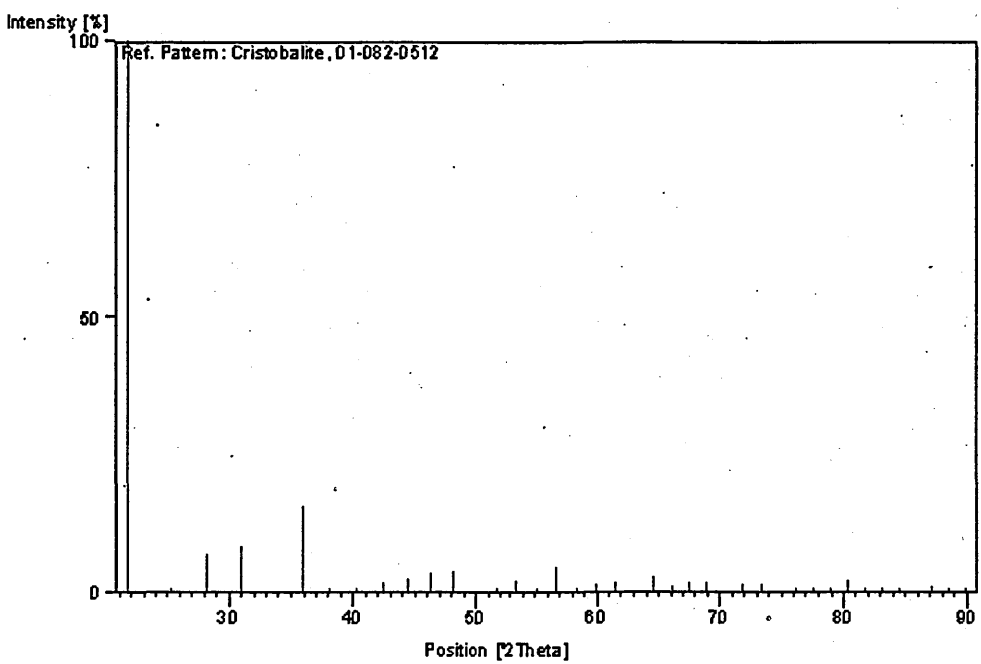
Primary reference: Calculated from ICSD using POWD-1.2++, (1997)
 Structure: Lacks, D.J., Gordon, R.G., *Phys Rev B: Condens. Matter* **48**, 2889, (1993)

Peak list

lo.	h	k	l	d [Å]	2Theta [deg]	I [%]
1	1	0	1	4.08064	21.762	100.0
2	1	1	0	3.53341	25.184	0.5
3	1	1	1	3.16066	28.212	7.2
4	1	0	2	2.88588	30.962	8.7
5	1	1	2	2.49650	35.914	15.9
6	2	0	1	2.35573	38.172	0.1
7	2	1	0	2.23473	40.326	0.1

8	1	0	3	2.13081	42.385	2.0
9	2	0	2	2.04032	44.363	2.8
10	1	1	3	1.96059	46.269	4.0
11	2	1	2	1.88893	48.133	4.3
12	0	0	4	1.76750	51.674	0.6
13	2	0	3	1.71436	53.400	2.3
14	1	0	4	1.66633	55.068	0.4
15	2	1	3	1.62128	56.734	4.7
16	2	2	2	1.58019	58.349	0.5
17	3	1	1	1.54214	59.934	1.8
18	3	0	2	1.50678	61.491	1.9
19	2	0	4	1.44262	64.547	2.9
20	2	2	3	1.41359	66.039	1.2
21	2	1	4	1.38630	67.511	2.1
22	1	0	5	1.36058	68.965	2.1
23	1	1	5	1.31246	71.877	1.5
24	3	2	2	1.29030	73.310	1.5
25	2	2	4	1.24953	76.118	0.8
26	2	0	5	1.23019	77.535	1.0
27	3	0	4	1.21195	78.927	1.2
28	2	1	5	1.19489	80.281	2.4
29	3	1	4	1.17804	81.670	1.1
30	3	3	1	1.16179	83.063	0.3
31	1	0	6	1.14644	84.429	0.2
32	1	1	6	1.11781	87.120	1.5
33	4	0	3	1.10366	88.526	1.2
34	3	2	4	1.09062	89.869	0.3

Stick Pattern



Name and formula

Reference code: 01-083-2465
 Mineral name: Quartz
 CSD name: Silicon Oxide
 Empirical formula: O₂Si
 Chemical formula: SiO₂

Crystallographic parameters

Crystal system: Hexagonal
 Space group: P3121
 Space group number: 152

a (Å): 4.9148
 b (Å): 4.9148
 c (Å): 5.4062
 Alpha (°): 90.0000
 Beta (°): 90.0000
 Gamma (°): 120.0000

Calculated density (g/cm³): 2.65
 Volume of cell (10⁶ pm³): 113.09
 Z: 3.00

RIR: 0.61

Subfiles and Quality

Subfiles: Inorganic
 Mineral
 Alloy, metal or intermetallic
 Modelled additional pattern
 Quality: Calculated (C)

Comments

CSD collection code: 200721
 Test from ICSD: No R value given.
 At least one TF implausible.

References

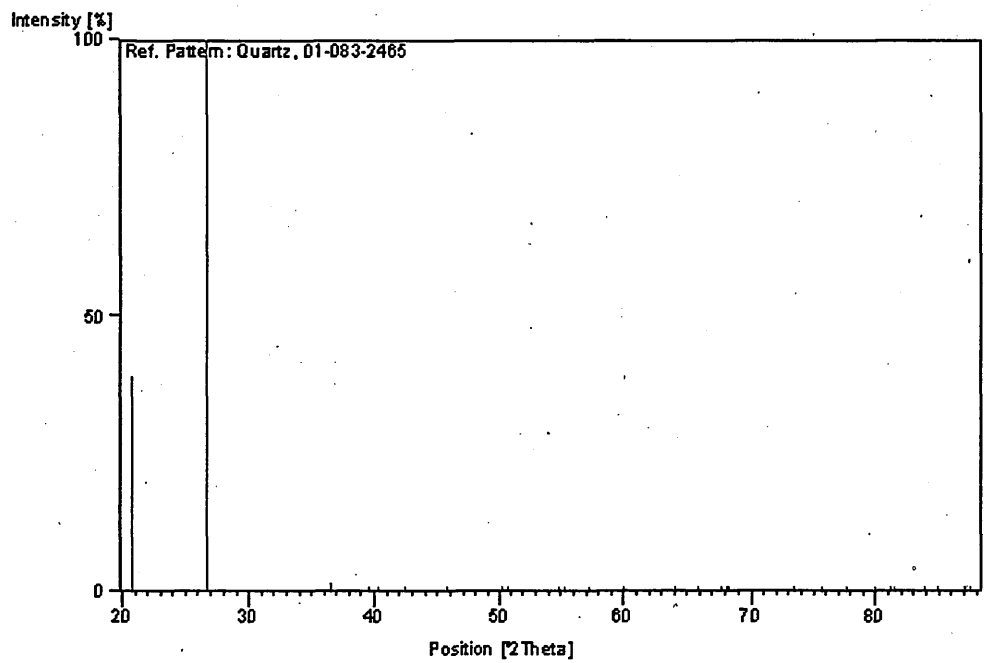
Primary reference: Calculated from ICSD using POWD-12++ (1997)
 Structure: Jorgensen, J.D., *J. Appl. Phys.* **49**, 5473, (1978)

Peak list

Io.	h	k	l	d [Å]	2Theta[deg]	I [%]
1	1	0	0	4.25634	20.853	38.8
2	1	0	1	3.34425	26.634	100.0
3	1	1	0	2.45740	36.536	1.7
4	0	1	2	2.28183	39.459	1.0
5	1	1	1	2.23713	40.281	0.4
6	2	0	0	2.12617	42.441	0.4
7	0	2	1	1.98026	45.783	0.1
8	1	1	2	1.81832	50.128	0.2

9	0	0	3	1.80207	50.612	0.1
10	2	0	2	1.67212	54.861	0.1
11	1	0	3	1.65946	55.315	0.1
12	2	1	0	1.60875	57.217	0.1
13	2	1	1	1.54192	59.943	0.1
14	1	1	3	1.45320	64.021	0.1
15	3	0	0	1.41878	65.767	0.1
16	2	1	2	1.38244	67.725	0.1
17	0	2	3	1.37526	68.127	0.1
18	3	0	1	1.37231	68.294	0.1
19	0	1	4	1.28817	73.451	0.1
20	0	3	2	1.25625	75.639	0.1
21	2	2	0	1.22870	77.647	0.1
22	1	2	3	1.20010	79.862	0.1
23	1	1	4	1.18425	81.152	0.1
24	3	1	0	1.18050	81.464	0.1
25	3	1	1	1.15332	83.810	0.1
26	0	2	4	1.14092	84.933	0.1
27	2	2	2	1.11856	87.047	0.1
28	0	3	3	1.11475	87.420	0.1

Stick Pattern



Name and formula

Reference code: 00-033-1161
Mineral name: Quartz, syn
Common name: silica
PDF index name: Silicon Oxide
Empirical formula: O₂Si
Chemical formula: SiO₂

Crystallographic parameters

Crystal system: Hexagonal
Space group: P3221
Space group number: 154

a (Å): 4.9134
c (Å): 4.9134
c/a: 5.4053
Alpha (°): 90.0000
Beta (°): 90.0000
Gamma (°): 120.0000

Calculated density (g/cm³): 2.65
Measured density (g/cm³): 2.66
Volume of cell (10⁻⁶ pm³): 113.01
Z: 3.00

RIR: 3.60

Status, subfiles and quality

Status: Marked as deleted by ICDD
Subfiles: Inorganic
Mineral
Alloy, metal or intermetallic
Cement and Hydration Product
Common Phase
Educational pattern
Forensic
NBS pattern
Quality: Star (S)

Comments

Deleted by: Deleted by 46-1045, higher F_N more complete, LRB 1/95.
Color: Colorless
General comments: Pattern reviewed by Holzer, J., McCarthy, G., North Dakota State Univ., Fargo, ND, USA, *ICDD Grant-in-Aid*(1990). Agrees well with experimental and calculated patterns.
Sample source: Sample from the Glass Section at NBS, Gaithersburg, MD, USA, ground single-crystals of optical quality.
Optical data: B=1.544, Q=1.553, Sign=+
Additional pattern: To replace 5-490 and validated by calculated pattern.
See ICSD 62405, 70005, 70006, 70007, 71392 (PDF 78-1253, 80-2146, 80-2147, 80-2148, 81-65).
Additional diffraction line(s): Plus 6 additional reflections to 0.9089.
Temperature: Pattern taken at 25 C.

References

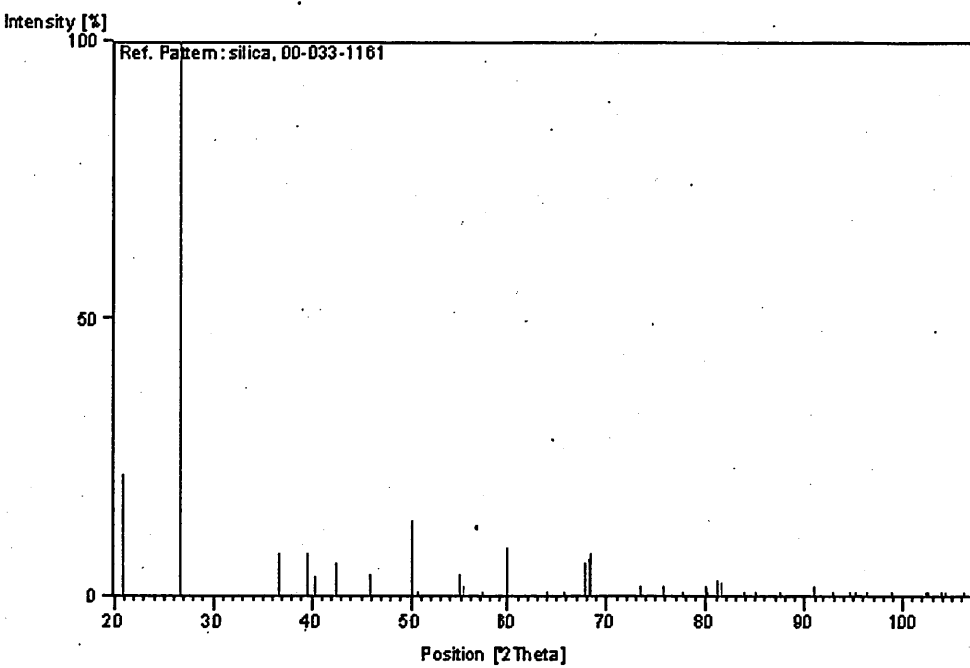
Primary reference:
Optical data:

Natl. Bur. Stand. (U.S.) Monogr. **25** **18**, 61, (1981)
Swanson, Fuyat., *Natl. Bur. Stand. (U.S.) Circ.* **53** **3**, 24, (1954)

Peak list

No.	h	k	l	d [Å]	2Theta[deg]	I [%]
1	1	0	0	4.25700	20.850	22.0
2	1	0	1	3.34200	26.652	100.0
3	1	1	0	2.45700	36.542	8.0
4	1	0	2	2.28200	39.456	8.0
5	1	1	1	2.23700	40.284	4.0
6	2	0	0	2.12700	42.465	6.0
7	2	0	1	1.97920	45.809	4.0
8	1	1	2	1.81790	50.141	14.0
9	0	0	3	1.80210	50.611	1.0
10	2	0	2	1.67190	54.869	4.0
11	1	0	3	1.65910	55.328	2.0
12	2	1	0	1.60820	57.238	1.0
13	2	1	1	1.54180	59.949	9.0
14	1	1	3	1.45360	64.001	1.0
15	3	0	0	1.41890	65.761	1.0
16	2	1	2	1.38200	67.750	6.0
17	2	0	3	1.37520	68.131	7.0
18	3	0	1	1.37180	68.323	8.0
19	1	0	4	1.28800	73.462	2.0
20	3	0	2	1.25580	75.671	2.0
21	2	2	0	1.22850	77.662	1.0
22	2	1	3	1.19990	79.878	2.0
23	2	2	1	1.19780	80.046	1.0
24	1	1	4	1.18430	81.148	3.0
25	3	1	0	1.18040	81.472	3.0
26	3	1	1	1.15320	83.821	1.0
27	2	0	4	1.14050	84.971	1.0
28	3	0	3	1.11430	87.464	1.0
29	3	1	2	1.08130	90.858	2.0
30	4	0	0	1.06350	92.822	1.0
31	1	0	5	1.04760	94.665	1.0
32	4	0	1	1.04380	95.119	1.0
33	2	1	4	1.03470	96.227	1.0
34	2	2	3	1.01500	98.738	1.0
35	4	0	2	0.98980	102.199	1.0
36	3	1	3	0.98730	102.559	1.0
37	3	0	4	0.97830	103.884	1.0
38	3	2	0	0.97620	104.199	1.0
39	2	0	5	0.96360	106.145	1.0

Stick Pattern



Name and formula

Reference code: 01-085-0335
 Mineral name: Quartz low
 CSD name: Silicon Oxide
 Empirical formula: O₂Si
 Chemical formula: SiO₂

Crystallographic parameters

Crystal system: Hexagonal
 Space group: P3221
 Space group number: 154

a (Å): 4.9134
 c (Å): 4.9134
 β (Å): 5.4052
 Alpha (°): 90.0000
 Beta (°): 90.0000
 Gamma (°): 120.0000

Calculated density (g/cm³): 2.65
 Volume of cell (10⁶ pm³): 113.01
 Z: 3.00

RIR: 0.14

Subfiles and Quality

Subfiles: Inorganic
 Mineral
 Alloy, metal or intermetallic
 Modelled additional pattern
 Quality: Calculated (C)

Comments

CSD collection code: 000174
 Test from ICSD: At least one TF implausible.

References

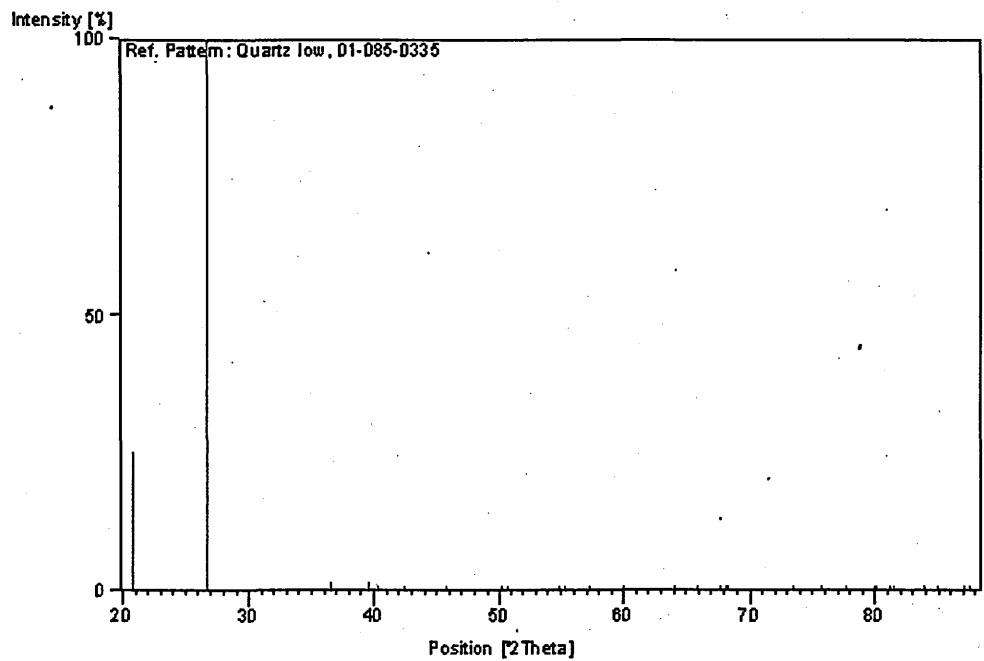
Primary reference: Calculated from ICSD using POWD-12++ (1997)
 Structure: le-Page, Y., Donnay, G., *Acta Crystallogr. Sec. B* **32**, 2456, (1976)

Peak list

No.	h	k	l	d [Å]	2Theta[deg]	I [%]
1	1	0	0	4.25513	20.859	25.2
2	0	1	1	3.34342	26.640	100.0
3	1	1	0	2.45670	36.547	1.6
4	1	0	2	2.28134	39.468	1.8
5	1	1	-1	2.23653	40.292	0.9
6	2	0	0	2.12756	42.453	1.0
7	2	0	1	1.97972	45.796	0.1
8	1	1	-2	1.81788	50.141	0.1
9	0	0	3	1.80173	50.622	0.1

10	0	2	2	1.67171	54.876	0.1
11	1	0	3	1.65913	55.327	0.1
12	1	2	0	1.60829	57.234	0.1
13	1	2	-1	1.54150	59.961	0.1
14	1	1	-3	1.45288	64.036	0.1
15	3	0	0	1.41838	65.788	0.1
16	2	1	-2	1.38208	67.745	0.1
17	0	2	3	1.37494	68.145	0.1
18	0	3	1	1.37193	68.315	0.1
19	0	1	4	1.28792	73.467	0.1
20	0	3	2	1.25592	75.662	0.1
21	2	2	0	1.22835	77.673	0.1
22	2	1	-3	1.19982	79.884	0.1
23	2	2	1	1.19781	80.045	0.1
24	1	1	-4	1.18401	81.172	0.1
25	3	1	0	1.18016	81.492	0.1
26	1	3	1	1.15300	83.839	0.1
27	0	2	4	1.14067	84.956	0.1
28	2	2	-2	1.11826	87.076	0.1
29	0	3	3	1.11447	87.447	0.1

Stick Pattern



APPENDIX 3a

DEDUCTION OF MG-SiC700 PARTICLE SIZES DERIVED FROM BATCH C RICE HUSK EXPERIMENTAL RESULTS.

Using the following parameters for MG-SiC700;

Full width at half maximum (FWHM) = 0.1506

The angle (θ) = $28.326/2 = 14.163$

Standard x-ray wavelength (λ) for used XRD equipment = 1.5416\AA

From Scherrer's equation,

$$D = \frac{0.9\lambda}{\beta \cos \theta};$$

where D is the crystallite size, β is the broadening of diffraction line measured at half of its maximum intensity (rad) (FWHM).

Converting \AA to m, where $1\text{\AA} = 10^{-10}\text{m}$;

It therefore implies $\lambda = 1.5416 \times 10^{-10}\text{m}$ for the standard X'pert instrument used.

$$\beta = \text{Conversion of FWHM to radian} = 0.1506 \times 0.01745 = 2.13588 \times 10^{-3} \text{ rad.}$$

By substituting parameters into Scherrer's equation,

$$D = \frac{0.9 \times 1.5416 \times 10^{-10}}{2.62797 \times 10^{-3} \cos 14.163}$$

$$D = 54.46\text{nm}$$

APPENDIX 3b

DEDUCTION OF MG-Si C800 PARTICLE SIZES DERIVED FROM BATCH C RICE HUSK EXPERIMENTAL RESULTS.

Using the following parameters for MG-SiC800;

Full width at half maximum (FWHM) = 0.1506

The angle (θ) = $28.5207/2 = 14.26035$

Standard x-ray wavelength (λ) for used XRD equipment = 1.5416\AA

From Scherrer's equation,

$$D = \frac{0.9\lambda}{\beta \cos \theta};$$

$$\beta = 0.1506 \times 0.01745 = 2.13588 \times 10^{-3} \text{ rad.}$$

$$D = \frac{0.9 \times 1.5416 \times 10^{-10}}{2.62797 \times 10^{-3} \cos 14.26035}$$

$$D = 54.49 \text{ nm}$$

APPENDIX 3c

DEDUCTION OF MG-Si C900 PARTICLE SIZES DERIVED FROM BATCH C RICE HUSK EXPERIMENTAL RESULTS.

Using the following parameters for MG-Si C900;

Full width at half maximum (FWHM) = 0.1338

The angle (θ) = $28.4606/2 = 14.2303$

Standard x-ray wavelength (λ) for used XRD equipment = 1.5416\AA

From Scherrer's equation,

$$D = \frac{0.9\lambda}{\beta \cos \theta};$$

β = Conversion of FWHM to radian = $0.1338 \times 0.01745 = 2.33481 \times 10^{-3}$ rad.

$$D = \frac{0.9 \times 1.5416 \times 10^{-10}}{2.33481 \times 10^{-3} \cos 14.2303}$$

$$D = 61.32\text{nm}$$

APPENDIX 3d

DEDUCTION OF MG-Si C1000 PARTICLE SIZES DERIVED FROM BATCH C RICE HUSK EXPERIMENTAL RESULTS.

Using the following parameters for MG-Si C1000;

Full width at half maximum (FWHM) = 0.1506

The angle (θ) = $28.5662/2 = 14.2831$

Standard x-ray wavelength (λ) for used XRD equipment = 1.5416\AA

From Scherrer's equation,

$$D = \frac{0.9\lambda}{\beta \cos \theta} ;$$

$$\beta = 0.1632 \times 0.01745 = 2.84784 \times 10^{-3} \text{ rad}$$

$$D = \frac{0.9 \times 1.5416 \times 10^{-10}}{2.84784 \times 10^{-3} \cos 14.2831}$$

$$D = 50.29 \text{ nm}$$

APPENDIX 3e

DEDUCTION OF Si Com PARTICLE SIZES DERIVED FROM BATCH C RICE HUSK EXPERIMENTAL RESULTS.

Using the following parameters for Si Com;

Full width at half maximum (FWHM) = 0.1506

The angle (θ) = $28.7451/2 = 14.37255$

Standard x-ray wavelength (λ) for used XRD equipment = 1.5416\AA

From Scherrer's equation,

$$D = \frac{0.9\lambda}{\beta \cos \theta};$$

$$\beta = 0.1224 \times 0.01745 = 2.13588 \times 10^{-3} \text{ rad}$$

$$D = \frac{0.9 \times 1.5416 \times 10^{-10}}{2.13588 \times 10^{-3} \cos 14.37255}$$

$$D = 67.08 \text{ nm}$$